UNIVERSITÀ
DEGLI STUDI
DI BRESCIA

DOTTORATO DI RICERCA IN PRECISION MEDICINE

settore scientifico disciplinare: CHIM/03

CICLO: XXXVII

TITOLO TESI:

EXPLORING THE EXTRACELLULAR VESICLE-NANOSTRUCTURED SECRETOME INTERFACE TOWARD CLINICAL TRANSLATION

DOTTORANDO:
Angelo Musicò

RELATORE:
Prof.ssa Annalisa Radeghieri

CO-RELATORE:
Prof. Paolo Bergese

A Marina

INDEX

Riassunto

Le vescicole extracellulari (EVs), in quanto nanoparticelle biogeniche, offrono un grande potenziale diagnostico e terapeutico grazie alla loro biocompatibilità, alla capacità di trasportare molecole bioattive e alla possibilità di fornire un rilascio mirato di farmaci. Tuttavia, la loro traslazione clinica incontra sfide legate alle loro proprietà chimico-fisiche, ai fenomeni interfacciali e alle loro interazioni dinamiche nei fluidi biologici, che alterano la loro identità biologica e funzione. Pertanto, questa tesi di dottorato ha avuto l'obiettivo di studiare le interazioni all'interfaccia tra le EVs e il secretoma nanostrutturato, con l'intento di favorire la traslazione delle EV in medicina di precisione colmando il divario tra i risultati sperimentali e l'applicazione clinica.

Nello specifico, il Capitolo 1 offre una panoramica completa delle EVs nella nanomedicina, delineando le loro applicazioni nella diagnostica, nel rilascio di farmaci e nelle terapie, evidenziando al contempo le attuali limitazioni per la loro applicazione clinica. Il Capitolo 2 introduce i fenomeni all'interfaccia tra EVs e secretoma nanostrutturato, concentrandosi sulla formazione della corona biomolecolare (BC) e le sue implicazioni sull'identità, la funzione e la biodistribuzione delle EVs.

Nel Capitolo 3, lo studio indaga l'effetto del fisisorbimento di proteine durante la funzionalizzazione superficiale delle EVs con anticorpi, sottolineando l'importanza di controllare tutte le fasi del processo, poiché questo adsorbimento può andare ad influenzare significativamente l'efficacia del targeting per cui la formulazione di EVs è stata progettata.

Il Capitolo 4 presenta un approccio innovativo basato sulla spettroscopia di correlazione di fluorescenza (FCS) per studiare la dinamica di formazione della BC su due diverse sottopopolazioni di EVs in condizioni fisiologiche, fornendo nuovi dati su come la composizione e le proprietà superficiali delle EVs influenzano il loro comportamento biologico.

Nel Capitolo 5, vengono esaminate le interazioni tra EVs e lipoproteine (HDL, LDL, VLDL) utilizzando la spettroscopia di correlazione incrociata di fluorescenza (FCCS). I risultati rivelano modelli di interazione distinti, potenzialmente rilevanti dal punto di vista biologico a causa del ruolo degli aggregati EV-lipoproteine in condizioni patologiche come, per esempio, la metastasi tumorale.

Infine, il Capitolo 6 descrive lo sviluppo di una piattaforma multimodale per il rilascio di farmaci basata su EVs, mirata al trattamento del carcinoma mammario triplo negativo (TNBC). Ingegnerizzando le EVs per trasportare cetuximab e cisplatino, questo approccio migliora l'efficienza del rilascio dei farmaci, riduce la chemioresistenza e attiva meccanismi di morte cellulare come la ferroptosi, offrendo una promettente soluzione per il trattamento del TNBC.

Complessivamente, questa tesi rappresenta un avanzamento nella comprensione dei fenomeni interfacciali delle EVs e delle loro applicazioni nei sistemi di trasporto di farmaci. I risultati forniscono una base per studi futuri che potrebbero portare alla traslazione clinica di terapie basate su EVs, specialmente nel contesto della medicina di precisione, aprendo nuove strade per lo sviluppo di farmaci nanotecnologici specifici per patologie complicate da trattare, come il TNBC.

Abstract

Extracellular Vesicles (EVs), as biogenic nanoparticles, hold great potential for disease diagnosis and treatment due to their biocompatibility, ability to transport bioactive molecules, and capacity for targeted delivery. However, their clinical translation faces challenges related to their physicochemical properties, interfacial phenomena, and dynamic interactions within biological fluids that alter their biological identity and function. Thus, this PhD thesis aims to investigate the interface between EVs and nanostructured secretomes, aiming to advance precision medicine by bridging experimental findings with clinical applications.

Specifically, Chapter 1 provides a comprehensive overview of EVs in nanomedicine, outlining their applications in diagnostics, drug delivery, and therapy, while also discussing current limitations in their clinical application. Chapter 2 explores the EV-nanostructured secretome interface, focusing on the formation of the biomolecular corona (BC) on the EV surface and its implications for EV identity, function, and biodistribution.

In Chapter 3, the study investigates the effect of protein physisorption during EV surface functionalization with targeting antibodies, emphasizing the importance of controlling functionalization steps, as protein adsorption can significantly affect the efficacy of EV-based therapies.

Chapter 4 presents a novel fluorescence correlation spectroscopy (FCS)-based approach to study BC dynamic formation on two distinct EV subpopulations in physiological conditions, revealing how differences in EV origin and, in turn, composition and surface properties affect their interactions and biological behavior.

Chapter 5 examines the interactions between EVs and lipoproteins (HDL, LDL, VLDL) using fluorescence cross-correlation spectroscopy (FCCS). The results reveal distinct interaction patterns, which may be biologically relevant due to the role of EV-lipoprotein aggregates in pathological conditions, such as cancer metastasis.

Finally, Chapter 6 details the development of a multimodal EV-based drug delivery (nano)platform for triple-negative breast cancer (TNBC). By engineering EVs to carry cetuximab and cisplatin, this approach enhances drug delivery efficiency, reduces chemoresistance, and activates cell-death pathways such as ferroptosis, offering a promising solution for TNBC treatment.

Overall, this thesis provides a focused exploration of EV interfacial interactions and their implications for clinical applications, particularly in drug delivery systems. By addressing knowledge gaps and presenting new methodologies, this thesis lays a foundation for future studies

aimed at advancing the clinical translation of EV-based therapies and developing targeted treatments for challenging diseases like TNBC.

Disclosure Statement and Publications

The results presented in this thesis have been obtained during my Ph.D. studies (November 2021 – November 2024) at the University of Brescia (Brescia, Italy) and CICbiomaGUNE (San Sebastian, Spain), at the Soft Matter and Nanotechnology Lab., led by Dr. Sergio Moya. Some of the experimental chapters, hereafter described, contain several not-yet-published data.

Publications

During my Ph.D. studies, I contributed to several projects regarding extracellular vesicles (EVs) that led to the publication of the papers listed below (and reported as front page in the Appendix):

1) **Elucidating the 3D Structure of a Surface Membrane Antigen from Trypanosoma cruzi as a Serodiagnostic Biomarker of Chagas Disease**. Flavio Di Pisa, Stefano De Benedetti, Enrico Mario Alessandro Fassi, Mauro Bombaci, Renata Grifantini, **Angelo Musicò**, Roberto Frigerio, Angela Pontillo, Cinzia Rigo, Sandra Abelli, Romualdo Grande, Nadia Zanchetta, Davide Mileto, Alessandro Mancon, Alberto Rizzo, Alessandro Gori, Marina Cretich, Giorgio Colombo, Martino Bolognesi, Louise Jane Gourlay. 2022/1/3. *Vaccines*
2) **Composite Peptide–Agarose Hydrogels for Robust and High-Sensitivity 3D Immunoassays**. Greta Bergamaschi, **Angelo Musicò**, Roberto Frigerio, Alessandro Strada, Andrea Pizzi, Benedetta Talone, Jacopo Ghezzi, Alfonso Gautieri, Marcella Chiari, Pierangelo Metrangolo, Renzo Vanna, Francesca Baldelli Bombelli, Marina Cretich, Alessandro Gori. 2022/1/21. *ACS Applied Materials & Interfaces*
3) **Comparing digital detection platforms in high sensitivity immune-phenotyping of extracellular vesicles**. Roberto Frigerio, **Angelo Musicò**, Alessandro Strada, Greta Bergamaschi, Stefano Panella, Cristina Grange, Marcello Marelli, Anna M Ferretti, Gabriella Andriolo, Benedetta Bussolati, Lucio Barile, Marcella Chiari, Alessandro Gori, Marina Cretich. 2022/8. *Journal of Extracellular Biology*
4) **Epitope Mapping on Microarrays Highlights a Sequence on the N Protein with Strong Immune Response in SARS-CoV-2 Patients**. Roberto Frigerio, **Angelo Musicò**, Alessandro Strada, Alessandro Mussida, Paola Gagni, Greta Bergamaschi, Marcella

Chiari, Luisa Barzon, Alessandro Gori, Marina Cretich. 2022/9/25. Book Chapter in: *Peptide Microarrays: Methods and Protocols*

5) **Hybrid Peptide–Agarose Hydrogels for 3D Immunoassays**. **Angelo Musicò**, Greta Bergamaschi, Alessandro Strada, Roberto Frigerio, Paola Gagni, Marina Cretich, Alessandro Gori. 2022/9/25. Book Chapter in: *Peptide Microarrays: Methods and Protocols*
6) **Surface functionalization of extracellular vesicle nanoparticles with antibodies: A first study on the protein corona "variable". Angelo Musicò**, Rossella Zenatelli, Miriam Romano, Andrea Zendrini, Silvia Alacqua, Selene Tassoni, Lucia Paolini, Chiara Urbinati, Marco Rusnati, Paolo Bergese, Giuseppe Pomarico, Annalisa Radeghieri. 2023. *Nanoscale Advances*
7) **Particle profiling of EV-lipoprotein mixtures by AFM nanomechanical imaging**. Andrea Ridolfi, Laura Conti, Marco Brucale, Roberto Frigerio, Jacopo Cardellini, **Angelo Musicò**, Miriam Romano, Andrea Zendrini, Laura Polito, Greta Bergamaschi, Alessandro Gori, Costanza Montis, Stefano Panella, Lucio Barile, Debora Berti, Annalisa Radeghieri, Paolo Bergese, Marina Cretich, Francesco Valle. 2023/10. *Journal of Extracellular Vesicles*
8) **Extracellular vesicle analysis in supramolecular 3D hydrogels: a proof-of-concept**. Greta Bergamaschi, Roberto Frigerio, **Angelo Musicò**, Giulia Lodigiani, Paola Gagni, Riccardo Vago, Marina Cretich, Alessandro Gori. 2024. *Sensors & Diagnostics*
9) **Minimal information for studies of extracellular vesicles (MISEV2023): From basic to advanced approaches**. Joshua A. Welsh, Deborah C. I. Goberdhan, Lorraine O'Driscoll, Edit I. Buzas, Cherie Blenkiron, Benedetta Bussolati, Houjian Cai, Dolores Di Vizio, Tom A. P. Driedonks, Uta Erdbrügger, Juan M. Falcon-Perez, Qing-Ling Fu, Andrew F. Hill, Metka Lenassi, Sai Kiang Lim, Mỹ G. Mahoney, Sujata Mohanty, Andreas Möller, Rienk Nieuwland, Takahiro Ochiya, Susmita Sahoo, Ana C. Torrecilhas, Lei Zheng, Andries Zijlstra, Sarah Abuelreich, Reem Bagabas, Paolo Bergese, Esther M. Bridges, Marco Brucale, Dylan Burger, Randy P. Carney, Emanuele Cocucci, Rossella Crescitelli, Edveena Hanser, Adrian L. Harris, Norman J. Haughey, An Hendrix, Alexander R. Ivanov, Tijana Jovanovic-Talisman, Nicole A. Kruh-Garcia, Vroniqa Ku'ulei-Lyn Faustino, Diego Kyburz, Cecilia Lässer, Kathleen M. Lennon, Jan Lötvall, Adam L. Maddox, Elena S. Martens-Uzunova, Rachel R. Mizenko, Lauren A. Newman, Andrea Ridolfi, Eva Rohde, Tatu Rojalin, Andrew Rowland, Andras Saftics, Ursula S. Sandau, Julie A. Saugstad, Faezeh Shekari, Simon Swift, Dmitry Ter-Ovanesyan, Juan P.

Tosar, Zivile Useckaite, Francesco Valle, Zoltan Varga, Edwin van der Pol, Martijn J. C. van Herwijnen, Marca H. M. Wauben, Ann M. Wehman, Sarah Williams, Andrea Zendrini, Alan J. Zimmerman, **MISEV Consortium**, Clotilde Théry, Kenneth W. Witwer. 2024/2. *Journal of extracellular vesicles*

10) **Extracellular vesicles of different cellular origin feature distinct biomolecular corona dynamics. Angelo Musicò**, Andrea Zendrini, Santiago Gimenez Reyes, Valentina Mangolini, Lucia Paolini, Miriam Romano, Andrea Papait, Antonietta Rosa Silini, Paolo Di Gianvincenzo, Arabella Neva, Marina Cretich, Ornella Parolini, Camillo Almici, Sergio Moya, Annalisa Radeghieri, Paolo Bergese. 2024/10/24. *Nanoscale Horizons*

Chapter 1 - Extracellular vesicles in Nanomedicine

Nanomedicine is a field of medicine that utilizes nanotechnology for disease prevention, monitoring, and treatment through advanced imaging, diagnostics, and therapeutic approaches, as well as the repair and regeneration of biological systems[1]. Nanomedicine research aims to bring innovative therapies, diagnostic methods, and more effective biomaterials for tissue regeneration into clinical practice, ultimately enhancing patient health and quality of life[2]. It is anticipated that nanomedicine will enable the development of improved devices, drugs, and other applications for the early diagnosis and treatment of various diseases with high specificity, efficacy, and personalization[3]. Classifying nanomedicines is a complex process due to the diversity of nanoparticles (NPs) and nanomaterials (NMs). NMs can be grouped based on various criteria, including dimensionality, morphology, physical state, chemical composition, or nanotoxicology[4–6]. They are commonly categorized as either synthetic or biogenic, depending on their method of production. The work presented in this thesis is focused on the exploitability of Extracellular Vesicles (EVs) as vectors for advanced biogenic nanomedicine. Indeed, EVs have garnered significant interest for their diagnostic and therapeutic potential due to several key properties: I) their ability to transport various active biomolecules, making them suitable for delivering therapeutic drugs[7–9], II) their capacity to carry and protect a diverse range of nucleic acids, which can be functionally delivered into recipient cells[10,11], III) their inherent stability in circulation, attributed to their negatively charged surface and ability to avoid the mononuclear phagocytic system (MPS) by displaying "don't eat me" signals[12–14], IV) their extensive biological functions, including shuttling large molecules between cells and crossing biological barriers[15–17], and V) their targeting capabilities, which are determined by the lipid composition and protein content of EVs[18,19]. However, several limitations are still hindering the actual translation of EVs in nanomedicine, as better explained in Chapter 2. This chapter introduces EVs nanoparticles with their key features and biological roles, their possible applications as diagnostics and therapeutics, and the different state-of-the-art strategies to engineer their surface and load drugs.

1.1 Extracellular Vesicles

Extracellular vesicles (EVs) are soft nanoparticles composed of a phospholipid bilayer membrane that encloses an aqueous core enriched in proteins, nucleic acids, and metabolites[20,21]. They play a crucial role in cell-to-cell and cell-to-microenvironment communication and are emerging as universal agents in intra- and cross-organism communication for a wide range of organisms,

including mammals, viruses, bacteria, archaea, microbes, parasites, fungi, and plants[22,23]. EVs are traditionally categorized into exosomes and microvesicles (MVs) based on their biogenesis. Exosomes, which range in size from 30 to 250 nm, originate from intracytoplasmic multivesicular bodies (MVBs) and are released into the extracellular space when the MVB membrane fuses with the plasma membrane[24]. MVs, on the other hand, bud directly from the plasma membrane and range in size from 150 to 800 nm[25]. Due to the overlap in size and shared biomarkers between exosomes and MVs, a more recent classification refers to EVs in the 30–250 nm range as small EVs and those in the 150–800 nm range as large EVs[26]. EVs represent a third mode of cell communication, alongside direct intercellular physical stimuli and paracrine secretion of active molecules. They act as vehicles for bioactive cargoes, protecting them from degradation and delivering them to target cells[27]. EVs participate in various physiological processes, such as coagulation and immune system activation, but they also facilitate the maintenance and spread of pathological processes[28–30]. For example, malignant tumors utilize EVs to establish pre-metastatic niches and colonize healthy organs[31]. EVs are present in all biological fluids and reflect the phenotype of the releasing cell, including its functions. They also exhibit specific compositional enrichment, particularly in lipids and proteins[32–34]. For instance, EVs isolated from mesenchymal stem cells (MSCs) replicate some of the biological effects of MSCs, especially those related to their regenerative potential[35].

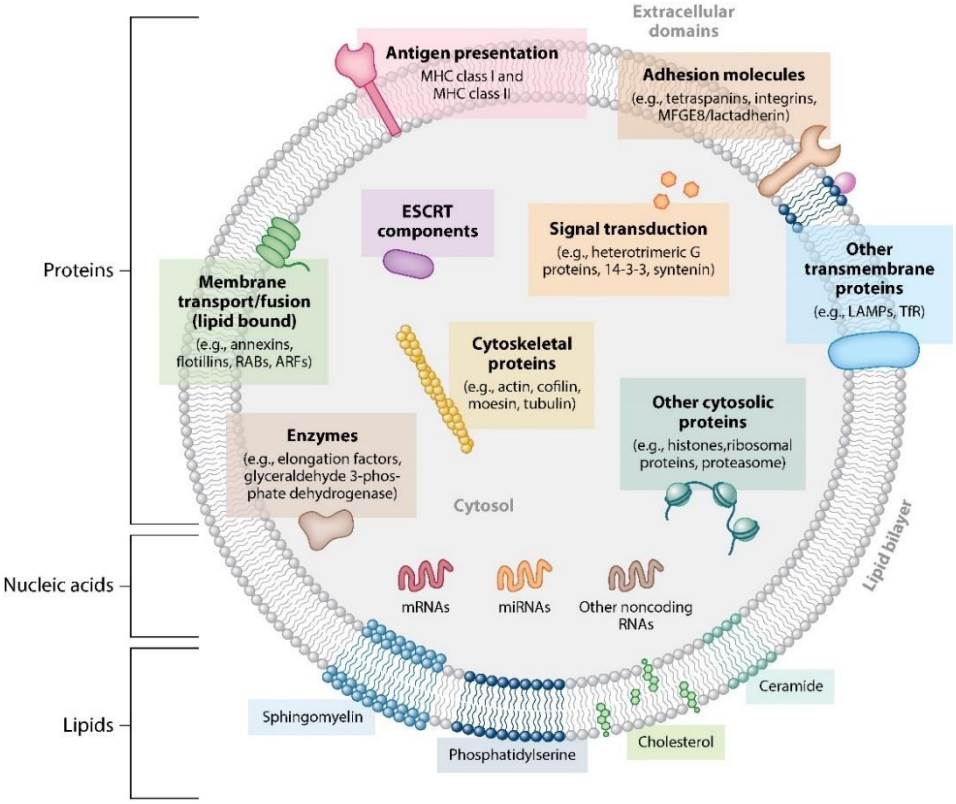

Figure 1.1. Schematic representation of EVs[21].

Regardless of their origin, vesicles are taken up by target cells through various mechanisms, including endocytic pathways (such as receptor-mediated, clathrin-dependent, or caveolin-mediated endocytosis, phagocytosis, macropinocytosis, and lipid raft-mediated internalization), or by fusing directly with the plasma membrane[22]. Extracellular vesicles (EVs) can activate multiple entry routes into a cell, with the primary mode of entry determined by the cell type and the EV's composition. The transfer of EVs facilitates the exchange of materials between "donor" and "recipient" cells, playing a key role in intercellular communication in vivo[36]. EVs influence essential biological processes by: (i) directly activating cell surface receptors through protein and bioactive lipid ligands, (ii) integrating their membrane components into the recipient cell's plasma membrane, and (iii) delivering effectors such as transcription factors, oncogenes, regulatory RNAs (including miRNAs and mRNAs), and infectious particles[13]. Each cell adjusts EV biogenesis, quantity, and content based on its physiological condition, releasing EVs with specific lipid, protein, and nucleic acid profiles. Additionally, evidence shows that EV production is influenced by various pathological conditions or altered physiological states, such as pregnancy.

1.2 Applications in diagnostics and therapeutics

EVs are present in all biofluids, released by various cell types, and differ in molecular content based on the cells of origin and their pathophysiological state. This makes them valuable sources of biomarkers in both physiological and pathological conditions[37]. EVs act as stable and easily accessible fingerprints of parent cells, providing a means for minimally invasive liquid biopsies[38–40]. Their cargo is protected from degradation, offering a reliable source of biomarkers[41,42]. EVs have been linked to numerous processes, including cancer progression, where they can promote growth by inhibiting immune recognition and preparing pre-metastatic niches[43–46]. They also play roles in viral spread[47] and are associated with various diseases, making them potential biomarkers for conditions like neurological, metabolic, cardiovascular, and kidney diseases[48–54]. EVs carry molecular markers such as proteins, carbohydrates, and nucleic acids, and their size, concentration, and mechanical properties can also serve as biophysical markers[33]. These characteristics have been used to detect diseases like pancreatic cancer and multiple myeloma[55–57]. However, challenges like the lack of standardized purification protocols limit the full exploitation of EVs as biomarkers[58–61].

EVs also hold promise in therapeutic applications, including drug delivery[62], vaccination[63], and regenerative medicine[64–67]. They can deliver biomolecules between cells, including therapeutic RNAs, chemotherapeutics, and small molecules[32,68]. EVs' proteo-lipid structure protects their cargo, and their self-derived nature minimizes immune response. They also exhibit targeting properties, making them effective drug delivery systems[69–71]. EV targeting properties can be

intrinsic (modulated by pristine EV characteristics, e.g. homing mechanisms)[72,73] or acquired by engineering processes, as better explained in Chapter 1.2.2. As vaccine carriers, EVs can modulate immune responses. For instance, parasite-derived EVs carrying antigens can be used as vaccines, and tumor-derived EVs can be used to induce an antitumor immune response[74]. In regenerative medicine, EVs from mesenchymal stem cells (MSCs) mimic the therapeutic effects of MSCs, promoting tissue repair and regeneration[75,76]. EVs offer also advantages over cell therapy, such as avoiding the risk of neoplastic transformation and providing stability[77–80]. They have been studied in preclinical settings for treating various conditions, including graft-versus-host disease and chronic kidney diseases[35,81–83].

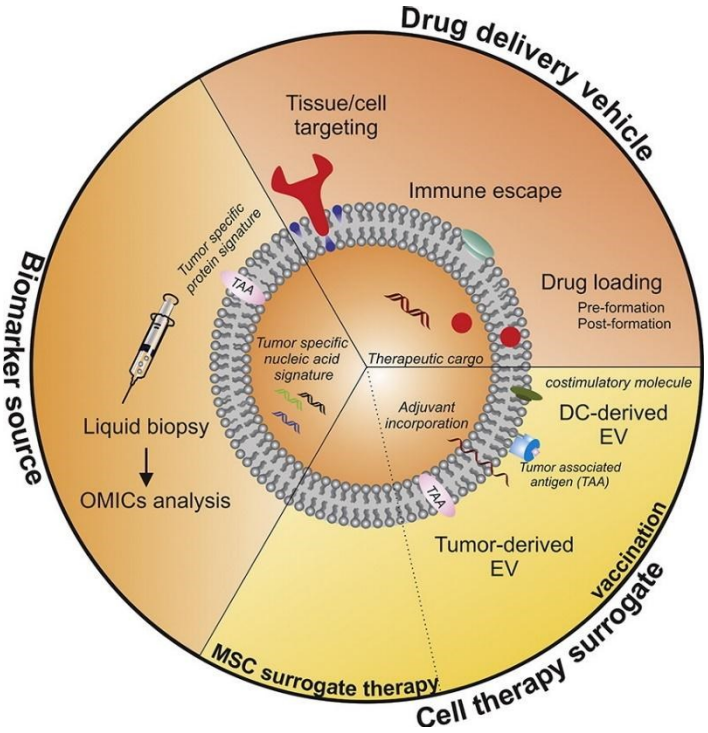

Figure 2.1. Schematic representation of the EV emerging diagnostic and therapeutic applications. EVs may represent a powerful source of biomarkers, as well as a promising therapeutic platform. EV applications in clinics include the use of EVs as highly biocompatible drug delivery vehicles[61].

The work presented in this thesis is mainly oriented towards the development of EV-based drug delivery systems and therapeutics. For this reason, the EV models used in this study (presented from Chapter 3 to Chapter 6) are Red Blood Cells-derived EVs (REVs) and Mesenchymal Stem Cells-derived EVs (MEVs). These two EV subpopulations are emerging as the most promising candidates for EV-based therapeutics due to their key features, which are resumed as follows:

Red Blood Cells-derived EVs: REVs are lipid vesicles released from red blood cells (RBCs), typically 100–200 nm in size, and include microvesicles derived from the plasma membrane[84].

They are released during RBC aging, erythropoiesis, disease conditions, and environmental stress. RBC microvesicles form through plasma membrane budding, driven by complement-mediated calcium influx[85]. These vesicles play roles in regulating NO and O2 balance, redox homeostasis, and immune modulation. REV biogenesis involves structural changes to the RBC membrane, triggered by oxidative damage, increased intracellular calcium, and RBC storage. Two main mechanisms drive this process: band 3 protein oxidation and clustering, and changes in phospholipid distribution in the membrane[86]. REVs contain various lipids, proteins, cholesterol, and miRNAs and differ from intact RBCs by having fewer cytoskeletal proteins. They are enriched in miRNAs like miR-125b-5p, miR-4454, and miR-451a, and express CD47, which helps them evade immune detection[87]. In medicine, REVs are promising for drug delivery due to their low immunogenicity, biocompatibility, and ability to be autologously sourced, reducing immune risks[88].

Mesenchymal Stem Cells-derived EVs: MEVs have gained significant attention as a novel therapeutic platform. These extracellular vesicles, which include exosomes and microvesicles, are small membrane-bound particles secreted by mesenchymal stem cells (MSCs)[89]. They carry a diverse cargo of bioactive molecules, such as proteins, lipids, RNA, and microRNAs, that are crucial in mediating cell-to-cell communication and tissue repair processes[90]. MSC-EVs mimic many of the therapeutic effects of MSCs, including anti-inflammatory, immunomodulatory, and regenerative properties, but without the risks associated with cell-based therapies, such as immune rejection or uncontrolled cell growth[91]. They offer several advantages, including ease of storage, the ability to cross biological barriers, and a lower risk of tumor formation or embolism compared to MSCs themselves. Moreover, MSC-EVs can be engineered to enhance their therapeutic potential by loading them with specific drugs or genetic material[92]. These properties make MSC-EVs a highly attractive candidate for treating a wide range of conditions, including inflammatory diseases, autoimmune disorders, tissue injuries, and even neurodegenerative diseases[93]. Their versatility and safety profile have positioned them at the forefront of research into cell-free regenerative medicine therapies.

1.2.1 EV surface engineering

To improve EV targeting abilities for their exploitation in precision medicine several engineering strategies have been developed to decorate EV surface with targeting moieties such as peptides, antibodies, small molecules, etc[94,95]. A key advantage of using EVs as drug delivery systems over synthetic carriers is the ability to modify EV surfaces by altering their parent cells. Surface functionalization can be achieved before EV isolation through various methods, including genetic,

metabolic, and direct parent cell membrane engineering techniques. Also, EVs offer several synthetic opportunities due to their amphiphilic nature and the presence of different reactive groups on their surface. So, EV surface engineering strategies can be resumed in two macro classes: pre-isolation and post-isolation engineering[96,97].

Pre-isolation engineering: Genetic engineering strategies for EV surface functionalization involve expressing transgenes that produce proteins or chimeric proteins known to be enriched in EVs. This method, pioneered by Matthew Wood's lab, involves fusing targeting peptides to EV proteins like Lamp2b, leading to their exterior expression on EVs[10]. For instance, Lamp2b fusions with IL-3 or cardiomyocyte-specific peptides increase EV uptake by specific cells both in vitro and in vivo[10]. Additionally, constructs with the PDGFR transmembrane domain fused to targeting peptides have been used to target EVs to specific cells, enhancing anti-tumor immunity by recruiting T-cells[40]. Another strategy involves attaching targeting proteins to EV membranes using GPI-anchor signal peptides[98]. These methods, while effective in targeting specific cells, don't significantly alter biodistribution profiles compared to unmodified EVs. Genetic engineering can also enhance EVs with pharmaceutical activities. For example, expressing TRAIL, a cancer cell apoptosis-inducing protein, in mesenchymal stem cells leads to its incorporation into EVs, showing higher efficacy in inducing cancer cell apoptosis than soluble TRAIL[99]. EVs can also be engineered to express decoy receptors that reduce disease activity of pro-inflammatory cytokines, showing higher efficacy than soluble receptors[56]. Additionally, expressing tumor-associated antigens on EVs can induce stronger antigen-specific immune responses for cancer immunotherapy[100]. Moreover, genetic strategies enable fluorescent, luminescent, or radioactive tracking of EVs, facilitating live evaluation of EV uptake, distribution, and pharmacokinetics. Fusion proteins with fluorescent or luminescent markers allow parallel imaging techniques for in vivo tracking[101–105]. Overall, the genetic engineering of EVs offers significant potential for targeting, tracking, and therapeutic applications[98,106]. Key considerations include optimizing fusion constructs for maximum expression and ensuring the integrity of targeting or therapeutic moieties[107,108]. Metabolic and direct parent cell membrane engineering are others pre-isolation approaches, which offer alternative methods for EV functionalization, allowing the incorporation of biorthogonal chemical groups or functional lipids into EV membranes[109,110].

Post-isolation engineering: Surface modification of EVs can also occur post-isolation, requiring more steps and time but offering distinct advantages. Unlike genetic modification, which is limited to proteins or peptides, post-isolation methods can employ various molecules or ligands without the need for parent cell engineering. This is particularly beneficial for EVs derived from sources like patient plasma and eliminates the need for extensive knowledge of surface proteins. Post-

isolation surface modification methods include physical interactions and chemical modifications, sometimes combining both. One promising approach is fusing EVs with liposomes, which can be monitored using Förster resonance energy transfer (FRET)[111]. A study by Sato et al. used freeze-thaw cycles to fuse EVs with liposomes, noting increased uptake with PEGylation but not addressing hemifusion or purification[111]. Piffoux et al. improved on this by developing a PEG-mediated fusion method, achieving up to 62% fusion efficiency and transferring liposome cargoes effectively. Despite promising results, the method's main downside is the slow and complicated purification process[112].

Other physical methods, like phospholipid- and cholesterol-post-insertion, allow surface functionalization without organic solvents. Phospholipids require higher temperatures for insertion compared to cholesterol, which inserts more easily but is less stable. These methods have shown success in various applications, such as targeting specific cells or silencing genes[113–115]. Adsorption-based modifications target specific EV surface features or rely on general properties like surface charge. For example, Gao et al. used adsorption to target muscle tissue, while others used cationized pullulan for liver targeting[116–118]. Chemical surface modifications involve the covalent linkage of molecules to EV surfaces, primarily through amino groups. Techniques like azide-alkyne cycloaddition (CuAAC and SPAAC) are commonly used. SPAAC is favored due to its mild conditions and high selectivity, making it suitable for EV labeling[119–122]. However, optimizing these methods requires further evaluation of the effects on EV functionality and addressing potential side reactions from non-vesicular material. Overall, while physical methods for EV-engineering are less explored than genetic ones, PEG-mediated fusion and chemical surface engineering hold significant promise for future applications, allowing simultaneous drug encapsulation and targeting moiety introduction without compromising EV integrity[123–125].

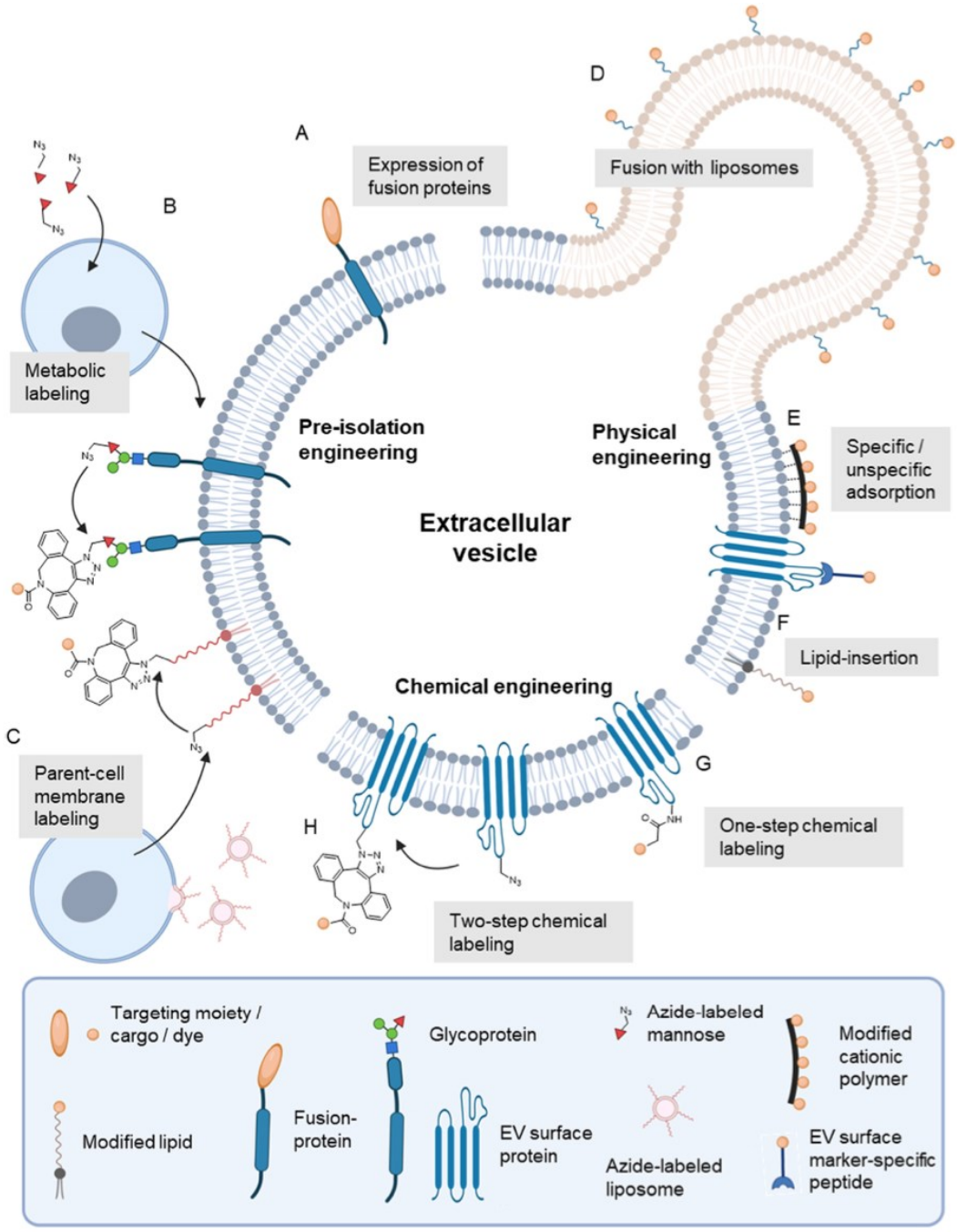

Figure 3.1. Overview of EV surface engineering methods. Modification can take place before EV-isolation by: expressing fusion proteins of EV membrane-proteins and the protein of interest (A); feeding the parent cells with azide-labeled metabolites (metabolic labeling, B) or fusing them with azide-labeled liposomes (parent-cell membrane labeling, C), to generate EVs bearing azide groups. After EV-isolation, the vesicles can be engineered by physical or chemical means. Physical engineering can take place through fusion with liposomes (D), specific or unspecific adsorption of molecules to the EV-surface (E), and the insertion of lipids (F). Chemical engineering with simple molecules can be carried out in one step through reaction with amino acid side-chains of EV surface-proteins (G), while more complex molecules can be coupled chemically to EVs by first introducing azide groups that may subsequently be labeled (H)[85].

1.2.2 EV drug-loading

EVs are physiological carriers of biomaterials involved in cell-to-cell communication, for this reason, they went under the spotlight for the development of new drug delivery systems. To do this, researchers developed several different strategies to load drugs into EVs[126]. These strategies exploit different mechanisms, and, as surface engineering methods, they can be resumed in pre-isolation and post-isolation methods.

Incubation: Incubation is a straightforward method for drug loading into extracellular vesicles (EVs). For instance, Sun et al. (2010) loaded curcumin into exosomes derived from a lymphoma cell line by incubating for 5 minutes at room temperature (22°C), followed by purification via sucrose gradient centrifugation[127,128]. Curcumin-loaded exosomes exhibited enhanced anti-inflammatory activity compared to free curcumin both in vitro and in vivo. Similarly, other researchers reported drug loading into bovine milk-derived exosomes using room temperature incubation, confirming drug loading via ultracentrifugation and UPLC. These EVs showed significantly higher anticancer effects than free drugs[129].

Sonication: Sonication employs mechanical shear force to disrupt EV membranes for effective drug loading[130]. Kim and coworkers demonstrated that sonication provided higher Paclitaxel loading efficiency compared to incubation and sonication, resulting in improved drug delivery and efficacy against lung cancer cells[131]. It has also been shown that catalase-loaded exosomes via sonication accumulated effectively in brain cells, offering neuroprotective effects in a Parkinson's disease model[132].

Electroporation: uses an electrical field to temporarily create pores in EV membranes for drug entry[133]. Tian et al. used electroporation to load doxorubicin into dendritic cell-derived exosomes, achieving higher cytotoxicity in cancer cells[134].

Freeze-Thaw: this method involves cycles of freezing and thawing to load drugs into EVs. While effective, it can cause the degradation of EV proteins and structural changes.

Extrusion: Extruding EVs through nanosized filters can load drugs into EVs as demonstrated by Kalimuthu et al., they used this method to load PTX into EVs, resulting in significant inhibition of breast cancer cell viability and tumor growth[135].

Saponification: Saponin treatment creates small pores in EV membranes, facilitating drug entry[136]. For example, Haney's group reported that saponin-based catalase-loaded exosomes had potent neuroprotective effects in a Parkinson's disease model[132].

Drug Treatment of Parental Cells: This approach involves treating cells with drugs before EV isolation. Pascucci et al. loaded paclitaxel into mesenchymal stem cell-derived EVs, showing strong antiproliferative activity against pancreatic adenocarcinoma[137].

Gene Engineering of Parental Cells: Gene engineering of cells to produce EVs with specific RNAs or proteins is a sophisticated loading method that has been used to engineer cells to produce EVs loaded with miRNA or therapeutic proteins, demonstrating targeted delivery and therapeutic efficacy[130,138,139].

Loading Strategies	Loading Methods	Advantages	Disadvantages
Pre-loading	Co-incubation	1. Simple 2. Cost-effective 3. EV-friendly	1. Low encapsulation efficiency 2. Strict cargo selection
	Transfection	Target molecule overexpression	1. Time-consuming 2. Highly dependent on cell viability 3. Potential toxicity and genetic changes
Post-loading	Co-incubation	1. Easy operation 2. No extra equipment is required 3. Minimal destruction to EVs	1. Low loading efficiency 2. Limited variety
	Electroporation	1. Effective loading efficiency 2. Loading of large biomolecules	1. Affect EVs integrity 2. Risk of EVs aggregation 3. Heat can cause damage
	Sonication	High loading efficiency	1. EVs membrane degradation 2. EV aggregation risk
	Freeze–thawing cycle	1. Cost-effective 2. Applicable for most cargoes	1. Low loading efficiency 2. EVs membrane damage 3. EVs aggregation risk
	Surfactant administration	1. Affordable 2. Applicable for most cargoes	EVs surface potential and functionality may be altered

Table 1.1. Methods for loading EVs with drugs[115].

1.3 Limitations for the application of EVs in nanomedicine

EVs offer remarkable opportunities for medical translation, particularly in their applications as therapeutic agents (e.g., drug delivery systems, vaccines) and diagnostic tools (e.g., biomarker sources). Currently, EVs are used in various preclinical studies as therapeutics for translational medicine. Despite promising preclinical results, several challenges hinder the clinical adoption of EV-based therapies[140]. One major issue is the lack of methods to isolate pure EV populations and the absence of standardized characterization procedures, which significantly limits clinical implementation[64]. Traditional EV purification techniques often suffer from drawbacks like low purity and lengthy processing times, making them insufficient for research and clinical needs. Therefore, advancing superior purification methods and ensuring EV purity is critical. Another challenge lies in the undefined biodistribution and circulation kinetics of EVs[69,70,141]. Non-invasive imaging techniques and animal models could help clarify the mechanisms of EV action, optimal dosing, and their accumulation in certain organs, such as the lungs or liver, which is crucial for practical applications. However, the physicochemical properties and interfacial phenomena of EVs are driving a paradigm shift in the field. In biofluids, EVs dynamically interact with other

(bio)components of the complex biological matrix, significantly altering their biological and intrinsic identity. These interactions contribute to several key challenges, such as the purity of EV preparations, their biodistribution, and pharmacokinetics, all of which are closely tied to the physicochemical characteristics and interfacial behavior of EVs. A deeper understanding and fine-tuning of these aspects are essential for overcoming these limitations and advancing EVs toward clinical application. Chapter 2 will delve into these topics, aligning them with the aim of this thesis.

1.4 References

(1) Liz-Marzán, L. M.; Nel, A. E.; Brinker, C. J.; Chan, W. C. W.; Chen, C.; Chen, X.; Ho, D.; Hu, T.; Kataoka, K.; Kotov, N. A.; Parak, W. J.; Stevens, M. M. What Do We Mean When We Say Nanomedicine? *ACS Nano*. American Chemical Society September 27, 2022, pp 13257–13259. https://doi.org/10.1021/acsnano.2c08675.

(2) Pelaz, B.; Alexiou, C.; Alvarez-Puebla, R. A.; Alves, F.; Andrews, A. M.; Ashraf, S.; Balogh, L. P.; Ballerini, L.; Bestetti, A.; Brendel, C.; Bosi, S.; Carril, M.; Chan, W. C. W.; Chen, C.; Chen, X.; Chen, X.; Cheng, Z.; Cui, D.; Du, J.; Dullin, C.; Escudero, A.; Feliu, N.; Gao, M.; George, M.; Gogotsi, Y.; Grünweller, A.; Gu, Z.; Halas, N. J.; Hampp, N.; Hartmann, R. K.; Hersam, M. C.; Hunziker, P.; Jian, J.; Jiang, X.; Jungebluth, P.; Kadhiresan, P.; Kataoka, K.; Khademhosseini, A.; Kopeček, J.; Kotov, N. A.; Krug, H. F.; Lee, D. S.; Lehr, C. M.; Leong, K. W.; Liang, X. J.; Lim, M. L.; Liz-Marzán, L. M.; Ma, X.; Macchiarini, P.; Meng, H.; Möhwald, H.; Mulvaney, P.; Nel, A. E.; Nie, S.; Nordlander, P.; Okano, T.; Oliveira, J.; Park, T. H.; Penner, R. M.; Prato, M.; Puntes, V.; Rotello, V. M.; Samarakoon, A.; Schaak, R. E.; Shen, Y.; Sjöqvist, S.; Skirtach, A. G.; Soliman, M. G.; Stevens, M. M.; Sung, H. W.; Tang, B. Z.; Tietze, R.; Udugama, B. N.; Scott VanEpps, J.; Weil, T.; Weiss, P. S.; Willner, I.; Wu, Y.; Yang, L.; Yue, Z.; Zhang, Q.; Zhang, Q.; Zhang, X. E.; Zhao, Y.; Zhou, X.; Parak, W. J. Diverse Applications of Nanomedicine. *ACS Nano* **2017**, *11* (3), 2313–2381. https://doi.org/10.1021/acsnano.6b06040.

(3) Taha, M. S.; Padmakumar, S.; Singh, A.; Amiji, M. M. Critical Quality Attributes in the Development of Therapeutic Nanomedicines toward Clinical Translation. *Drug Delivery and Translational Research*. Springer June 1, 2020, pp 766–790. https://doi.org/10.1007/s13346-020-00744-1.

(4) Saleh, T. A. Nanomaterials: Classification, Properties, and Environmental Toxicities. *Environmental Technology and Innovation*. Elsevier B.V. November 1, 2020. https://doi.org/10.1016/j.eti.2020.101067.

(5) Keck, C. M.; Müller, R. H. Nanotoxicological Classification System (NCS) - A Guide for the Risk-Benefit Assessment of Nanoparticulate Drug Delivery Systems. *European Journal of*

Pharmaceutics and Biopharmaceutics. August 2013, pp 445–448. https://doi.org/10.1016/j.ejpb.2013.01.001.

(6) Khan, Y.; Sadia, H.; Ali Shah, S. Z.; Khan, M. N.; Shah, A. A.; Ullah, N.; Ullah, M. F.; Bibi, H.; Bafakeeh, O. T.; Khedher, N. Ben; Eldin, S. M.; Fadhl, B. M.; Khan, M. I. Classification, Synthetic, and Characterization Approaches to Nanoparticles, and Their Applications in Various Fields of Nanotechnology: A Review. *Catalysts*. MDPI November 1, 2022. https://doi.org/10.3390/catal12111386.

(7) Watanabe, K. Bacterial Membrane Vesicles (MVs): Novel Tools as Nature- and Nano-Carriers for Immunogenic Antigen, Enzyme Support, and Drug Delivery. *Applied Microbiology and Biotechnology*. Springer Verlag December 1, 2016, pp 9837–9843. https://doi.org/10.1007/s00253-016-7916-7.

(8) Valadi, H.; Ekström, K.; Bossios, A.; Sjöstrand, M.; Lee, J. J.; Lötvall, J. O. Exosome-Mediated Transfer of MRNAs and MicroRNAs Is a Novel Mechanism of Genetic Exchange between Cells. *Nat Cell Biol* **2007**, *9* (6), 654–659. https://doi.org/10.1038/ncb1596.

(9) De Jong, O. G.; Kooijmans, S. A. A.; Murphy, D. E.; Jiang, L.; Evers, M. J. W.; Sluijter, J. P. G.; Vader, P.; Schiffelers, R. M. Drug Delivery with Extracellular Vesicles: From Imagination to Innovation. *Acc Chem Res* **2019**, *52* (7), 1761–1770. https://doi.org/10.1021/acs.accounts.9b00109.

(10) Alvarez-Erviti, L.; Seow, Y.; Yin, H.; Betts, C.; Lakhal, S.; Wood, M. J. A. Delivery of SiRNA to the Mouse Brain by Systemic Injection of Targeted Exosomes. *Nat Biotechnol* **2011**, *29* (4), 341–345. https://doi.org/10.1038/nbt.1807.

(11) Cooper, J. M.; Wiklander, P. B. O.; Nordin, J. Z.; Al-Shawi, R.; Wood, M. J.; Vithlani, M.; Schapira, A. H. V.; Simons, J. P.; El-Andaloussi, S.; Alvarez-Erviti, L. Systemic Exosomal SiRNA Delivery Reduced Alpha-Synuclein Aggregates in Brains of Transgenic Mice. *Movement Disorders* **2014**, *29* (12), 1476–1485. https://doi.org/10.1002/mds.25978.

(12) Murphy, D. E.; de Jong, O. G.; Brouwer, M.; Wood, M. J.; Lavieu, G.; Schiffelers, R. M.; Vader, P. Extracellular Vesicle-Based Therapeutics: Natural versus Engineered Targeting and Trafficking. *Experimental and Molecular Medicine*. Nature Publishing Group March 1, 2019. https://doi.org/10.1038/s12276-019-0223-5.

(13) Turturici, G.; Tinnirello, R.; Sconzo, G.; Geraci, F. Extracellular Membrane Vesicles as a Mechanism of Cell-to-Cell Communication: Advantages and Disadvantages. *Am J Physiol Cell Physiol* **2014**, *306*, 621–633. https://doi.org/10.1152/ajpcell.00228.2013.-Microvesicles.

(14) Turturici, G.; Tinnirello, R.; Sconzo, G.; Geraci, F. Extracellular Membrane Vesicles as a Mechanism of Cell-to-Cell Communication: Advantages and Disadvantages. *Am J Physiol Cell Physiol* **2014**, *306*, 621–633. https://doi.org/10.1152/ajpcell.00228.2013.-Microvesicles.

(15) Zhang, H.; Freitas, D.; Kim, H. S.; Fabijanic, K.; Li, Z.; Chen, H.; Mark, M. T.; Molina, H.; Martin, A. B.; Bojmar, L.; Fang, J.; Rampersaud, S.; Hoshino, A.; Matei, I.; Kenific, C. M.; Nakajima, M.; Mutvei, A. P.; Sansone, P.; Buehring, W.; Wang, H.; Jimenez, J. P.; Cohen-Gould, L.; Paknejad, N.; Brendel, M.; Manova-Todorova, K.; Magalhães, A.; Ferreira, J. A.; Osório, H.; Silva, A. M.; Massey, A.; Cubillos-Ruiz, J. R.; Galletti, G.; Giannakakou, P.; Cuervo, A. M.; Blenis, J.; Schwartz, R.; Brady, M. S.; Peinado, H.; Bromberg, J.; Matsui, H.; Reis, C. A.; Lyden, D. Identification of Distinct Nanoparticles and Subsets of Extracellular Vesicles by Asymmetric Flow Field-Flow Fractionation. *Nat Cell Biol* **2018**, *20* (3), 332–343. https://doi.org/10.1038/s41556-018-0040-4.

(16) Pant, S.; Hilton, H.; Burczynski, M. E. The Multifaceted Exosome: Biogenesis, Role in Normal and Aberrant Cellular Function, and Frontiers for Pharmacological and Biomarker Opportunities. *Biochemical Pharmacology*. Elsevier Inc. June 1, 2012, pp 1484–1494. https://doi.org/10.1016/j.bcp.2011.12.037.

(17) Kalluri, R. The Biology and Function of Exosomes in Cancer. *Journal of Clinical Investigation*. American Society for Clinical Investigation April 1, 2016, pp 1208–1215. https://doi.org/10.1172/JCI81135.

(18) Kamerkar, S.; Lebleu, V. S.; Sugimoto, H.; Yang, S.; Ruivo, C. F.; Melo, S. A.; Lee, J. J.; Kalluri, R. Exosomes Facilitate Therapeutic Targeting of Oncogenic KRAS in Pancreatic Cancer. *Nature* **2017**, *546* (7659), 498–503. https://doi.org/10.1038/nature22341.

(19) Gudbergsson, J. M.; Jønsson, K.; Simonsen, J. B.; Johnsen, K. B. Systematic Review of Targeted Extracellular Vesicles for Drug Delivery – Considerations on Methodological and Biological Heterogeneity. *Journal of Controlled Release*. Elsevier B.V. July 28, 2019, pp 108–120. https://doi.org/10.1016/j.jconrel.2019.06.006.

(20) Welsh, J. A.; Goberdhan, D. C. I.; O'Driscoll, L.; Buzas, E. I.; Blenkiron, C.; Bussolati, B.; Cai, H.; Di Vizio, D.; Driedonks, T. A. P.; Erdbrügger, U.; Falcon-Perez, J. M.; Fu, Q.; Hill, A. F.; Lenassi, M.; Lim, S. K.; Mahoney, M. G.; Mohanty, S.; Möller, A.; Nieuwland, R.; Ochiya, T.; Sahoo, S.; Torrecilhas, A. C.; Zheng, L.; Zijlstra, A.; Abuelreich, S.; Bagabas, R.; Bergese, P.; Bridges, E. M.; Brucale, M.; Burger, D.; Carney, R. P.; Cocucci, E.; Crescitelli, R.; Hanser, E.; Harris, A. L.; Haughey, N. J.; Hendrix, A.; Ivanov, A. R.; Jovanovic-Talisman, T.; Kruh-Garcia, N. A.; Ku'ulei-Lyn Faustino, V.; Kyburz, D.; Lässer, C.; Lennon, K. M.; Lötvall, J.; Maddox, A. L.; Martens-Uzunova, E. S.; Mizenko, R. R.; Newman, L. A.; Ridolfi, A.; Rohde, E.; Rojalin, T.;

Rowland, A.; Saftics, A.; Sandau, U. S.; Saugstad, J. A.; Shekari, F.; Swift, S.; Ter-Ovanesyan, D.; Tosar, J. P.; Useckaite, Z.; Valle, F.; Varga, Z.; van der Pol, E.; van Herwijnen, M. J. C.; Wauben, M. H. M.; Wehman, A. M.; Williams, S.; Zendrini, A.; Zimmerman, A. J.; Théry, C.; Witwer, K. W. Minimal Information for Studies of Extracellular Vesicles (MISEV2023): From Basic to Advanced Approaches. *J Extracell Vesicles* **2024**, *13* (2). https://doi.org/10.1002/jev2.12404.

(21) Van Niel, G.; D'Angelo, G.; Raposo, G. Shedding Light on the Cell Biology of Extracellular Vesicles. *Nature Reviews Molecular Cell Biology*. Nature Publishing Group April 1, 2018, pp 213–228. https://doi.org/10.1038/nrm.2017.125.

(22) Mathieu, M.; Martin-Jaular, L.; Lavieu, G.; Théry, C. Specificities of Secretion and Uptake of Exosomes and Other Extracellular Vesicles for Cell-to-Cell Communication. *Nature Cell Biology*. Nature Publishing Group January 1, 2019, pp 9–17. https://doi.org/10.1038/s41556-018-0250-9.

(23) Maas, S. L. N.; Breakefield, X. O.; Weaver, A. M. Extracellular Vesicles: Unique Intercellular Delivery Vehicles. *Trends in Cell Biology*. Elsevier Ltd March 1, 2017, pp 172–188. https://doi.org/10.1016/j.tcb.2016.11.003.

(24) Vlassov, A. V.; Magdaleno, S.; Setterquist, R.; Conrad, R. Exosomes: Current Knowledge of Their Composition, Biological Functions, and Diagnostic and Therapeutic Potentials. *Biochimica et Biophysica Acta - General Subjects*. July 2012, pp 940–948. https://doi.org/10.1016/j.bbagen.2012.03.017.

(25) Cocucci, E.; Racchetti, G.; Meldolesi, J. Shedding Microvesicles: Artefacts No More. *Trends in Cell Biology*. February 2009, pp 43–51. https://doi.org/10.1016/j.tcb.2008.11.003.

(26) Raposo, G.; Stoorvogel, W. Extracellular Vesicles: Exosomes, Microvesicles, and Friends. *Journal of Cell Biology*. February 2013, pp 373–383. https://doi.org/10.1083/jcb.201211138.

(27) Van Niel, G.; D'Angelo, G.; Raposo, G. Shedding Light on the Cell Biology of Extracellular Vesicles. *Nature Reviews Molecular Cell Biology*. Nature Publishing Group April 1, 2018, pp 213–228. https://doi.org/10.1038/nrm.2017.125.

(28) Yáñez-Mó, M.; Siljander, P. R. M.; Andreu, Z.; Zavec, A. B.; Borràs, F. E.; Buzas, E. I.; Buzas, K.; Casal, E.; Cappello, F.; Carvalho, J.; Colás, E.; Cordeiro-Da Silva, A.; Fais, S.; Falcon-Perez, J. M.; Ghobrial, I. M.; Giebel, B.; Gimona, M.; Graner, M.; Gursel, I.; Gursel, M.; Heegaard, N. H. H.; Hendrix, A.; Kierulf, P.; Kokubun, K.; Kosanovic, M.; Kralj-Iglic, V.; Krämer-Albers, E. M.; Laitinen, S.; Lässer, C.; Lener, T.; Ligeti, E.; Line, A.; Lipps, G.; Llorente, A.; Lötvall, J.; Manček-Keber, M.; Marcilla, A.; Mittelbrunn, M.; Nazarenko, I.; Nolte-'t Hoen, E. N. M.; Nyman, T. A.; O'Driscoll, L.; Olivan, M.; Oliveira, C.; Pállinger, É.; Del Portillo, H. A.; Reventós, J.;

Rigau, M.; Rohde, E.; Sammar, M.; Sánchez-Madrid, F.; Santarém, N.; Schallmoser, K.; Ostenfeld, M. S.; Stoorvogel, W.; Stukelj, R.; Van Der Grein, S. G.; Helena Vasconcelos, M.; Wauben, M. H. M.; De Wever, O. Biological Properties of Extracellular Vesicles and Their Physiological Functions. *Journal of Extracellular Vesicles*. Co-Action Publishing 2015, pp 1–60. https://doi.org/10.3402/jev.v4.27066.

(29) Mrowczynski, O. D.; Madhankumar, A. B.; Slagle-Webb, B.; Lee, S. Y.; Zacharia, B. E.; Connor, J. R. HFE Genotype Affects Exosome Phenotype in Cancer. *Biochim Biophys Acta Gen Subj* **2017**, *1861* (8), 1921–1928. https://doi.org/10.1016/j.bbagen.2017.05.014.

(30) Vescovi, R.; Monti, M.; Moratto, D.; Paolini, L.; Consoli, F.; Benerini, L.; Melocchi, L.; Calza, S.; Chiudinelli, M.; Rossi, G.; Bugatti, M.; Maio, M.; Fonsatti, E.; Farisoglio, C.; Simbolo, M.; Almici, C.; Verardi, R.; Scarpa, A.; Bergese, P.; Manganoni, A.; Facchetti, F.; Vermi, W. Collapse of the Plasmacytoid Dendritic Cell Compartment in Advanced Cutaneous Melanomas by Components of the Tumor Cell Secretome. *Cancer Immunol Res* **2019**, *7* (1), 12–28. https://doi.org/10.1158/2326-6066.CIR-18-0141.

(31) Peinado, H.; Alečković, M.; Lavotshkin, S.; Matei, I.; Costa-Silva, B.; Moreno-Bueno, G.; Hergueta-Redondo, M.; Williams, C.; García-Santos, G.; Ghajar, C. M.; Nitadori-Hoshino, A.; Hoffman, C.; Badal, K.; Garcia, B. A.; Callahan, M. K.; Yuan, J.; Martins, V. R.; Skog, J.; Kaplan, R. N.; Brady, M. S.; Wolchok, J. D.; Chapman, P. B.; Kang, Y.; Bromberg, J.; Lyden, D. Melanoma Exosomes Educate Bone Marrow Progenitor Cells toward a Pro-Metastatic Phenotype through MET. *Nat Med* **2012**, *18* (6), 883–891. https://doi.org/10.1038/nm.2753.

(32) Alfonsi, R.; Grassi, L.; Signore, M.; Bonci, D. The Double Face of Exosome-Carried Micrornas in Cancer Immunomodulation. *International Journal of Molecular Sciences*. MDPI AG April 13, 2018. https://doi.org/10.3390/ijms19041183.

(33) Whitehead, B.; Wu, L. P.; Hvam, M. L.; Aslan, H.; Dong, M.; DyrskjØt, L.; Ostenfeld, M. S.; Moghimi, S. M.; Howard, K. A. Tumour Exosomes Display Differential Mechanical and Complement Activation Properties Dependent on Malignant State: Implications in Endothelial Leakiness. *Journal of Extracellular Vesicles*. Taylor and Francis Ltd. 2015. https://doi.org/10.3402/jev.v4.29685.

(34) Seo, Y.; Kim, H. S.; Hong, I. S. Stem Cell-Derived Extracellular Vesicles as Immunomodulatory Therapeutics. *Stem Cells International*. Hindawi Limited 2019. https://doi.org/10.1155/2019/5126156.

(35) Kordelas, L.; Rebmann, V.; Ludwig, A. K.; Radtke, S.; Ruesing, J.; Doeppner, T. R.; Epple, M.; Horn, P. A.; Beelen, D. W.; Giebel, B. MSC-Derived Exosomes: A Novel Tool to Treat

Therapy-Refractory Graft-versus-Host Disease. *Leukemia*. Nature Publishing Group 2014, pp 970–973. https://doi.org/10.1038/leu.2014.41.

(36) van Niel, G.; Carter, D. R. F.; Clayton, A.; Lambert, D. W.; Raposo, G.; Vader, P. Challenges and Directions in Studying Cell–Cell Communication by Extracellular Vesicles. *Nat Rev Mol Cell Biol* **2022**, *23* (5), 369–382. https://doi.org/10.1038/s41580-022-00460-3.

(37) Stremersch, S.; De Smedt, S. C.; Raemdonck, K. Therapeutic and Diagnostic Applications of Extracellular Vesicles. *Journal of Controlled Release* **2016**, *244*, 167–183. https://doi.org/10.1016/j.jconrel.2016.07.054.

(38) de Jong, O. G.; Verhaar, M. C.; Chen, Y.; Vader, P.; Gremmels, H.; Posthuma, G.; Schiffelers, R. M.; Gucek, M.; van Balkom, B. W. M. Cellular Stress Conditions Are Reflected in the Protein and RNA Content of Endothelial Cell-Derived Exosomes. *J Extracell Vesicles* **2012**, *1* (1). https://doi.org/10.3402/jev.v1i0.18396.

(39) Wieckowski, E. U.; Visus, C.; Szajnik, M.; Szczepanski, M. J.; Storkus, W. J.; Whiteside, T. L. Tumor-Derived Microvesicles Promote Regulatory T Cell Expansion and Induce Apoptosis in Tumor-Reactive Activated CD8+ T Lymphocytes. *The Journal of Immunology* **2009**, *183* (6), 3720–3730. https://doi.org/10.4049/jimmunol.0900970.

(40) Abusamra, A. J.; Zhong, Z.; Zheng, X.; Li, M.; Ichim, T. E.; Chin, J. L.; Min, W. P. Tumor Exosomes Expressing Fas Ligand Mediate CD8+ T-Cell Apoptosis. *Blood Cells Mol Dis* **2005**, *35* (2), 169–173. https://doi.org/10.1016/j.bcmd.2005.07.001.

(41) Rabinowits, G.; Gerçel-Taylor, C.; Day, J. M.; Taylor, D. D.; Kloecker, G. H. Exosomal MicroRNA: A Diagnostic Marker for Lung Cancer. *Clin Lung Cancer* **2009**, *10* (1), 42–46. https://doi.org/10.3816/CLC.2009.n.006.

(42) Hoshino, A.; Costa-Silva, B.; Shen, T. L.; Rodrigues, G.; Hashimoto, A.; Tesic Mark, M.; Molina, H.; Kohsaka, S.; Di Giannatale, A.; Ceder, S.; Singh, S.; Williams, C.; Soplop, N.; Uryu, K.; Pharmer, L.; King, T.; Bojmar, L.; Davies, A. E.; Ararso, Y.; Zhang, T.; Zhang, H.; Hernandez, J.; Weiss, J. M.; Dumont-Cole, V. D.; Kramer, K.; Wexler, L. H.; Narendran, A.; Schwartz, G. K.; Healey, J. H.; Sandstrom, P.; Jørgen Labori, K.; Kure, E. H.; Grandgenett, P. M.; Hollingsworth, M. A.; De Sousa, M.; Kaur, S.; Jain, M.; Mallya, K.; Batra, S. K.; Jarnagin, W. R.; Brady, M. S.; Fodstad, O.; Muller, V.; Pantel, K.; Minn, A. J.; Bissell, M. J.; Garcia, B. A.; Kang, Y.; Rajasekhar, V. K.; Ghajar, C. M.; Matei, I.; Peinado, H.; Bromberg, J.; Lyden, D. Tumour Exosome Integrins Determine Organotropic Metastasis. *Nature* **2015**, *527* (7578), 329–335. https://doi.org/10.1038/nature15756.

(43) Garnier, D.; Jabado, N.; Rak, J. Extracellular Vesicles as Prospective Carriers of Oncogenic Protein Signatures in Adult and Paediatric Brain Tumours. *Proteomics*. May 2013, pp 1595–1607. https://doi.org/10.1002/pmic.201200360.

(44) Peinado, H.; Alečković, M.; Lavotshkin, S.; Matei, I.; Costa-Silva, B.; Moreno-Bueno, G.; Hergueta-Redondo, M.; Williams, C.; García-Santos, G.; Ghajar, C. M.; Nitadori-Hoshino, A.; Hoffman, C.; Badal, K.; Garcia, B. A.; Callahan, M. K.; Yuan, J.; Martins, V. R.; Skog, J.; Kaplan, R. N.; Brady, M. S.; Wolchok, J. D.; Chapman, P. B.; Kang, Y.; Bromberg, J.; Lyden, D. Melanoma Exosomes Educate Bone Marrow Progenitor Cells toward a Pro-Metastatic Phenotype through MET. *Nat Med* **2012**, *18* (6), 883–891. https://doi.org/10.1038/nm.2753.

(45) Berardocco, M.; Radeghieri, A.; Busatto, S.; Gallorini, M.; Raggi, C.; Gissi, C.; D'agnano, I.; Bergese, P.; Felsani, A.; Berardi, A. C. *RNA-Seq Reveals Distinctive RNA Profiles of Small Extracellular Vesicles from Different Human Liver Cancer Cell Lines*. www.impactjournals.com/oncotarget.

(46) Blackwell, R. H.; Foreman, K. E.; Gupta, G. N. The Role of Cancer-Derived Exosomes in Tumorigenicity & Epithelial-to-Mesenchymal Transition. *Cancers*. MDPI AG August 10, 2017. https://doi.org/10.3390/cancers9080105.

(47) Wurdinger, T.; Gatson, N. N.; Balaj, L.; Kaur, B.; Breakefield, X. O.; Pegtel, D. M. Extracellular Vesicles and Their Convergence with Viral Pathways. *Advances in Virology*. 2012. https://doi.org/10.1155/2012/767694.

(48) Zhang, W.; Zhou, X.; Zhang, H.; Yao, Q.; Liu, Y.; Dong, Z. Extracellular Vesicles in Diagnosis and Therapy of Kidney Diseases. *Am J Physiol Renal Physiol* **2016**, *311*, 844–851. https://doi.org/10.1152/ajprenal.00429.2016.-Extracel.

(49) Salvi, A.; Vezzoli, M.; Busatto, S.; Paolini, L.; Faranda, T.; Abeni, E.; Caracausi, M.; Antonaros, F.; Piovesan, A.; Locatelli, C.; Cocchi, G.; Alvisi, G.; De Petro, G.; Ricotta, D.; Bergese, P.; Radeghieri, A. Analysis of a Nanoparticle-enriched Fraction of Plasma Reveals MiRNA Candidates for down Syndrome Pathogenesis. *Int J Mol Med* **2019**, *43* (6), 2303–2318. https://doi.org/10.3892/ijmm.2019.4158.

(50) M., K.; Das, S. Extracellular Vesicles in Heart Disease: Excitement for the Future ? *Exosomes Microvesicles* **2014**, 1. https://doi.org/10.5772/58390.

(51) Colombo, E.; Borgiani, B.; Verderio, C.; Furlan, R. Microvesicles: Novel Biomarkers for Neurological Disorders. *Frontiers in Physiology*. 2012. https://doi.org/10.3389/fphys.2012.00063.

(52) Buzas, E. I.; György, B.; Nagy, G.; Falus, A.; Gay, S. Emerging Role of Extracellular Vesicles in Inflammatory Diseases. *Nature Reviews Rheumatology*. Nature Publishing Group 2014, pp 356–364. https://doi.org/10.1038/nrrheum.2014.19.

(53) Théry, C.; Zitvogel, L.; Amigorena, S. Exosomes: Composition, Biogenesis and Function. *Nature Reviews Immunology*. European Association for Cardio-Thoracic Surgery 2002, pp 569–579. https://doi.org/10.1038/nri855.

(54) Vella, L. J.; Hill, A. F.; Cheng, L. Focus on Extracellular Vesicles: Exosomes and Their Role in Protein Trafficking and Biomarker Potential in Alzheimer's and Parkinson's Disease. *International Journal of Molecular Sciences*. MDPI AG February 6, 2016. https://doi.org/10.3390/ijms17020173.

(55) Di Noto, G.; Bugatti, A.; Zendrini, A.; Mazzoldi, E. L.; Montanelli, A.; Caimi, L.; Rusnati, M.; Ricotta, D.; Bergese, P. Merging Colloidal Nanoplasmonics and Surface Plasmon Resonance Spectroscopy for Enhanced Profiling of Multiple Myeloma-Derived Exosomes. *Biosens Bioelectron* **2016**, *77*, 518–524. https://doi.org/10.1016/j.bios.2015.09.061.

(56) Bellavia, D.; Raimondo, S.; Calabrese, G.; Forte, S.; Cristaldi, M.; Patinella, A.; Memeo, L.; Manno, M.; Raccosta, S.; Diana, P.; Cirrincione, G.; Giavaresi, G.; Monteleone, F.; Fontana, S.; Leo, G. De; Alessandro, R. Interleukin 3- Receptor Targeted Exosomes Inhibit in Vitro and in Vivo Chronic Myelogenous Leukemia Cell Growth. *Theranostics* **2017**, *7* (5), 1333–1345. https://doi.org/10.7150/thno.17092.

(57) Castillo, J.; Bernard, V.; San Lucas, F. A.; Allenson, K.; Capello, M.; Kim, D. U.; Gascoyne, P.; Mulu, F. C.; Stephens, B. M.; Huang, J.; Wang, H.; Momin, A. A.; Jacamo, R. O.; Katz, M.; Wolff, R.; Javle, M.; Varadhachary, G.; Wistuba, I. I.; Hanash, S.; Maitra, A.; Alvarez, H. Surfaceome Profiling Enables Isolation of Cancerspecific Exosomal Cargo in Liquid Biopsies from Pancreatic Cancer Patients. *Annals of Oncology* **2018**, *29* (1), 223–229. https://doi.org/10.1093/annonc/mdx542.

(58) Lee, J. C.; Byeon, S. K.; Moon, M. H. Relative Quantification of Phospholipids Based on Isotope-Labeled Methylation by Nanoflow Ultrahigh Performance Liquid Chromatography-Tandem Mass Spectrometry: Enhancement in Cardiolipin Profiling. *Anal Chem* **2017**, *89* (9), 4969–4977. https://doi.org/10.1021/acs.analchem.7b00297.

(59) Zonneveld, M. I.; Brisson, A. R.; van Herwijnen, M. J. C.; Tan, S.; van de Lest, C. H. A.; Redegeld, F. A.; Garssen, J.; Wauben, M. H. M.; Hoen, E. N. t. N. M. Recovery of Extracellular Vesicles from Human Breast Milk Is Influenced by Sample Collection and Vesicle Isolation Procedures. *J Extracell Vesicles* **2014**, *3* (1). https://doi.org/10.3402/jev.v3.24215.

(60) Muller, L.; Hong, C. S.; Stolz, D. B.; Watkins, S. C.; Whiteside, T. L. Isolation of Biologically-Active Exosomes from Human Plasma. *J Immunol Methods* **2014**, *411*, 55–65. https://doi.org/10.1016/j.jim.2014.06.007.

(61) Rubin, O.; Crettaz, D.; Tissot, J. D.; Lion, N. Pre-Analytical and Methodological Challenges in Red Blood Cell Microparticle Proteomics. *Talanta*. Elsevier B.V. June 30, 2010, pp 1–8. https://doi.org/10.1016/j.talanta.2010.04.025.

(62) Fuhrmann, G.; Herrmann, I. K.; Stevens, M. M. Cell-Derived Vesicles for Drug Therapy and Diagnostics: Opportunities and Challenges. *Nano Today*. Elsevier B.V. July 22, 2015, pp 397–409. https://doi.org/10.1016/j.nantod.2015.04.004.

(63) Tan, K.; Li, R.; Huang, X.; Liu, Q. Outer Membrane Vesicles: Current Status and Future Direction of These Novel Vaccine Adjuvants. *Frontiers in Microbiology*. Frontiers Media S.A. April 26, 2018. https://doi.org/10.3389/fmicb.2018.00783.

(64) El Andaloussi, S.; Mäger, I.; Breakefield, X. O.; Wood, M. J. A. Extracellular Vesicles: Biology and Emerging Therapeutic Opportunities. *Nature Reviews Drug Discovery*. May 2013, pp 347–357. https://doi.org/10.1038/nrd3978.

(65) Stremersch, S.; De Smedt, S. C.; Raemdonck, K. Therapeutic and Diagnostic Applications of Extracellular Vesicles. *Journal of Controlled Release* **2016**, *244*, 167–183. https://doi.org/10.1016/j.jconrel.2016.07.054.

(66) Chulpanova, D. S.; Kitaeva, K. V.; James, V.; Rizvanov, A. A.; Solovyeva, V. V. Therapeutic Prospects of Extracellular Vesicles in Cancer Treatment. *Frontiers in Immunology*. Frontiers Media S.A. 2018. https://doi.org/10.3389/fimmu.2018.01534.

(67) Haney, M. J.; Klyachko, N. L.; Zhao, Y.; Gupta, R.; Plotnikova, E. G.; He, Z.; Patel, T.; Piroyan, A.; Sokolsky, M.; Kabanov, A. V.; Batrakova, E. V. Exosomes as Drug Delivery Vehicles for Parkinson's Disease Therapy. *Journal of Controlled Release* **2015**, *207*, 18–30. https://doi.org/10.1016/j.jconrel.2015.03.033.

(68) Morishita, M.; Takahashi, Y.; Matsumoto, A.; Nishikawa, M.; Takakura, Y. Exosome-Based Tumor Antigens–Adjuvant Co-Delivery Utilizing Genetically Engineered Tumor Cell-Derived Exosomes with Immunostimulatory CpG DNA. *Biomaterials* **2016**, *111*, 55–65. https://doi.org/10.1016/j.biomaterials.2016.09.031.

(69) Smyth, T.; Kullberg, M.; Malik, N.; Smith-Jones, P.; Graner, M. W.; Anchordoquy, T. J. Biodistribution and Delivery Efficiency of Unmodified Tumor-Derived Exosomes. *Journal of Controlled Release* **2015**, *199*, 145–155. https://doi.org/10.1016/j.jconrel.2014.12.013.

(70) Wiklander, O. P. B.; Nordin, J. Z.; O'Loughlin, A.; Gustafsson, Y.; Corso, G.; Mäger, I.; Vader, P.; Lee, Y.; Sork, H.; Seow, Y.; Heldring, N.; Alvarez-Erviti, L.; Edvard Smith, C. I.; Le Blanc, K.; Macchiarini, P.; Jungebluth, P.; Wood, M. J. A.; El Andaloussi, S. Extracellular Vesicle in Vivo Biodistribution Is Determined by Cell Source, Route of Administration and Targeting. *J Extracell Vesicles* **2015**, *4* (2015), 1–13. https://doi.org/10.3402/jev.v4.26316.

(71) Ohno, S. I.; Takanashi, M.; Sudo, K.; Ueda, S.; Ishikawa, A.; Matsuyama, N.; Fujita, K.; Mizutani, T.; Ohgi, T.; Ochiya, T.; Gotoh, N.; Kuroda, M. Systemically Injected Exosomes Targeted to EGFR Deliver Antitumor Microrna to Breast Cancer Cells. *Molecular Therapy* **2013**, *21* (1), 185–191. https://doi.org/10.1038/mt.2012.180.

(72) Designed Research; A, C. G. J. CD9 Tetraspanin Generates Fusion Competent Sites on the Egg Membrane for Mammalian Fertilization. **2011**, *108* (27). https://doi.org/10.1073/pnas.1017400108/-/DCSupplemental.

(73) Teissier, É.; Pécheur, E. I. Lipids as Modulators of Membrane Fusion Mediated by Viral Fusion Proteins. *European Biophysics Journal*. November 2007, pp 887–899. https://doi.org/10.1007/s00249-007-0201-z.

(74) Lafferty, K. D. Interacting Parasites. *Science*. October 8, 2010, pp 187–188. https://doi.org/10.1126/science.1196915.

(75) Timmers, L.; Lim, S. K.; Arslan, F.; Armstrong, J. S.; Hoefer, I. E.; Doevendans, P. A.; Piek, J. J.; El Oakley, R. M.; Choo, A.; Lee, C. N.; Pasterkamp, G.; de Kleijn, D. P. V. Reduction of Myocardial Infarct Size by Human Mesenchymal Stem Cell Conditioned Medium. *Stem Cell Res* **2008**, *1* (2), 129–137. https://doi.org/10.1016/j.scr.2008.02.002.

(76) van Koppen, A.; Joles, J. A.; van Balkom, B. W. M.; Lim, S. K.; de Kleijn, D.; Giles, R. H.; Verhaar, M. C. Human Embryonic Mesenchymal Stem Cell-Derived Conditioned Medium Rescues Kidney Function in Rats with Established Chronic Kidney Disease. *PLoS One* **2012**, *7* (6). https://doi.org/10.1371/journal.pone.0038746.

(77) Armstrong, J. P. K.; Stevens, M. M. Strategic Design of Extracellular Vesicle Drug Delivery Systems. *Advanced Drug Delivery Reviews*. Elsevier B.V. May 1, 2018, pp 12–16. https://doi.org/10.1016/j.addr.2018.06.017.

(78) Martin, F.; Roth, D. M.; Jans, D. A.; Pouton, C. W.; Partridge, L. J.; Monk, P. N.; Moseley, G. W. Tetraspanins in Viral Infections: A Fundamental Role in Viral Biology? *J Virol* **2005**, *79* (17), 10839–10851. https://doi.org/10.1128/jvi.79.17.10839-10851.2005.

(79) Parolini, I.; Federici, C.; Raggi, C.; Lugini, L.; Palleschi, S.; De Milito, A.; Coscia, C.; Iessi, E.; Logozzi, M.; Molinari, A.; Colone, M.; Tatti, M.; Sargiacomo, M.; Fais, S. Microenvironmental PH Is a Key Factor for Exosome Traffic in Tumor Cells. *Journal of Biological Chemistry* **2009**, *284* (49), 34211–34222. https://doi.org/10.1074/jbc.M109.041152.

(80) Katsuda, T.; Tsuchiya, R.; Kosaka, N.; Yoshioka, Y.; Takagaki, K.; Oki, K.; Takeshita, F.; Sakai, Y.; Kuroda, M.; Ochiya, T. Human Adipose Tissue-Derived Mesenchymal Stem Cells Secrete Functional Neprilysin-Bound Exosomes. *Sci Rep* **2013**, *3*. https://doi.org/10.1038/srep01197.

(81) Riazifar, M.; Pone, E. J.; Lotval, J.; Zhao, W. Stem Cell Extracellular Vesicles: Extended Messages of Regeneration. *Annual Review of Pharmacology and Toxicology*. Annual Reviews Inc. January 6, 2017, pp 125–154. https://doi.org/10.1146/annurev-pharmtox-061616-030146.

(82) Radeghieri, A.; Savio, G.; Zendrini, A.; Di Noto, G.; Salvi, A.; Bergese, P.; Piovani, G. Cultured Human Amniocytes Express HTERT, Which Is Distributed between Nucleus and Cytoplasm and Is Secreted in Extracellular Vesicles. *Biochem Biophys Res Commun* **2017**, *483* (1), 706–711. https://doi.org/10.1016/j.bbrc.2016.12.077.

(83) Nassar, W.; El-Ansary, M.; Sabry, D.; Mostafa, M. A.; Fayad, T.; Kotb, E.; Temraz, M.; Saad, A. N.; Essa, W.; Adel, H. Umbilical Cord Mesenchymal Stem Cells Derived Extracellular Vesicles Can Safely Ameliorate the Progression of Chronic Kidney Diseases. *Biomater Res* **2016**, *20* (1). https://doi.org/10.1186/s40824-016-0068-0.

(84) Nguyen, D. B.; Thuy Ly, T. B.; Wesseling, M. C.; Hittinger, M.; Torge, A.; Devitt, A.; Perrie, Y.; Bernhardt, I. Characterization of Microvesicles Released from Human Red Blood Cells. *Cellular Physiology and Biochemistry* **2016**, *38* (3), 1085–1099. https://doi.org/10.1159/000443059.

(85) Tissot, J. D.; Rubin, O.; Canellini, G. Analysis and Clinical Relevance of Microparticles from Red Blood Cells. *Current Opinion in Hematology*. November 2010, pp 571–577. https://doi.org/10.1097/MOH.0b013e32833ec217.

(86) Usman, W. M.; Pham, T. C.; Kwok, Y. Y.; Vu, L. T.; Ma, V.; Peng, B.; Chan, Y. S.; Wei, L.; Chin, S. M.; Azad, A.; He, A. B. L.; Leung, A. Y. H.; Yang, M.; Shyh-Chang, N.; Cho, W. C.; Shi, J.; Le, M. T. N. Efficient RNA Drug Delivery Using Red Blood Cell Extracellular Vesicles. *Nat Commun* **2018**, *9* (1). https://doi.org/10.1038/s41467-018-04791-8.

(87) Nguyen, P. H. D.; Jayasinghe, M. K.; Le, A. H.; Peng, B.; Le, M. T. N. Advances in Drug Delivery Systems Based on Red Blood Cells and Their Membrane-Derived Nanoparticles. *ACS Nano*. American Chemical Society March 28, 2023, pp 5187–5210. https://doi.org/10.1021/acsnano.2c11965.

(88) Chiangjong, W.; Netsirisawan, P.; Hongeng, S.; Chutipongtanate, S. Red Blood Cell Extracellular Vesicle-Based Drug Delivery: Challenges and Opportunities. *Frontiers in Medicine*. Frontiers Media S.A. December 24, 2021. https://doi.org/10.3389/fmed.2021.761362.

(89) Baberg, F.; Geyh, S.; Waldera-Lupa, D.; Stefanski, A.; Zilkens, C.; Haas, R.; Schroeder, T.; Stühler, K. Secretome Analysis of Human Bone Marrow Derived Mesenchymal Stromal Cells. *Biochim Biophys Acta Proteins Proteom* **2019**, *1867* (4), 434–441. https://doi.org/10.1016/j.bbapap.2019.01.013.

(90) Skovronova, R.; Grange, C.; Dimuccio, V.; Deregibus, M. C.; Camussi, G.; Bussolati, B.; Chiara, M. Surface Marker Expression in Small and Medium/Large Mesenchymal Stromal Cell-Derived Extracellular Vesicles in Naïve or Apoptotic Condition Using Orthogonal Techniques. https://doi.org/10.1101/2021.09.16.460620.

(91) Kou, M.; Huang, L.; Yang, J.; Chiang, Z.; Chen, S.; Liu, J.; Guo, L.; Zhang, X.; Zhou, X.; Xu, X.; Yan, X.; Wang, Y.; Zhang, J.; Xu, A.; Tse, H. fat; Lian, Q. Mesenchymal Stem Cell-Derived Extracellular Vesicles for Immunomodulation and Regeneration: A next Generation Therapeutic Tool? *Cell Death and Disease*. Springer Nature July 1, 2022. https://doi.org/10.1038/s41419-022-05034-x.

(92) Valiukevičius, P.; Mačiulaitis, J.; Pangonytė, D.; Siratavičiūtė, V.; Kluszczyńska, K.; Kuzaitytė, U.; Insodaitė, R.; Čiapienė, I.; Grigalevičiūtė, R.; Zigmantaitė, V.; Vitkauskienė, A.; Mačiulaitis, R. Human Placental Mesenchymal Stem Cells and Derived Extracellular Vesicles Ameliorate Lung Injury in Acute Respiratory Distress Syndrome Murine Model. *Cells* **2023**, *12* (23). https://doi.org/10.3390/cells12232729.

(93) Lu, C. H.; Chen, Y. A.; Ke, C. C.; Liu, R. S. Mesenchymal Stem Cell-Derived Extracellular Vesicle: A Promising Alternative Therapy for Osteoporosis. *International Journal of Molecular Sciences*. MDPI December 1, 2021. https://doi.org/10.3390/ijms222312750.

(94) Suk, J. S.; Xu, Q.; Kim, N.; Hanes, J.; Ensign, L. M. PEGylation as a Strategy for Improving Nanoparticle-Based Drug and Gene Delivery. *Advanced Drug Delivery Reviews*. Elsevier B.V. April 1, 2016, pp 28–51. https://doi.org/10.1016/j.addr.2015.09.012.

(95) Haney, M. J.; Klyachko, N. L.; Zhao, Y.; Gupta, R.; Plotnikova, E. G.; He, Z.; Patel, T.; Piroyan, A.; Sokolsky, M.; Kabanov, A. V.; Batrakova, E. V. Exosomes as Drug Delivery Vehicles for Parkinson's Disease Therapy. *Journal of Controlled Release* **2015**, *207*, 18–30. https://doi.org/10.1016/j.jconrel.2015.03.033.

(96) Richter, M.; Vader, P.; Fuhrmann, G. Approaches to Surface Engineering of Extracellular Vesicles. *Adv Drug Deliv Rev* **2021**, *173*, 416–426. https://doi.org/10.1016/j.addr.2021.03.020.

(97) Di, H.; Zeng, E.; Zhang, P.; Liu, X.; Zhang, C.; Yang, J.; Liu, D. General Approach to Engineering Extracellular Vesicles for Biomedical Analysis. *Anal Chem* **2019**, *91* (20), 12752–12759. https://doi.org/10.1021/acs.analchem.9b02268.

(98) Kooijmans, S. A. A.; Aleza, C. G.; Roffler, S. R.; van Solinge, W. W.; Vader, P.; Schiffelers, R. M. Display of GPI-Anchored Anti-EGFR Nanobodies on Extracellular Vesicles Promotes Tumour Cell Targeting. *J Extracell Vesicles* **2016**, *5* (1). https://doi.org/10.3402/jev.v5.31053.

(99) Yuan, Z. Q.; Kolluri, K. K.; Gowers, K. H. C.; Janes, S. M. TRAIL Delivery by MSC-Derived Extracellular Vesicles Is an Effective Anticancer Therapy. *J Extracell Vesicles* **2017**, *6* (1). https://doi.org/10.1080/20013078.2017.1265291.

(100) Faruqu, F. N.; Wang, J. T. W.; Xu, L.; McNickle, L.; Chong, E. M. Y.; Walters, A.; Gurney, M.; Clayton, A.; Smyth, L. A.; Hider, R.; Sosabowski, J.; Al-Jamal, K. T. Membrane Radiolabelling of Exosomes for Comparative Biodistribution Analysis in Immunocompetent and Immunodeficient Mice – A Novel and Universal Approach. *Theranostics* **2019**, *9* (6), 1666–1682. https://doi.org/10.7150/thno.27891.

(101) Simonsen, J. B. Pitfalls Associated with Lipophilic Fluorophore Staining of Extracellular Vesicles for Uptake Studies. *J Extracell Vesicles* **2019**, *8* (1). https://doi.org/10.1080/20013078.2019.1582237.

(102) Fuhrmann, G.; Serio, A.; Mazo, M.; Nair, R.; Stevens, M. M. Active Loading into Extracellular Vesicles Significantly Improves the Cellular Uptake and Photodynamic Effect of Porphyrins. *Journal of Controlled Release* **2015**, *205*, 35–44. https://doi.org/10.1016/j.jconrel.2014.11.029.

(103) Choi, E. S.; Song, J.; Kang, Y. Y.; Mok, H. Mannose-Modified Serum Exosomes for the Elevated Uptake to Murine Dendritic Cells and Lymphatic Accumulation. *Macromol Biosci* **2019**, *19* (7). https://doi.org/10.1002/mabi.201900042.

(104) Takov, K.; Yellon, D. M.; Davidson, S. M. Confounding Factors in Vesicle Uptake Studies Using Fluorescent Lipophilic Membrane Dyes. *J Extracell Vesicles* **2017**, *6* (1). https://doi.org/10.1080/20013078.2017.1388731.

(105) Gupta, D.; Liang, X.; Pavlova, S.; Wiklander, O. P. B.; Corso, G.; Zhao, Y.; Saher, O.; Bost, J.; Zickler, A. M.; Piffko, A.; Maire, C. L.; Ricklefs, F. L.; Gustafsson, O.; Llorente, V. C.; Gustafsson, M. O.; Bostancioglu, R. B.; Mamand, D. R.; Hagey, D. W.; Görgens, A.; Nordin, J. Z.; EL Andaloussi, S. Quantification of Extracellular Vesicles in Vitro and in Vivo Using Sensitive Bioluminescence Imaging. *J Extracell Vesicles* **2020**, *9* (1). https://doi.org/10.1080/20013078.2020.1800222.

(106) Mentkowski, K. I.; Lang, J. K. Exosomes Engineered to Express a Cardiomyocyte Binding Peptide Demonstrate Improved Cardiac Retention in Vivo. *Sci Rep* **2019**, *9* (1). https://doi.org/10.1038/s41598-019-46407-1.

(107) Zou, X.; Yuan, M.; Zhang, T.; Wei, H.; Xu, S.; Jiang, N.; Zheng, N.; Wu, Z. Extracellular Vesicles Expressing a Single-Chain Variable Fragment of an HIV-1 Specific Antibody Selectively Target Env+ Tissues. *Theranostics* **2019**, *9* (19), 5657–5671. https://doi.org/10.7150/thno.33925.

(108) Hung, M. E.; Leonard, J. N. Stabilization of Exosome-Targeting Peptides via Engineered Glycosylation. *Journal of Biological Chemistry* **2015**, *290* (13), 8166–8172. https://doi.org/10.1074/jbc.M114.621383.

(109) Cheng, Q.; Shi, X.; Han, M.; Smbatyan, G.; Lenz, H. J.; Zhang, Y. Reprogramming Exosomes as Nanoscale Controllers of Cellular Immunity. *J Am Chem Soc* **2018**, *140* (48), 16413–16417. https://doi.org/10.1021/jacs.8b10047.

(110) Lee, J.; Lee, H.; Goh, U.; Kim, J.; Jeong, M.; Lee, J.; Park, J. H. Cellular Engineering with Membrane Fusogenic Liposomes to Produce Functionalized Extracellular Vesicles. *ACS Appl Mater Interfaces* **2016**, *8* (11), 6790–6795. https://doi.org/10.1021/acsami.6b01315.

(111) Sato, Y. T.; Umezaki, K.; Sawada, S.; Mukai, S. A.; Sasaki, Y.; Harada, N.; Shiku, H.; Akiyoshi, K. Engineering Hybrid Exosomes by Membrane Fusion with Liposomes. *Sci Rep* **2016**, *6*. https://doi.org/10.1038/srep21933.

(112) Piffoux, M.; Silva, A. K. A.; Wilhelm, C.; Gazeau, F.; Tareste, D. Modification of Extracellular Vesicles by Fusion with Liposomes for the Design of Personalized Biogenic Drug Delivery Systems. *ACS Nano* **2018**, *12* (7), 6830–6842. https://doi.org/10.1021/acsnano.8b02053.

(113) Kooijmans, S. A. A.; Gitz-Francois, J. J. J. M.; Schiffelers, R. M.; Vader, P. Recombinant Phosphatidylserine-Binding Nanobodies for Targeting of Extracellular Vesicles to Tumor Cells: A Plug-and-Play Approach. *Nanoscale* **2018**, *10* (5), 2413–2426. https://doi.org/10.1039/c7nr06966a.

(114) Didiot, M. C.; Hall, L. M.; Coles, A. H.; Haraszti, R. A.; Godinho, B. M. D. C.; Chase, K.; Sapp, E.; Ly, S.; Alterman, J. F.; Hassler, M. R.; Echeverria, D.; Raj, L.; Morrissey, D. V.; Di Figlia, M.; Aronin, N.; Khvorova, A. Exosome-Mediated Delivery of Hydrophobically Modified SiRNA for Huntingtin MRNA Silencing. *Molecular Therapy* **2016**, *24* (10), 1836–1847. https://doi.org/10.1038/mt.2016.126.

(115) O'Loughlin, A. J.; Mäger, I.; de Jong, O. G.; Varela, M. A.; Schiffelers, R. M.; El Andaloussi, S.; Wood, M. J. A.; Vader, P. Functional Delivery of Lipid-Conjugated SiRNA by Extracellular Vesicles. *Molecular Therapy* **2017**, *25* (7), 1580–1587. https://doi.org/10.1016/j.ymthe.2017.03.021.

(116) Gao, X.; Ran, N.; Dong, X.; Zuo, B.; Yang, R.; Zhou, Q.; Moulton, H. M.; Seow, Y.; Yin, H. *Anchor Peptide Captures, Targets, and Loads Exosomes of Diverse Origins for Diagnostics and Therapy*; 2018; Vol. 10. https://www.science.org.

(117) Tian, T.; Zhang, H. X.; He, C. P.; Fan, S.; Zhu, Y. L.; Qi, C.; Huang, N. P.; Xiao, Z. D.; Lu, Z. H.; Tannous, B. A.; Gao, J. Surface Functionalized Exosomes as Targeted Drug Delivery

Vehicles for Cerebral Ischemia Therapy. *Biomaterials* **2018**, *150*, 137–149. https://doi.org/10.1016/j.biomaterials.2017.10.012.

(118) Tamura, R.; Uemoto, S.; Tabata, Y. Augmented Liver Targeting of Exosomes by Surface Modification with Cationized Pullulan. *Acta Biomater* **2017**, *57*, 274–284. https://doi.org/10.1016/j.actbio.2017.05.013.

(119) Smyth, T.; Petrova, K.; Payton, N. M.; Persaud, I.; Redzic, J. S.; Graner, M. W.; Smith-Jones, P.; Anchordoquy, T. J. Surface Functionalization of Exosomes Using Click Chemistry. *Bioconjug Chem* **2014**, *25* (10), 1777–1784. https://doi.org/10.1021/bc500291r.

(120) Wang, M.; Altinoglu, S.; Takeda, Y. S.; Xu, Q. Integrating Protein Engineering and Bioorthogonal Click Conjugation for Extracellular Vesicle Modulation and Intracellular Delivery. *PLoS One* **2015**, *10* (11). https://doi.org/10.1371/journal.pone.0141860.

(121) Changa, P. V.; Preschera, J. A.; Sletten, E. M.; Baskin, J. M.; Miller, I. A.; Agard, N. J.; Lo, A.; Bertozzi, C. R. Copper-Free Click Chemistry in Living Animals. *Proc Natl Acad Sci U S A* **2010**, *107* (5), 1821–1826. https://doi.org/10.1073/pnas.0911116107.

(122) Lang, K.; Chin, J. W. Bioorthogonal Reactions for Labeling Proteins. *ACS Chem Biol* **2014**, *9* (1), 16–20. https://doi.org/10.1021/cb4009292.

(123) Steenpaß, T.; Lung, A.; Schubert, R. Tresylated PEG-Sterols for Coupling of Proteins to Preformed Plain or PEGylated Liposomes. *Biochim Biophys Acta Biomembr* **2006**, *1758* (1), 20–28. https://doi.org/10.1016/j.bbamem.2005.12.010.

(124) Gnopo, Y. M. D.; Misra, A.; Hsu, H. L.; DeLisa, M. P.; Daniel, S.; Putnam, D. Induced Fusion and Aggregation of Bacterial Outer Membrane Vesicles: Experimental and Theoretical Analysis. *J Colloid Interface Sci* **2020**, *578*, 522–532. https://doi.org/10.1016/j.jcis.2020.04.068.

(125) Kooijmans, S. A. A.; Fliervoet, L. A. L.; Van Der Meel, R.; Fens, M. H. A. M.; Heijnen, H. F. G.; Van Bergen En Henegouwen, P. M. P.; Vader, P.; Schiffelers, R. M. PEGylated and Targeted Extracellular Vesicles Display Enhanced Cell Specificity and Circulation Time. *Journal of Controlled Release* **2016**, *224*, 77–85. https://doi.org/10.1016/j.jconrel.2016.01.009.

(126) Nasiri Kenari, A.; Cheng, L.; Hill, A. F. Methods for Loading Therapeutics into Extracellular Vesicles and Generating Extracellular Vesicles Mimetic-Nanovesicles. *Methods*. Academic Press Inc. May 1, 2020, pp 103–113. https://doi.org/10.1016/j.ymeth.2020.01.001.

(127) Sun, D.; Zhuang, X.; Xiang, X.; Liu, Y.; Zhang, S.; Liu, C.; Barnes, S.; Grizzle, W.; Miller, D.; Zhang, H. G. A Novel Nanoparticle Drug Delivery System: The Anti-Inflammatory Activity of Curcumin Is Enhanced When Encapsulated in Exosomes. *Molecular Therapy* **2010**, *18* (9), 1606–1614. https://doi.org/10.1038/mt.2010.105.

(128) Sun, D.; Zhuang, X.; Xiang, X.; Liu, Y.; Zhang, S.; Liu, C.; Barnes, S.; Grizzle, W.; Miller, D.; Zhang, H. G. A Novel Nanoparticle Drug Delivery System: The Anti-Inflammatory Activity of Curcumin Is Enhanced When Encapsulated in Exosomes. *Molecular Therapy* **2010**, *18* (9), 1606–1614. https://doi.org/10.1038/mt.2010.105.

(129) Munagala, R.; Aqil, F.; Jeyabalan, J.; Gupta, R. C. Bovine Milk-Derived Exosomes for Drug Delivery. *Cancer Lett* **2016**, *371* (1), 48–61. https://doi.org/10.1016/j.canlet.2015.10.020.

(130) Lamichhane, T. N.; Jeyaram, A.; Patel, D. B.; Parajuli, B.; Livingston, N. K.; Arumugasaamy, N.; Schardt, J. S.; Jay, S. M. Oncogene Knockdown via Active Loading of Small RNAs into Extracellular Vesicles by Sonication. *Cell Mol Bioeng* **2016**, *9* (3), 315–324. https://doi.org/10.1007/s12195-016-0457-4.

(131) Kim, M. S.; Haney, M. J.; Zhao, Y.; Mahajan, V.; Deygen, I.; Klyachko, N. L.; Inskoe, E.; Piroyan, A.; Sokolsky, M.; Okolie, O.; Hingtgen, S. D.; Kabanov, A. V.; Batrakova, E. V. Development of Exosome-Encapsulated Paclitaxel to Overcome MDR in Cancer Cells. *Nanomedicine* **2016**, *12* (3), 655–664. https://doi.org/10.1016/j.nano.2015.10.012.

(132) Haney, M. J.; Klyachko, N. L.; Zhao, Y.; Gupta, R.; Plotnikova, E. G.; He, Z.; Patel, T.; Piroyan, A.; Sokolsky, M.; Kabanov, A. V.; Batrakova, E. V. Exosomes as Drug Delivery Vehicles for Parkinson's Disease Therapy. *Journal of Controlled Release* **2015**, *207*, 18–30. https://doi.org/10.1016/j.jconrel.2015.03.033.

(133) Lamichhane, T. N.; Raiker, R. S.; Jay, S. M. Exogenous DNA Loading into Extracellular Vesicles via Electroporation Is Size-Dependent and Enables Limited Gene Delivery. *Mol Pharm* **2015**, *12* (10), 3650–3657. https://doi.org/10.1021/acs.molpharmaceut.5b00364.

(134) Tian, Y.; Li, S.; Song, J.; Ji, T.; Zhu, M.; Anderson, G. J.; Wei, J.; Nie, G. A Doxorubicin Delivery Platform Using Engineered Natural Membrane Vesicle Exosomes for Targeted Tumor Therapy. *Biomaterials* **2014**, *35* (7), 2383–2390. https://doi.org/10.1016/j.biomaterials.2013.11.083.

(135) Kalimuthu, S.; Gangadaran, P.; Rajendran, R. L.; Zhu, L.; Oh, J. M.; Lee, H. W.; Gopal, A.; Baek, S. H.; Jeong, S. Y.; Lee, S. W.; Lee, J.; Ahn, B. C. A New Approach for Loading Anticancer Drugs into Mesenchymal Stem Cell-Derived Exosome Mimetics for Cancer Therapy. *Front Pharmacol* **2018**, *9* (SEP). https://doi.org/10.3389/fphar.2018.01116.

(136) Jacob, M. C.; Favre, M.; Bensa, J. -C. Membrane Cell Permeabilisation with Saponin and Multiparametric Analysis by Flow Cytometry. *Cytometry* **1991**, *12* (6), 550–558. https://doi.org/10.1002/cyto.990120612.

(137) Pascucci, L.; Coccè, V.; Bonomi, A.; Ami, D.; Ceccarelli, P.; Ciusani, E.; Viganò, L.; Locatelli, A.; Sisto, F.; Doglia, S. M.; Parati, E.; Bernardo, M. E.; Muraca, M.; Alessandri, G.;

Bondiolotti, G.; Pessina, A. Paclitaxel Is Incorporated by Mesenchymal Stromal Cells and Released in Exosomes That Inhibit in Vitro Tumor Growth: A New Approach for Drug Delivery. *Journal of Controlled Release* **2014**, *192*, 262–270. https://doi.org/10.1016/j.jconrel.2014.07.042.

(138) Zhang, D.; Lee, H.; Zhu, Z.; Minhas, J. K.; Jin, Y. Enrichment of Selective MiRNAs in Exosomes and Delivery of Exosomal MiRNAs in Vitro and in Vivo. *Am J Physiol Lung Cell Mol Physiol* **2017**, *312*, 110–121. https://doi.org/10.1152/ajplung.00423.2016.-Exosomes.

(139) Naseri, Z.; Oskuee, R. K.; Jaafari, M. R.; Moghadam, M. F. Exosome-Mediated Delivery of Functionally Active MiRNA-142-3p Inhibitor Reduces Tumorigenicity of Breast Cancer in Vitro and in Vivo. *Int J Nanomedicine* **2018**, *13*, 7727–7747. https://doi.org/10.2147/IJN.S182384.

(140) Margolis, L.; Sadovsky, Y. The Biology of Extracellular Vesicles: The Known Unknowns. *PLoS Biol* **2019**, *17* (7). https://doi.org/10.1371/journal.pbio.3000363.

(141) Wiklander, O. P. B.; Nordin, J. Z.; O'Loughlin, A.; Gustafsson, Y.; Corso, G.; Mäger, I.; Vader, P.; Lee, Y.; Sork, H.; Seow, Y.; Heldring, N.; Alvarez-Erviti, L.; Edvard Smith, C. I.; Le Blanc, K.; Macchiarini, P.; Jungebluth, P.; Wood, M. J. A.; El Andaloussi, S. Extracellular Vesicle in Vivo Biodistribution Is Determined by Cell Source, Route of Administration and Targeting. *J Extracell Vesicles* **2015**, *4* (2015), 1–13. https://doi.org/10.3402/jev.v4.26316.

Chapter 2 - Exploring the Extracellular Vesicle-Nanostructured Secretome Interface Toward Clinical Translation

EVs are not the only nanoparticles present in biological fluids; they are components of a heterogeneous group of secreted nanoparticles, i.e. “nanostructured secretome’’, with which they continuously and dynamically interact. To finally reach EV clinical translation as stated in Chapter 1, it is essential to have a deeper knowledge of “the players in the game”, and understand how they interact with each other, since all this plays a crucial role in defining EV's biological identity and role. This chapter introduces the concept and the composition of the nanostructured secretome, the state-of-the-art knowledge about the dynamic interactions occurring on EVs in physiological conditions and relative challenges, and, finally, the aim of this thesis.

2.1 The Nanostructured Secretome

Traditionally, the term "secretome" refers to individual proteins, hormones, and neurotransmitters[1]. However, it should now be expanded to include a variety of nanoparticles secreted by cells into the extracellular space, ranging from a few nanometers to hundreds of nanometers. These secreted nanoparticles, known as the nanostructured secretome[2], are "made by cells for cells" and represent a paradigm shift in nanomedicine. They promise to surpass synthetic nanoparticles in circulation, targeting abilities, precision, and sustainability. Looking further ahead, advanced manipulation could potentially enable the use of these biogenic nanoparticles as building blocks for future nanotechnology. In recent years, it has become increasingly evident that cell-to-cell sharing of macromolecular information also occurs via the nanostructured secretome. These "nanolines" of communication complement the "classical" paracrine signaling of single molecules. Under both physiological and pathological conditions, cells secrete a wide variety of nanoparticles with diverse compositions, structures, and functions. These nanoparticles include macromolecular complexes (such as ferritin and RNA-binding proteins)[3,4], membranous particles (such as EVs and fat globules)[5,6], and micellar structures (such as lipoproteins and casein micelles)[7,8], with sizes ranging from a few to hundreds of nanometers[2]. Released into the extracellular space alongside single molecules, these nanoparticles are present in all biological fluids (e.g., blood, cerebrospinal fluid, saliva, urine, and milk). The biological function of the nanostructured secretome is determined by the molecular and colloidal properties (composition, size, structure, surface charge, energetic stability, etc.) of the nanoparticles that comprise it.

Besides EVs (already introduced in Chapter 1), the other principal classes of nanoparticles composing the nanostructured secretome are:

Lipoproteins: a class of secreted nanoparticles found in plasma and tissues, primarily responsible for lipid transport and delivery. These nanosized complexes consist of a central hydrophobic core of non-polar lipids, surrounded by a monolayered amphiphilic membrane made of phospholipids, cholesterol, and apolipoproteins. The lipid and protein content of a lipoprotein is heterogeneous and evolves during its lifespan and circulation[8]. There are four classes of lipoprotein:

1) Chylomicrons: The largest and least dense subclass, primarily composed of triacylglycerols, with smaller amounts of phospholipids, cholesterol, cholesteryl esters, and ApoB. Chylomicrons are assembled in enterocytes (intestinal cells) during dietary lipid absorption. They bypass the liver and transport dietary lipids to storage tissues (adipose and skeletal muscle) and cardiac tissue. After transferring triacylglycerols to peripheral tissues, chylomicrons are catabolized by the liver[8].
2) Very Low-Density Lipoproteins (VLDLs): Synthesized by hepatocytes (liver cells), VLDLs contain triacylglycerols and cholesteryl esters combined with apolipoproteins, mainly ApoB-100. VLDLs, initially sized at 30–80 nm, are quickly degraded as their fatty acid content is cleaved, transforming them into smaller and denser Low-Density Lipoproteins (LDLs) via Intermediate-Density Lipoproteins (IDLs). VLDLs and LDLs circulate and transport lipids to peripheral tissues, with LDLs being a significant risk factor for atherosclerosis due to their uptake by atherosclerotic plaque endothelium[9].
3) Low-Density Lipoproteins (LDLs): Formed from VLDLs, LDLs are smaller and denser, transporting lipids to peripheral tissues. They are notable for their association with atherosclerotic plaque formation[10].
4) High-Density Lipoproteins (HDLs): Smaller and denser than LDLs, with a diameter below 10 nm and a density of 1.060–1.200 g/cm³. HDLs are rich in cholesterol and apolipoproteins such as ApoA-I, A-II, ApoE, and ApoC. They are extensively studied for their protective role against cardiovascular diseases. HDL biosynthesis begins with the synthesis of ApoA-I in the liver or intestine. Subsequent lipidation of ApoA-I forms nascent, discoidal particles, which become spherical HDLs through the internalization of cholesterol esters into their core, catalyzed by lecithin cholesterol acyltransferase. HDLs remove excess cholesterol from tissues, transporting it back to the liver and steroidogenic organs for recycling. Additionally, HDLs carry molecules other than apolipoproteins and

lipids, such as small non-coding RNAs (mainly microRNAs) and other proteins like metalloproteinases[11].

In summary, lipoproteins are essential for lipid transport, with each class playing a specific role in lipid metabolism and overall health, from nutrient absorption to cardiovascular protection.

Albumin: The most abundant plasma protein, albumin is a small globular protein (66 kDa)[12] with high affinity for metals, fatty acids, amino acids, metabolites, and lipophilic xenobiotics[13]. Its three-dimensional structure, consisting of three homologous domains, forms a heart-shaped molecule. Albumin's main roles are to transport solutes to target organs and maintain plasma pH and osmotic pressure[14].

Ferritin: Ferritin stores excess cellular iron, with its 24 subunits forming protein cages.[15] H-ferritin oxidizes ferrous iron (Fe2+) to ferric iron (Fe3+), while L-ferritin facilitates ferroxidase turnover.[16] Ferritin can be disassembled and reassembled at varying pH levels, allowing it to load different compounds. Its association with exosomes indicates converging intracellular trafficking and secretion pathways[4].

Transferrin: This iron carrier controls iron's toxic and insoluble characteristics. It is a single-chain glycoprotein (~80 kDa) with two homologous lobes, each capable of binding an Fe3+ ion. Iron binding and release involve the closing and opening of these lobe domains.[16]

Argonaute-2 (Ago2): A ribonucleoprotein complex, Ago2 carries circulating miRNAs and regulates small RNA-guided gene silencing[17]. It is composed of four major domains (N, PAZ, MID, and PIWI) that form a bi-lobe structure accommodating guide small RNAs and their complementary fragments[3].

Exomeres: Recently discovered, exomeres are small (~35 nm), non-membranous particles rich in specific enzymes and nucleic acids. They have unique biophysical features, such as a mildly negative ζ-potential and greater stiffness compared to EVs. Exomeres transport functional, bioactive cargoes and alter the metabolism of recipient cells, though much about them remains unknown[18].

Milk-derived nanoparticles: Milk, a mammary gland secretion, serves as both a processed food product and a primary nutrient source for newborns. It supplies nutrients through proteins and fat nanoparticles, regulates immune defense, and interacts with the gut microbiome[19,20]. Milk is an emulsion of fat globules, lactose, and soluble proteins, primarily caseins. Over 95% of milk lipids are triglycerides, derived from circulating lipids or synthesized in the mammary gland. Fat globules, ranging from hundreds of nanometers to tens of micrometers, originate in the cytoplasm of epithelial lactating cells, gaining a single-layer lipid coat and an additional bilayer during secretion[7,21]. These globules, functionalized with multiple proteins, impact lipid metabolism, the

immune system, and intestinal physiology. Caseins, major milk proteins, self-assemble into micelles (50 to 250 nm) containing water, calcium, phosphorus salts, and enzymes. The function and precise structure of casein micelles are still under study[22].

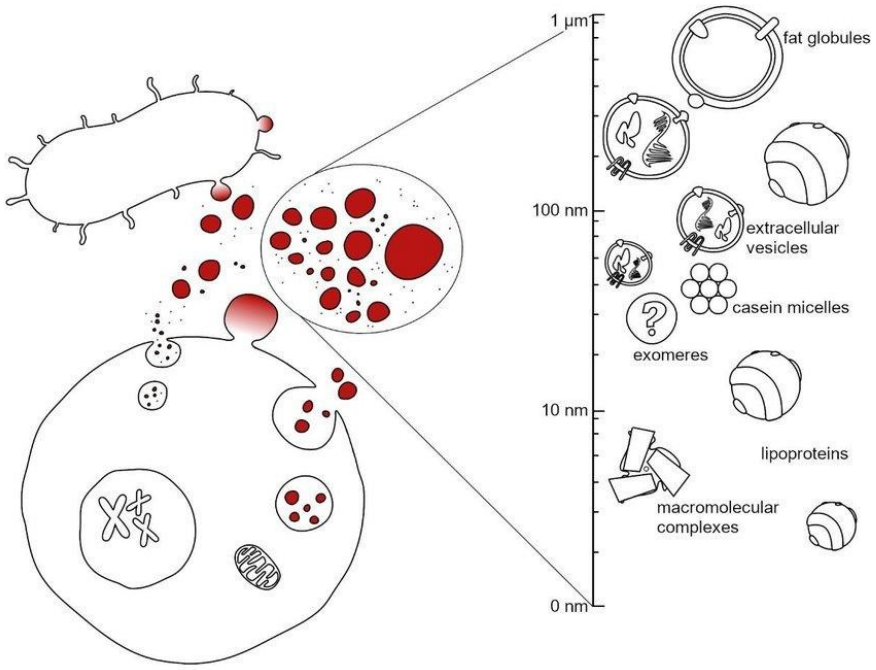

Figure 1.2. Illustration and composition of the nanostructured secretome[1].

2.2 The physicochemical landscape of EVs

Since their discovery, EVs have predominantly been studied from biological and medical perspectives, focusing on their roles in disease mechanisms and potential applications in diagnostics and therapeutics[23,24]. However, their physicochemical characteristics and interactions with nanostructures have often been overlooked. EVs are complex, biogenic particles that exhibit a wide range of properties, including variations in size, composition, surface charge, and membrane stiffness[2,25]. A key feature of EVs is their high surface-to-volume ratio, which facilitates dynamic interactions with other molecules and particles in their environment[25,26]. EVs are part of the nanostructured secretome of cells, a colloidal system densely populated with biogenic nanoparticles such as protein aggregates, exomers[27], lipoproteins[8], and midbody remnants[28]. This crowded system exhibits significant surface free energy, driving the formation of a biomolecular corona (BC)[29]. The BC forms around EVs through dynamic interactions at physiological temperature, altering EV biological identity. These "sticky" interactions, including EV-protein coronas and EV-lipoprotein aggregates, are now recognized as intrinsic components of biological fluids containing EVs[26,30,31].

The complexity of EVs presents significant challenges for clinical translation, particularly in defining their identity, purity[33,35], and in isolating homogeneous sub-populations[36], challenges that

distinguish them from more conventional biologics[37]. However, this complexity also presents unique opportunities[38,39]. The selective molecular enrichment mechanisms involved in EV formation provide an advantage in biological functions such as targeted delivery, crucial for intercellular communication[39]. By better understanding and manipulating the physicochemical landscape of EVs, we can unlock their full potential in areas like drug delivery[40] and regenerative medicine. Furthermore, as cell-derived particles, EVs offer diagnostic opportunities. Their biomolecular corona, enriched with circulating biomolecules, reflects the physiological state of their originating cells, making EVs valuable tools for liquid biopsy[41] and biomarker discovery in complex biofluids[33,42].

2.2.1 The Biomolecular Corona

When nanoparticles enter a biological system, their surfaces rapidly become coated with a variety of molecules, including proteins, lipids, and nucleic acids, resulting in the formation of multiple layers collectively known as the biomolecular corona (BC)[43,44]. Initially, the BC was primarily studied in the context of synthetic nanoparticles used for drug delivery, to understand its impact on bioavailability and biodistribution[43]. However, it has been demonstrated that similar BC formation occurs around viruses, and more recently, EVs have also been found to be subjected to this phenomenon[25,26]. Due to their high surface-to-volume ratio, nanoparticles exhibit a high surface energy, making them inherently metastable. To reach a stable state, they bind various molecules present in the surrounding media. Initially, nanoparticles form transient complexes with these molecules under favorable thermodynamic conditions. As time progresses, competition among molecules for the nanoparticle surface occurs, with those of higher affinity (hard corona) gradually displacing others (soft corona), a phenomenon known as the Vroman effect[45]. This effect is influenced by the concentration of proteins relative to the available surface area and their diffusion coefficients. Moreover, the curved surface of nanoparticles can induce structural changes in adsorbed proteins, sometimes leading to irreversible alterations in their secondary structure affecting protein function and potentially triggering undesirable immune responses. BC also induces changes in the physicochemical properties of the nanoparticle surface, including size, zeta potential, hydrodynamic radius, and stability. Since nanoparticle behavior and identity are closely tied to their surface characteristics, which govern their interactions with the surrounding microenvironment and cells, BC can significantly influence cellular uptake, bioavailability, biological targeting, biodistribution, and toxicity[30,38,46].

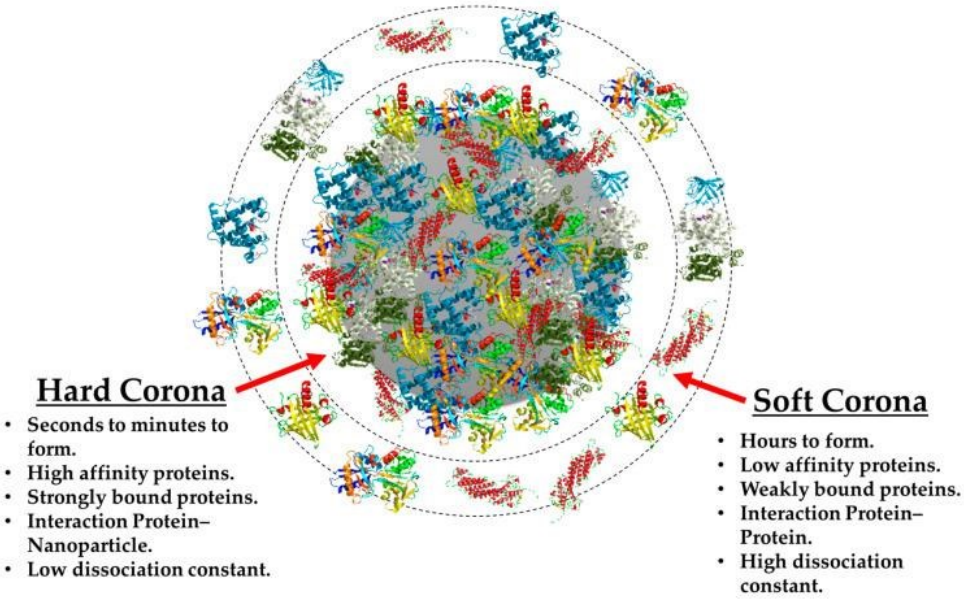

Figure 2.2 Schematic illustration of the "hard" and "soft" corona of nanoparticles[47].

When EVs are released by cells and enter biological fluids, they adsorb numerous molecules onto their surface, forming the EV corona[48]. The formation of the EV-BC is mainly driven by non-covalent interactions, probably based on Van der Waals forces. Additionally, the formation of hydrogen bonds between the EV surface and components of the biomolecular corona cannot be excluded, as well as pi interactions. Finally, hydrophobic interactions may play a role. For such interactions to occur, adsorbed proteins might need to expose their hydrophobic regions, facilitating interaction with the hydrophobic part of the EV membrane. However, these considerations are speculative and adapted to EV-BC from BC of synthetic nanoparticles, since at the state-of-the-art no work has dealt with the fundamental mechanisms of EV-BC. The formation of the BC is not only a superficial event but a thermodynamically favored process that is linked to the energies involved in EV formation itself. Indeed, the elastic energy required to bend the EV membrane into a spherical shape is comparable to the energy needed for the adsorption of multiple proteins during corona formation[32]. Consequently, it's not possible to separate EVs from some other components (co-isolates) without compromising their structural integrity[61]. Therefore, biomolecules in the corona that interact with the EV surface with higher energy may be considered integral to EVs, contributing to their biological identity and offering potential as biomarkers[33,34]. Interestingly, this suggests that EV biogenesis may not conclude when the EV is secreted by the cell, but rather when its surface achieves thermodynamic stability within complex biological matrices.

The surface properties of EVs, which are crucial for their interaction with cell membranes, mobility, cellular uptake, and immune recognition, can be significantly altered by the presence of

the molecules acquired with the corona formation. The EV corona may include apolipoproteins, immunoglobulins, coagulation factors, DNA, cytokines, and enzymes. The presence of these molecules can alter the structure and properties of EVs, but the corona also holds functional significance[30]. Different corona compositions can have distinct biological implications, which could be leveraged for diagnostic purposes[33]. Furthermore, the elevated surface free energy characterizing the EV interface drives dynamic interactions with other components of the nanostructured secretome, contributing to the intrinsic "stickiness" of these nanoparticles. As a result, nanoparticles have a strong tendency to form complexes with other particles, making it difficult to isolate specific classes of biogenic nanoparticles without simultaneously co-isolating a diverse array of other entities[49,50]. Recent research suggests that this co-isolation may be more than a mere artifact of the purification process; rather, biogenic nanoparticle complexes appear to hold biological relevance. A prime example is the interaction between EVs and lipoproteins, underscoring the importance of understanding how biogenic nanoparticles interact to fully harness the potential of the nanostructured secretome [31].

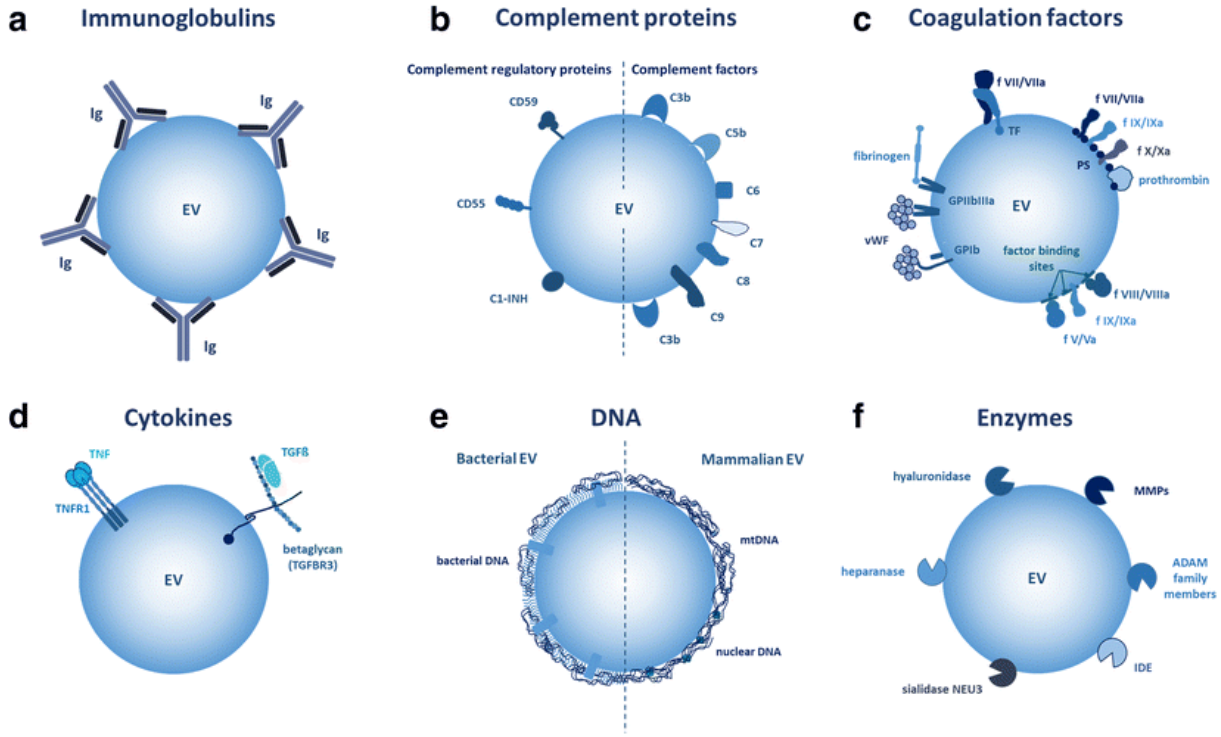

Figure 3.2 Illustration of the main molecules involved in EV biomolecular corona[25].

2.2.2 Extracellular vesicle identity and inter-, intra-, and acquired heterogeneity

The concept of identity and purity in EV preparations is currently under debate, largely due to the complex interdisciplinary considerations needed to formulate a meaningful interpretation of these concepts for EVs, which significantly hinders their translation to clinical applications. Identity is a fundamental attribute of any biological product, closely tied to its functional efficacy and dosing.

Purity, derived from identity, indicates the absence of contaminants, namely everything that is not identified as an EV. Defining identity is particularly challenging in the context of EVs for two primary reasons: (i) EVs are inherently heterogeneous, encompassing a diverse population of vesicles that vary in size, composition, structure, and biological activity[51,52]; and (ii) EV preparations often contain a broad range of co-isolates, such as lipoproteins, that are difficult or impossible to separate from EVs[50,53]. These co-isolates may be intrinsic to the starting material or may emerge during the manufacturing process, and they can potentially contribute to the overall biological activity of the EV preparation[30,54]. To accurately define the identity of a mixture within a mixture, such as EV preparations, requires a shift from traditional concepts of purity to a more detailed understanding of the distinct characteristics that define the EVs themselves. Physicochemical and colloidal properties serve as critical "identity descriptors" for EV preparations, offering a quantitative means to assess their composition[55]. Historically, homogeneity in size and density has been used to define identity, but these metrics fall short when dealing with complex extracellular nanoparticle populations[2] whose size and density may overlap with those of EVs, or which may associate with EVs to form structures like the biomolecular corona[53]. For instance, recent studies have shown that EV-lipoprotein complexes can form under various physiological conditions[31,49] or due to manipulation, further complicating the clear definition of EV identity and purity[50,53]. The international EV scientific community suggests providing specific stoichiometric ratios, such as the volumetric number density of nanoparticles relative to the volumetric mass density of proteins, lipids, or other EV-associated molecules, to accurately define the identity of EV preparations[35,56,57]. Additionally, a proposed identity index measures the volumetric mass density of proteins commonly found in co-isolates within EV preparations. This approach acknowledges that depending on the source of EVs, the expected co-isolates should be well-defined and accounted for[36,58–60]. Thus, this concept of identity in EV preparations extends beyond mere purity, encompassing a comprehensive understanding of the physicochemical landscape that defines these complex biological entities[35].

Similarly, the concept of heterogeneity is closely related to identity and refers to differences between EVs identified in a precise group. For instance, EVs produced by the same cell source can have differences in size and/or molecular composition, depending on the pathway of secretion, defining a certain level of heterogeneity in the preparation that must be considered.

Thus, EV heterogeneity can be mainly classified into three distinct levels[44]:

1. **Inter-EV heterogeneity**: This refers to the differences between EVs produced by different cells, implying that biological fluids contain a heterogeneous mix of EV subpopulations with diverse biological roles, compositions, and physicochemical properties.
2. **Intra-EV heterogeneity**: This refers to the differences found within individual EVs produced by the same cells, as cells can produce EVs through different pathways, leading to the production of nanoparticles with varied characteristics and biological functions.
3. **Acquired heterogeneity**: This refers to the heterogeneity that arises post-biogenesis, for example, due to the adsorption of biomolecules in the biomolecular corona. Since BC formation is a dynamic phenomenon, EV-acquired heterogeneity is complex and can evolve in response to various physiological conditions, such as changes in temperature and pH across different body fluids and tissues. This evolving heterogeneity may modulate the physiological roles of EVs over time and space.

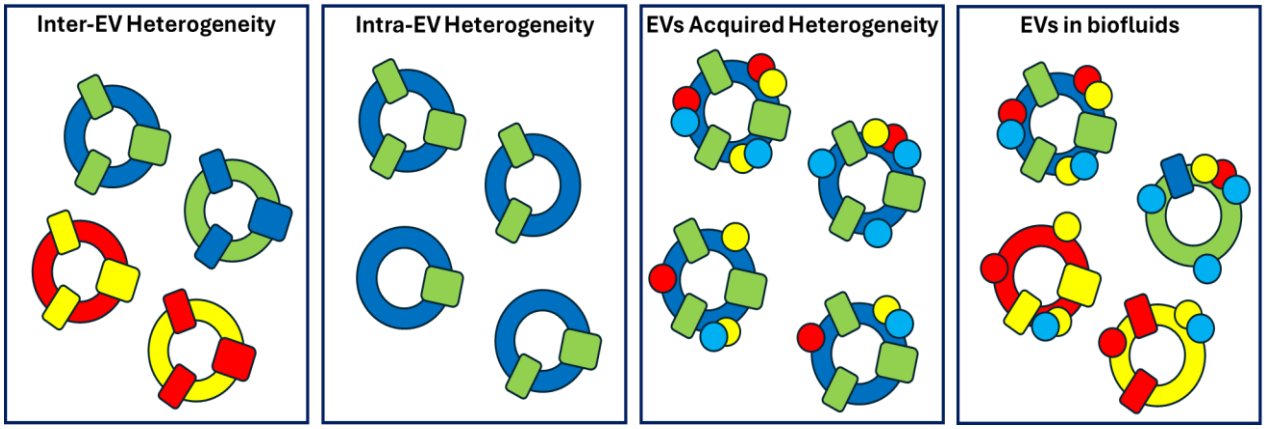

Figure 4.2 Schematic representation of the different levels of heterogeneity of EV populations, and the expected situation in real complex biofluids. EVs and EV proteins with different colors indicate different sources. The colored balls in ''EVs Acquired Heterogeneity'' and ''EVs in biofluids'' indicate different components of the nanostructured secretome.

2.3 Aim of the thesis

The field of EVs is advancing rapidly by combining innovative ideas, cutting-edge technologies, novel observations, and rigorous data analysis. Significant progress is being made to address the challenges hindering EVs' clinical translation. However, the increasing knowledge about physicochemical properties and interfacial phenomena of EVs is driving a paradigm shift in the field. In biofluids, EVs interact dynamically with various (bio)components, significantly altering their biological identity. These interactions pose challenges related to the purity of EV preparations, their biodistribution, and pharmacokinetics, all linked to the physicochemical

characteristics and interfacial behavior of EVs. A deeper understanding of these aspects is essential for advancing EVs toward clinical applications.

This thesis is positioned within this dynamic landscape, focusing on the study of the BC on EVs in physiological conditions by exploring original approaches and developing an EV-based drug delivery system for precision nanomedicine toward triple negative breast cancer (TNBC). Specifically, this thesis is organized into 4 distinct works:

- In the first work the effect of the protein corona during EV surface engineering with antibodies for targeting has been studied. EVs, once immersed in protein-enriched fluids, are subjected to the physisorption of these proteins on their surface. In state-of-the-art protocols for EV surface engineering it is common to immerse EVs in a solution enriched with the protein of interest for a chemical reaction, underestimating the potential physisorption that could occur at the EV surface and its effect on the engineering process. Results related to this project are shown in Chapter 3.
- The second work, detailed in Chapter 4, explored the different dynamic formations of the BC in two distinct EV subpopulations, by an original Fluorescence Correlation Spectroscopy (FCS) method. The findings obtained from this project are important for better understanding the connection between EV composition, physicochemical properties, and biological functions; and address new challenges in the comprehension and definition of EV heterogeneity.
- In the third work (Chapter 5), the interaction between EVs and lipoproteins (LPs) was studied by Fluorescence Cross-Correlation Spectroscopy (FCCS). Recently, interactions between different components of the nanostructured secretome have been published in the literature, underlying a significant biological role, especially in pathological states (i.e., metastasis formation). This project investigated these interactions from a physicochemical point of view, addressing apparent affinity constants between the different components in physiological conditions.
- EV surface engineering strategies developed in the previous three works has been applied in the fourth one (detailed in Chapter 6), to design and produce an EV-based drug delivery system with Cetuximab and Cisplatin for the synergistic and multimodal therapy of triple-negative breast cancer (TNBC). This work is focused on the biological effects of this drug delivery system, by transcriptomic, *in vitro*, and *ex vivo* analysis.

The findings presented in this thesis contribute to the ongoing efforts in EV research, with many results already published in international journals and additional papers in preparation. Through

these studies, the thesis aims to further the understanding of the EV-nanostructured secretome interface and its potential in clinical applications.

2.4 References

(1) Tjalsma, H.; Antelmann, H.; Jongbloed, J. D. H.; Braun, P. G.; Darmon, E.; Dorenbos, R.; Dubois, J.-Y. F.; Westers, H.; Zanen, G.; Quax, W. J.; Kuipers, O. P.; Bron, S.; Hecker, M.; van Dijl, J. M. Proteomics of Protein Secretion by Bacillus Subtilis : Separating the "Secrets" of the Secretome . *Microbiology and Molecular Biology Reviews* **2004**, *68* (2), 207–233. https://doi.org/10.1128/mmbr.68.2.207-233.2004.

(2) Busatto, S.; Zendrini, A.; Radeghieri, A.; Paolini, L.; Romano, M.; Presta, M.; Bergese, P. The Nanostructured Secretome. *Biomaterials Science*. Royal Society of Chemistry January 1, 2020, pp 39–63. https://doi.org/10.1039/c9bm01007f.

(3) Arroyo, J. D.; Chevillet, J. R.; Kroh, E. M.; Ruf, I. K.; Pritchard, C. C.; Gibson, D. F.; Mitchell, P. S.; Bennett, C. F.; Pogosova-Agadjanyan, E. L.; Stirewalt, D. L.; Tait, J. F.; Tewari, M. Argonaute2 Complexes Carry a Population of Circulating MicroRNAs Independent of Vesicles in Human Plasma. *Proc Natl Acad Sci U S A* **2011**, *108* (12), 5003–5008. https://doi.org/10.1073/pnas.1019055108.

(4) Truman-Rosentsvit, M.; Berenbaum, D.; Spektor, L.; Cohen, L. A.; Belizowsky-Moshe, S.; Lifshitz, L.; Ma, J.; Li, W.; Kesselman, E.; Abutbul-Ionita, I.; Danino, D.; Gutierrez, L.; Li, H.; Li, K.; Lou, H.; Regoni, M.; Poli, M.; Glaser, F.; Rouault, T. A.; Meyron-Holtz, E. G. *Ferritin Is Secreted via 2 Distinct Nonclassical Vesicular Pathways*. http://ashpublications.org/blood/article-pdf/131/3/342/1406320/blood768580.pdf.

(5) Rehan, F.; Ahemad, N.; Gupta, M. Casein Nanomicelle as an Emerging Biomaterial—A Comprehensive Review. *Colloids and Surfaces B: Biointerfaces*. Elsevier B.V. July 1, 2019, pp 280–292. https://doi.org/10.1016/j.colsurfb.2019.03.051.

(6) Théry, C.; Witwer, K. W.; Aikawa, E.; Jose Alcaraz, M.; Anderson, J. D.; Andriantsitohaina, R.; Antoniou, A.; Bach, M.; Bachurski, D.; Baharvand, H.; Balaj, L.; Baldacchino, S.; Bauer, N. N.; Baxter, A. A.; Bebawy, M.; Beckham, C.; Bedina Zavec, A.; Benmoussa, A.; Berardi, A. C.; Bergese, P.; Bielska, E.; Blenkiron, C.; Bobis-Wozowicz, S.; Boilard, E.; Boireau, W.; Bongiovanni, A.; Borràs, F. E.; Bosch, S.; Boulanger, C. M.; Breakefield, X.; Breglio, A. M.; Á Brennan, M.; Brigstock, D. R.; Brisson, A.; Broekman, M. L.; Bromberg, J. F.; Bryl-Górecka, P.; Buch, S.; Buck, A. H.; Burger, D.; Busatto, S.; Buschmann, D.; Bussolati, B.; Buzás, E. I.; Bryan Byrd, J.; Camussi, G.; Carter, D. R.; Caruso, S.; Chamley, L. W.; Chang, Y.-T.; Chen, C.; Chen, S.; Cheng, L.; Chin, A. R.; Clayton, A.; Clerici, S. P.; Cocks, A.; Cocucci, E.; Coffey, R. J.; Cordeiro-da-Silva, A.; Couch, Y.; Coumans, F. A.; Coyle, B.; Crescitelli, R.;

Ferreira Criado, M.; Das, S.; Datta Chaudhuri, A.; de Candia, P.; De Santana Junior, E. F.; De Wever, O.; del Portillo, H. A.; Demaret, T.; Deville, S.; Devitt, A.; Dhondt, B.; Di Vizio, D.; Dieterich, L. C.; Dolo, V.; Paula Dominguez Rubio, A.; Dominici, M.; Dourado, M. R.; Driedonks, T. A.; Duarte, F. V; Duncan, H. M.; Eichenberger, R. M.; Ekström, K.; Andaloussi, S. EL; Elie-Caille, C.; Erdbrügger, U.; Falcón-Pérez, J. M.; Fatima, F.; Fish, J. E.; Flores-Bellver, M.; Försönits, A.; Frelet-Barrand, A.; Fricke, F.; Fuhrmann, G.; Gabrielsson, S.; Gámez-Valero, A.; Gardiner, C.; Gärtner, K.; Gaudin, R.; Song Gho, Y.; Giebel, B.; Gilbert, C.; Gimona, M.; Giusti, I.; Goberdhan, D. C.; Görgens, A.; Gorski, S. M.; Greening, D. W.; Christina Gross, J.; Gualerzi, A.; Gupta, G. N.; Gustafson, D.; Handberg, A.; Haraszti, R. A.; Harrison, P.; Hegyesi, H.; Hendrix, A.; Hill, A. F.; Hochberg, F. H.; Hoffmann, K. F.; Holder, B.; Holthofer, H.; Hosseinkhani, B.; Hu, G.; Huang, Y.; Huber, V.; Hunt, S.; Gamal-Eldin Ibrahim, A.; Ikezu, T.; Inal, J. M.; Isin, M.; Ivanova, A.; Jackson, H. K.; Jacobsen, S.; Jay, S. M.; Jayachandran, M.; Jenster, G.; Jiang, L.; Johnson, S. M.; Jones, J. C.; Jong, A.; Jovanovic-Talisman, T.; Jung, S. Journal of Extracellular Vesicles Minimal Information for Studies of Extracellular Vesicles 2018 (MISEV2018): A Position Statement of the International Society for Extracellular Vesicles and Update of the MISEV2014 Guidelines.

(7) Singh, H.; Gallier, S. Nature's Complex Emulsion: The Fat Globules of Milk. *Food Hydrocoll* **2017**, *68*, 81–89. https://doi.org/10.1016/j.foodhyd.2016.10.011.

(8) Ramasamy, I. Recent Advances in Physiological Lipoprotein Metabolism. *Clinical Chemistry and Laboratory Medicine*. Walter de Gruyter GmbH December 1, 2014, pp 1695–1727. https://doi.org/10.1515/cclm-2013-0358.

(9) Karimi, N.; Cvjetkovic, A.; Jang, S. C.; Crescitelli, R.; Hosseinpour Feizi, M. A.; Nieuwland, R.; Lötvall, J.; Lässer, C. Detailed Analysis of the Plasma Extracellular Vesicle Proteome after Separation from Lipoproteins. *Cellular and Molecular Life Sciences* **2018**, *75* (15), 2873–2886. https://doi.org/10.1007/s00018-018-2773-4.

(10) Augé, N.; Maupas-Schwalm, F.; Elbaz, M.; Thiers, J. C.; Waysbort, A.; Itohara, S.; Krell, H. W.; Salvayre, R.; Nègre-Salvayre, A. Role for Matrix Metalloproteinase-2 in Oxidized Low-Density Lipoprotein-Induced Activation of the Sphingomyelin/Ceramide Pathway and Smooth Muscle Cell Proliferation. *Circulation* **2004**, *110* (5), 571–578. https://doi.org/10.1161/01.CIR.0000136995.83451.1D.

(11) Ishikawa, H.; Yamada, H.; Taromaru, N.; Kondo, K.; Nagura, A.; Yamazaki, M.; Ando, Y.; Munetsuna, E.; Suzuki, K.; Ohashi, K.; Teradaira, R. Stability of Serum High-Density Lipoprotein-MicroRNAs for Preanalytical Conditions. *Ann Clin Biochem* **2017**, *54* (1), 134–142. https://doi.org/10.1177/0004563216647086.

(12) Sugio, S.; Kashima, A.; Mochizuki, S.; Noda, M.; Kobayashi, K. *Crystal Structure of Human Serum Albumin at 2.5 Å Resolution*; 1999; Vol. 12.

(13) Lexa, K. W.; Dolghih, E.; Jacobson, M. P. A Structure-Based Model for Predicting Serum Albumin Binding. *PLoS One* **2014**, *9* (4). https://doi.org/10.1371/journal.pone.0093323.

(14) Quinlan, G. J.; Martin, G. S.; Evans, T. W. Albumin: Biochemical Properties and Therapeutic Potential. *Hepatology*. June 2005, pp 1211–1219. https://doi.org/10.1002/hep.20720.

(15) Zhang, Y.; Orner, B. P. Self-Assembly in the Ferritin Nano-Cage Protein Superfamily. *International Journal of Molecular Sciences*. August 2011, pp 5406–5421. https://doi.org/10.3390/ijms12085406.

(16) Chiou, B.; Connor, J. R. Emerging and Dynamic Biomedical Uses of Ferritin. *Pharmaceuticals*. MDPI AG November 13, 2018. https://doi.org/10.3390/ph11040124.

(17) Ye, Z. L.; Jin, H. J.; Qian, Q. J. Argonaute 2: A Novel Rising Star in Cancer Research. *Journal of Cancer*. Ivyspring International Publisher 2015, pp 877–882. https://doi.org/10.7150/jca.11735.

(18) Zhang, Q.; Higginbotham, J. N.; Jeppesen, D. K.; Yang, Y. P.; Li, W.; McKinley, E. T.; Graves-Deal, R.; Ping, J.; Britain, C. M.; Dorsett, K. A.; Hartman, C. L.; Ford, D. A.; Allen, R. M.; Vickers, K. C.; Liu, Q.; Franklin, J. L.; Bellis, S. L.; Coffey, R. J. Transfer of Functional Cargo in Exomeres. *Cell Rep* **2019**, *27* (3), 940-954.e6. https://doi.org/10.1016/j.celrep.2019.01.009.

(19) Lopez, C.; Cauty, C.; Guyomarc'h, F. Organization of Lipids in Milks, Infant Milk Formulas and Various Dairy Products: Role of Technological Processes and Potential Impacts. *Dairy Science and Technology*. Springer-Verlag France November 1, 2015, pp 863–893. https://doi.org/10.1007/s13594-015-0263-0.

(20) Andreas, N. J.; Kampmann, B.; Mehring Le-Doare, K. Human Breast Milk: A Review on Its Composition and Bioactivity. *Early Human Development*. Elsevier Ireland Ltd November 1, 2015, pp 629–635. https://doi.org/10.1016/j.earlhumdev.2015.08.013.

(21) Argov, N.; Lemay, D. G.; German, J. B. Milk Fat Globule Structure and Function: Nanoscience Comes to Milk Production. *Trends in Food Science and Technology*. December 2008, pp 617–623. https://doi.org/10.1016/j.tifs.2008.07.006.

(22) Jukkola, A.; Partanen, R.; Rojas, O. J.; Heino, A. Separation of Milk Fat Globules via Microfiltration: Effect of Diafiltration Media and Opportunities for Stream Valorization. *J Dairy Sci* **2016**, *99* (11), 8644–8654. https://doi.org/10.3168/jds.2016-11422.

(23) Raposo, G.; Stoorvogel, W. Extracellular Vesicles: Exosomes, Microvesicles, and Friends. *Journal of Cell Biology*. February 2013, pp 373–383. https://doi.org/10.1083/jcb.201211138.

(24) Vlassov, A. V.; Magdaleno, S.; Setterquist, R.; Conrad, R. Exosomes: Current Knowledge of Their Composition, Biological Functions, and Diagnostic and Therapeutic Potentials. *Biochimica et Biophysica Acta - General Subjects*. July 2012, pp 940–948. https://doi.org/10.1016/j.bbagen.2012.03.017.

(25) Buzás, E. I.; Tóth, E.; Sódar, B. W.; Szabó-Taylor, K. Molecular Interactions at the Surface of Extracellular Vesicles. *Seminars in Immunopathology*. Springer Verlag September 1, 2018, pp 453–464. https://doi.org/10.1007/s00281-018-0682-0.

(26) Tóth, E.; Turiák, L.; Visnovitz, T.; Cserép, C.; Mázló, A.; Sódar, B. W.; Försönits, A. I.; Petővári, G.; Sebestyén, A.; Komlósi, Z.; Drahos, L.; Kittel, Á.; Nagy, G.; Bácsi, A.; Dénes, Á.; Gho, Y. S.; Szabó-Taylor, K.; Buzás, E. I. Formation of a Protein Corona on the Surface of Extracellular Vesicles in Blood Plasma. *J Extracell Vesicles* **2021**, *10* (11). https://doi.org/10.1002/jev2.12140.

(27) Zhang, Q.; Jeppesen, D. K.; Higginbotham, J. N.; Graves-Deal, R.; Trinh, V. Q.; Ramirez, M. A.; Sohn, Y.; Neininger, A. C.; Taneja, N.; McKinley, E. T.; Niitsu, H.; Cao, Z.; Evans, R.; Glass, S. E.; Ray, K. C.; Fissell, W. H.; Hill, S.; Rose, K. L.; Huh, W. J.; Washington, M. K.; Ayers, G. D.; Burnette, D. T.; Sharma, S.; Rome, L. H.; Franklin, J. L.; Lee, Y. A.; Liu, Q.; Coffey, R. J. Supermeres Are Functional Extracellular Nanoparticles Replete with Disease Biomarkers and Therapeutic Targets. *Nat Cell Biol* **2021**, *23* (12), 1240–1254. https://doi.org/10.1038/s41556-021-00805-8.

(28) Rai, A.; Greening, D. W.; Xu, R.; Chen, M.; Suwakulsiri, W.; Simpson, R. J. Secreted Midbody Remnants Are a Class of Extracellular Vesicles Molecularly Distinct from Exosomes and Microparticles. *Commun Biol* **2021**, *4* (1). https://doi.org/10.1038/s42003-021-01882-z.

(29) Zendrini, A.; Guerra, G.; Sagini, K.; Vagner, T.; Di Vizio, D.; Bergese, P. On the Surface-to-Bulk Partition of Proteins in Extracellular Vesicles. *Colloids Surf B Biointerfaces* **2022**, *218*. https://doi.org/10.1016/j.colsurfb.2022.112728.

(30) Wolf, M.; Poupardin, R. W.; Ebner-Peking, P.; Andrade, A. C.; Blöchl, C.; Obermayer, A.; Gomes, F. G.; Vari, B.; Maeding, N.; Eminger, E.; Binder, H. M.; Raninger, A. M.; Hochmann, S.; Brachtl, G.; Spittler, A.; Heuser, T.; Ofir, R.; Huber, C. G.; Aberman, Z.; Schallmoser, K.; Volk, H. D.; Strunk, D. A Functional Corona around Extracellular Vesicles Enhances Angiogenesis, Skin Regeneration and Immunomodulation. *J Extracell Vesicles* **2022**, *11* (4). https://doi.org/10.1002/jev2.12207.

(31) Busatto, S.; Yang, Y.; Walker, S. A.; Davidovich, I.; Lin, W. H.; Lewis-Tuffin, L.; Anastasiadis, P. Z.; Sarkaria, J.; Talmon, Y.; Wurtz, G.; Wolfram, J. Brain Metastases-Derived

Extracellular Vesicles Induce Binding and Aggregation of Low-Density Lipoprotein. *J Nanobiotechnology* **2020**, *18* (1). https://doi.org/10.1186/s12951-020-00722-2.

(32) Hu, M.; Briguglio, J. J.; Deserno, M. Determining the Gaussian Curvature Modulus of Lipid Membranes in Simulations. *Biophys J* **2012**, *102* (6), 1403–1410. https://doi.org/10.1016/j.bpj.2012.02.013.

(33) Radeghieri, A.; Bergese, P. The Biomolecular Corona of Extracellular Nanoparticles Holds New Promises for Advancing Clinical Molecular Diagnostics. *Expert Review of Molecular Diagnostics*. Taylor and Francis Ltd. 2023, pp 471–474. https://doi.org/10.1080/14737159.2023.2215927.

(34) Corti, G.; Buchet, R.; Magrini, A.; Ciancaglini, P.; Mebarek, S.; Bottini, M. The Surface Proteomic Profile of Serum Extracellular Vesicles as a Diagnostic and Prognostic Tool in Breast Cancer. *Current Opinion in Physiology*. Elsevier Ltd February 1, 2024. https://doi.org/10.1016/j.cophys.2023.100734.

(35) Webber, J.; Clayton, A. How Pure Are Your Vesicles? *J Extracell Vesicles* **2013**, *2* (1). https://doi.org/10.3402/jev.v2i0.19861.

(36) Witwer, K. W.; Buzás, E. I.; Bemis, L. T.; Bora, A.; Lässer, C.; Lötvall, J.; Nolte-'t Hoen, E. N.; Piper, M. G.; Sivaraman, S.; Skog, J.; Théry, C.; Wauben, M. H.; Hochberg, F. Standardization of Sample Collection, Isolation and Analysis Methods in Extracellular Vesicle Research. *J Extracell Vesicles* **2013**, *2* (1). https://doi.org/10.3402/jev.v2i0.20360.

(37) Hoen, E. N.; Cremer, T.; Gallo, R. C.; Margolis, L. B. Extracellular Vesicles and Viruses: Are They Close Relatives? *Proceedings of the National Academy of Sciences of the United States of America*. National Academy of Sciences August 16, 2016, pp 9155–9161. https://doi.org/10.1073/pnas.1605146113.

(38) Buzas, E. I. Opportunities and Challenges in Studying the Extracellular Vesicle Corona. *Nature Cell Biology*. Nature Research September 1, 2022, pp 1322–1325. https://doi.org/10.1038/s41556-022-00983-z.

(39) van Niel, G.; Carter, D. R. F.; Clayton, A.; Lambert, D. W.; Raposo, G.; Vader, P. Challenges and Directions in Studying Cell–Cell Communication by Extracellular Vesicles. *Nat Rev Mol Cell Biol* **2022**, *23* (5), 369–382. https://doi.org/10.1038/s41580-022-00460-3.

(40) Musicò, A.; Zenatelli, R.; Romano, M.; Zendrini, A.; Alacqua, S.; Tassoni, S.; Paolini, L.; Urbinati, C.; Rusnati, M.; Bergese, P.; Pomarico, G.; Radeghieri, A. Surface Functionalization of Extracellular Vesicle Nanoparticles with Antibodies: A First Study on the Protein Corona "Variable." *Nanoscale Adv* **2023**, *5* (18), 4703–4717. https://doi.org/10.1039/D3NA00280B.

(41) Stremersch, S.; De Smedt, S. C.; Raemdonck, K. Therapeutic and Diagnostic Applications of Extracellular Vesicles. *Journal of Controlled Release* **2016**, *244*, 167–183. https://doi.org/10.1016/j.jconrel.2016.07.054.

(42) Radeghieri, A.; Alacqua, S.; Zendrini, A.; Previcini, V.; Todaro, F.; Martini, G.; Ricotta, D.; Bergese, P. Active Antithrombin Glycoforms Are Selectively Physiosorbed on Plasma Extracellular Vesicles. *Journal of Extracellular Biology* **2022**, *1* (9). https://doi.org/10.1002/jex2.57.

(43) Dawson, K. A.; Yan, Y. Current Understanding of Biological Identity at the Nanoscale and Future Prospects. *Nat Nanotechnol* **2021**, *16* (3), 229–242. https://doi.org/10.1038/s41565-021-00860-0.

(44) Latreille, P. L.; Le Goas, M.; Salimi, S.; Robert, J.; De Crescenzo, G.; Boffito, D. C.; Martinez, V. A.; Hildgen, P.; Banquy, X. Scratching the Surface of the Protein Corona: Challenging Measurements and Controversies. *ACS Nano*. American Chemical Society February 22, 2022, pp 1689–1707. https://doi.org/10.1021/acsnano.1c05901.

(45) Ren, J.; Andrikopoulos, N.; Velonia, K.; Tang, H.; Cai, R.; Ding, F.; Ke, P. C.; Chen, C. Chemical and Biophysical Signatures of the Protein Corona in Nanomedicine. *Journal of the American Chemical Society*. American Chemical Society June 1, 2022, pp 9184–9205. https://doi.org/10.1021/jacs.2c02277.

(46) Liam-Or, R.; Faruqu, F. N.; Walters, A.; Han, S.; Xu, L.; Wang, J. T. W.; Oberlaender, J.; Sanchez-Fueyo, A.; Lombardi, G.; Dazzi, F.; Mailaender, V.; Al-Jamal, K. T. Cellular Uptake and in Vivo Distribution of Mesenchymal-Stem-Cell-Derived Extracellular Vesicles Are Protein Corona Dependent. *Nat Nanotechnol* **2024**, *19* (6), 846–855. https://doi.org/10.1038/s41565-023-01585-y.

(47) García-álvarez, R.; Vallet-Regí, M. Hard and Soft Protein Corona of Nanomaterials: Analysis and Relevance. *Nanomaterials* **2021**, *11* (4). https://doi.org/10.3390/nano11040888.

(48) Margolis, L.; Sadovsky, Y. The Biology of Extracellular Vesicles: The Known Unknowns. *PLoS Biol* **2019**, *17* (7). https://doi.org/10.1371/journal.pbio.3000363.

(49) Busatto, S.; Yang, Y.; Iannotta, D.; Davidovich, I.; Talmon, Y.; Wolfram, J. Considerations for Extracellular Vesicle and Lipoprotein Interactions in Cell Culture Assays. *Journal of Extracellular Vesicles*. John Wiley and Sons Inc April 1, 2022. https://doi.org/10.1002/jev2.12202.

(50) Ridolfi, A.; Conti, L.; Brucale, M.; Frigerio, R.; Cardellini, J.; Musicò, A.; Romano, M.; Zendrini, A.; Polito, L.; Bergamaschi, G.; Gori, A.; Montis, C.; Panella, S.; Barile, L.; Berti, D.; Radeghieri, A.; Bergese, P.; Cretich, M.; Valle, F. Particle Profiling of EV-Lipoprotein Mixtures

by AFM Nanomechanical Imaging. *J Extracell Vesicles* **2023**, *12* (10). https://doi.org/10.1002/jev2.12349.

(51) Nikoloff, J. M.; Saucedo-Espinosa, M. A.; Kling, A.; Dittrich, P. S. Identifying Extracellular Vesicle Populations from Single Cells. **2021**. https://doi.org/10.1073/pnas.2106630118/-/DCSupplemental.

(52) Subra, C.; Laulagnier, K.; Perret, B.; Record, M. Exosome Lipidomics Unravels Lipid Sorting at the Level of Multivesicular Bodies. *Biochimie*. February 2007, pp 205–212. https://doi.org/10.1016/j.biochi.2006.10.014.

(53) Lozano-Andrés, E.; Enciso-Martinez, A.; Gijsbers, A.; Ridolfi, A.; Van Niel, G.; Libregts, S. F. W. M.; Pinheiro, C.; van Herwijnen, M. J. C.; Hendrix, A.; Brucale, M.; Valle, F.; Peters, P. J.; Otto, C.; Arkesteijn, G. J. A.; Wauben, M. H. M. Physical Association of Low Density Lipoprotein Particles and Extracellular Vesicles Unveiled by Single Particle Analysis. *J Extracell Vesicles* **2023**, *12* (11). https://doi.org/10.1002/jev2.12376.

(54) Dietz, L.; Oberländer, J.; Mateos-Maroto, A.; Schunke, J.; Fichter, M.; Krämer-Albers, E. M.; Landfester, K.; Mailänder, V. Uptake of Extracellular Vesicles into Immune Cells Is Enhanced by the Protein Corona. *J Extracell Vesicles* **2023**, *12* (12). https://doi.org/10.1002/jev2.12399.

(55) Maiolo, D.; Paolini, L.; Di Noto, G.; Zendrini, A.; Berti, D.; Bergese, P.; Ricotta, D. Colorimetric Nanoplasmonic Assay to Determine Purity and Titrate Extracellular Vesicles. *Anal Chem* **2015**, *87* (8), 4168–4176. https://doi.org/10.1021/ac504861d.

(56) Welsh, J. A.; Goberdhan, D. C. I.; O'Driscoll, L.; Buzas, E. I.; Blenkiron, C.; Bussolati, B.; Cai, H.; Di Vizio, D.; Driedonks, T. A. P.; Erdbrügger, U.; Falcon-Perez, J. M.; Fu, Q.; Hill, A. F.; Lenassi, M.; Lim, S. K.; Mahoney, M. G.; Mohanty, S.; Möller, A.; Nieuwland, R.; Ochiya, T.; Sahoo, S.; Torrecilhas, A. C.; Zheng, L.; Zijlstra, A.; Abuelreich, S.; Bagabas, R.; Bergese, P.; Bridges, E. M.; Brucale, M.; Burger, D.; Carney, R. P.; Cocucci, E.; Crescitelli, R.; Hanser, E.; Harris, A. L.; Haughey, N. J.; Hendrix, A.; Ivanov, A. R.; Jovanovic-Talisman, T.; Kruh-Garcia, N. A.; Ku'ulei-Lyn Faustino, V.; Kyburz, D.; Lässer, C.; Lennon, K. M.; Lötvall, J.; Maddox, A. L.; Martens-Uzunova, E. S.; Mizenko, R. R.; Newman, L. A.; Ridolfi, A.; Rohde, E.; Rojalin, T.; Rowland, A.; Saftics, A.; Sandau, U. S.; Saugstad, J. A.; Shekari, F.; Swift, S.; Ter-Ovanesyan, D.; Tosar, J. P.; Useckaite, Z.; Valle, F.; Varga, Z.; van der Pol, E.; van Herwijnen, M. J. C.; Wauben, M. H. M.; Wehman, A. M.; Williams, S.; Zendrini, A.; Zimmerman, A. J.; Théry, C.; Witwer, K. W. Minimal Information for Studies of Extracellular Vesicles (MISEV2023): From Basic to Advanced Approaches. *J Extracell Vesicles* **2024**, *13* (2). https://doi.org/10.1002/jev2.12404.

(57) Osteikoetxea, X.; Balogh, A.; Szabó-Taylor, K.; Németh, A.; Szabó, T. G.; Pálóczi, K.; Sódar, B.; Kittel, Á.; György, B.; Pállinger, É.; Matkó, J.; Buzás, E. I. Improved Characterization of EV Preparations Based on Protein to Lipid Ratio and Lipid Properties. *PLoS One* **2015**, *10* (3). https://doi.org/10.1371/journal.pone.0121184.

(58) Cvjetkovic, A.; Lötvall, J.; Lässer, C. The Influence of Rotor Type and Centrifugation Time on the Yield and Purity of Extracellular Vesicles. *J Extracell Vesicles* **2014**, *3* (1). https://doi.org/10.3402/jev.v3.23111.

(59) Gupta, D.; Zickler, A. M.; El Andaloussi, S. Dosing Extracellular Vesicles. *Advanced Drug Delivery Reviews*. Elsevier B.V. November 1, 2021. https://doi.org/10.1016/j.addr.2021.113961.

(60) Picciotto, S.; Barone, M. E.; Fierli, D.; Aranyos, A.; Adamo, G.; Božič, D.; Romancino, D. P.; Stanly, C.; Parkes, R.; Morsbach, S.; Raccosta, S.; Paganini, C.; Cusimano, A.; Martorana, V.; Noto, R.; Carrotta, R.; Librizzi, F.; Capasso Palmiero, U.; Santonicola, P.; Iglič, A.; Gai, M.; Corcuera, L.; Kisslinger, A.; Di Schiavi, E.; Landfester, K.; Liguori, G. L.; Kralj-Iglič, V.; Arosio, P.; Pocsfalvi, G.; Manno, M.; Touzet, N.; Bongiovanni, A. Isolation of Extracellular Vesicles from Microalgae: Towards the Production of Sustainable and Natural Nanocarriers of Bioactive Compounds. *Biomater Sci* **2021**, *9* (8), 2917–2930. https://doi.org/10.1039/d0bm01696a.

(61) Manno, M., Bongiovanni, A., Margolis, L., Bergese, P., Paolo, Arosio, P. The physico-chemical landscape of extracellular vesicles. *Nat Rev Bioeng* **2024** https://doi.org/10.1038/s44222-024-00255-5

Chapter 3 - Extracellular Vesicles Surface Engineering and the Protein Corona "variable''

This chapter is adjusted from our paper: **Angelo Musicò**, Rossella Zenatelli, Miriam Romano, Andrea Zendrini, Silvia Alacqua, Selene Tassoni, Lucia Paolini, Chiara Urbinati, Marco Rusnati, Paolo Bergese, Giuseppe Pomarico, Annalisa Radeghieri (2023). Surface functionalization of extracellular vesicle nanoparticles with antibodies: a first study on the protein corona "variable". Nanoscale Advances. DOI: 10.1039/D3NA00280B. This study investigates protein corona formation during exogenous EV surface functionalization, using red blood cell-derived EVs functionalized with Cetuximab (CTX), comparing their properties to non-functionalized EVs.

3.1 Introduction

Extracellular nanoparticles (ENPs) are nanoparticles originating from cells and biological systems, including Extracellular Vesicles (EVs), lipoproteins, and protein nanoaggregates. They constitute the nanostructured secretome and differentiate each other in biological roles and biophysical properties.[1] Due to their biological origin, ENPs present lower cytotoxicity and higher colloidal stability in biological fluids than their synthetic counterparts (e.g., liposomes, and synthetic nanoparticles - SNPs).[2-4] For these reasons, ENPs are emerging in different medical fields as promising therapeutics and imaging agents.[5-10] Among the ENPs, EVs have gained much interest during the last decade mainly due to their outstanding therapeutic performances in cancer therapy[11] and regenerative medicine.[6,12] EVs are composed of a phospholipid bilayer membrane enriched with lipids, proteins, and carbohydrates enclosing an aqueous core containing soluble proteins, nucleic acids, and metabolites.[1,13] The complexity of EV structure allows their application as up-and-comer biological delivery systems. However, despite promising preclinical data, EV-based therapeutic approaches have been hampered by different issues, including EV-based therapeutics stability, scalability, safety, [14,] and accumulation in specific organs (e.g., liver and spleen). [15] A promising approach to tackle EV-based therapeutics pharmacokinetics[16] and tropism limits[9,17,18] is represented by the functionalization of EV surface that can be achieved by endogenous or exogenous strategies. Endogenous EV surface functionalization exploits cellular machinery and involves genetic modification of EV-secreting cells. This challenging approach could lead to unintended cell changes and may not be suitable for introducing unnatural or short-term stable molecules. Contrarily, exogenous EV surface functionalization can be achieved by manipulating

the EVs after their isolation,[16] thus overcoming some of the limitations mentioned above related to the endogenous strategy. Indeed, exogenous modification of EVs is not affected by cellular activity and exploits the richness of chemistry conferred to the biological surface by the presence of tuneable molecules such as proteins and carbohydrates[18]. Finally, it can be applied to introduce both natural and artificial moieties. One of the most investigated exogenous surface functionalization methods is based on covalently binding target ligands to suitable moieties of membrane proteins or phospholipids[19–21] present on EV membranes[18–20]. While small molecules such as fluorophores or drugs can be added with a one-step reaction to EV surface components, larger moieties as antibodies require the preliminary introduction of spacers and clickable groups onto the EV surface, followed by a reaction with suitable units on antibodies or proteins to achieve EV functionalization. During this procedure, EVs are generally reacted with a target protein-enriched solution to achieve a satisfactory increase in the kinetics of the reaction and the conjugation yield.[16–19]. It has been widely acknowledged that synthetic nanoparticles, when immersed in biofluids, are almost immediately covered by multiple layers of macromolecules (i.e., biomolecular corona - BC).[3,4] The BC is a dynamic entity made by some tightly adsorbed macromolecules (the so-called hard corona) and surrounded by weakly adsorbed layer(s) of macromolecules (soft corona). The overall composition is in equilibrium with the medium with which it constantly exchanges macromolecules. [22,23] The BC plays a pivotal role in defining the biological properties of the SNPs (e.g., nanoparticle uptake, biodistribution, and toxicity).[2,24,25] The most common type of BC is the protein corona (PC), where proteins are the most abundant macromolecules adsorbed on the SNP surface. Very recent studies have demonstrated PC also forms around EV surface during *in vivo* circulation[26–30] (and since then, exponentially increasing efforts have been launched to tackle understanding of its role on EV colloidal, biophysical, and biological properties). Therefore, it is reasonable to hypothesize that a PC can also form *in vitro* during the incubation of EVs with macromolecule-enriched fluids, i.e., during the exogenous surface functionalization of EVs. In this work, we explore this aspect for the first time, using EVs derived from Red Blood Cells (REVs) functionalized with an anti-epidermal growth factor receptor (EGFR) monoclonal antibody (Cetuximab, CTX). Functionalized and pristine EVs were compared in terms of morphology, functionalization efficiency, binding activity, and *in vitro* uptake.

3.2 Experimental section

3.2.1 Reagents

Solvents were purchased from Merck and Carlo Erba and used as received without further purification. PBS, DMEM, FBS, and Penicillin/Streptomycin were purchased from Corning (Mediatech Inc., Manassas, VA, USA). NaN_3 was purchased from Sigma Aldrich (St. Louis, MO, USA). Sulfo-Cyanine7.5 NHS ester was purchased from Lumiprobe GmbH (Germany). DBCO-STP Ester, Azido-PEG_4-NHS Ester, and Cy3 Azide were purchased from ClickChemistryTools, (Scottsdale, Az, US). MemGlow™ 488 was purchased from Cytoskeleton, Inc. (Denver, USA). Calcium ionophore (A23187) was purchased from Sigma Aldrich (St. Louis, USA).

3.2.2 Instrumentation

Centrifugation was performed with a 5804R Eppendorf Centrifuge, A-4-44 rotor, using 15 mL tubes. Ultracentrifugation for large volumes (up to 50 mL) was performed with Optima XPN-100 equipped with a TY45 Ti rotor (Beckman Coulter, USA) while for small volumes (up to 1.5 mL) we used an Optima MAX-XP using a TLA-55 and a MLS-50 rotor (Beckman Coulter, USA). Images from western blot and gel fluorescence were acquired with Syngene G:BOX Chemi XX9 (SYNGENE, UK) and were analyzed and quantified with the software Genesys and GeneTools (SYNGENE, UK). NanoDrop™ OneC (ThermoFisher, Rockford, USA) was used to characterize mCTX. Zeiss LSM510 with a Plan-Apochromat 63x/1.4 Oil DIC objective (Germany) was used to perform fluorescence confocal microscopy. All the VivaSpin columns used in this work were purchased from Sartorius Stedim Lab Lid (Sperry Way, Stonehouse, UK). NanoSight NS300 system was used to determine the size distribution and the particle concentration of REV samples (Malvern Technologies, Malvern, UK). BIAcore X-100 instrument was used for SPR (Cytiva Life Science, Marlborough, MA, USA).

3.2.3 Red Blood Cell EV (REVs) collection (isolation\separation)

We have submitted all relevant data of our experiments to the EV-TRACK knowledge base (EV-TRACK ID: EV230439).[31] REVs were isolated following the guidelines from Usman et al.[5] Briefly, after blood collection (100 mL), RBCs were pelleted by centrifugation at 1000 × *g* for 8 minutes at 4 °C and washed three times in PBS without calcium and magnesium. RBCs were further washed two times with CPBS (PBS + 0.1 g/L calcium chloride) and transferred into a 75 mm^2 tissue culture flask. Calcium ionophore was added to the flask (final concentration 10 mM) and incubated overnight at 37 °C. RBCs (75 mL) were gently collected from the flask, and cellular debris was removed by differential centrifugation (600 × *g* for 20 min, 1600 × *g* for 15 min, 3260 × *g* for 15 min, and 10,000 × *g* for 30 min at 4 °C). The pellet was discarded at every step, transferring the supernatant into a fresh tube. The supernatants were filtered through 0.45 μm nylon

syringe filters. EVs were collected by ultracentrifugation at 100,000 × g for 70 min at 4 °C. EV pellets were then resuspended in cold PBS, layered above 2 mL frozen 60% sucrose cushion, and centrifuged at 100,000 × *g* for 16 h at 4 °C, with deceleration speed set to 0. The red layer of EVs was collected and washed twice with cold PBS and spun at 100,000 × *g* for 70 min at 4 °C. Finally, EVs were resuspended in 1 mL of cold PBS.

3.2.4 Cell culture

Two cell lines were used: the epithelial breast cancer cells MDA-MB-231 (ATCC #HTB-26) and the kidney embryo cells HEK293 (ATCC #CRL-1573). Both the cell lines were purchased from the American Type Culture Collection (ATCC), Manassas, VA, USA. Cells were cultured in DMEM supplemented with 10% Fetal Bovine Serum (FBS) and 1% Penicillin/Streptomycin and maintained at 37 °C under 5% CO_2. Cells were routinely tested for mycoplasma.

3.2.5 Cetuximab functionalization

Cetuximab (CTX) was kindly provided by Prof. Fabio Corsi (University of Milan) in storage buffer (sterile PBS + 0.1 mM NaN_3). The storage buffer was replaced with 0.1 mM $NaHCO_3$, pH 8.4 using VivaSpin2000 column with 50 kDa cut-off. CTX solutions were centrifuged at 2000 × *g* for 15 minutes. The buffer exchange step was carried out thrice by adding 2 mL of $NaHCO_3$ 0.1 mM, pH 8.4 at each step. CTX concentration after the buffer exchange process was quantified by NanoDrop™ OneC. For antibody functionalization, 200 µL of CTX 0.016 mM was incubated overnight on continuous mixing at 4 °C with 12 equivalents of Sulfo Cyanine 7.5 NHS ester (0.2 mM in DMSO) and 6 equivalents of DBCO STF ester (0.1 mM in DMSO), thus obtaining modified CTX (mCTX). For deactivation, mCTX was incubated overnight at 4 °C with 1 µM of NaN_3 in PBS pH 7.4. DBCO conjugation yield was estimated by incubating a small aliquot of functionalized mCTX with azido-Sulfo Cyanine 3 overnight on continuous mixing at 4 °C. Excess of reagents (Sulfo Cyanine 7.5 NHS ester, DBCO STF ester, azido-Sulfo Cyanine 3 or NaN_3) was removed after every step with Vivaspin500 column with 30 kDa cut off by centrifuging the mCTX solution at 12000 × *g* for 15 min and washing it with 500 µL of PBS until no significant signal from the free fluorescent dyes could be detected by UV-Vis spectroscopy. mCTX characterization is reported in SI.

3.2.6 Bicinchoninic acid (BCA) assay

Protein concentrations of REVs and RBC homogenate samples were determined with Pierce™ BCA Protein Assay Kit (ThermoFisher, Rockford, USA), following the manufacturer's instructions.

3.2.7 SDS-Page and Western Blotting

Samples were boiled in reducing SDS sample buffer (80 mM Tris, pH 6.8, 2% SDS, 7.5% glycerol, 0.01% bromophenol blue) supplemented with 2% 2-mercaptoethanol for 5 min at 95 °C and separated by SDS-PAGE on acrylamide/bisacrylamide 10% gel.[32] For densitometric analysis, we used the Image Lab software (Biorad, Hercules, CA, US). For CTX quantification, after the electrophoresis run, the gel was imaged by Syngene G:BOX Chemi XX9 with an acquisition time of 2 min and 800 nm wavelength. For the WB analysis, samples were transferred onto a PVDF membrane and blocked overnight with 5% fat-free milk in PBS-0.05% Tween-20 (PBST).[32] The PVDF membranes were incubated with the following antibodies (at dilution 1:1000) for 90 min in PBST + fat-free milk 1%: mouse anti-GM130 (610823, clone 35/GM130, BD Biosciences, Germany), mouse anti-Alix (sc-53539, 2H12, Santa Cruz Biotechnology, USA), rabbit ant-Annexin XI (GTX33010, polyclonal, GeneTex, USA), mouse anti-CD47 (sc-59079, BRIC 126, Santa Cruz Biotechnology, USA), mouse anti-CD45 (sc-1178, 35-Z6, Santa Cruz Biotechnology, USA), rabbit anti-EGFR (4406, clone 15F8, Cell Signalling Technology Inc.), mouse anti-HBA1 (H00003039-M02, clone 4F9, Abnova, Jhouzih St., Taipei, Taiwan), mouse anti-HBB (2H3Abnova, Jhouzih St., Taipei, Taiwan). The membranes were washed thrice for 10 min with PBST and incubated for 1 h with the following secondary antibodies (at dilution 1:3000): rabbit anti-mouse and goat anti-rabbit (Zymed). Blots were detected using Luminata Classic HRP western substrate (Millipore). Images were acquired using a G: Box Chemi XT Imaging system, as described in Alvisi *et al.*[33].

3.2.8 COlorimetric NANoplasmonic (CONAN) assay

The purity of REV preparations from soluble contaminants was tested with the CONAN assay. The assay is a colorimetric test that exploits the aggregation of citrate-capped gold nanoparticles (AuNPs) onto the EV membrane and the formation of the protein corona onto the AuNP surface to detect soluble proteins in EV preparations. CONAN assay was performed according to Zendrini *et al.*[34]

3.2.9 Atomic Force Microscopy (AFM) imaging

Atomic Force Microscopy (AFM) imaging was performed on a Nanosurf NaioAFM equipped with a Multi75-AI-G tip (Budget Sensors). For sample preparation, EVs were resuspended in 100 µL sterile H_2O (Milli-Q, Merck Millipore) and diluted 1:10 in H_2O. 5 µL of the sample were then spotted onto freshly cleaved mica sheets (Grade V-1, thickness 0.15 mm, size 15 × 15 mm^2) and dried at 37 °C for 10 minutes. Images were acquired in tapping mode, with a scan size ranging

from 1.5 to 25 μm and a scan speed of 1 s per scanning line. Image processing was performed on Gwyddion ver. 2.61.

3.2.10 Nanoparticle Tracking Analysis (NTA)

Nanoparticle Tracking Analysis (NTA) was performed according to the manufacturer's instructions using a NanoSight NS300 system configured with a 532 nm laser. Samples were diluted 1:1000 in filtered PBS (0.22 μm) to a final volume of 1 mL to obtain the optimal particle per frame value (20–100 particles/frame). A syringe pump with constant flow injection was used (20 μl/min), and the temperature was set constant at 25 °C. Particles were detected at a camera level of 10 and three videos of 60 s were captured and analyzed with NTA software ver 3.2. The mean, mode, and median EV sizes from each video were used to calculate sample concentration, expressed in particles/mL.[35]

3.2.11 REV functionalization and labeling

REVs were functionalized following a two-step labeling strategy. 200 μL of $8x10^{11}$ EV/mL REV solution was reacted with 200, 500, or 1000 equivalent of -ester (diluted in PBS) overnight on continuous mixing at 4 °C. PEG excess was removed using Vivaspin500 column with 10 kDa cut-off, washing the samples five times with 500 μL of PBS. Pegylated REVs were recovered from the column with 200 μL of PBS. 200 μL of pegylated REVs ($8*10^{11}$ particles/ml) were then reacted overnight on continuous mixing at 4 °C with 200, 500, or 1000 equivalent of mCTX (in PBS, pH 7.4). The unreacted antibody was removed by ultracentrifugation (100,000 × *g*, 2 h), and the pellet was resuspended in 100 μL of PBS and stored at 4 °C until use. REV labeling with MemGlow™ 488 was performed following standard customer protocols. REVs were incubated with MemGlow™ 488 100 nM for 15 min, then MemGlow™ 488 excess was removed by ultracentrifugation (100,000 × *g*, 2 h).

3.2.12 Surface Plasmon Resonance (SPR)

The BIAcore X-100 instrument was used. Human EGFR was immobilized by standard amine-coupling chemistry on a research grade CM5 sensorchip, whose surface consists of a carboxymethylated dextran matrix. In detail, EGFR was resuspended at 15 μg/mL in 10 mM sodium acetate pH 4.8 and injected for 180 sec. at a flow rate of 10 mL/min on one cell of the sensorchip previously activated with a mixture of 1-ethyl-3-(3-dimethylamino propyl) carbodiimide hydrochloride (0.2 M) and *N*-hydroxy-succinimide (0.5 M). Following EGFR binding the surface was deactivated with ethanolamine. With this procedure, three different biosensors have been generated and used for the analysis presented in the work with an amount of

immobilized EGFR receptor varying between 1,400 and 2,500 resonance units (RU) (equal to 8-13 fmol/mm^2). On the second cell, used as a negative control for blank subtraction, was performed a blank immobilization. For binding analysis, increasing concentrations of the various proteins and EVs were resuspended in 0.01 M HEPES pH 7.4, 0.15 M NaCl, 3.0 mM EDTA, 0.005% v/v Surfactant P20 (HBS), injected over the sensorchips for 180 sec. at a flow rate of 30 µL/min to allow their association with the immobilized EGFR and then washed until dissociation. To preserve the immobilized receptor, the single cycle model was adopted,[36] where the compounds are injected at increasing concentrations within a single scan without regeneration of the surface after each injection.

3.2.13 In vitro uptake assay

MDA-MB-231 cells were seeded on 12 mm-sized coverslips, precoated with 50 µg/mL Type I Bovine Collagen (TB03, Alphabioregen) as 200000 cells/mL in 150 µL of complete media. After 24 h, cells were treated for 4 h and 24 h with MemGlow™ 488 labeled REVs, REVs-physi-mCTX, REVs-click-mCTX, and mCTX in media with or without FBS. Each treatment was carried out using comparable amounts of REVs (10^{10} EVs/mL) and CTX (1.61×10^{-1} nM). Cells were washed once with PBS 1X without $CaCl_2$ and $MgCl_2$ (21-040-CV, Corning) and then fixed with 3% paraformaldehyde (PFA) solution for 15 minutes at room temperature (RT). PFA was quenched with 50 mM NH_4Cl for 10 minutes at RT. Cells were washed twice with PBS 1x and permeabilized with 0.3%. Saponin in PBS 1x for 10 minutes at RT. Cellular nuclei were stained with DAPI (Invitrogen, 1:600). Cells were washed twice with PBS 1x, once with bidistilled H_2O, and coverslips were mounted using ProLong™ Gold Antifade Mountant (P36934, Invitrogen). For EV uptake analysis, 512 x 512 pixel images were acquired with a Zeiss LSM510 with a Plan-Apochromat 63x/1.4 Oil DIC objective, with a 0.2% 405 nm laser for DAPI and 0.2% 488 nm for MemGlow™ 488. Images were quantified with the software ZEN 3.6. For mCTX uptake analysis, coverslips were also acquired with Syngene G:BOX Chemi XX9 following standard protocols present in the software for detecting Cy7.5 and DAPI. For each treatment, MemGlow™ 488 and CTX fluorescence signals were normalized to DAPI fluorescence.

3.3 Results and Discussion

3.3.1 CTX modification and characterization

CTX chemical modification was optimized for REV surface functionalization. We exploited the coupling between primary amines (mainly the amino group on the side chain of lysines of the antibody) and activated esters (see experimental section). We adopted this strategy to covalently bind the fluorophore (Sulfo Cyanine 7.5, Cy7.5) and the alkyne unit (dibenzocyclooctyne, DBCO)

in order to permit tracking of CTX and coupling with the azido groups added on the REV surface (see REV surface functionalization section), respectively (see Fig. 1.3). CTX modification was optimized to introduce functional units while keeping antibody binding ability. Two reaction ratios were tested to find the better condition to bind approximately 1 DBCO and 2 Cy7.5 to the CTX. In the optimized protocol, CTX was reacted with 12 equivalents of Cy7.5 and 6 equivalents of DBCO. After purification, modified CTX (mCTX), was characterized by UV-Vis spectroscopy (Fig. 1.3B) to determine the number of dyes attached to the antibody by the following equations:

$$M = \frac{A280 - (Amax\ x\ C)}{\varepsilon} x\ D \qquad (1)$$

$$R = \frac{Amax}{\varepsilon' x\ M} x\ D \qquad (2)$$

Equation (1) was used to estimate the CTX molar concentration (M), while equation (2) was used to calculate the antibody/dye ratio. In the equations, D is the dilution factor, A_{280} is the absorbance at 280 nm, A_{max} is the absorbance of the peak of the fluorophore, C is the correction factor, while ε and ε' are the molar extinction coefficients of the antibody (210000 $M^{-1}cm^{-1}$) and the dye (Cy7.5: 220000 $M^{-1}cm^{-1}$, Cy3: 150000 $M^{-1}cm^{-1}$) respectively. DBCO quantification was performed by reacting an aliquot of mCTX with 6 equivalents of azido-sulfo Cyanine 3 (Cy3). This step is required due to the low molar extinction coefficient of the DBCO and to the proximity of its peak with the more intense protein signal at 280 nm, which hampers direct DBCO quantification by UV-Vis spectroscopy. UV-Vis spectra of mCTX-Cy3 (Fig. 1.3C) were used to calculate the degree of CTX labeling by Cy3 using equations (1) and (2), and assuming that DBCO is completely consumed to bind Cy3, due to the high kinetics and excess used for the reaction. Our calculations showed that each CTX binds on average 1.3 molecules of DBCO and 2 molecules of Cy7.5. The approximately 1:1 ratio between CTX and DBCO is pivotal to avoid CTX with multiple DBCO units could bind different REVs at the same time. To create a control sample unable to bind azido groups (de-activated modified CTX, DmCTX), an aliquot of mCTX was reacted with NaN_3 to consume any DBCO (see experimental section). DmCTX showed not to bind Cy3 ligation, indicating the successful deactivation of DBCO (Fig. 1.3D).

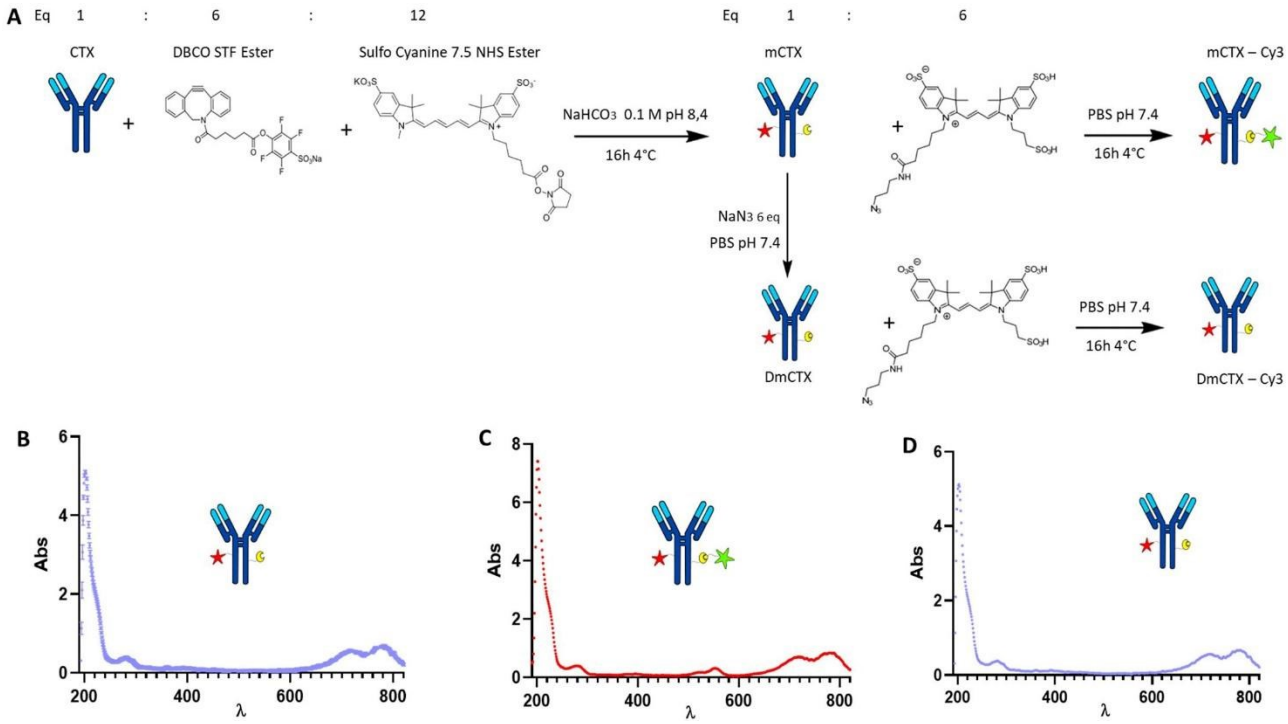

Figure 1.3: CTX modification and characterization. A) Workflow followed to obtain mCTX, mCTX-Cy3, and DmCTX. B) UV-Vis spectra of mCTX. C) UV-Vis spectra of mCTX-Cy3. D) UV-Vis spectra of DmCTX.

3.3.2 Biophysical and biochemical characterization of Red Blood Cell-EVs

REVs were characterized according to the most updated guidelines. In the specific, Nanoparticle Tracking Analysis (NTA) was used to determine REV particle number and size distribution, Atomic Force Microscopy (AFM) was used to evaluate REV morphology, and Western Blot was used to assess REV protein markers. NTA measurements showed a monomodal size distribution, with a peak at 160 ± 2.3 nm in diameter (see Figure 2.3A) and a REV concentration of $1.81*10^{12}$ ± $8.8*10^{11}$ particles/mL, in agreement with what was already observed in the literature about REVs . Correlating BCA and NTA data, we found that $2*10^{9}$ REVs correspond to 1,06 µg of total proteins (see Figure 2.3B), which is compliant with the theoretical calculations by Sverdlov and Zendrini *et al.*[5] Western Blot analysis (see Figure 2.3C) revealed the presence of typical REV markers, like Alix and Annexin XI, and hemoglobin subtypes HBB and HBA, confirming the RBC origin of our REVs. The absence of contaminants, such as Golgi-derived vesicles (GM130) or leukocyte-derived EVs (CD45) was verified, together with the expression of CD47. This protein is often referred to as a "don't eat me" signal and highlights REV immune-evasion potential useful for drug delivery applications. Also, we evaluated the expression of EGFR - the natural ligand of CTX, and we found a negligible signal. The absence of EFGR on REVs is mandatory, as it avoids specific, undesired binding of CTX to the surface of REV during functionalization processes. The presence of spherical nano-objects in the size range typical of EVs dried on a flat surface was confirmed by AFM imaging (see Figure 2.3D). Finally, the presence of soluble protein-

contaminants in the REV preparations was assessed with the CONAN assay. The fluctuation of the Aggregation Index (AI) (see Figure 2.3E) at different dilutions and the relative AI value lower than the purity threshold indicated the presence of a negligible amount of no EV-associated soluble proteins, as previously reported. All these data together confirm the high quality of our REV preparations. In particular, the monomodal size distribution and the negligible amount of soluble proteins avoid possible interferences during functionalization processes.

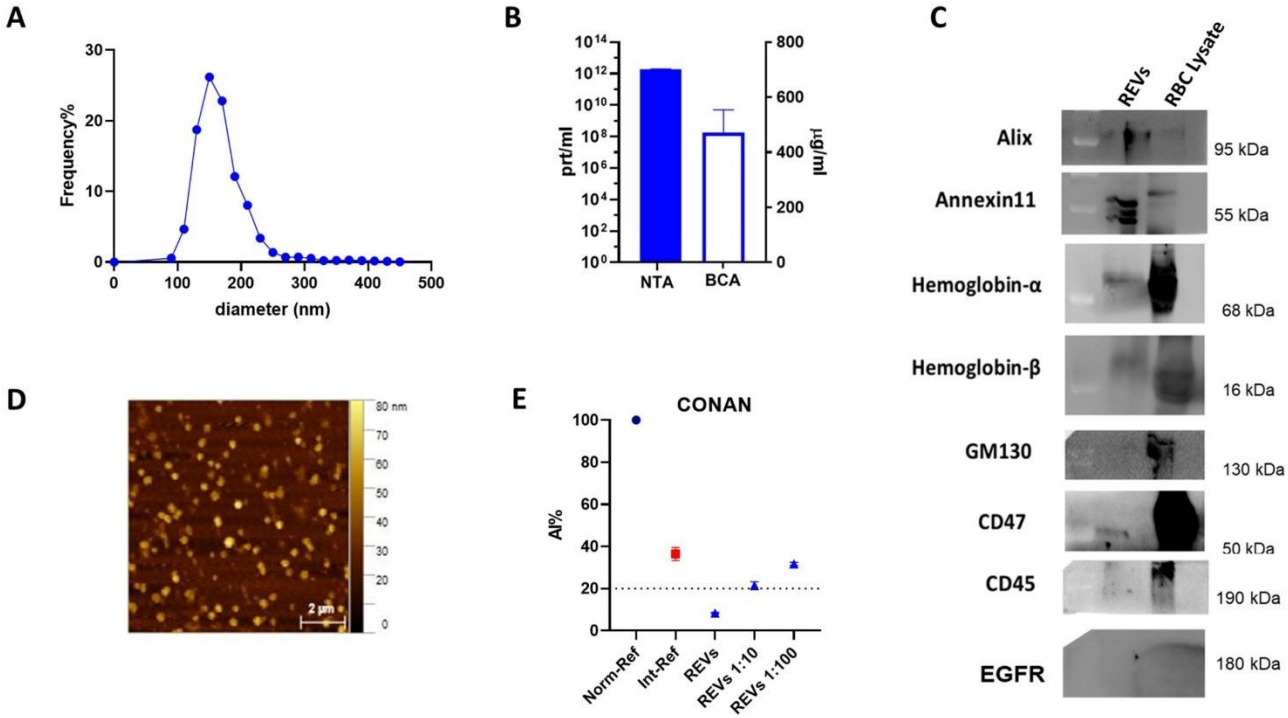

Figure 2.3: REV characterization. A) The size distribution graph obtained by NTA shows a monomodal distribution of our REVs. Data are expressed in frequency%, and the diameter bin has been selected as 20 nm. n = 3. B) The correlation between particle count and protein content obtained by BCA assay, of the native REV samples, indicates the absence of soluble proteins. n = 3. C) Representative Western Blots of REVs and RBC lysate with specific EV markers (Alix, Annexin XI), REV markers (hemoglobin á and â, CD47), and negative controls (GM130, CD45, and EGFR). D) Representative AFM image showing the morphological structure of REVs as spherical nano-objects. E) In the CONAN assay, the Int-REF AI ratio defines the threshold below which the spectral redshift is only due to the interaction between the AuNPs and the EVs. The dotted line represents the CONAN assay threshold for soluble protein detection (<20% AI ratio means that the soluble protein content is ≤0.05 µg/µL).

3.3.3 REV surface functionalization

For REV surface functionalization, we followed the experimental workflow depicted in Fig. 3.3A. We adopted a two-step chemical labeling strategy[16] (see experimental section), exploiting the Strain-Promoted Alkyne-Azide Cycloaddition (SPAAC) reaction between an azido group and an alkyne to covalently bind mCTX to the EV surface. REVs were first reacted with an N_3-$(PEG)_4$-NHS ester (reaction ratio 1:200 REVs:N_3-$(PEG)_4$-NHS ester) to introduce a clickable group onto the REV surface. A non-clickable (without azido-PEG) control sample was prepared to explore the eventual physisorption of mCTX onto the EV surface (REVs underwent the same workup

procedure as pegylated REVs). Clickable and non-clickable samples were reacted with mCTX (reaction ratio 1:200 REVs:mCTX) and washed by dilution with PBS followed by ultracentrifugation to remove unreacted antibodies, obtaining REVs-click-mCTX and REVs-physi-mCTX, respectively. As shown in Fig. 3.3B, the size distribution of REVs was not affected by the functionalization process, indicating no significant morphological changes due to surface functionalization. The CONAN assay was performed to verify the presence of non-EV-associated antibodies.[34]. The samples tested showed the same AuNP aggregation properties of native EVs, thus indicating that the eventual amount of free antibody present in the solution is negligible (see Fig. 3.3C). CTX binding on REV was evaluated by SDS-PAGE followed by fluorescence imaging exploiting the fluorescent dye (Cy7.5) linked to mCTX. The densitometric fluorescence profile was acquired from the gel image, and differences between REVs-click-mCTX, REVs-physi-mCTX, and mCTX were observed (Fig. 3.3D), strongly suggesting the successful covalent ligation of mCTX to EV proteins by click-chemistry reaction. Indeed, lane 1 of SDS-PAGE displays the electrophoretic profile of REVs-click-mCTX as composed of higher molecular weight bands with respect to free mCTX (lane 3). This profile is likely ascribable to an increase in mCTX heavy and light chains' molecular weight due to the covalent bonding with EV membrane proteins. Interestingly, the intensity of light chain and heavy chain band signals was lower in REVs-click-mCTX than mCTX, further confirming the covalent bonding. REVs-physi-mCTX (lane 2) showed the presence of mCTX heavy chain and light chain with a densitometric profile similar to mCTX (lane 3), suggesting that mCTX might be physisorbed on EV surface without the azido-PEG unit. In order to quantify CTX on functionalized REVs, a calibration curve based on total lane fluorescence intensity was obtained by loading different amounts of mCTX (0.02 – 2 μg range) in an SDS-PAGE gel. Quantification of CTX molar concentration, normalized for REV molar concentration, is shown in Fig. 3.3E. Data indicated that a similar number of antibodies was present on REVs-click-mCTX and REVs-physi-mCTX (approximately 90 molecules of mCTX per EV), despite the differences in the densitometric profile described above. Furthermore, we performed a control reaction of the functionalization process using the DmCTX, and the reaction yield was quantified as above. As shown in Fig. 3.3E, about 90 DmCTX molecules per EV were co-isolated with REVs-physi-DmCTX, while REVs-click-DmCTX showed a negligible co-isolation yield, suggesting that active DBCO is required to react with the azido group on pegylated REVs. This result fosters the hypothesis of the anti-fouling properties exerted by PEG on the REV surface. PEG anti-fouling effect was already largely explored and exploited for synthetic NPs,[40,41] and our data highlight the role of pegylation in inhibiting the physisorption of DmCTX. All these experimental pieces of evidence strongly indicate that our strategies led to REV surface

functionalization through the two different mechanisms we aimed at: the first mechanism featuring chemisorption, through the formation of a covalent bond by click-chemistry reaction, while the second featuring the formation of a physisorbed PC.

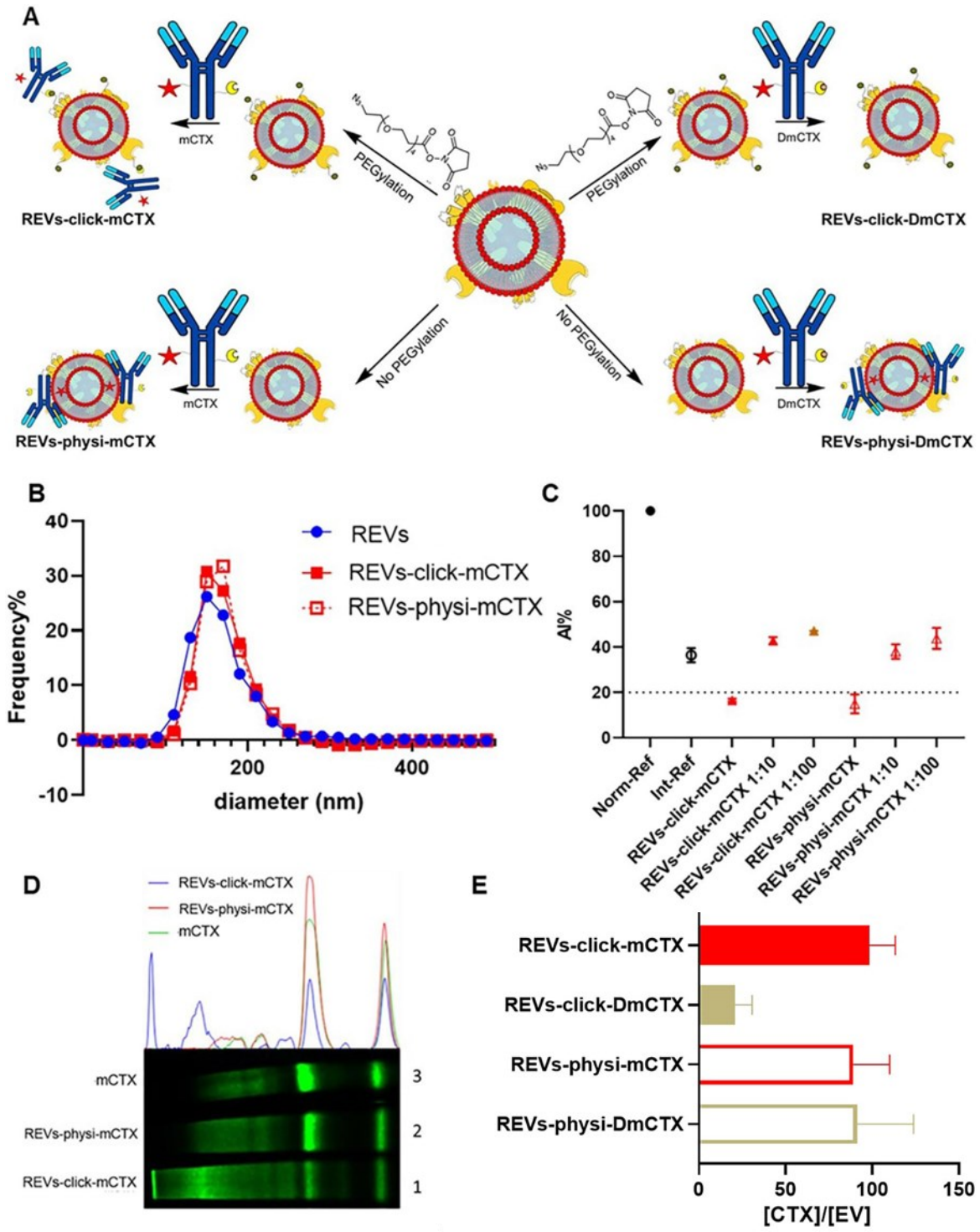

Figure 3.3: REV surface functionalization by chemical or physical strategy. (A) Schematic representation of the functionalization processes followed. (B) Size distribution of functionalized samples determined by NTA shows no significant differences compared to the native REVs. Data are expressed in frequency %, and the diameter bin has been selected as 20 nm. N = 3. (C) In the CONAN assay,[34] the Int-REF AI ratio defines the threshold below which the spectral redshift is only due to the interaction between the AuNPs and the EVs. Functionalized REVs were tested undiluted and after dilutions of 10 and 100-fold. The dotted line represents the CONAN assay threshold for soluble protein detection (< 20% AI ratio means that the soluble protein content is ≤ 0.05 μg/μL)(D). SDS-PAGE and relative fluorescence densitometric profile of REVs-click-mCTX (lane 1, 20 μL), REVs-physi-mCTX (lane 2, 20 μL) and mCTX (lane 3, 1 μg). (E) mCTX and

DmCTX per REV yields of functionalized samples. Data are elaborated as the molar concentration of mCTX normalized by the molar concentration of REVs of the sample. N = 5.

Next, we performed a dose-dependent functionalization assay to optimize the functionalization process by modifying REVs by CTX chemisorption or physisorption as described above, with different mCTX-to-REV ratios. mCTX/REV amount relative to samples produced with three different REV:mCTX reaction ratios of 1:200, 1:500, and 1:1000 (azido-PEG were reacted in the same excess of mCTX) was quantified immediately after the first wash following functionalization (Fig. 4.3A and B, blue bar). Moreover, to evaluate the stability of the binding, a second and third wash was performed (red and green bars, respectively, Fig. 4.3A and B), as described in the experimental section. Concerning REVs-click-mCTX, results indicated that 200 equivalents of antibodies per REVs allowed the saturation of the binding sites present on the REV surface, and theoretical calculations (normalizing the total area generated by the antibodies for the surface of the REVs and approximating mCTX to a sphere with a radius of 5.5 nm) indicated that under these conditions mCTX covered approximately 10-15% of the REV surface. In addition, REVs-click-mCTX showed a constant mCTX amount per REV for all the reaction ratios after every washing step (see Fig. 4.3A), again supporting that mCTX was covalently bound to the REV surface. Considering that the REV surface is for the 23% occupied by membrane proteins,[42] such a result about surface coverage is probably due to a combination of the saturation of the binding sites on the REV surface, the antifouling properties of PEG chains, and the steric hindrance generated by mCTX attached to the REV surface. On the other hand, the REVs-physi-mCTX samples showed a proportional increase in the co-isolation of mCTX per EV with increasing reaction ratios after the first wash (see Fig. 4.3B, blue bars). In the higher reaction ratio (1:1000, blue bar), mCTX covers up to 30% of the total REV surface, but after further washes, the mCTX amount per REV dramatically decreases, indicating that antibodies are likely to be physisorbed on the REV surface rather than being stably bound. For 1:200 and 1:500 ratios, after the second wash, the amount of mCTX per REV reached a stable value of ~50 mCTX/REV, representing 5% of the surface coverage. This data could indicate the formation of a first layer of mCTX more strongly physisorbed onto the REV surface than the others. These considerations are in accordance with the general description of the PC as a multilayered entity with the stability of the protein layers decreasing with the distance from the EV surface[43,44]: the more stable layer constitutes the so-called hard PC, while the soft PC is made by the layers more loosely attached.[24]

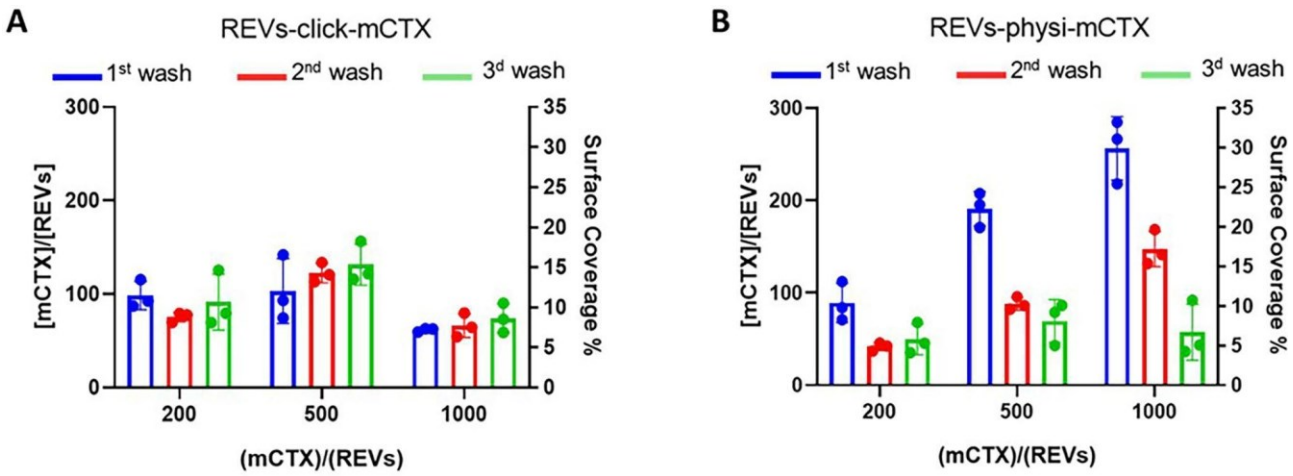

Figure 4.3: mCTX dose-dependent functionalization assay and mCTX stability assay on REVs. (A) mCTX per REV ratio and % of REV surface coverage by CTX of REVs-click-mCTX, obtained by different REV/mCTX reaction ratios (1:200, 1:500, 1:1000) were determined after one (blue bar), two (red bar) and three (green bar) washes following the chemical functionalization strategy. n = 3. (B) mCTX per REV ratio and % of REV surface coverage by CTX of REVs-physi-mCTX, obtained by different REV/mCTX reaction ratios (1:200, 1:500, 1:1000) were determined after one (blue bar), two (red bar) and three (green bar) washes following the chemical functionalization strategy. n = 3.

3.3.4 Evaluation of the binding capacity of REVs-click-mCTX and REVs-physi-mCTX to EGFR

We next evaluated the binding of REVs-click-mCTX and REVs-physi-mCTX towards EGFR by Surface Plasmon Resonance (SPR) technology, already exploited by our group for binding studies of growth factors and EVs[45,46]). To this aim, EGFR was immobilized onto an SPR sensorchip by amine-coupling procedure (see experimental section). Firstly, the functionality of the EGFR-containing biosensor was validated using the epidermal growth factor (EGF), the natural ligand of EGFR. Saturation curves plotted with the binding values at equilibrium (Fig. 5.3) were obtained which allowed the calculation of the dissociation constant (K_d) value, which is inversely proportional to the binding affinity. As shown in Fig. 5.3A, EGF bonded to EGFR in a dose-dependent and saturable way with a K_d equal to 67.3 nM, thus in line with the values already reported in the literature.[47] The EGFR-containing biosensor was then used to evaluate the binding of CTX before or after its chemical modification. As shown in Fig 5.3B, CTX bonded to EGFR in a saturable and dose-dependent way with a K_d equal to 1.8 nM, as already reported in literature[48] The chemical modification introduced in mCTX leads to an apparent, limited decrease of affinity equal to 3.6 nM,. On the basis of the positive results obtained with control proteins, the EGFR-containing biosensor was then used to evaluate the EGFR-binding affinity of the differently functionalized REVs. The binding resulted CTX-dependent, as demonstrated by the lack of binding of native REVs, devoid of surface-associated antibodies (Fig. 5.3C). The K_d for the REVs-click-mCTX/EGFR interaction is equal to 0.17 nM. Also, REVs-physi-mCTX binds to EGFR in

a specific, stable, dose-dependent, and saturable way (Fig. 5.3C), with an affinity that is similar to that of REVs-click-mCTX. This result suggests that the association between mCTX and REVs is quantitatively similar despite the different functionalization strategies. It is also worthy of mentioning the high affinity of the EGFR/REVs-click-mCTX interaction, which is 10 times higher than that of free mCTX. It is tentative to hypothesize that a cooperative interaction process,[49,50] occurred at the interface between the sensorchip surface and the vesicle that generates a very high affinity binding. Interestingly, a high-affinity cooperative binding has been already demonstrated for the interaction of immunoliposomes carrying anti-ephrin A2 single chain fragment with ephrin A2.[51] The saturation response (R_{max}) is known to be dependent on the amount of surface-immobilized ligand available to the binding. REVs-physi-mCTX showed a R_{max} value that is four times lower than that of REVs-click-mCTX (33 $\pm$ 2.5 and 150.0 $\pm$ 35.5, respectively, Fig. 5.3C). It is tentative to hypothesize that when weakly adsorbed on REVs-physi-mCTX, the antibody "moves" from the vesicle to the EGFR-coated surface, where it remains firmly bound, decreasing the amount of EGFR available to interact with other REVs. Conversely, this does not occur in REVs-click-mCTX, where mCTX is covalently anchored to the REV surface. The stability of the association of CTX to REVs obtained by physisorption or by chemical strategy considerations may have important implications on the vesicle uptake *in vitro* (see below) and their practical therapeutic use.[52] In this work, DmCTX has been generated to demonstrate the essential role of DBCO in mCTX association with REVs and the anti-fouling properties of pegylation (see above). As expected, based on the similar amount of antibody associated, REVs-physi-DmCTX retains an EGFR-binding affinity very close to that of REVs-physi-mCTX, confirming that DmCTX behaves as mCTX in interacting with EGFR and that it can be absorbed on REV surface as mCTX. Although endowed with a negligible amount of associated antibody REVs-click-DmCTX binds EGFR with high capacity (measured as maximal RU bound) but occurs in a non-saturable manner (Fig. 5.3C) and with a very low affinity (K_d > than 33 μM), indicating a non-specific interaction.[53] This anomalous behavior is likely due to the presence on REVs of unreacted azido-PEG that, as already reported[45,46], could interact in a non-specific way with biosensor surfaces. Whatever the cause of this non-specific binding, these results confirm that the interaction of CTX with the azido-pegylated EV surface occurs only when it possesses a reactive DBCO group. To summarize, SPR experiments confirmed that REVs can be functionalized with mCTX following biorthogonal and physisorption strategies, where both methods produce samples with a similar affinity for EGFR but with different stability of the antibody association.

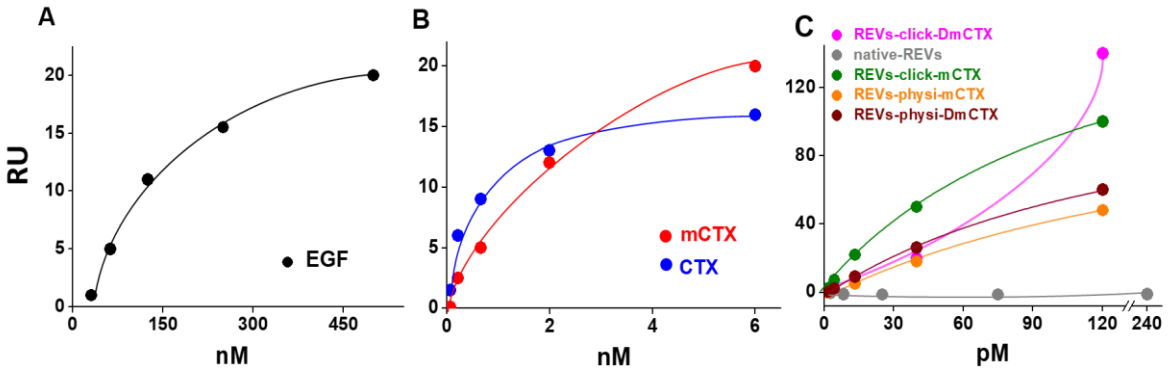

Figure 5.3: SPR binding analysis on the EGFR-functionalized biosensor. Significative binding isotherms obtained by fitting the amount of formed complex at equilibrium (in resonance units, RU, obtained from single cycle analysis) versus concentrations in solution of EGF (A) and CTX and mCTX (B), REVs (C). In the binding isotherms of the REVs (C), the REV concentration (and not that of the associated mCTX) are used. N = 3

3.3.5 In vitro cell uptake of REVs-click-mCTX and REVs-physi-mCTX

Modifying the EV surface by introducing suitable molecules for targeted drug delivery increases the chances for EVs to be taken up by cells *via* specific receptor-mediated endocytosis[43,44]. SPR data showed that REVs-click-mCTX and REVs-physi-mCTX have the same affinity towards EGFR. Therefore, in principle, at the cellular level, both functionalized EVs are in the position to trigger the same uptake pathway by activating EGFR-mediated endocytosis. We assessed the targeting and uptake of the modified REV samples *in vitro* using MDA-MB-231 triple-negative breast cancer cells expressing high levels of EGFR.[54,55] EGFR expression in MDA-MB-231 cells was confirmed by Western blot analysis, showing a 1.55-fold expression level when compared with control cells, namely HEK293T epithelial-like immortalized kidney cells[53] known to express basal levels of EGFR (data not shown).[56] Cells were treated with equal particle number of REVs-click-mCTX and REVs-physi-mCTX for 4 and 24 h in the presence or absence of Fetal Bovine Serum (FBS), used here to best mimic the physiological environment. The cellular internalization of the REVs was evaluated by following both mCTX and REV uptake quantifying the fluorescence of Sulfo Cyanine 7.5 (mCTX, red) and the Fluorogenic Membrane Probe MemGlow™ 488[57] (REVs, green), respectively. At first glance, it was evident that the addition of FBS decreases the overall uptake of both mCTX and REVs at 4 and 24 h (Fig. 6.3), thus suggesting a competition mechanism between the heterogeneous FBS components with REVs, as observed by Salvati et al. for transferrin-functionalized NPs.[58] After 4 h treatments, REVs-click-mCTX showed a significantly higher mCTX uptake than REVs-physi-mCTX whether the treatments were carried out with or without FBS (Fig. 6.3A). However, we did not observe relevant differences in REV uptake between functionalized samples and the control pristine REVs, suggesting that other interactions, independent from mCTX-EGFR recognition, can still happen at early time points[59]

(Fig. 6.3B). After 24 h, REV-click-mCTX showed significantly higher mCTX uptake compared to REV-physi-mCTX only in presence of FBS (Fig. 6.3C). This difference is also reflected in REV uptake related to REV-click-mCTX, that is significantly higher than pristine REVs and REV-physi-mCTX (Fig. 6.3D). Interestingly, REVs and REVs-physi-mCTX uptake was experimentally equal at each time point in FBS-containing conditions. These data can be, at first instance, explained by the fact that REV-physi-mCTX should be more sensitive to protein exchange when immersed in biological media, leading to decreased EGFR-mediated cellular uptake. As mentioned earlier, pristine NPs and EVs are immediately coated by a BC once immersed in a biofluid, which (re)sets their targeting, uptake, and biodistribution profiles.[22,29] Mostly due to its dynamic properties.[60,61] In biofluids, BC features and morphology evolve due to the continuous adsorption/desorption of loosely bound proteins, primarily enriched in the soft corona.[24,62] Altogether, these results suggested that in biological fluid containing a physiological concentration of proteins, such as the one containing FBS, REVs-click-mCTX, and REVs-physi-mCTX did not maintain the same EGFR-targeting ability and that mCTX functionalization by physisorption did not improve EV targeting ability in respect to pristine REVs (Fig. 6.3D).

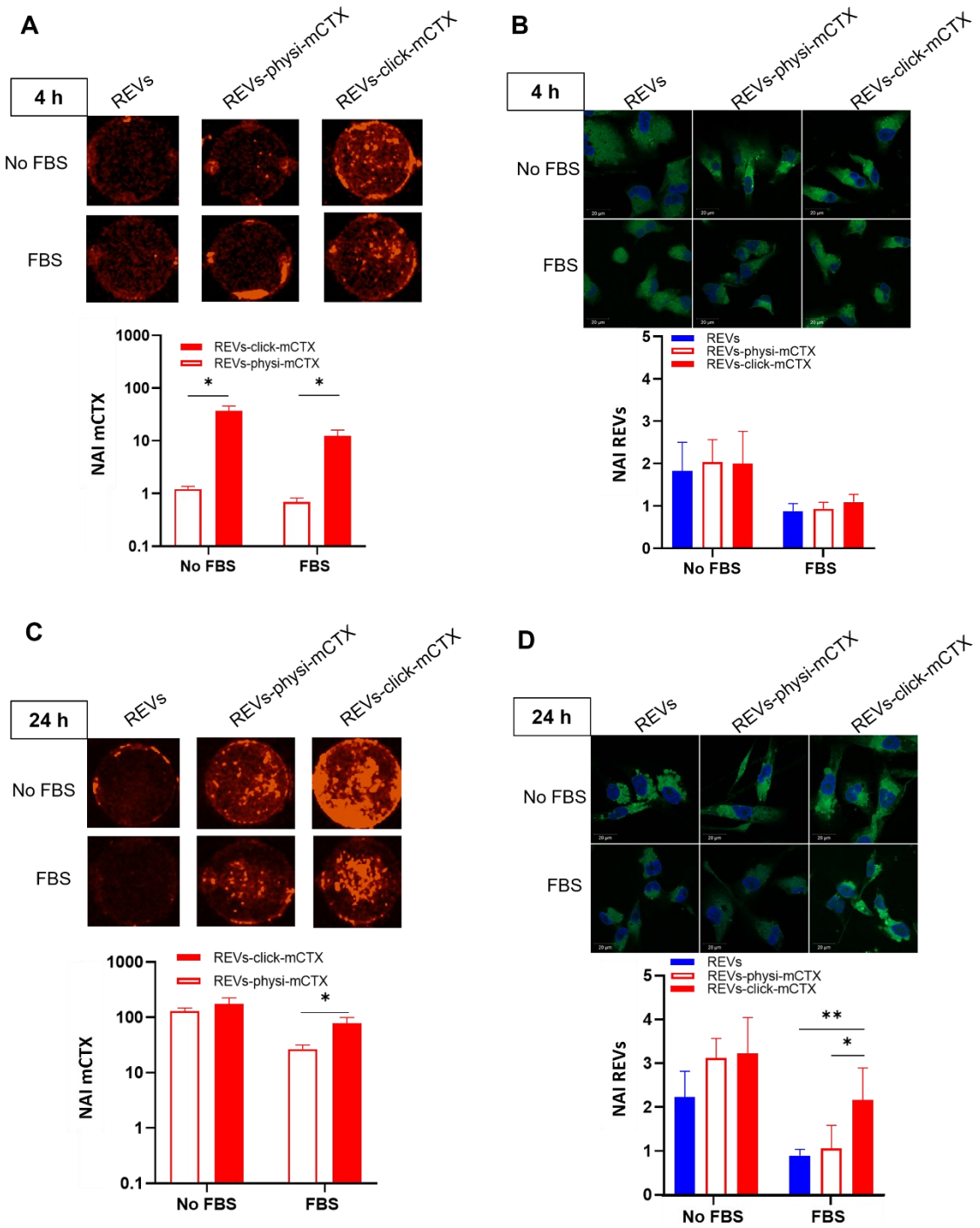

*Figure 6.3: (A). In vitro mCTX uptake assay. Fluorescence image and quantification of MDA-MB-231 cells after the treatment with REVs-click-mCTX and REVs-physi-mCTX at 4 h in the absence (No FBS) and in presence of FBS. The red fluorescence is related to mCTX. * = p value < 0.05. (B). In vitro REV uptake assay. Confocal microscopy image and quantification of MDA-MB-231 cells after the treatment with REVs-click-mCTX and REVs-physi-mCTX at 4 h in the absence (No FBS) and in presence of FBS. The green fluorescence is related to MemGlow™ 488, while the blue is to DAPI. * = p value < 0.05. (C) In vitro mCTX uptake assay. Fluorescence image and quantification of MDA-MB-231 cells after the treatment with REVs-click-mCTX and REVs-physi-mCTX at 24 h in the absence and in presence of FBS. The red fluorescence is related to mCTX. * = p value < 0.05. (D) In vitro REV uptake assay. Confocal microscopy image and quantification of MDA-MB-231 cells after the treatment with REVs-click-mCTX and REVs-physi-mCTX at 24 h in the absence (No FBS) and in presence of FBS. The green fluorescence is related to MemGlow™*

*488, while the blue is to DAPI. * = p value < 0.05; ** = p value < 0.01. NAI = Normalized Adjusted Intensity. The y axis is reported as logarithmic scale for graphs in A) and C) and linear scale for B) and D). N = 5*

3.4 Conclusions

This work opens to the exploration of the influence and role BC has in the exogenous surface functionalization of EVs with targeting antibodies. In parallel, it evidences the key importance of the rigorous understanding and control of all the functionalization processes – from the choice and preparation of the antibodies to the final *in vitro* functional evaluation, a characteristic too often underrated in the literature. We developed and optimized the modified CTX by introducing a red-emitting fluorophore (Cy7.5) and clickable unit (DBCO). mCTX was then used to functionalize REV surfaces by chemisorption (covalent binding of mCTX via biorthogonal click-chemistry) and physisorption (formation of a CTX corona). Both approaches did not affect REV morphology. The covalent bonds established between REV surface proteins and mCTX by click-chemistry allowed the functionalization of the REV surface, resulting in changes in the mCTX electrophoretic profile. Besides, mCTX physisorbed on the REV surface was dynamic and in equilibrium with the media. mCTX-EGFR molecular recognition was carefully verified by comparing mCTX and CTX's binding curves on an EGFR-functionalized biosensor, demonstrating that the modification of the antibody did not affect its binding. The same biosensor was then used to study the binding of functionalized REVs. SPR functional assay demonstrated that both REVs functionalized by chemisorbed and physisorbed mCTX bind EGFR with fairly consistent affinity. *In vitro* tests showed that in the presence of FBS, a condition closer to the physiological milieu, only the covalent anchorage of mCTX led to increased uptake of the REVs correlated with the increased uptake of mCTX. On the other hand, the presence of FBS-related proteins forces an exchange of biomolecules between the PC made by mCTX on the REV surface and the medium, leading to a loss of functionality. Although EV-BC derived from biofluids has been shown to bestow functional features to EVs,[63] the PC derived from EV surface functionalization by physisorption seems not to be functional for drug delivery applications. Future studies on the kinetic of release and on the residual number of CTX molecules still adsorbed on EVs after incubation in an FBS complex medium could help to explain the different functionality between chemi- and physisorbed EVs. Thus, the covalent anchorage of antibodies onto the EV surface is required to improve specific EV recognition by the cells and guarantee the delivery of therapeutic cargo. These findings give a first evaluation of the effect of the (spontaneous and unavoidable) biomolecule physisorption during EV surface functionalization (namely BC formation) and they should be carefully considered (and further elaborated) when designing and preparing surface-functionalized EVs. Further work is needed to characterize the role of BC in the formulation of surface-functionalized EVs with other

molecules, such as proteins and peptides, to support the exploitation of different functionalization strategies for developing delivery vehicles, imaging agents, or bio nano-therapeutics. For these reasons, we developed a Fluorescence Correlation Spectroscopy protocol to further study the exchange of macromolecules at the EV surface and the dynamic BC formation in chemical and physically engineered EVs. The results of this work are reported in Chapter 4.

3.5 References

1. S. Busatto, A. Zendrini, A. Radeghieri, L. Paolini, M. Romano, M. Presta and P. Bergese, The nanostructured secretome, *Biomater. Sci.*, 2020, **8**, 39–63. https://doi.org/10.1039/c9bm01007f.

2. C. Corbo, R. Molinaro, M. Tabatabaei, O. C. Farokhzad and M. Mahmoudi, Personalized Protein Corona on Nanoparticles and Its Clinical Implications, *Biomater. Sci.*, 2017, **5**, 378–387. https://doi.org/10.1039/c6bm00921b.

3. Z. Ji,X. Jin, S. George, T. Xia, H. Meng, X. Wang, X.; E. Suarez, H. Zhang, E. M. V. Hoek, H. Godwin, A. E. Nel and J. I. Zink, Dispersion and Stability Optimization of TiO_2 Nanoparticles in Cell Culture Media, *Environ. Sci. Technol.*, 2010, **44**, 7309–7314. https://doi.org/10.1021/es100417s

4. E. Casals, T. Pfaller, A. Duschl, G. J. Oostingh and V. F. Puntes, Hardening of the Nanoparticle-Protein Corona in Metal (Au, Ag) and Oxide (Fe_3O_4, CoO, and CeO_2) Nanoparticles, *Small*, 2011, **7**, 3479–3486. https://doi.org/10.1002/smll.201101511.

5. W. M. Usman, T. C. Pham, Y. Y. Kwok, L. T. Vu, V. Ma, B. Peng, Y. S. Chan, L. Wei, S. M. Chin, A. Azad, A. B. L. He, A. Y. H. Leung, M. Yang, N. Shyh-Chang, W. C. Cho, J. Shi and M. T. N. Le, Efficient RNA Drug Delivery Using Red Blood Cell Extracellular Vesicles, *Nat. Commun.*, 2018, **9***,* Article number: 2359. https://doi.org/10.1038/s41467-018-04791-8.

6. Tsiapalis D, O'Driscoll L. Mesenchymal Stem Cell Derived Extracellular Vesicles for Tissue Engineering and D. Tsiapalis and L. O'Driscoll, Mesenchymal Stem Cell Derived Extracellular Vesicles for Tissue Engineering and Regenerative Medicine Applications, *Cells*, 2020, **9**, 991. https://doi.org/10.3390/cells9040991.

7. G. Go, H. J. Park, J. H. Lee, C. W. Yun, and S. H. Lee, Inhibitory Effect of Oxaliplatin-Loaded Engineered Milk Extracellular Vesicles on Tumor Progression, *Anticancer Res.*, 2022, **42**, 857–866. https://doi.org/10.21873/anticanres.15543.

8. A. A. Khan, F. Man, F. N. Faruqu, J. Kim, F. Al-Salemee, A. Carrascal-Miniño, A. Volpe, R. Liam-Or, P. Simpson, G. O. Fruhwirth, K. T. Al-Jamal and R. T. M. de Rosales, PET Imaging of Small Extracellular Vesicles via [^{89}Zr]Zr(Oxinate)$_4$ Direct Radiolabeling, *Bioconjugate Chem.*, 2022, **33**, 473–485. https://doi.org/10.1021/acs.bioconjchem.1c00597.

9. I. K. Herrmann, M. J. A. Wood and G. Fuhrmann, Extracellular Vesicles as a Next-Generation Drug Delivery Platform, *Nat. Nanotechnol*., 2021, **16**, 748–759. https://doi.org/10.1038/s41565-021-00931-2.

10. T. Tian, H. X. Zhang, C. P. He, S. Fan, Y. L. Zhu, C. Qi, N. P. Huang, Z. D. Xiao, Z. H. Lu, B. A. Tannous and J. Gao, Surface Functionalized Exosomes as Targeted Drug Delivery Vehicles for Cerebral Ischemia Therapy, *Biomaterials,* 2018, **150**, 137–149. https://doi.org/10.1016/j.biomaterials.2017.10.012.

11. T. Lener, M. Gimona, L. Aigner, V. Börger, E. Buzas, G. Camussi, N. Chaput, D. Chatterjee, F. A. Court, H. A. del Portillo, L. O'Driscoll, S. Fais, J. M. Falcon-Perez, U. Felderhoff-Mueser, L. Fraile, Y. S. Gho, A. Görgens, R. C. Gupta, A. Hendrix, D. M. Hermann, A. F. Hill, F. Hochberg, P. A. Horn, D. de Kleijn, L. Kordelas, B. W. Kramer, E. M. Krämer-Albers, S. Laner-Plamberger, S. Laitinen, T. Leonardi, M. J. Lorenowicz, S. K. Lim, J. Lötvall, C. A. Maguire, A. Marcilla, I. Nazarenko, T. Ochiya, T. Patel, S. Pedersen, G. Pocsfalvi, S. Pluchino, P. Quesenberry, I. G. Reischl, F. J. Rivera, R. Sanzenbacher, K. Schallmoser, I. Slaper-Cortenbach, D. Strunk, T. Tonn, P. Vader, B. W. M. van Balkom, M. H. M. Wauben, S. el Andaloussi, C. Théry, E. Rohde and B. Giebel, Applying Extracellular Vesicles Based Therapeutics in Clinical Trials - An ISEV Position Paper, *J. Extra. Vesicles*, 2015, *4*, 30087. https://doi.org/10.3402/jev.v4.30087.

12. D. Todorova, S. Simoncini, R. Lacroix, F. Sabatier and F. Dignat-George, Extracellular Vesicles in Angiogenesis, *Circ. Res*., 2017, **120***,* 1658–1673. https://doi.org/10.1161/CIRCRESAHA.117.309681.

13. J. M. Pitt, G. Kroemer and L. Zitvogel, Extracellular Vesicles: Masters of Intercellular Communication and Potential Clinical Interventions, *J. Clin. Invest*., 2016, **126**, 1139–1143. https://doi.org/10.1172/JCI87316.

14. L. Paolini, M. Monguió-Tortajada, M. Costa, F. Antenucci, M. Barilani, M. Clos-Sansalvador, A. Cronemberger Andrade, T. A. P. Driedonks, S. Giancaterino, S. M. Kronstadt, R. R. Mizenko, M. Nawaz, X. Osteikoetxea, C. Pereira, S. Shrivastava, A. Toftegaard Boysen, S. I. van de Wakker, M. J. C. van Herwijnen, X. Wang, D. C. Watson, M. Gimona, M. Kaparakis-Liaskos, K. Konstantinov, S. K. Lim, N. Meisner-Kober, M. Stork, P. Nejsum, A. Radeghieri, E. Rohde, N. Touzet, M. H. M. Wauben, K. W. Witwer, A. Bongiovanni and P. Bergese, Large-scale production of extracellular vesicles: Report on the "massivEVs" ISEV workshop, *J. Extracell. Biol.*, 2022, **1**, e63. https://doi.org/10.1002/jex2.63

15. O. P. B. Wiklander, J. Z. Nordin, A. O'Loughlin, Y. Gustafsson, G. Corso, I. Mäger, P. Vader, Y. Lee, H. Sork, Y. Seow, N. Heldring, L. Alvarez-Erviti, C. I. Edvard Smith, K. le Blanc,

P. Macchiarini, P. Jungebluth, M. J. A. Wood and S. el Andaloussi, S. Extracellular Vesicle in Vivo Biodistribution Is Determined by Cell Source, Route of Administration and Targeting, *J. Extra. Vesicles*, 2015, **4**, 1–13. https://doi.org/10.3402/jev.v4.26316.

16. M. Richter, P. Vader and G. Fuhrmann, Approaches to Surface Engineering of Extracellular Vesicles, *Adv. Drug Deliv. Rev.*, 2021, **173**, 416–426. https://doi.org/10.1016/j.addr.2021.03.020.

17. M. Gai, J. Simon, I. Lieberwirth, V. Mailänder, S. Morsbach and K. Landfester, A Bio-Orthogonal Functionalization Strategy for Site-Specific Coupling of Antibodies on Vesicle Surfaces after Self-Assembly, *Polym. Chem.*, 2020, **11**, 527–540. https://doi.org/10.1039/c9py01136f.

18. T. Smyth, K. Petrova, N. M. Payton, I. Persaud, J. S. Redzic, M. W. Graner, P. Smith-Jones and T. J. Anchordoquy, Surface Functionalization of Exosomes Using Click Chemistry, *Bioconjugate Chem.*, 2014, **25**, 1777–1784. https://doi.org/10.1021/bc500291r.

19. M. Wang, S. Altinoglu, Y. S. Takeda, and Q. Xu, Integrating Protein Engineering and Bioorthogonal Click Conjugation for Extracellular Vesicle Modulation and Intracellular Delivery, *PLoS One*, 2015, **10**, e0141860. https://doi.org/10.1371/journal.pone.0141860.

20. F. N. Faruqu, L. Xu and K. T. Al-Jamal, Preparation of Exosomes for SiRNA Delivery to Cancer Cells, *J. Vis. Exp.*, 2018, **142**, e58814. https://doi.org/10.3791/58814.

21. H. C. Huang, M. Pigula, Y. Fang and T. Hasan, Immobilization of Photo-Immunoconjugates on Nanoparticles Leads to Enhanced Light-Activated Biological Effects, *Small,* 2018, **14**, 1800236. https://doi.org/10.1002/smll.201800236.

22. M. P. Monopoli, C. Åberg, A. Salvati and K. A. Dawson, Biomolecular Coronas Provide the Biological Identity of Nanosized Materials. *Nat. Nanotechnol.,* 2012, **7**, 779–786. https://doi.org/10.1038/nnano.2012.207.

23. M. Mahmoudi, I. Lynch, M. R. Ejtehadi, M. P. Monopoli, F. B. Bombelli and S. Laurent, Protein-Nanoparticle Interactions: Opportunities and Challenges. *Chem. Rev*., 2011, **111**, 5610–5637. https://doi.org/10.1021/cr100440g.

24. K. Kristensen, T. B. Engel, A. Stensballe, J. B. Simonsen and T. L. Andresen, The hard protein corona of stealth liposomes is sparse, *J. Control. Release*, 2019, **307**, 1–15. https://doi.org/10.1016/j.jconrel.2019.05.042.

25. A. L. Capriotti, C. Cavaliere and S. Piovesana, Liposome protein corona characterization as a new approach in nanomedicine, *Anal. Bioanal. Chem*., 2019, **411**, 4313–4326. https://doi.org/10.1007/s00216-019-01656-x.

26. E. I. Buzás, E. Tóth, B. W. Sódar and K. Szabó-Taylor, Molecular interactions at the surface of extracellular vesicles, *Semin. Immunopathol.*, 2018, **40**, 453–464. https://doi.org/10.1007/s00281-018-0682-0.

27. A. Radeghieri, S. Alacqua, A. Zendrini, V. Previcini, F. Todaro, G. Martini, D. Ricotta, and P. Bergese,Antithrombin glycoforms are selectively physiosorbed on plasma extracellular vesicles, *J. Extra. Biol.*, 2022, **1**, e57. https://doi.org/10.1101/2021.07.16.452649.

28. E. Tóth, L. Turiák, T. Visnovitz, C. Cserép, A. Mázló, B. W. Sódar, A. I. Försönits, G. Petővári, A. Sebestyén, Z. Komlósi, L. Drahos, Á. Kittel, G. Nagy, A. Bácsi, Á. Dénes, Y. S. Gho, K. Szabó-Taylor, and E. I. Buzás, Formation of a protein corona on the surface of extracellular vesicles in blood plasma, *J. Extra. Vesicles,* 2021, **10**, e12140. https://doi.org/10.1002/jev2.12140.

29. S. S. Yerneni, T. Solomon, J. Smith and P. G. Campbell, Radioiodination of extravesicular surface constituents to study the biocorona, cell trafficking and storage stability of extracellular vesicles. *Biochim. Biophys. Acta*, 2022, **1866**, 130069. https://doi.org/10.1016/j.bbagen.2021.130069.

30. A. Radeghieri and P. Bergese, The biomolecular corona of extracellular nanoparticles holds new promises for advancing clinical molecular diagnostics, *Expert Rev. Mol. Diagn.*, 2023, **23**, 471-474. https://doi.org/10.1080/14737159.2023.2215927.

31. EV-TRACK Consortium, J. Van Deun, P. Mestdagh, P. Agostinis, Ö. Akay, S. Anand, J. Anckaert, Z. A. Martinez, T. Baetens, E. Beghein, L. Bertier, G. Berx, J. Boere, S. Boukouris, M. Bremer, D. Buschmann, J. B Byrd, C. Casert, L. Cheng, A. Cmoch, D. Daveloose, E. De Smedt, S. Demirsoy, V. Depoorter, B. Dhondt, T. A. P. Driedonks, A. Dudek, A. Elsharawy, I. Floris, A. D. Foers, K. Gärtner, A. D. Garg, E. Geeurickx, J. Gettemans, F. Ghazavi, B. Giebel, T. Groot Kormelink, G. Hancock, H. Helsmoortel, A. F Hill, V. Hyenne, H. Kalra, D. Kim, J. Kowal, S. Kraemer, P. Leidinger, C. Leonelli, Y. Liang, L. Lippens, S. Liu, A. Lo Cicero, S. Martin, S. Mathivanan, P. Mathiyalagan, T. Matusek, G. Milani, M. Monguió-Tortajada, L. M. Mus, D. C. Muth, A. Németh, E. N. M. Nolte-'t Hoen, L. O'Driscoll, R. Palmulli, M. W. Pfaffl, B. Primdal-Bengtson, E. Romano, Q. Rousseau, S. Sahoo, N. Sampaio, M. Samuel, B. Scicluna, B. Soen, A. Steels, J. V. Swinnen, M. Takatalo, S. Thaminy, C. Théry, J. Tulkens, I. Van Audenhove, S. van der Grein, A. Van Goethem, M. J. van Herwijnen, G. Van Niel, N. Van Roy, A. R. Van Vliet, N. Vandamme, S. Vanhauwaert, G. Vergauwen, F. Verweij, A. Wallaert, M. Wauben, K. W. Witwer, M. I. Zonneveld, O. De Wever, J. Vandesompele and A. Hendrix. EV-TRACK: Transparent reporting and centralizing knowledge in extracellular vesicle research, *Nat. Methods*, 2017, **14**, 228-232. https://doi.org/10.1038/nmeth.4185

32. L. Paolini, A. Radeghieri, S. Civini, L. S, Caimi and D. Ricotta, The epsilon hinge-ear region regulates membrane localization of the AP-4 complex, *Traffic*, 2011 **12**, 1604–1619. https://doi.org/10.1111/j.1600-0854.2011.01262.x

33. G. Alvisi, L. Paolini, A. ContariniC. Zambarda C, V. Di Antonio, A. Colosini, N. Mercanelli, M. Timmoneri, G. Palù, L. Caimi, D. Ricotta and A. Radeghieri, Intersectin goes nuclear: Secret life of an endocytic protein, *Biochem. J.*, 2018, **475**,1455–1472. https://doi.org/10.1042/BCJ20170897

34. A. Zendrini, L. Paolini, S. Busatto, A. Radeghieri, M. Romano, M. H. M. Wauben, M. J. C. van Herwijnen, P. Nejsum, A. Borup, A. Ridolfi, C Montis and P Bergese, Augmented COlorimetric NANoplasmonic (CONAN) Method for Grading Purity and Determine Concentration of EV Microliter Volume Solutions, *Front. Bioeng. Biotechnol.*, 2020, **7**, 452. https://doi.org/10.3389/fbioe.2019.00452.

35. A. Borup, A. T. Boysen, A. Ridolfi, M. Brucale, F. Valle, L. Paolini, P. Bergese and P. Nejsum Comparison of separation methods for immunomodulatory extracellular vesicles from helminths, *J. of Extracellular Bio*., 2022, **1**, e41.. https://doi.org/10.1002/jex2.41.

36. H. H. Trutnau HH. New multi-step kinetics using common affinity biosensors saves time and sample at full access to kinetics and concentration, *J. Biotechnol.,* 2006, **124**, 191-195. https://doi.org/10.1016/j.jbiotec.2006.01.006

37. C. Théry , , et al.,Minimal information for studies of extracellular vesicles 2018 (MISEV2018): a position statement of the International Society for Extracellular Vesicles and update of the MISEV2014 guidelines. *J. Extracell. Vesicles*, 2018, **7**, 1535750. https://doi.org/10.1080/20013078.2018.1535750.

38. A. Zendrini, G. Guerra, K. Sagini T. Vagner, D Di Vizio and P. Bergese, On the surface-to-bulk partition of proteins in extracellular vesicles, *Colloids Surf. B Biointerfaces*, 2022, **218**, 112728. https://doi.org/10.1016/j.colsurfb.2022.112728.

39. E. D. Sverdlov,. Amedeo Avogadro's cry: What is 1μg of exosomes? *BioEssays*, 2012, **34**, 873–875. https://doi.org/10.1002/bies.201200045

40. D. Pozzi, V. Colapicchioni, G. Caracciolo, S. Piovesana, A. L. Capriotti, S. Palchetti, S. De Grossi, A. Riccioli, H. Amenitsch and A. Laganà, Effect of polyethyleneglycol (PEG) chain length on the bio-nano- interactions between PEGylated lipid nanoparticles and biological fluids: From nanostructure to uptake in cancer cells, *Nanoscale*, 2014,**6**, 2782–2792. https://doi.org/10.1039/C3NR05559K

41. S. Palchetti, V. Colapicchioni, L. Digiacomo, G. Caracciolo, D. PozziA. L. Capriotti, G. La Barbera and A. Laganà, The protein corona of circulating PEGylated liposomes, *Biochim.*

Biophys. Acta Biomembranes, 2016, **1858**, 189-196. http://dx.doi.org/10.1016/j.bbamem.2015.11.012

42. A. D. Dupuy and D. M. Engelman, Protein area occupancy at the center of the red blood cell membrane, **PNAS**, 2008, **105**, 2848-2852. www.pnas.orgcgidoi10.1073pnas.0712379105

43. C. J. Richards, M. Ahmadi, M. C. A. Stuart, B. J. Kooi, C. Åberg and W. H. Roos, The effect of biomolecular corona on adsorption onto and desorption from a model lipid membrane, *Nanoscale*, 2023, **15**, 248-253. https://doi.org/10.1039/D2NR05296B.

44. P. L. Latreille, M. Le Goas, S. Salimi, J. Robert, G. De Crescenzo, D. C. Boffito, V. A. Martinez, P. Hildgen and X. Banquy, Scratching the Surface of the Protein Corona: Challenging Measurements and Controversies, *ACS Nano*, 2022, **16**, 1689-1707. .https://doi.org/10.1021/acsnano.1c05901

45. G. Di Noto, A. Bugatti, A. Zendrini, E. L. Mazzoldi, A Montanelli, L. Caimi, M. Rusnati, D. Ricotta and P. Bergese, Merging colloidal nanoplasmonics and surface plasmon resonance spectroscopy for enhanced profiling of multiple myeloma-derived exosomes, *Biosens. Bioelectron.*, 2016, **77**, 518–524. https://doi.org/10.1016/j.bios.2015.09.061

46. P. Chiodelli, S. Rezzola, C. Urbinati, F. Federici Signori, E Monti, R. Ronca, M. Presta and M. Rusnati, Contribution of vascular endothelial growth factor receptor-2 sialylation to the process of angiogenesis, *Oncogene*, 2017, **36**, 6531–6541. https://doi.org/10.1038/onc.2017.243

47. A. E. G. Lenferink, E. J. J. Van Zoelen, M. J. H. Van Vugt, S. Grothe S, W. Van Rotterdam, M. L. M. Van De Poll and M. D. O?Connor-McCourt, Superagonistic activation of ErbB-1 by EGF-related growth factors with enhanced association and dissociation rate constants, *J. Biol. Chem.*, 2000 **275**, 26748–26753. https://doi.org/10.1016/S0021-9258(19)61439-0

48. M. L. Alvarenga, J. Kikhney, J, Hannewald, A. U. Metzger, K. J. Steffens, J. Bomke, A. Krah and A. Wegener, In-depth biophysical analysis of interactions between therapeutic antibodies and the extracellular domain of the epidermal growth factor receptor, *Anal. Biochem.*, 2012, **421**, 138–151.

49. F. Fagagna, M. Giacca and M. Presta, Multiple Interactions of HIV-I Tat Protein with Size-defined Heparin Oligosaccharides, *J. Biol. Chem*., 1999, **274**, 28198-28295. https://doi.org/10.1074/jbc.274.40.28198

50. T. Sugiyama, T. Asai, Y. M. Nedachi, Y. Katanasaka, K. Shimizu, N. Maeda and N. Oku, Enhanced Active Targeting via Cooperative Binding of Ligands on Liposomes to Target Receptors, *PLoS One*, 2013, **8**, e67550. https://doi.org/10.1371/journal.pone.0067550

51. Z. R. Huang, S. K. Tipparaju, D. B. Kirpotin, C. Pien, T. Kornaga, C. O. Noble, A. Koshkaryev, J. Tran, W. S. Kamoun and D. C. Drummond, Formulation optimization of an ephrin

A2 targeted immunoliposome encapsulating reversibly modified taxane prodrugs, *J. Control. Release*, 2019, **310**, 47–57. https://doi.org/10.1016/j.jconrel.2019.08.006

52. L. Paolini, A. Zendrini, G. Di Noto, S. Busatto, E. Lottini, A Radeghieri, A. Dossi, A. Caneschi, D. Ricotta and P. Bergese, Residual matrix from different separation techniques impacts exosome biological activity, *Sci. Rep.*, 2016, **6**, article number 23550. https://doi.org/10.1038/srep23550

53. P. D'Ursi, M. Uggeri, C. Urbinati,E. Millo, G. Paiardi, L. Milanesi, R. C. Ford, J. Clews, X. Meng, P. Bergese, A. Ridolfi, N. Pedemonte, P. Fossa, A. orro and M. Rusnati, Exploitation of a novel biosensor based on the full-length human F508del-CFTR with computational studies, biochemical and biological assays for the characterization of a new Lumacaftor/Tezacaftor analogue, *Sens. Actuators B Chem.*, 2019, **301**, 127131. https://doi.org/10.1016/j.snb.2019.127131

54. K. Manupati, N. R. Dhoke, T. Debnath, R. Yeeravalli, K. Guguloth, S. Saeidpour, U. C. De, S. Debnath and A. Das . Inhibiting epidermal growth factor receptor signalling potentiates mesenchymal–epithelial transition of breast cancer stem cells and their responsiveness to anticancer drugs, *FEBS J.*, 2017, **284**, 1830–1854. https://doi.org/10.1111/febs.14084

55. C. Garbar, C.e Mascaux, J. Giustiniani, Y. Merrouche and A. Bensussan,. Chemotherapy treatment induces an increase of autophagy in the luminal breast cancer cell MCF7, but not in the triple-negative MDA-MB231, *Sci. Rep.*, 2017, **7**, article number 7201. https://doi.org/10.1038/s41598-017-07489-x

56. M. H. Schmidt, F. B. Furnari, W. H. Cavenee andO. Bögler, Epidermal growth factor receptor signaling intensity determines intracellular protein interactions, ubiquitination, and internalization, *PNAS*, 2003, **100**, 6505-6510. https://doi.org/10.1073/pnas.10317901

57. M. Collot, P. Ashokkumar, H. Anton, E. Boutant, O. Faklaris, T.Galli, Y. Mély, L. Danglot and A. S. Klymchenko, MemBright: A Family of Fluorescent Membrane Probes for Advanced Cellular Imaging and Neuroscience, *Cell Chem. Biol.*, 2019, 26, 600–614.e1–e7. https://doi.org/10.1016/j.chembiol.2019.01.009

58. A. Salvati, A. S. Pitek, M. P. Monopoli, K. Prapainop, F. Baldelli Bombelli,D. H. Hristov, P. M. Kelly, C. Åberg, E. Mahon and K. A. DawsonTransferrin-functionalized nanoparticles lose their targeting capabilities when a biomolecule corona adsorbs on the surface, *Nat. Nanotechnol.*, 2013, **8**, 137-143. https://doi.org/10.1038/nnano.2012.237

59. S. Avvakumova, L. Pandolfi, E. Soprano, L. Moretto, M. Bellini, E. Galbiati, M. A. Rizzuto, M. Colombo, R. Allevi, F. Corsi, A. Sánchez Iglesiasf and D. Prosperi, Does conjugation strategy matter? Cetuximab-conjugated gold nanocages for targeting triple-negative breast cancer cells, *Nanoscale*, 2019, **1**, 3626-3638. DOI https://doi.org/10.1039/C9NA00241C

60. H. Mohammad-Beigi, Y. Hayashi, C. Moeslund Zeuthen, H. Eskandari, C. Scavenius, K. Juul-Madsen, T. Vorup-Jensen, J. J. Enghild and D. S. Sutherland Mapping and identification of soft corona proteins at nanoparticles and their impact on cellular association, *Nat. Commun.*, 2020, **11**, article number 4535.https://doi.org/10.1038/s41467-020-18237-7 61. A. Nandakumar, W. Wei, G. Siddiqui, H. Tang, Y. Li, A. Kakinen, X. Wan, K. Koppel, S. Lin, T. P. Davis, D. T. Leong, D. J. Creek, F. Ding, Y. Song and P. C. Ke, Dynamic Protein Corona of Gold Nanoparticles with an Evolving Morphology, *ACS Appl. Mater. Interfaces*, 2021, **13**, 58238–58251. https://doi.org/10.1021/acsami.1c19824

62. D. Di Silvio, A. Silvestri, L. LayL. Polito and S. E. Moya, Impact of ConcanavalinA affinity in the intracellular fate of Protein Corona on Glucosamine Au nanoparticles, *Sci. Rep.*, 2018, **8**, article number 9046. https://doi.org/10.1038/s41598-018-27418-w

63. M. Wolf, R. W. Poupardin, P. Ebner-Peking, A. Cronemberger Andrade, C. Blöchl, A. Obermayer, F. G. Gomes, B. Vari, N.e Maeding, E. Eminger, H.-M. Binder, A. M. Raninger, S. Hochmann, G. Brachtl, A. Spittler, T. Heuser, R. Ofir, C. G. Huber, Z. Aberman, K. Schallmoser, H.-D. Volk and D. Strunk, . A functional corona around extracellular vesicles enhances angiogenesis, skin regeneration and immunomodulation, J. Extra. Vesicles, 2022, 11, e12207. https://doi.org/10.1002/jev2.12207.

Chapter 4 - Extracellular Vesicles with Different Cell Origins have Different Biomolecular Corona Dynamics

This chapter is adjusted from our just accepted paper: **Angelo Musicò**, Andrea Zendrini, Santiago Gimenez Reyes, Valentina Mangolini, Lucia Paolini, Miriam Romano, Andrea Papait, Antonietta Rosa Silini, Paolo Di Gianvincenzo, Arabella Neva, Marina Cretich, Ornella Parolini, Camillo Almici, Sergio Moya, Annalisa Radeghieri, Paolo Bergese. Extracellular Vesicles with different cell origins have different biomolecular corona dynamics, Nanoscale Horizons. The research reported in this study has been carried out thanks to a grant received by the NFFa Consortium (https://nffa.eu/), to visit CICbiomaGUNE (San Sebastian, Spain) for one month to conduct Fluorescence Correlation Spectroscopy experiments. In Chapter 3 we highlighted the different cellular uptake of chemically and physically engineered REVs, which could be due to the presence of FBS. This could lead to an exchange of molecules at the Rev's surface, displacing the targeting antibody, and, in turn, reducing the cellular uptake. To prove this, and to give new insight into the field of EV-BC, we developed a Fluorescence Correlation Spectroscopy (FCS) method to characterize these aspects.

4.1 Introduction

The biomolecular corona (BC) refers to the dynamic coating that biomolecules form on the surface of nanoparticles (NPs) when these are immersed in biological fluids. BC redefines some of the native physicochemical properties of the NPs (synthetic identity) – including surface composition, structure and energy, surface charge, NP hydrodynamic radius, and aggregation/stability – giving the NPs diverse biological identities at the nanoscale, and ultimately impacting on their biological behavior[1–3]. The concept of BC was originally introduced in 2007, exclusively referring to synthetic NPs [4,5]. Currently, within that context, it is a topic of great research vitality and far from being exhausted. For example, lively debates on the composition, structure, and kinetics of BC formation are still underway [6]. On the other hand, the fact that the BC enriches specific biomolecular patterns “hidden” in the biological fluid represents a potential breakthrough for diagnostics [7,8]. In recent years, it has been realized that biological fluids inherently display nanoscale features given that, besides soluble proteins, they contain several kinds of extracellular NPs, e.g. exomeres, lipoproteins, extracellular vesicles, midbody remnants, and many others [9]. In turn, since 2018 [10], few researchers have started to highlight the presence and biological significance of “BC-like” dynamic associations involving soluble proteins, lipoproteins, and

extracellular vesicles (EVs). Complexes formed by EVs and lipoproteins (EV-LP) have been shown to occur under physiological conditions [11] and during nanoscale manipulation [12], exhibiting features like EV-LP fusion [13]. EVs derived from brain metastases have been observed to induce the binding and aggregation of lipoproteins [14]. It has also been reported that a BC forms around EVs in blood plasma [15], and that this BC has a functional impact [16,17], enhancing angiogenesis, skin regeneration, and immunomodulation [18,19]. The EV BC also has potential in diagnostics [8,20] and should be critically considered in EV surface engineering [21]. Both the specific cell type from which EVs originate and the EV intracellular biogenesis pathway shape the surface of each EV type. As a result, EVs derived from various cells can exhibit distinct surface properties. We speculate that this variability influences, together with the molecular composition of the BC [10,15] also its dynamics, because changes in EV surface physicochemical properties are expected to be mirrored in time required for BC formation, BC evolution over time, and biomolecule exchange rate at the interface. To investigate the dynamics of the EV BC, it is necessary to put in place new *in situ* methodologies that work in physiological conditions and in real-time, overcoming the limitations associated with static *ex situ* methods, which have been conventionally employed in EV-BC analysis. Worth of note, measuring BC formation even with *ex situ* approaches previously developed for synthetic NPs has yet proven to be extremely challenging, due to the inherent physicochemical characteristics of EVs, e.g. difficulty in not altering or even breaking the EVs and/or in distinguishing corona components from the internal EV cargo upon corona "peeling" [10,15,17,19,22]. Furthermore, *ex-situ* methods, such as mass spectrometry [23] and gel electrophoresis [20,21], cannot provide information about the BC dynamics as they require pre-analytical separation of the EV-BC complexes (i.e., by size exclusion chromatography, SEC, or ultracentrifugation) which may result in altering the complexes by the loss of weakly associated components [18]. Fluorescence Correlation Spectroscopy (FCS) is an *in situ* spectroscopic technique that measures the fluctuations of fluorescence in a confocal volume, which can be related to the movement of the fluorescent species in and out of the volume [24]. From the autocorrelation function describing the time evolution of fluorescence, it is possible to extrapolate the diffusion coefficient of the fluorescent species and relate it with their size and mass [25,26]. FCS has been successfully used to characterize the colloidal stability of synthetic NPs in different biological fluids [27–29]. FCS is an optimal technique for measuring in situ as it allows to trace diffusion of specific molecular components, provided that these are fluorescently labelled. Therefore, if we selectively label proteins present in media or the EVs, or even both with different fluorophores with not overlapping fluorescence, we will be capable of tracing the fate of proteins, EVs or both, respectively, without the need of separating EV BC complexes from other proteins or biomolecules present in the

media[30]. In this work, we implement for the first time a dedicated FCS methodology based on competition experiments of physisorption to track the dynamic formation of plasma BC on two different model EV types: Red Blood Cells EVs (REVs) and placental Mesenchymal Stromal Cells EVs (MEVs). Both EV types are now in the spotlight for their great potential in clinical translation. REVs for personalized medicine and drug delivery [31–33], MEVs for regenerative medicine and immunomodulation [34–37]. We will show that our methodology does not require the separation of the EVs from the media, thus reducing potential artifacts due to the separation processes. Furthermore, we implemented stoichiometric and geometric models to use FCS results for estimating the architecture of the BC.

4.2 Experimental section

4.2.1 Human amniotic mesenchymal stromal cell isolation and conditioned medium preparation

The study adhered to the principles outlined in the Declaration of Helsinki, and informed consent was obtained by the mothers following the guidelines established by the local ethical committee "Comitato Etico Provinciale di Brescia," Italy (approval number NP 2243, January 19, 2016). The isolated hAMSCs met the minimal criteria for MSCs, demonstrating positivity for mesenchymal markers CD13 (97.7 ± 1.6% mean ± SD), CD73 (88.3 ± 6.4%), CD90 (94.8 ± 7.4%), while lacking the expression of hematopoietic markers such as CD45 (1.8 ± 1.0%), CD66b (0%), and the epithelial marker CD324 (1.7 ± 1.0%) (10.1186/s13287-021-02607-z). After in vitro expansion to passage 1, hAMSCs were cultured for 5 days in 24-well plates (Corning, NY, USA) at a density of 5 × 105 cells/well in 0.5 mL of DMEM-F12 medium (Sigma-Aldrich) without serum, supplemented with 2 mM L-glutamine (Sigma-Aldrich) and 1% P/S, as previously described (10.1186/s13287-021-02607-z). Following culture, the cell-conditioned medium was collected, centrifuged, filtered through a 0.2-µm sterile filter (Sartorius Stedim, Florence, Italy), and stored at −80 °C. Two pools of conditioned medium were generated, each derived from a minimum of three different placenta donors.

4.2.2 Red Blood Cells EV (REV) and Mesenchymal Stem Cell EV (MEV) collection (isolation\separation)

For details about REVs collection refer to *Chapter 3.2.3.* For MEVs, EVs were prepared from the conditioned medium using differential centrifugation steps. All preparation and centrifugation steps were performed at 4°C. Briefly, collected cell-media were subjected to a first centrifugation at 2,000×g for 30 min to remove apoptotic bodies, and a second centrifugation at 16,000×g for 20 min to remove larger vesicles. EVs were then pelleted from the purified supernatant by centrifugation at 120,000×g for 70 min in 38 mL polycarbonate tubes. This EV-enriched pellet

was resuspended in PBS, and the centrifugation was repeated as above. The final EV pellets were resuspended in PBS, and stored at -80°C until their use.

4.2.3 Cetuximab(CTX) functionalization
For details about CTX functionalization refer to *Chapter 3.2.5.*

4.2.4 Bicinchoninic acid (BCA) assay
For details about BCA refer to *Chapter 3.2.6.*

4.2.5 SDS-PAGE and Western Blotting
SDS-PAGE and Western Blotting were conducted according to *Chapter 3.2.7.* For Western Blot analysis, the samples were transferred onto a PVDF membrane and subsequently blocked overnight with a solution of 5% fat-free milk in PBS-0.05% Tween-20 (PBST). The PVDF membranes were then incubated with the following antibodies, each at a 1:1000 dilution, for 90 minutes in PBST with 1% fat-free milk: mouse anti-GM130 (clone 35/GM130, BD Biosciences, GermanyDE), mouse anti-Alix (2H12, Santa Cruz Biotechnology, USA), rabbit anti-LAMP1 (polyclonal, GeneTex, USA), mouse anti-CD63 (Santa Cruz Biotechnology, USA), mouse anti-BAND3 (Santa Cruz Biotechnology, USA), rabbit anti-EGFR (clone 15F8, Cell Signalling Technology Inc., Danvers, MA, US), mouse anti-TSG101 (Santa Cruz Biotechnology, USA). Following this, the membranes were washed three times for 10 minutes with PBST and incubated for 1 hour with rabbit anti-mouse or goat anti-rabbit secondary antibodies (Zymed, San Francisco, CA, US) at a dilution of 1:3000. The blots were then detected and revealed using Luminata Classic HRP western substrate from Merck-Millipore, and the images were acquired using a G: Box Chemi XT Imaging system.

4.2.6 Colorimetric NANoplasmonic (CONAN) assay
CONAN assay were conducted according to *Chapter 3.2.8.*

4.2.7 Transmission Electron Microscopy (TEM)
Carbon-coated copper grids (Ted Pella, Inc.) were hydrophilized, and 1.5 µL of the sample with 0.04% of paraformaldehyde was applied and left to incubate on the grid for 3 minutes. The excess solution was removed with filter paper and 1.5 µL of 1.5% uranyl acetate solution for positive staining was added to the grid and left for 3 minutes, followed by two washing steps. Imaging was conducted with a LaB6-TEM of type JEOL JEM-1400PLUS (40kV - 120kV, HC pole piece) equipped with a GATAN US1000 CCD camera (2k x 2k).

4.2.8 Nanoparticle Tracking Analysis (NTA)
NTA were conducted according to *Chapter 3.2.10.*

4.2.9 REV and MEV chemisorption and physisorption

Chemisorption and physisorption of REVs and MEVs were accomplished through a two-step labeling procedure. Initially, 200 µL of REVs or MEVs with a concentration of $8x10^{11}$ particles/mL were subjected to a reaction with 200 equivalents of PEG_4-NHS-ester (diluted in PBS) overnight, with continuous mixing at 4°C. Excess PEG was subsequently removed using a Vivaspin500 column with a 10 kDa cut-off, involving five washes with 500 µL of PBS. The pegylated REVs were recovered from the column with 200 µL of PBS. Next, 200 µL of pegylated REVs or MEVs were subjected to an overnight reaction with 200 equivalents of mCTX (in PBS at pH 7.4) with continuous mixing at 4°C. Any unreacted antibody was removed by repeating two times ultracentrifugation at 100,000 × g for 2 hours. The resulting pellet was resuspended in 200 µL of PBS and stored at 4 °C for later use.

4.2.10 Dynamic Light Scattering (DLS)

Dynamic light scattering measurements were carried out with a Malvern ZetaSizer Ultra instrument in backscattering mode. All studies were performed at a 173° scattering angle, and temperature was kept at 25 °C in 1 ml polystyrene cuvettes. After initial equilibration, the measurements consisted of at least 15 runs. All samples were measured three times, and the standard deviation was represented with error bars.

4.2.11 Fluorescence Correlation Spectroscopy (FCS)

FCS measurements were recorded with a Zeiss LSM 880 confocal microscope and analysed with Zen black software. A HeNe laser was used for excitation at 633 nm. Emission was recorded using the PMT (650 – 715 nm) detector. Measurements were conducted with a Zeiss C-Apochromat 40x, numerical aperture 1.2 water immersion objective. 100 µL of the particle dispersion was filled up to 200 µL final sample volume and transferred to a chambered polymer coverslip (Ibidi) for FCS measurement. Prior to sample measurement, the confocal volume was calibrated with a 100 nM solution of Rhodamine 6G in UHPLC-grade water using a diffusion coefficient of 430.00 $\mu m^2/s$ (Absolute Diffusion Coefficients: Compilation of Reference Data for FCS Calibration, picoquant.com). One measurement consisted of 20 runs of 20 seconds and each sample was recorded three times. The data fitting was done with QuickFit 3.0 software using the global fit of 1, 2 and 3-components and 3D normal diffusion model. Specifically, FCS measurements were performed on all our fluorescent building blocks to validate our protocol and determine the diffusion coefficients first of Cy5, and second of mCTX, which were analyzed as two components preparation (free Cy5 and mCTX). Indeed, this information is crucial for rigorously and accurately analyzing the data related to the chemisorbed and physisorbed EVs, which were considered a three-component preparation (free Cy5, mCTX, and EVs). The resulting diffusion coefficients were used to calculate the hydrodynamic diameter (HD) with the Stokes-Einstein equation.

$$D = \frac{k_B T}{6\eta\pi r_h}$$

4.2.12 Stoichiometric evaluation of BC corona formation

A stoichiometric model was developed to estimate the BC volume as a function of EV and protein diameters. The model also allows for a rough estimation of the number of proteins populating each BC layer and their total weight, provided some assumptions are made. The model is based on simple geometrical calculations, and aspects such as membrane roughness, curvature, protein-protein interactions, etc., are not considered in the evaluation of BC. As a first geometric approximation, the volume V_{BC} occupied by a single layer of proteins in a BC on the surface of an EV having volume V_{EV} can be defined as follows:

$$V_{BC} = (V_{tot} - V_{EV}) \cdot p \qquad (1)$$

Being V_{tot} the sum of the EV and BC volumes and p the packing factor defining the packing density of the proteins forming the layer.

Both EVs and proteins have various shapes but in solution are often modelized as perfect spheres or spheroids (e.g., when calculating their size/concentration by DLS, NTA, etc.). For spherical proteins and EVs having diameter d_p and d_{EV} respectively, eq. 1 can be reformulated:

$$V_{BC} = \frac{4}{3}\pi\left[\left(d_p + \frac{d_{EV}}{2}\right)^3 - \left(\frac{d_{EV}}{2}\right)^3\right] \cdot p \qquad (2)$$

In a lattice of packed non-overlapping spheres, p describes the fraction of the volume occupied by the spheres in relation to the total volume of the containing space. p is linked to spheres' spatial arrangement within the lattice; in a system comprising only spheres of identical size, p usually ranges from 0.05 to ~ 0.74. Other p values often found in physical systems are, i.e., ~ 0.34, ~ 0.52, or ~ 0.63.

It is also possible to estimate the number of proteins (n) occupying V_{BC}*:*

$$n = \frac{V_{BC}}{Vp} \qquad (3)$$

Being Vp the protein volume.

Again, for spherical particles, eq. 3 is reformulated and factored out as follows:

$$n = \frac{\left[\left(d_p + \frac{d_{EV}}{2}\right)^3 - \left(\frac{d_{EV}}{2}\right)^3\right] \cdot p}{\left(\frac{d_p}{2}\right)^3} \qquad (4)$$

Furthermore, after calculating *n*, it is in principle possible to approximate the total protein mass T_m transported by a defined coronal layer by assuming all the carried proteins have similar molecular weight a_{MW}:

$$T_m = n \cdot a_{MW} \cdot 1.66 \cdot 10^{-24}\text{g} \qquad (5)$$

If needed, the equations can be further extended for the calculation of multiple stacked layers of spherical proteins with given *d* and *p*.

The presented equations were applied to estimate BC topology on MEVs and REVs, starting from the data collected through FCS analysis (average d_{MEV} and d_{REV}). All the calculations were performed assuming $d_p = 7 \cdot 10^{-9}\, m$ and $a_{MW} = 67000\, Da = 1.11 \cdot 10^{-19}$g, that are respectively the hydrodynamic diameter and the mass of human serum albumin, here used as a model protein. *p* was set to 0.63, which corresponds to a random close-pack sphere geometry.

4.3 Results and Discussion

4.3.1 Cetuximab modification and characterization

Cetuximab (CTX) was labeled with Sulfo Cyanine 5 NHS ester (Cy5) and characterized following the protocol previously described in Musicò et al.[21] (Chapter 3). Sulfo Cyanine 5 NHS-ester was used instead of Sulfo Cyanine 7.5 NHS-ester, due to better suitability for FCS measurements. According to stoichiometric estimations, each fluorescently labelled CTX (mCTX) bears approximately 3.4 fluorophore molecules and 1.3 DBCO molecules. Detailed mCTX preparation protocol and characterization are reported in Figure 1.4.

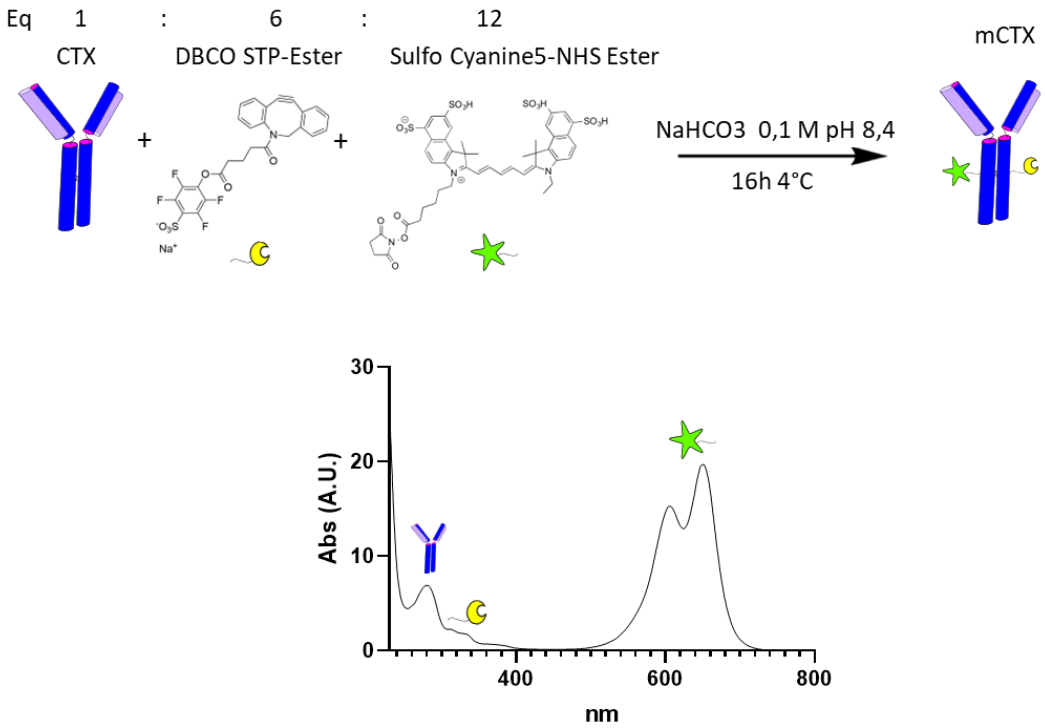

Figure 1.4: CTX modification and characterization. To obtain mCTX we reacted the monoclonal antibody with respectively 6 and 12 equivalent of DBCO-STP-Ester and Sulfo Cyanine5-NHS-Ester, in a single pot reaction as reported in the figure. UV-Vis spectrum of mCTX is reported, highlighting with symbols the correspondence of a peak with functional groups.

4.3.2 Separation, biophysical, and biochemical characterization of REVs and MEVs

REVs and MEVs were separated and characterized according to most updated international standards[38]. Briefly, EVs were separated by differential centrifugation of, respectively, a suspension of Red Blood Cells induced by Calcium Ionophore following protocols reported in [39] and a Mesenchymal Stromal Cell conditioned medium following protocols reported in [40]. Nanoparticle Tracking Analysis (NTA), Dynamic Light Scattering (DLS), Bicinchonicic Acid Assay (BCA), Transmission Electron Microscopy (TEM), Western Blot, and the CONAN assay [41] were used to determine EV particle number density, EV size distribution, (sample) protein concentration, EV morphology, EV protein markers, and the presence of exogenous single or aggregated soluble protein contaminants, respectively. Characterization data highlighted that REV and MEV preparations were similar in terms of size distribution (MEVs 78.88 ± 3.12 nm and REVs 108 ± 5.22 nm in HD, Fig. 2.4A and 2.4C), protein content (MEVs 833.72 ± 257.02 µg/ml and REVs 942.99 ± 105.08 µg/ml, Fig. 2.4B), and morphology (Fig. 2.4D), but have, as expected, different protein markers, due to the different cell source (Fig. 2.4E). Additionally, the minimal presence of soluble proteins [42,43] in both EV types (Fig. 2F), which otherwise could generate artifacts during the EV functionalization, makes them suitable for both the mCTX physisorption and the chemisorption processes.

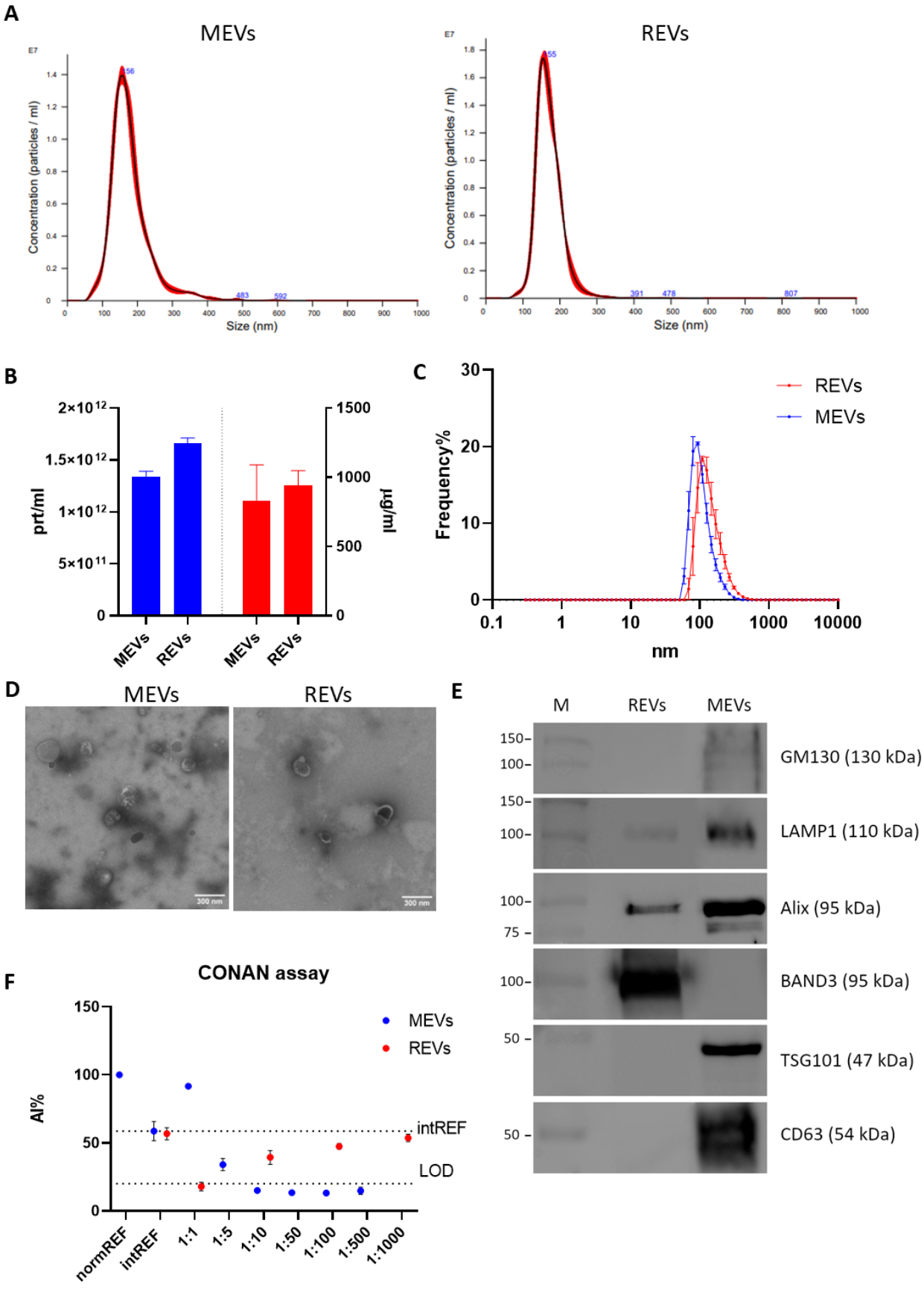
A
MEVs
REVs
Concentration (particles / ml)
Size (nm)
B
prt/ml
µg/ml
MEVs
REVs
C
Frequency%
nm
REVs
MEVs
D
MEVs
REVs
E
M
REVs
MEVs
GM130 (130 kDa)
LAMP1 (110 kDa)
Alix (95 kDa)
BAND3 (95 kDa)
TSG101 (47 kDa)
CD63 (54 kDa)
F
CONAN assay
AI%
intREF
LOD
normREF
intREF
1:1
1:5
1:10
1:50
1:100
1:500
1:1000

Figure 2.4: MEVs and REVs were characterized following MISEV2023 guidelines. (A) MEVs (left) and REVs (right) size distribution profiles obtained by NTA are reported. (B) Blue bars indicate the particle concentration (expressed as prt/ml) of MEVs and REVs preparations obtained by NTA, Red bars indicate the protein concentration (expressed as μg/ml of proteins) of REVs and MEVs preparations obtained by BCA assay. (C) MEVs (blue) and REVs (red) size distribution profiles obtained by DLS. (D) TEM images of MEVs (left panel) and REVs (right panel). (E) Western blot of MEVs and REVs highlight the different origins of these two EV subtypes. REVs and MEVs have in common general EV markers such as LAMP1 and Alix, but REVs only express BAND3, while MEVs only express TSG101, and CD63. In both EV subtypes the contaminant GM130 is negligible present. (F) The Int-REF AI ratio defines the threshold below which the spectral redshift is only due to the interaction between the AuNPs and the EVs. The dotted line represents the CONAN assay threshold for soluble protein detection (<20% AI ratio means that the soluble protein content is ≤0.05 μg/μL). In both MEVs (blue dots) and REVs (red dots) the AI is lower than 20% at a certain dilution, indicating a ≤0.05 μg/μL content of soluble proteins in the preparation. N = 3

4.3.3 Preparation of REVs and MEVs with (physisorbed) fluorescent cetuximab probe (mCTX)

mCTX was physisorbed on both REVs and MEVs., i.e. leading to the formation of a mCTX corona. As a control for the physisorption competition experiments REVs and MEVs were also chemisorbed through the covalent binding of mCTX via bioorthogonal click-chemistry. We quantified mCTX per EV *ex-situ* by combining fluorometer and NTA measurements (Fig. 3.4A). We concluded that by physisorption we obtained a consistent mCTX coverage of the same order of magnitude for the two EV types, with a slightly higher coverage for MEVs. This preliminary *ex-situ* data first points to the fact that different protein coronas may form on REVs and MEVs. In both cases, assuming an even distribution on all the EVs, the number of 30-40 mCTX per EV indicates a non-uniform EV surface coverage (between 3-5% of the total EV surface. For a uniform monolayer a minimum of about 800 mCTX can be estimated, by using the procedure reported in Experimental Section).

The SDS-PAGE densitometric profiles of the mCTX obtained from the mCTX physisorbed EV samples and the stock solution of free mCTX (Fig. 3.4B), are experimentally identical, indicating no covalent interactions of the antibody with EV surface proteins. Differences in the number of mCTX per EV and densitometric profiles are visible in chemisorbed samples, as shown in Fig. 3.4B.

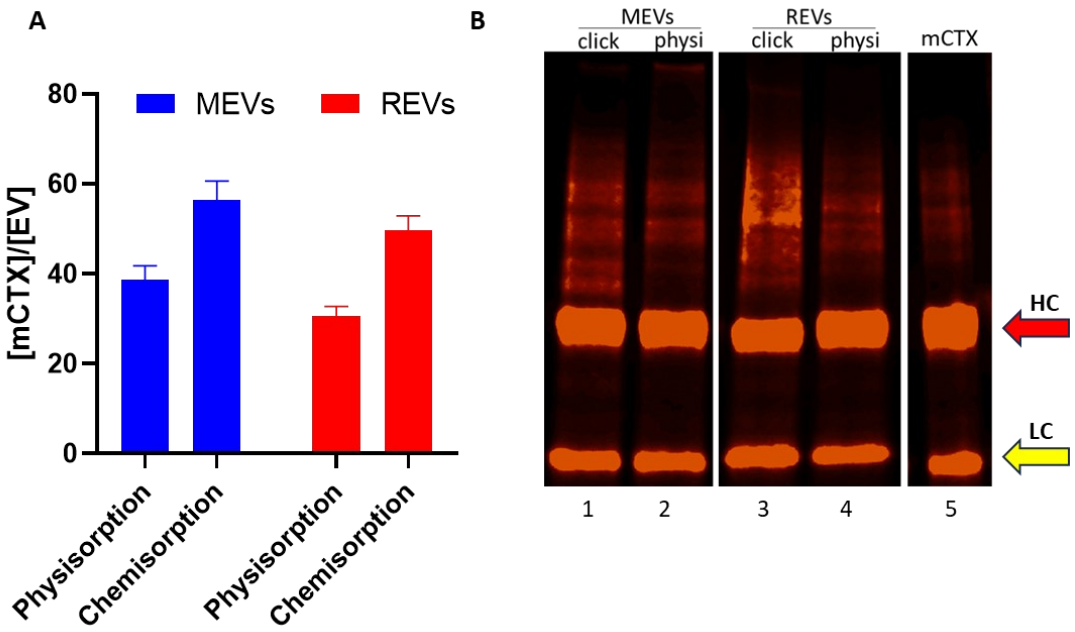

Figure 3.4: (A) MEVs and REVs showed a similar mCTX yield in both chemisorption and physisorption. The chemisorption strategy gave in both EV subtypes a higher mCTX molecules per EV ratio, compared to physisorption. (B) Fluorescent electrophoretic profile of mCTX physisorbed and chemisorbed MEVs and REVs, in both EV subtypes the lane regarding the chemisorption strategy (lane 1 for MEVs, lane 3 for REVs) shows the presence of smeared signals, indicating the covalent bonding of mCTX with membrane proteins. N = 3

4.3.4 Determination of plasma BC dynamics by Fluorescence Correlation Spectroscopy (FCS)

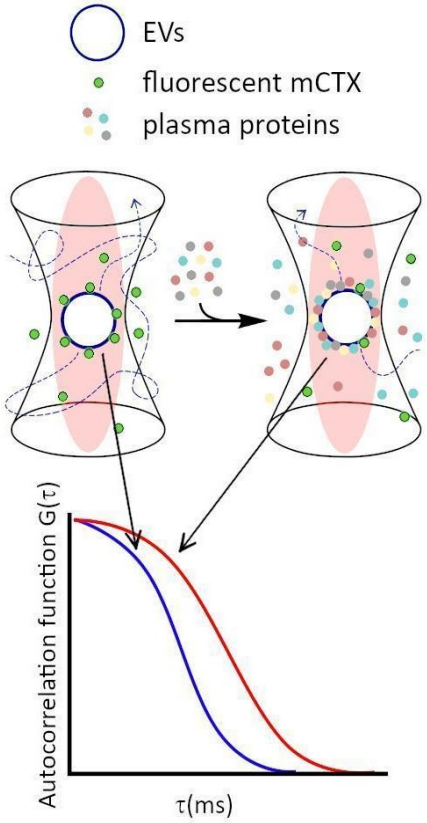

Figure 4.4: Sketch of the FCS experiments for non-destructive, dynamic investigation of EV-BC in physiological conditions ("in situ" investigations). A fluorescently labelled protein (mCTX) previously physisorbed on the EV is used as the FCS probe to detect competitive physisorption of proteins from plasma. Physisorption, viz. formation of the corona, changes the hydrodynamic diameter (HD) and, in turn, alters diffusion of the EV, which is quantitatively mirrored by variation of the autocorrelation function G(τ).

To set up FCS measurements, we first measured by fluorimetry the fluorescence spectra of all the fluorescent molecules employed in this study, determining the dynamic range of measurement for the detector. No significant differences in fluorescence spectra were found between unbound Cy5, free mCTX, and mCTX physisorbed and chemisorbed onto EVs (data not shown). This suggests that the association of the fluorophore to other macromolecules and nanostructures did not significantly alter its excitation and emission ranges. FCS experimental methodology is explained in Experimental Section. The hydrodynamic diameter (HD) of unbound Cy5 and free mCTX were extrapolated from the respective FCS autocorrelation functions, resulting in 1.93 ± 0.06 nm and 20.82 ± 2.24 nm respectively, showing good concordance with those reported in the literature [44]. Moreover, the measurement also highlighted the presence of free (unbound) Cy5 in mCTX preparations (data not shown), which could not be removed, regardless of the number of washing steps performed. Normalized autocorrelation functions of Cy5, mCTX, and mCTX physisorbed

MEVs and REVs (hereafter referred to as MEVs-physi and REVs-physi) are reported in Fig. 5.4A (Cy5 in violet, mCTX in green, MEVs-physi in blue, and REVs-physi in red). The shift trend in the diffusion time of each fluorescent species is as expected since it depends on their HD. By extrapolating the HD from the autocorrelation functions of the EV samples, we found that MEVs-physi and REVs-physi have an HD equal to 66.18 ± 10.86 nm and 86.28 ± 16.76 nm, as reported in Fig. 5.4B. Then, from the fitting of the autocorrelation functions of all samples (the method is reported in Experimental Secction) we determined the fraction (ρ) of the three fluorescent entities tracked by FCS, namely unbound Cy5, free mCTX, and EVs. mCTX is either free or attached to the EVs. When mCTX attaches to the EVs, these become fluorescent objects. Each labeled EV, independently of the number of mCTX associated will count as one single fluorescent object. Therefore, from FCS we detect the relative number of free mCTX molecules and the number of labeled EVs in the confocal volume. Results are summarized in Fig. 5.4C, showing three main features. First, an equal fraction of unbound Cy5 (blue bars) is present in both MEV-physi and REV-physi samples and can therefore be considered as background noise. Second, MEV-physi samples have a significantly more abundant fraction of EVs (green bar) than REV-Physi samples. In turn, the REV-physi sample displays a larger fraction of free mCTX (red bar) than the MEV-physi sample does, indicating that mCTX is weakly associated with (has a lower affinity for) REV surface than to MEV surface. Or, in other words, the physisorption equilibrium (*viz.* the mCTX surface-to-solution partition) is less favored for REVs compared to MEVs. The partition difference very likely occurs because of differences in surface composition and structure between MEVs and REVs, and provides, *per se*, a strong clue about the link connecting BC dynamics and the origin of EVs.

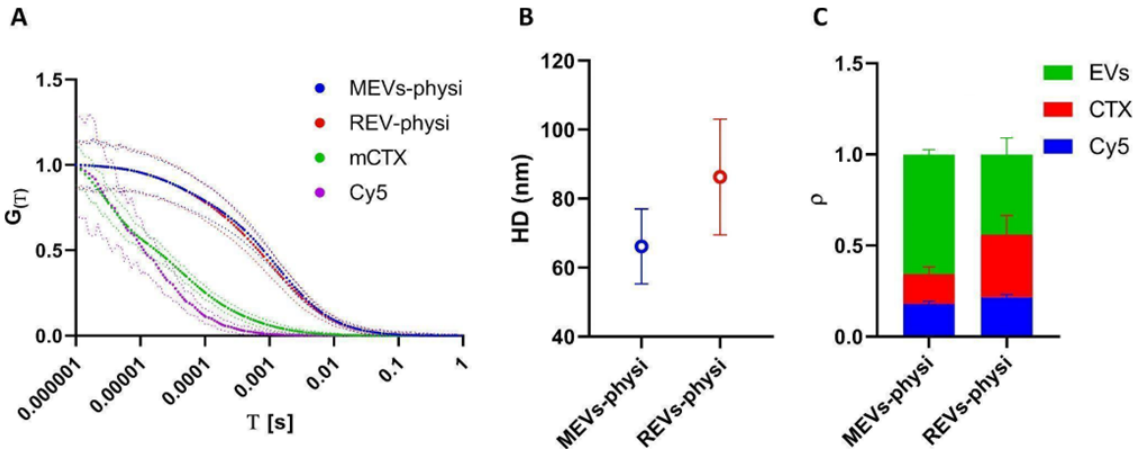

Figure 5.4: (A) Normalized fluorescence correlation graphs of MEVs-physi (blue) and REVs-physi (red), mCTX (green), and Cy5 (violet). The dotted lines represent the standard deviation of the respective autocorrelation function (solid lines). (B) HD extrapolated from autocorrelation functions of physisorbed MEVs and REVs. (C) Fractions of fluorescent components in each preparation. ρ indicates the fraction of each component, namely Cy5 (blue), mCTX (red), and EVs (green). N = 3

Titration experiments were performed by the addition of plasma to MEVs-physi and REV-Physi to gain information about i) the tendency of the two EV populations to form the BC from plasma and ii) the average architecture of such BC. Defined amounts (corresponding to 0.3, 3, 30, 300 µg/ml of proteins) of EV-depleted plasma, were added to the EV samples. The system was incubated O/N to attain equilibrium and was subsequently measured by FCS to determine the competitive substitution of mCTX by plasma proteins, that is the formation of a plasma BC. Results are reported in Fig. 6.4. In Fig. 6.4A reports the variation of the molar concentration of mCTX in solution with respect to the molar concentration of EVs, which is related to the amount of mCTX competitively displaced by plasma proteins. In Fig. 6.4B the variations in the hydrodynamic diameter (HD) of the EVs, which is related to the amount of physisorbed plasma proteins, are reported.

Interestingly, REVs-physi and MEVs-physi displayed a significant detachment of mCTX (Fig. 6.4A), confirming the weak interaction between the antibody and the EV surface, which led to mCTX displacement due to the adsorption of plasma proteins. Moreover, despite both REVs-physi and MEVs-physi showing a consistent detachment of mCTX after the addition of plasma proteins, for REVs-physi the mCTX detachment is much more pronounced than for MEVs-physi, confirming that the two EV types have different affinities for mCTX and plasma proteins.

Indeed, the detachment of mCTX from the EV surface is probably dependent on the affinity competition between plasma proteins and mCTX. These data strongly support that physisorbed mCTX on MEVs-physi is more stably anchored than mCTX on REVs-physi, being also evident for not-spiked samples.

The analysis of the HD fluctuations on the physisorbed samples showed that plasma protein adsorption onto REVs-physi and MEVs-physi occurred following two different dynamics. In specific, REVs-physi HD grows rapidly, reaching a plateau at the concentration of 30 µg/ml of spiked plasma proteins (Fig. 6.4B, red squares). On the contrary, MEVs-physi HD increases slowly and does not reach a plateau, even at the higher concentration of spiked plasma proteins tested (Fig. 6.4B, blue dots). To our knowledge, no appropriate models can correctly fit our data providing apparent affinity constants and/or repartition coefficients. This is probably due to the complexity and heterogeneity of the interactions that can occur during the formation of the BC on the EV surface, which cannot be described by classic fitting models.

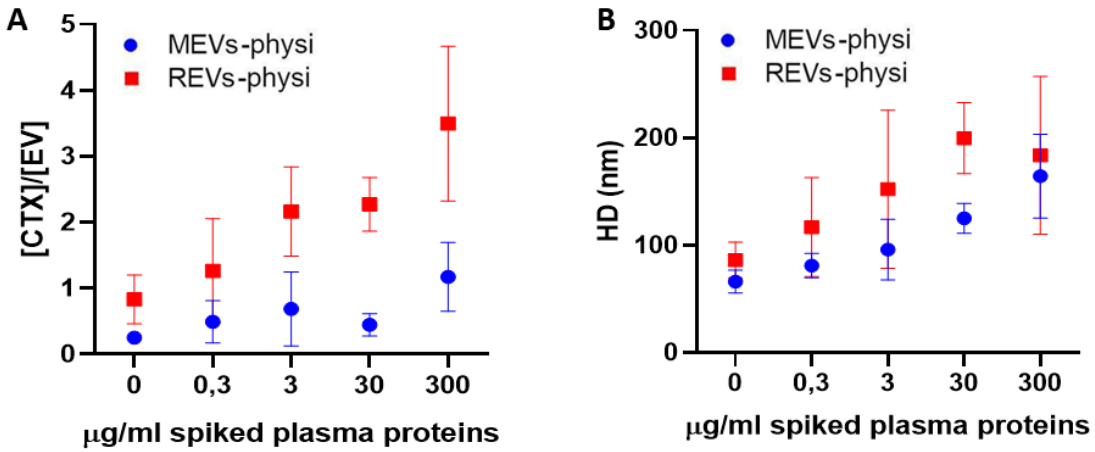

Figure 6.4: (A) Fluctuation of the ratio between the molar concentration of free mCTX and physisorbed EVs after each spike of plasma proteins. An increase in this value indicates detachment of mCTX from the EV surface. MEVs-physi and REVs-physi data are reported respectively in blue and in red. (B) Fluctuation of the HD of physisorbed EVs after each spike of plasma proteins. An increase in this value indicates the physisorption of macromolecules onto the EV surface. MEVs-physi and REVs-physi data are reported respectively in blue and in red. N = 3

Chemisorbed REVs and MEVs were prepared to generate a negative control for mCTX displacement, as mCTX bound to the EV surface in this way is stably anchored and should not be exchanged with other proteins[21]. Accordingly, these samples showed a minimal detachment of mCTX after the addition of plasma proteins (Fig. 7.4A), confirming that mCTX in the preparation is mostly covalently bound to the EV surface and not physisorbed. Interestingly, the surface functionalization of EVs gave them new surface properties, which are strictly dependent on the functionalization and not on the composition of their membrane. Indeed, chemisorbed MEVs and REVs have a very similar trend in hydrodynamic diameter fluctuation, thus indicating that this parameter is normalized by the surface functionalization of the two EV subtypes (Fig. 7.4B). Furthermore, only at a spike of 30 µg/ml of plasma proteins does the hydrodynamic diameter of chemisorbed EVs increase, indicating the formation of a BC.

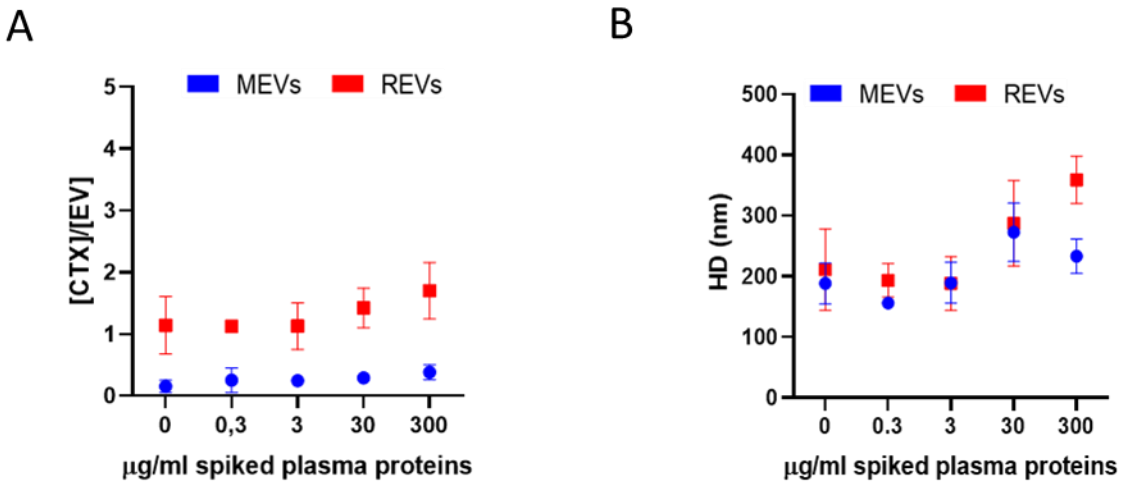

Figure 7.4: (A) Fluctuation of the ratio between the molar concentration of mCTX and chemisorbed EVs after each spike of plasma proteins. An increase in this value indicates a detachment of mCTX from the EV surface. MEVs and REVs data are reported respectively in blue and red. (B) Fluctuation of the hydrodynamic diameter of chemisorbed EVs after each spike of plasma proteins. An increase in this value indicates the physisorption of macromolecules onto the EV surface. MEVs and REVs data are reported respectively in blue and red. N = 3

4.3.5 Evaluation of the BC architecture

The possible architecture of the formed plasma BC can be inferred by comparing the experimental and nominal HD, where the experimental HD is the one determined by FCS, and the nominal is calculated by the following stoichiometric and geometric arguments. The nominal HD is obtained by assuming that all the plasma proteins introduced in each spike are physisorbed on each EV by an identical layer-by-layer process, where each monolayer starts forming only after the underlying layer has been completed. Pristine EVs are modeled as identical spheres (with the diameter determined by FCS, 66 ± 10.9 nm and 86 ± 16.8 nm for MEVs-physi and REVs-physi, respectively) and all the plasma proteins as identical spheres of 7 nm diameter adsorbing in monolayers with a packing factor of 0.63 (see the section "Stoichiometric Evaluation of BC Corona Formation" in the SI for details). This results in a monolayer thickness of 7 nm and, in turn, a 14 nm increase in the EV HD. From this, the nominal HD of the EVs (hereafter referred HD_{nom}) that builds from the number of the nominal monolayers for a given spike of plasma proteins can be calculated, and finally compared with the experimental HD (hereafter referred HD_{exp}) determined by FCS. Results are summarized in Table 1.4. In the case of REVs-physi, for the first plasma spike, corresponding to 0.3 µg/ml of proteins, the number of proteins is far lower than that needed to complete a monolayer, as indicated by the nominal number of monolayers, which is 0.02. Considering that this tiny fraction of monolayer (corresponding to less than 10 proteins) cannot cause an increase in the HD of the pristine EV, one obtains HD_{nom} = 86 ± 16.8 nm, which

is lower than HD_{exp} = (116 ± 36.2) nm. This discrepancy suggests that the BC accumulates in discrete regions forming protruding aggregates, which cause an overall increase in the HD_{exp}. The significant error on HD_{exp}, about 30%, indicates a substantial particle-to-particle variability, suggesting that BC can also organize in non-uniform monolayers, with negligible impact on HD_{exp}. Analogous reasoning holds for REVs-physi when exposed to 3.0 μg/ml plasma protein spikes, as well as for MEVs-physi upon the 0.3 μg/ml and 3.0 μg/ml plasma protein spikes.

On the other hand, when spiking REVs-physi and MEVs-physi with higher concentrations of plasma proteins (30.0 and 300.0 μg/ml) we estimated an increase in the HD of the pristine EVs due to the formation of multiple monolayers of BC. Specifically, with a spike of 30.0 μg/ml of plasma proteins, HD_{nom} for MEVs and REVs are respectively 94 ± 10.9 and 114 ± 16.8 nm, while with 300.0 μg/ml of plasma proteins, HD_{nom} for the two EV subtypes are 136 ± 10.9 nm (MEVs) and 142 ± 16.8 nm (REVs). Again, the HD_{exp} is higher than the HD_{nom} in both the cases and at every spike of plasma protein, specifically for MEVs-physi and REVs-physi, measured HD_{exp} are respectively 125 ± 13.9 nm and 199 ± 53.6 nm at 30.0 μg/ml, while, at 300.0 μg/ml, 164 ± 39.1 nm and 183 ± 33.2 nm. These discrepancies suggest again that the BC accumulates in discrete regions of protruding aggregates, causing such an increase in the HD_{exp}, however in this case we can speculate about the possible formation of complete layers of BC on the EV surface due to the high concentration of proteins. Notably, the difference between HD_{nom} and HD_{exp} in MEVs, spiked with 300.0 μg/ml, is around 28 nm, while for REVs is 57 nm, which corresponds to 2 and 4 further BC layers respectively, thus indicating the formation of aggregates with a bigger size in REVs-physi samples compared to MEVs.

On a final note, we remark that the above variety in BC architecture (sketched in Fig. 8.4), spanning from non-uniform layers (patches) to localized aggregates, holds at the "suspension (collective) level" [45] that is averaged over the whole population of EVs but is well mirrored by a previous report which demonstrated (by single-particle optical microscopy) that single EVs can exactly adopt these BC architectures [15].

Spiked plasma proteins (µg/ml)	REVs-physi				MEVs-physi			
	HD_{exp} (nm)	HD_{nom} (nm)	nominal number of monolayers	probable BC architecture(s)	HD_{exp} (nm)	HD_{nom} (nm)	nominal number of monolayers	probable BC architecture(s)
0.3	116 ± 36.2	86 ± 16.8	0.02	Non-uniform monolayer and aggregates	81 ± 11.5	66 ± 10.9	0.03	Non-uniform monolayer and aggregates
3.0	152 ± 53.6	86 ± 16.8	0.17	Non-uniform monolayer and aggregates	95 ± 18.2	66 ± 10.9	0.27	Non-uniform monolayer and aggregates
30.0	199 ± 53.6	114 ± 16.8	1.5	Monolayers and aggregates	125 ± 13.9	94 ± 10.9	2	Monolayers and aggregates
300.0	183 ± 33.2	142 ± 16.8	4	Monolayers and aggregates	164 ± 39.1	136 ± 10.9	5	Monolayers and aggregates

Table 1.4: Geometric and stoichiometric calculations and hypothesized BC architecture. The ''HD_{exp}" column reports the EV HD measured by FCS (fig. 4B). The "HD_{nom} (nm)" column reports the nominal HD that should be obtained with the layer-by-layer adsorption of all the amount of proteins spiked in the preparation (calculated following the approach reported in SI, section "Stoichiometric evaluation of BC corona formation"). The column "nominal number of monolayers" reports the nominal number of layers of BC that should be formed after the layer-by-layer adsorption of all the amount of proteins spiked in the preparation. By crossing FCS and stoichiometric/geometric data, the "possible BC architecture" has been hypothesized and sketched.

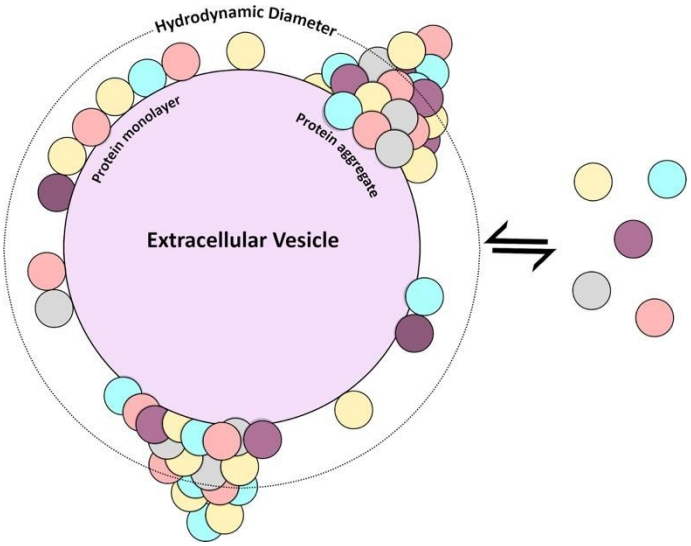

Figure 8.4: Scheme of probable BC architectures.

4.4 Conclusions

In this study, we developed an FCS-based methodology to monitor BC formation on REVs and MEVs in physiological conditions by an *in situ* protocol, unbiased from separation methods. By

spiking our EVs with different concentrations of plasma proteins and using the fluctuation of the HD as a readout of the adsorption of such proteins at the EV surface we evaluated the dynamic formation of the BC.

Our findings reveal distinct BC dynamics between REVs (red blood cell-derived EVs) and MEVs (mesenchymal stem cell-derived EVs), with REVs featuring a higher exchange. By interpreting experimental observations with geometrical and stoichiometric considerations, it also turned out that in both the EV populations the BC does not simply self-organize in a layer-by-layer process, but instead also piles up into discrete islands of protruding protein aggregates, with REVs showing a higher number of aggregates, or aggregates of bigger size. These findings add new insight into the EV-BC. They underscore that BC formation, evolution, and architecture may be influenced by the EV's origin, and in turn surface properties, highlighting an additional layer of heterogeneity among circulating EVs. From an applicative perspective, they suggest that BC dynamics should be a key consideration when considering the use of EVs as therapeutics and in diagnostics.

However, to provide more specific insight into EV-BC interactions, more studies about specific singular plasma components interacting with EVs are needed, in a sort of bottom-up approach. Chapter 5 reports the analysis and characterization of the interactions between EVs and different lipoproteins (LPs) under near-physiological conditions. The aim is to understand how these biogenic nanoparticles interact from a dynamic point of view. The study focuses on EV-LP interactions using Fluorescence Cross-Correlation Spectroscopy (FCCS) and contributes to the understanding of mesoscale phenomena, such as reversible adsorption and biomolecular corona formation, which are critical for the biomedical application of these nanoparticles.

4.5 References

(1) Dawson, K. A.; Yan, Y. Current Understanding of Biological Identity at the Nanoscale and Future Prospects. *Nat Nanotechnol* **2021**, *16* (3), 229–242. https://doi.org/10.1038/s41565-021-00860-0.

(2) Monopoli, M. P.; Åberg, C.; Salvati, A.; Dawson, K. A. Biomolecular Coronas Provide the Biological Identity of Nanosized Materials. *Nat Nanotechnol* **2012**, *7* (12), 779–786. https://doi.org/10.1038/nnano.2012.207.

(3) Ren, J.; Andrikopoulos, N.; Velonia, K.; Tang, H.; Cai, R.; Ding, F.; Ke, P. C.; Chen, C. Chemical and Biophysical Signatures of the Protein Corona in Nanomedicine. *Journal of the American Chemical Society*. American Chemical Society June 1, 2022, pp 9184–9205. https://doi.org/10.1021/jacs.2c02277.

(4) Cedervall, T.; Lynch, I.; Lindman, S.; Berggård, T.; Thulin, E.; Nilsson, H.; Dawson, K. A.; Linse, S. *Understanding the Nanoparticle-Protein Corona Using Methods to Quantify*

Exchange Rates and Affinities of Proteins for Nanoparticles; 2007. www.pnas.org/cgi/content/full/.

(5) Mahmoudi, M.; Landry, M. P.; Moore, A.; Coreas, R. The Protein Corona from Nanomedicine to Environmental Science. *Nature Reviews Materials*. Nature Research July 1, 2023, pp 422–438. https://doi.org/10.1038/s41578-023-00552-2.

(6) Latreille, P. L.; Le Goas, M.; Salimi, S.; Robert, J.; De Crescenzo, G.; Boffito, D. C.; Martinez, V. A.; Hildgen, P.; Banquy, X. Scratching the Surface of the Protein Corona: Challenging Measurements and Controversies. *ACS Nano*. American Chemical Society February 22, 2022, pp 1689–1707. https://doi.org/10.1021/acsnano.1c05901.

(7) Trinh, D. N.; Gardner, R. A.; Franciosi, A. N.; McCarthy, C.; Keane, M. P.; Soliman, M. G.; O'Donnell, J. S.; Meleady, P.; Spencer, D. I. R.; Monopoli, M. P. Nanoparticle Biomolecular Corona-Based Enrichment of Plasma Glycoproteins for N-Glycan Profiling and Application in Biomarker Discovery. *ACS Nano* **2022**, *16* (4), 5463–5475. https://doi.org/10.1021/acsnano.1c09564.

(8) Radeghieri, A.; Bergese, P. The Biomolecular Corona of Extracellular Nanoparticles Holds New Promises for Advancing Clinical Molecular Diagnostics. *Expert Review of Molecular Diagnostics*. Taylor and Francis Ltd. 2023, pp 471–474. https://doi.org/10.1080/14737159.2023.2215927.

(9) Busatto, S.; Zendrini, A.; Radeghieri, A.; Paolini, L.; Romano, M.; Presta, M.; Bergese, P. The Nanostructured Secretome. *Biomaterials Science*. Royal Society of Chemistry January 1, 2020, pp 39–63. https://doi.org/10.1039/c9bm01007f.

(10) Buzás, E. I.; Tóth, E.; Sódar, B. W.; Szabó-Taylor, K. Molecular Interactions at the Surface of Extracellular Vesicles. *Seminars in Immunopathology*. Springer Verlag September 1, 2018, pp 453–464. https://doi.org/10.1007/s00281-018-0682-0.

(11) Lozano-Andrés, E.; Enciso-Martinez, A.; Gijsbers, A.; Ridolfi, A.; Van Niel, G.; Libregts, S. F. W. M.; Pinheiro, C.; van Herwijnen, M. J. C.; Hendrix, A.; Brucale, M.; Valle, F.; Peters, P. J.; Otto, C.; Arkesteijn, G. J. A.; Wauben, M. H. M. Physical Association of Low Density Lipoprotein Particles and Extracellular Vesicles Unveiled by Single Particle Analysis. *J Extracell Vesicles* **2023**, *12* (11). https://doi.org/10.1002/jev2.12376.

(12) Ridolfi, A.; Conti, L.; Brucale, M.; Frigerio, R.; Cardellini, J.; Musicò, A.; Romano, M.; Zendrini, A.; Polito, L.; Bergamaschi, G.; Gori, A.; Montis, C.; Panella, S.; Barile, L.; Berti, D.; Radeghieri, A.; Bergese, P.; Cretich, M.; Valle, F. Particle Profiling of EV-Lipoprotein Mixtures by AFM Nanomechanical Imaging. *J Extracell Vesicles* **2023**, *12* (10). https://doi.org/10.1002/jev2.12349.

(13) Busatto, S.; Yang, Y.; Iannotta, D.; Davidovich, I.; Talmon, Y.; Wolfram, J. Considerations for Extracellular Vesicle and Lipoprotein Interactions in Cell Culture Assays. *Journal of Extracellular Vesicles*. John Wiley and Sons Inc April 1, 2022. https://doi.org/10.1002/jev2.12202.

(14) Busatto, S.; Yang, Y.; Walker, S. A.; Davidovich, I.; Lin, W. H.; Lewis-Tuffin, L.; Anastasiadis, P. Z.; Sarkaria, J.; Talmon, Y.; Wurtz, G.; Wolfram, J. Brain Metastases-Derived Extracellular Vesicles Induce Binding and Aggregation of Low-Density Lipoprotein. *J Nanobiotechnology* **2020**, *18* (1). https://doi.org/10.1186/s12951-020-00722-2.

(15) Tóth, E.; Turiák, L.; Visnovitz, T.; Cserép, C.; Mázló, A.; Sódar, B. W.; Försönits, A. I.; Petővári, G.; Sebestyén, A.; Komlósi, Z.; Drahos, L.; Kittel, Á.; Nagy, G.; Bácsi, A.; Dénes, Á.; Gho, Y. S.; Szabó-Taylor, K.; Buzás, E. I. Formation of a Protein Corona on the Surface of Extracellular Vesicles in Blood Plasma. *J Extracell Vesicles* **2021**, *10* (11). https://doi.org/10.1002/jev2.12140.

(16) Gomes, F. G.; Andrade, A. C.; Wolf, M.; Hochmann, S.; Krisch, L.; Maeding, N.; Regl, C.; Poupardin, R.; Ebner-Peking, P.; Huber, C. G.; Meisner-Kober, N.; Schallmoser, K.; Strunk, D. Synergy of Human Platelet-Derived Extracellular Vesicles with Secretome Proteins Promotes Regenerative Functions. *Biomedicines* **2022**, *10* (2). https://doi.org/10.3390/biomedicines10020238.

(17) Liam-Or, R.; Faruqu, F. N.; Walters, A.; Han, S.; Xu, L.; Wang, J. T. W.; Oberlaender, J.; Sanchez-Fueyo, A.; Lombardi, G.; Dazzi, F.; Mailaender, V.; Al-Jamal, K. T. Cellular Uptake and in Vivo Distribution of Mesenchymal-Stem-Cell-Derived Extracellular Vesicles Are Protein Corona Dependent. *Nat Nanotechnol* **2024**. https://doi.org/10.1038/s41565-023-01585-y.

(18) Wolf, M.; Poupardin, R. W.; Ebner-Peking, P.; Andrade, A. C.; Blöchl, C.; Obermayer, A.; Gomes, F. G.; Vari, B.; Maeding, N.; Eminger, E.; Binder, H. M.; Raninger, A. M.; Hochmann, S.; Brachtl, G.; Spittler, A.; Heuser, T.; Ofir, R.; Huber, C. G.; Aberman, Z.; Schallmoser, K.; Volk, H. D.; Strunk, D. A Functional Corona around Extracellular Vesicles Enhances Angiogenesis, Skin Regeneration and Immunomodulation. *J Extracell Vesicles* **2022**, *11* (4). https://doi.org/10.1002/jev2.12207.

(19) Dietz, L.; Oberländer, J.; Mateos-Maroto, A.; Schunke, J.; Fichter, M.; Krämer-Albers, E. M.; Landfester, K.; Mailänder, V. Uptake of Extracellular Vesicles into Immune Cells Is Enhanced by the Protein Corona. *J Extracell Vesicles* **2023**, *12* (12). https://doi.org/10.1002/jev2.12399.

(20) Radeghieri, A.; Alacqua, S.; Zendrini, A.; Previcini, V.; Todaro, F.; Martini, G.; Ricotta, D.; Bergese, P. Active Antithrombin Glycoforms Are Selectively Physiosorbed on Plasma

Extracellular Vesicles. *Journal of Extracellular Biology* **2022**, *1* (9). https://doi.org/10.1002/jex2.57.

(21) Musicò, A.; Zenatelli, R.; Romano, M.; Zendrini, A.; Alacqua, S.; Tassoni, S.; Paolini, L.; Urbinati, C.; Rusnati, M.; Bergese, P.; Pomarico, G.; Radeghieri, A. Surface Functionalization of Extracellular Vesicle Nanoparticles with Antibodies: A First Study on the Protein Corona "Variable." *Nanoscale Adv* **2023**, *5* (18), 4703–4717. https://doi.org/10.1039/D3NA00280B.

(22) Buzas, E. I. Opportunities and Challenges in Studying the Extracellular Vesicle Corona. *Nature Cell Biology*. Nature Research September 1, 2022, pp 1322–1325. https://doi.org/10.1038/s41556-022-00983-z.

(23) Choi, D.; Go, G.; Kim, D. K.; Lee, J.; Park, S. M.; Di Vizio, D.; Gho, Y. S. Quantitative Proteomic Analysis of Trypsin-Treated Extracellular Vesicles to Identify the Real-Vesicular Proteins. *J Extracell Vesicles* **2020**, *9* (1). https://doi.org/10.1080/20013078.2020.1757209.

(24) Di Silvio, D.; Silvestri, A.; Lay, L.; Polito, L.; Moya, S. E. Impact of ConcanavalinA Affinity in the Intracellular Fate of Protein Corona on Glucosamine Au Nanoparticles. *Sci Rep* **2018**, *8* (1). https://doi.org/10.1038/s41598-018-27418-w.

(25) Liedl, T.; Keller, S.; Simmel, F. C.; Rädler, J. O.; Parak, W. J. Fluorescent Nanocrystals as Colloidal Probes in Complex Fluids Measured by Fluorescence Correlation Spectroscopy. *Small* **2005**, *1* (10), 997–1003. https://doi.org/10.1002/smll.200500108.

(26) Joshi, N.; Basak, S.; Kundu, S.; De, G.; Mukhopadhyay, A.; Chattopadhyay, K. Attenuation of the Early Events of α-Synuclein Aggregation: A Fluorescence Correlation Spectroscopy and Laser Scanning Microscopy Study in the Presence of Surface-Coated Fe3O4 Nanoparticles. *Langmuir* **2015**, *31* (4), 1469–1478. https://doi.org/10.1021/la503749e.

(27) Shang, L.; Nienhaus, G. U. In Situ Characterization of Protein Adsorption onto Nanoparticles by Fluorescence Correlation Spectroscopy. *Acc Chem Res* **2017**, *50* (2), 387–395. https://doi.org/10.1021/acs.accounts.6b00579.

(28) Wang, H.; Lin, Y.; Nienhaus, K.; Nienhaus, G. U. The Protein Corona on Nanoparticles as Viewed from a Nanoparticle-Sizing Perspective. *Wiley Interdiscip Rev Nanomed Nanobiotechnol* **2018**, *10* (4). https://doi.org/10.1002/wnan.1500.

(29) Nienhaus, G. U.; Maffre, P.; Nienhaus, K. Studying the Protein Corona on Nanoparticles by FCS. In *Methods in Enzymology*; Academic Press Inc., 2013; Vol. 519, pp 115–137. https://doi.org/10.1016/B978-0-12-405539-1.00004-X.

(30) Martinez-Moro, M.; Di Silvio, D.; Moya, S. E. Fluorescence Correlation Spectroscopy as a Tool for the Study of the Intracellular Dynamics and Biological Fate of Protein Corona. *Biophys Chem* **2019**, *253*. https://doi.org/10.1016/j.bpc.2019.106218.

(31) Jayasinghe, M. K.; Pirisinu, M.; Yang, Y.; Peng, B.; Pham, T. T.; Yu Lee, C.; Tan, M.; Vu, L. T.; Dang, X. T. T.; Pham, T. C.; Chen, H.; Leung, A. Y. H.; Cho, W. C.; Shi, J.; Le, M. T. N. Surface-Engineered Extracellular Vesicles for Targeted Delivery of Therapeutic RNAs and Peptides for Cancer Therapy. *Theranostics* **2022**, *12* (8), 3288–3315. https://doi.org/10.7150/thno.68667.

(32) Peng, B.; Yang, Y.; Wu, Z.; Tan, R.; Pham, T. T.; Yeo, E. Y. M.; Pirisinu, M.; Jayasinghe, M. K.; Pham, T. C.; Liang, K.; Shyh-Chang, N.; Le, M. T. N. Red Blood Cell Extracellular Vesicles Deliver Therapeutic SiRNAs to Skeletal Muscles for Treatment of Cancer Cachexia. *Molecular Therapy* **2023**, *31* (5), 1418–1436. https://doi.org/10.1016/j.ymthe.2023.03.036.

(33) Nguyen, P. H. D.; Jayasinghe, M. K.; Le, A. H.; Peng, B.; Le, M. T. N. Advances in Drug Delivery Systems Based on Red Blood Cells and Their Membrane-Derived Nanoparticles. *ACS Nano*. American Chemical Society March 28, 2023, pp 5187–5210. https://doi.org/10.1021/acsnano.2c11965.

(34) Gissi, C.; Radeghieri, A.; Lamorgese Passeri, C. A.; Gallorini, M.; Calciano, L.; Oliva, F.; Veronesi, F.; Zendrini, A.; Cataldi, A.; Bergese, P.; Maffulli, N.; Berardi, A. C. Extracellular Vesicles from Rat-Bone-Marrow Mesenchymal Stromal/Stem Cells Improve Tendon Repair in Rat Achilles Tendon Injury Model in Dose-Dependent Manner: A Pilot Study. *PLoS One* **2020**, *15* (3). https://doi.org/10.1371/journal.pone.0229914.

(35) Marassi, V.; La Rocca, G.; Placci, A.; Muntiu, A.; Vincenzoni, F.; Vitali, A.; Desiderio, C.; Maraldi, T.; Beretti, F.; Russo, E.; Miceli, V.; Conaldi, P. G.; Papait, A.; Romele, P.; Cargnoni, A.; Silini, A. R.; Alviano, F.; Parolini, O.; Giordani, S.; Zattoni, A.; Reschiglian, P.; Roda, B. Native Characterization and QC Profiling of Human Amniotic Mesenchymal Stromal Cell Vesicular Fractions for Secretome-Based Therapy. *Talanta* **2024**, *276*. https://doi.org/10.1016/j.talanta.2024.126216.

(36) Valiukevičius, P.; Mačiulaitis, J.; Pangonytė, D.; Siratavičiūtė, V.; Kluszczyńska, K.; Kuzaitytė, U.; Insodaitė, R.; Čiapienė, I.; Grigalevičiūtė, R.; Zigmantaitė, V.; Vitkauskienė, A.; Mačiulaitis, R. Human Placental Mesenchymal Stem Cells and Derived Extracellular Vesicles Ameliorate Lung Injury in Acute Respiratory Distress Syndrome Murine Model. *Cells* **2023**, *12* (23). https://doi.org/10.3390/cells12232729.

(37) Romano, M.; Zendrini, A.; Paolini, L.; Busatto, S.; Berardi, A. C.; Bergese, P.; Radeghieri, A. Extracellular Vesicles in Regenerative Medicine. In *Nanomaterials for Theranostics and Tissue Engineering: Techniques, Trends and Applications*; Elsevier, 2020; pp 29–58. https://doi.org/10.1016/B978-0-12-817838-6.00002-4.

(38) Welsh, J. A.; Goberdhan, D. C. I.; O'Driscoll, L.; Buzas, E. I.; Blenkiron, C.; Bussolati, B.; Cai, H.; Di Vizio, D.; Driedonks, T. A. P.; Erdbrügger, U.; Falcon-Perez, J. M.; Fu, Q.; Hill, A. F.; Lenassi, M.; Lim, S. K.; Mahoney, M. G.; Mohanty, S.; Möller, A.; Nieuwland, R.; Ochiya, T.; Sahoo, S.; Torrecilhas, A. C.; Zheng, L.; Zijlstra, A.; Abuelreich, S.; Bagabas, R.; Bergese, P.; Bridges, E. M.; Brucale, M.; Burger, D.; Carney, R. P.; Cocucci, E.; Crescitelli, R.; Hanser, E.; Harris, A. L.; Haughey, N. J.; Hendrix, A.; Ivanov, A. R.; Jovanovic-Talisman, T.; Kruh-Garcia, N. A.; Ku'ulei-Lyn Faustino, V.; Kyburz, D.; Lässer, C.; Lennon, K. M.; Lötvall, J.; Maddox, A. L.; Martens-Uzunova, E. S.; Mizenko, R. R.; Newman, L. A.; Ridolfi, A.; Rohde, E.; Rojalin, T.; Rowland, A.; Saftics, A.; Sandau, U. S.; Saugstad, J. A.; Shekari, F.; Swift, S.; Ter-Ovanesyan, D.; Tosar, J. P.; Useckaite, Z.; Valle, F.; Varga, Z.; van der Pol, E.; van Herwijnen, M. J. C.; Wauben, M. H. M.; Wehman, A. M.; Williams, S.; Zendrini, A.; Zimmerman, A. J.; Théry, C.; Witwer, K. W. Minimal Information for Studies of Extracellular Vesicles (MISEV2023): From Basic to Advanced Approaches. *J Extracell Vesicles* **2024**, *13* (2). https://doi.org/10.1002/jev2.12404.

(39) Usman, W. M.; Pham, T. C.; Kwok, Y. Y.; Vu, L. T.; Ma, V.; Peng, B.; Chan, Y. S.; Wei, L.; Chin, S. M.; Azad, A.; He, A. B. L.; Leung, A. Y. H.; Yang, M.; Shyh-Chang, N.; Cho, W. C.; Shi, J.; Le, M. T. N. Efficient RNA Drug Delivery Using Red Blood Cell Extracellular Vesicles. *Nat Commun* **2018**, *9* (1). https://doi.org/10.1038/s41467-018-04791-8.

(40) Silini, A. R.; Papait, A.; Cargnoni, A.; Vertua, E.; Romele, P.; Bonassi Signoroni, P.; Magatti, M.; De Munari, S.; Masserdotti, A.; Pasotti, A.; Rota Nodari, S.; Pagani, G.; Bignardi, M.; Parolini, O. CM from Intact HAM: An Easily Obtained Product with Relevant Implications for Translation in Regenerative Medicine. *Stem Cell Res Ther* **2021**, *12* (1). https://doi.org/10.1186/s13287-021-02607-z.

(41) Zendrini, A.; Paolini, L.; Busatto, S.; Radeghieri, A.; Romano, M.; Wauben, M. H. M.; van Herwijnen, M. J. C.; Nejsum, P.; Borup, A.; Ridolfi, A.; Montis, C.; Bergese, P. Augmented COlorimetric NANoplasmonic (CONAN) Method for Grading Purity and Determine Concentration of EV Microliter Volume Solutions. *Front Bioeng Biotechnol* **2020**, *7*. https://doi.org/10.3389/fbioe.2019.00452.

(42) Zendrini, A.; Guerra, G.; Sagini, K.; Vagner, T.; Di Vizio, D.; Bergese, P. On the Surface-to-Bulk Partition of Proteins in Extracellular Vesicles. *Colloids Surf B Biointerfaces* **2022**, *218*. https://doi.org/10.1016/j.colsurfb.2022.112728.

(43) Sverdlov, E. D. Amedeo Avogadro's Cry: What Is 1μg of Exosomes? *BioEssays* **2012**, *34* (10), 873–875. https://doi.org/10.1002/bies.201200045.

(44) Imamura, H.; Sasaki, A.; Honda, S. Fate of a Stressed Therapeutic Antibody Tracked by Fluorescence Correlation Spectroscopy: Folded Monomers Survive Aggregation. *Journal of Physical Chemistry B* **2017**, *121* (34), 8085–8093. https://doi.org/10.1021/acs.jpcb.7b05603.

(45) Rabanel, J.-M.; Adibnia, V.; Tehrani, S. F.; Sanche, S.; Hildgen, P.; Banquy, X.; Ramassamy, C. *Nanoparticle Heterogeneity: An Emerging Structural Parameter 1 Influencing Particle Fate in Biological Media?*

Chapter 5 - Probing Extracellular Vesicle and Lipoprotein Dynamic Interaction by Fluorescence Cross-Correlation Spectroscopy

This chapter is the result of my visiting period of 8 months at CICbiomaGUNE (San Sebastian, Spain) in the Soft Matter and Nanotechnology Lab., led by Dr. Sergio Moya. Furthermore, this work is part of a bigger project in collaboration with SCITEC-CNR (Milan) and ETH-Z (Zurich). This project aims to characterize Extracellular Vesicles/Lipoproteins interaction with different orthogonal techniques, such as Fluorescence Cross-Correlation Spectroscopy, Super Resolution Microscopy (SRM), Single Molecule Array (SiMoA), and Fluorescence-Activated Cell Sorting (FCAS). These techniques can characterize this interaction by providing information, like apparent affinity and stability. Specifically, this Chapter reports all the results regarding FCCS.

5.1 Introduction

In biological fluids, nanoparticles such as extracellular vesicles (EVs) and lipoproteins (LPs) are not isolated entities but exist in dynamic equilibrium with their environment, interacting with surrounding biomolecules and each other. These interactions lead to the formation of a biomolecular corona (BC), a layer of proteins, lipids, and nucleic acids that adsorb onto the nanoparticle surface upon exposure to biological fluids[1,2]. The formation of this corona can significantly alter the physicochemical properties of the nanoparticle, influencing its biodistribution, cellular uptake, and ultimately, biological function[3–5]. Due to their unique nanostructure, a lipid bilayer encapsulating a variety of biomolecules, EVs possess a high surface-to-volume ratio[6,7], which makes them particularly prone to corona formation when they enter the extracellular milieu[8]. BC modifies their surface characteristics, affecting how EVs are recognized and internalized by recipient cells, as well as their immune evasion capabilities[9]. LPs, on the other hand, are micellar particles, composed of a phospholipid monolayer surface that encloses a hydrophobic core[10]. They are responsible for transporting hydrophobic molecules, such as cholesterol and triglycerides, within the bloodstream[11]. LPs are classified into different subclasses depending on their density, including high-density lipoproteins (HDL), low-density lipoproteins (LDL), and very low-density lipoproteins (VLDL). Like EVs, the surface properties of LPs make them susceptible to biomolecular corona formation, which can alter their lipid transport capacity and influence their interactions with other biological entities[12]. The interaction between EVs and

LPs is emerging as a critical area of research due to its potential biological significance. Both particle types co-exist in plasma and other bodily fluids and their mutual interactions could have profound implications[13,14]. Recent findings suggest that the association between EVs and LPs could also play a role in pathological processes [15]. EVs, which are known to be involved in cancer metastasis, cardiovascular diseases, and inflammatory responses, may exploit lipoproteins as a mechanism to enhance their circulation or facilitate tissue targeting. For example, a recent study reported that cancer EVs are susceptible to LDL aggregation, which enhances their ability to cross the blood-brain barrier and generate brain metastasis[16].

Furthermore, the formation of particle-particle complexes between EVs and LPs may affect the pharmacokinetics and biodistribution of EVs, which are increasingly studied as natural drug delivery systems[17]. These interactions can modify the biological identity of EVs, potentially influencing their capacity to target specific tissues, evade the immune system, or transport therapeutic agents[18,19]. Despite the growing recognition of EV-LP interactions, much remains unknown about the precise nature of these associations and their implications for health and disease. Understanding the biophysics of corona formation and the molecular dynamics at play when EVs and LPs interact is essential for leveraging these particles in biomedical applications such as drug delivery.

In this study, we characterized the interactions between EVs and three types of lipoproteins (HDL, LDL, and VLDL) under close to-physiological conditions. Fluorescence Cross-Correlation Spectroscopy (FCCS) is an analytical technique able to study the dynamic interaction of fluorescent objects passing through a confocal volume, directly in solution[20–22]. We applied this technique to evaluate EV-LP aggregation in different environments, by mimicking physiological conditions. Specifically, we used Red Blood Cells-derived EVs (REVs), an EV subtype particularly interesting for drug delivery purposes. We demonstrated that REVs interaction with different classes of LPs (HDL, LDL, and VLDL) is dose-dependent, but it follows different dynamics depending on the LPs in consideration. Also, we observed that the environment in which EVs-LPs aggregation takes place influences this phenomenon, highlighting the importance of performing experiments in physiological-like conditions. By focusing on the biomolecular corona formation and its impact on the physicochemical properties of both EVs and LPs, this research seeks to shed light on the dynamic nature of EVs-LPs interaction, which is a biologically relevant phenomenon that can be harnessed for therapeutic and diagnostic purposes.

5.2 Experimental section

5.2.1 REV extraction and purification
REV extraction and purification were conducted according to *Chapter 3.2.3.*

5.2.2 SDS PAGE and Western Blot
SDS Page and Western Blot were conducted according to *Chapter 3.2.7.*

5.2.3 BCA assay
BCA was conducted according to *Chapter 3.2.6.*

5.2.4 Dynamic Light Scattering
Dynamic Light Scattering (DLS) measures the fluctuations in the intensity of light scattered by particles as they undergo Brownian motion[25]. When a laser beam is directed at a sample containing particles, the particles scatter the light in all directions. The scattered light intensity fluctuates over time due to the random motion of particles. Smaller particles move more rapidly than larger particles, causing faster fluctuations in the scattered light intensity. The relationship between the speed of Brownian motion and particle size is governed by the Stokes-Einstein equation:

$$D = \frac{K_b T}{6\pi\eta R} \quad (1)$$

where:

- D is the diffusion coefficient.
- K_b is the Boltzmann constant.
- T is the absolute temperature.
- η is the viscosity of the solvent.
- R is the particle hydrodynamic radius.

From this equation, the size of particles can be inferred by measuring the diffusion coefficient from the fluctuation data. Furthermore, measurements of ζ-potential were performed using DLS. The analysis was performed using Zeta sizer ULtra (Malvern Panalytical, Malvern, UK). To measure the size, samples were diluted in PBS to a final concentration between 1-10 nM. After the preparation, the appropriate volume of diluted samples was transferred into the DLS cuvette for measurement. Before the measurement, a step of equilibration was settled to ensure the sample homogeneity and temperature stability. The time settled was 30 seconds for three times. At the end of each measurement, the correlogram and the count rate were evaluated to control the correct concentrations of the samples. The polydispersity index (PDI) was evaluated to verify the width

of the size distribution. For size measurement, the data analysis was performed considering the intensity, volume and number distributions and the size peaks. To measure the ζ-potential, samples were diluted 1:10 in PBS. Before the measurement, the ζ-potential cuvette was rinsed with water and then, the water was eliminated. At this point, 80 ul of diluted sample were put in the cuvette and a step of equilibration was performed. The time settled was 30 seconds for three times.

5.2.5 EV labelling with Atto NHS 633

Isolated EVs were labelled using the Atto N-hydroxysuccinimidyl (NHS) ester 633 fluorescent probe, which is an active ester of Atto 633 (Sigma Aldrich, St. Louis, USA). NHS-ester reacts readily with compounds containing amino groups, forming a chemically stable amide bond between the labelling reagent and amines of the membrane proteins of EVs. The NHS dye was dissolved in anhydrous *N, N*-Dimethylformamide (DMF) and the final concentration of the fluorescent solution was 0.014M. This solution was diluted 1:1000 in PBS and then, 24 µL of the diluted solution were added to an Eppendorf tube containing 1 mL of REVs. The final solution was then placed in dark on a shaker at room temperature overnight to ensure adequate labelling. Afterward, the labelled EVs were stored at 4°C until further use. To characterize labelled samples, fluorescent spectra were collected to assess the optimal range for the detector of FCS. FCS measurements were performed to detect the ratio of free fluorophore in the solution and the hydrodynamic diameters of labelled EVs.

5.2.6 Lipoprotein labelling with Atto DPPE 488

The stock of HDL, LDL and VLDL were stored at 4°C. The fluorophore consisted of 1,2-dipalmitoyl-sn-glycero-3-phosphoethanolamine (DPPE) labelled with Atto 488 (Sigma Aldrich, St. Louis, USA), was resuspended in a chloroform/methanol mixture (8:2 ratio) to a final concentration of 0.001 M, and stored at -20°C. To prepare labelled LPs, 1 µL of the fluorophore solution was mixed with 989 µL of PBS and 10 µL of LPs. This procedure was repeated for each type of lipoprotein (HDL, LDL, and VLDL). The resulting solutions were placed in dark on a shaker overnight at room temperature to allow adequate labelling. To characterize labelled samples, fluorescent spectra were collected to assess the optimal range for the detector of FCS. FCS measurements were performed to detect the ratio of free fluorophore in the solution and the hydrodynamic diameters of labelled EVs.

5.2.7 Spectrofluorometry

The FS5 spectrofluorometer (Edinburgh Instruments Ltd, Livingston, UK) was used to acquire the fluorescence spectra of labelled NPs to assess the optimal settings for FCS. In the analysis, various

standards of free fluorophores were prepared at concentrations of 0 nM, 50 nM, 100 nM, 200 nM, 400 nM, and 800 nM for each fluorophore to build a calibration curve. Subsequently, samples were analyzed with the same settings to determine their concentrations. The experiment involved acquiring emission scans of both the standards and the samples. The excitation wavelengths were precisely set for different samples to optimize fluorescence detection. The excitation wavelength for the REV sample and Atto NHS 633 standards was fixed at 633 nm. For the lipoprotein samples and Atto DPPE 488 standards, the excitation wavelength was set at 488 nm.

5.2.8 Fluorescence Correlation Spectroscopy

Fluorescence Correlation Spectroscopy (FCS) is a highly sensitive analytical technique that utilizes fluorescence microscopy to measure fluctuations in fluorescence intensity. These fluctuations are caused by fluorescent molecules moving in and out of a small, defined confocal volume, illuminated by the laser. FCS provides quantitative information about molecular dynamics, including diffusion coefficients, concentrations, and molecular sizes[26]. The correlation function is used to analyze fluorescence fluctuations, and the mathematic representation is:

$$G(\tau) = \frac{\langle \delta F(t) \delta F(t+\tau) \rangle}{\langle F(t) \rangle^2} \qquad (2)$$

where:

- $G(\tau)$ is the correlation function.
- $\langle \delta F(t) \delta F(t+\tau) \rangle$ is the autocorrelation of fluorescence fluctuation.
- τ is the time lag.
- $\langle F(t) \rangle$ is the average fluorescence intensity over time.
-

100 ul of samples were plated in an 8-well rectangular plate (Corning). The analysis was performed using ZeissNLO 880 (Group Zeiss, Oberkochen, GER), a fluorescence confocal microscope fitted with the following excitation lines: 405, Argon laser (458, 488, 514), DPSS 561, 590, and HeNE 633. The measurements were carried out using GaASP and PMTr detectors for single fluorescence molecule detection and dynamic characterization. The objective used was C-APOCHROMAT (Group Zeiss, Oberkochen, GER), a water immersion objective with a magnification of 40x and a numerical aperture of 1.20. Before the measurement, 10 µL of water were placed on the objective. Free fluorophores were analyzed to calibrate the instrument by adjusting the pinhole and determining the confocal volume. Depending on the sample concentration, the laser power was adjusted to achieve a count rate of approximately 200 kHz. To establish the linear range of laser

power, the linearity between laser power and counts per molecule (CPM) was verified before proceeding with the analysis. Following this setup, the FCS measurement was conducted using a measurement time of 10 seconds with 30 repetitions. To ensure statistical reliability, the series were repeated three times. After measurements, the resulting curves were fitted to appropriate models, using QuikFit software to extract diffusion coefficients and the hydrodynamic diameter.

5.2.9 Fluorescence Cross-Correlation Spectroscopy

Fluorescence Cross-Correlation Spectroscopy (FCCS) is an advanced biophysical technique used to study molecular interactions, diffusion dynamics, and concentrations of biomolecules in solution or within cellular environments. It is an extension of FCS, measuring the simultaneous fluctuations of fluorescence signals from two spectrally distinct fluorophores in real-time. This technique provides quantitative information about molecular interactions, diffusion dynamics, and the number of interacting particles. The core of FCCS analysis is the cross-correlation function (CCF), which is mathematically expressed as:

$$G_{xy}(\tau) = \frac{\langle \delta F_x(\tau) \delta F_y(t+\tau) \rangle}{\langle F_x(\tau) \rangle \langle F_y(\tau) \rangle} \qquad (3)$$

where:

- $G_{xy}(\tau)$ is the cross-correlation function.
- $\delta F_x(\tau)$ and $\delta F_y(\tau)$ are the fluorescence intensity fluctuations over time for each fluorophore.
- τ is the time lag.
- t is the fixed time at which the measurement is starting to observe the quantity F_y.
- $\langle \cdot \rangle$ denotes the time average.

The cross-correlation can result in a positive correlation, indicating that the fluorescent species are moving together, or in a negative or zero correlation, suggesting no interactions or independent movement of the species. The analysis was performed with the same instrument and the same settings of FCS. The excitation of the two fluorophores was achieved using a HeNe 633 nm laser and an Argon laser. The detector used was suitable for capturing the fluorescence emitted by both fluorophores. The procedure for the analysis was the same as FCS measurement. After measurements, the resulting curves were fitted to appropriate models, using QuikFit software to extract the cross-correlation data. The cross-correlation and the autocorrelation amplitudes were correct for free dye [27]. The correction for the autocorrelation curve is done as follows:

$$A_0 = \frac{1}{N_0} = \frac{A \cdot I_{tot}^2}{(I_{tot} - I_b)^2} \quad (4)$$

where:

- A_0 is the corrected FCS amplitude
- N_0 is the corrected N
- A is the measured amplitude (before correction)
- I_{tot} is the total intensity
- I_b is the averaged background intensity

The correction of the cross-correlation curve is done as follows:

$$Acc_0 = \frac{Acc \cdot I_{tot,green} \cdot I_{tot,red}}{(I_{tot,green} - I_{b,green}) \cdot (I_{tot,red} - I_{b,red})} \quad (5)$$

where:

- Acc_0 is the corrected cross-correlation amplitude
- Acc is the measured cross-correlation amplitude (before correction)
- $I_{tot,green}/I_{tot,red}$ are the total intensities in the green and red channels, respectively
- $I_{b,green}$ is the averaged background signal in the green channel
- $I_{b,red}$ is the averaged background signal in the red channel

5.3 Results and Discussion

5.3.1 Biophysical and biochemical characterization of REVs and LPs

REVs and lipoproteins (LPs) were thoroughly characterized biophysically and biochemically using BCA assay, Western blotting, and dynamic light scattering (DLS)[28,29]. REVs were isolated from blood samples following the protocol developed by Usman et al.[23], which employs calcium ionophore induction of red blood cells. The protein content of REVs, quantified using the BCA assay, was found to be 2.08 ± 0.12 μg/μL, while for HDL, LDL, and VLDL the protein concentration measured was 35.08 ± 2.31 μg/μL, 12.81 ± 2.14 μg/μL, and 4.17 ± 0.52 μg/μL respectively. DLS, a widely applied technique for nanoparticle analysis, was used to determine the size distribution, ζ-potential, and particle concentration of both REVs and LPs. For this analysis, size data were interpreted based on particle count rather than intensity to avoid the dominance of high-intensity peaks from larger particles, thus providing a more accurate

representation of nanoparticle populations. Results revealed monomodal size distributions for all particle types, with hydrodynamic diameters (HD) averaging 120 nm for REVs (Fig. 1.5A, blue curve), 30 nm for VLDL (Fig. 1.5A, purple curve), 15 nm for LDL (Fig. 1.5A, green curve), and 8 nm for HDL (Fig. 1.5A, red curve). Additionally, all particles exhibited negative ζ-potentials in PBS (Fig. 1.5B), indicating the presence of repulsive electrostatic forces. However, none of the particles displayed sufficiently high negative ζ-potentials to entirely prevent aggregation, suggesting that these repulsive forces may be inadequate for full stabilization in suspension. The particle concentrations were measured as 7.66×10^{11} particles/mL for REVs (Fig. 1.5C, blue column), 4.23×10^{15} particles/mL for HDL (Fig. 1.5C, red column), 5.38×10^{13} particles/mL for LDL (Fig. 1.5C, green column), and 2.92×10^{11} particles/mL for VLDL (Fig. 1.5C, purple column). These findings are consistent with those reported in the literature, supporting the validity of the measurements and methodologies used in this study[10,30–32]. Western blotting was employed to detect specific protein markers in a mixture separated by molecular weight. Primary antibodies targeting typical proteins of REVs and lipoproteins were used, followed by HRP-conjugated secondary antibodies for detection on the blotting membrane. For nanoparticle characterization, Band-3 was used as a biomarker for REVs, ApoA1 for HDL, and ApoB100 for LDL and VLDL (Fig. 1.5D). Each sample, corresponding to 10 µg of protein, was loaded for analysis. As anticipated, Band-3 was detected exclusively in the REV sample, ApoA1 in the HDL sample, and ApoB100 in both LDL and VLDL samples. These findings confirm the presence of the respective nanoparticles in each sample. Moreover, the absence of cross-reactivity or contamination was verified, as only the expected markers were identified. Specifically, REVs showed only Band-3, indicating no lipoprotein contamination; HDL exclusively contained ApoA1, while both LDL and VLDL samples displayed only ApoB100, confirming the purity of each sample and the absence of REVs or other lipoprotein contaminants.

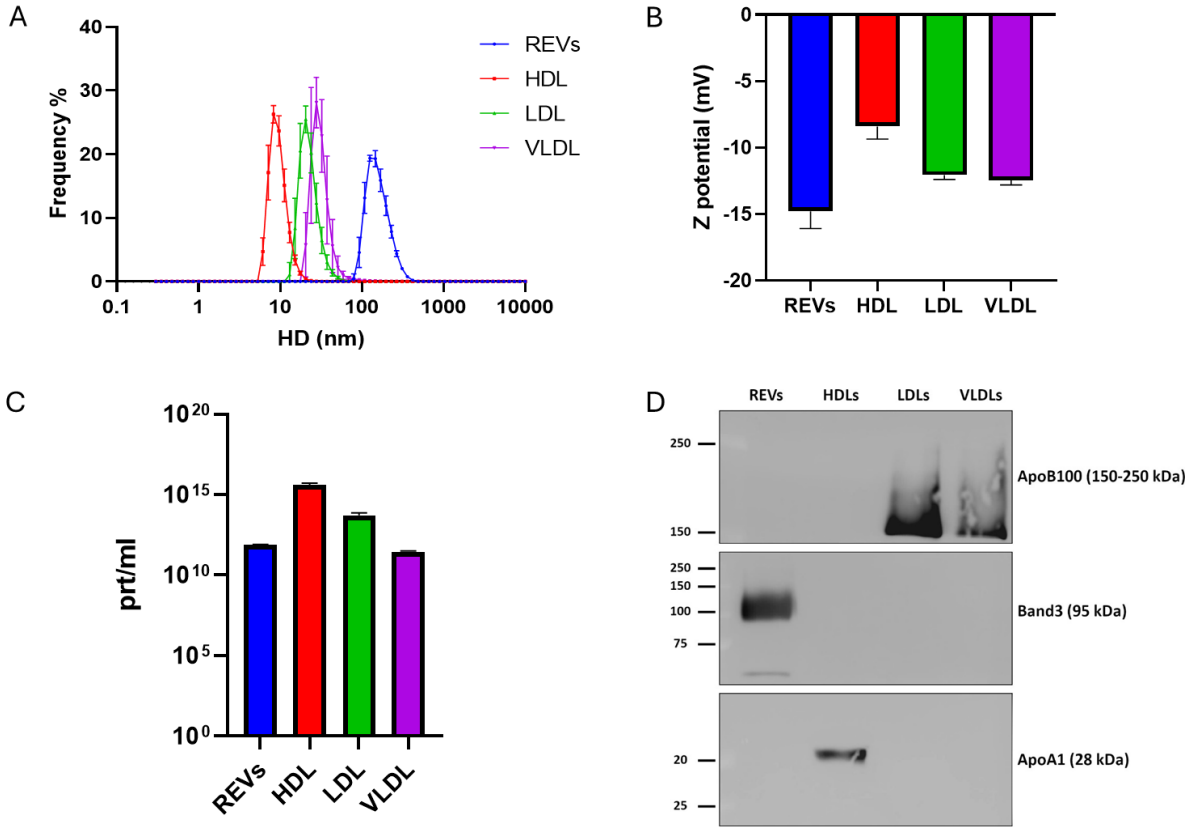

Figure 1.5: A) Size distribution graph, based on DLS measurements. B) All the particles exhibit a negative ζ-potential in DLS measurements. C) NPs concentrations were determined by DLS. D) Western Blot revelation of biomarkers on REVs and LPs

5.3.2 Characterization of labelled REVs and LPs

The fluorophores used in this work to label REVs and LPs for FCS and FCCS measurements are Atto NHS 633 and Atto DPPE 488. The emission and excitation spectra of the free fluorophores were analyzed via spectrofluorometry to confirm no spectral overlap, ensuring accurate differentiation during subsequent analyses (Fig. 2.5A). REVs and LPs were labeled respectively with Atto NHS 633 and Atto DPPE 488, by following the protocols described in the Experimental Section. The fluorophore concentration used for labeling was 250 nM and 1 µM respectively for REVs and LPs. After overnight incubation, Atto NHS 633-labeled REVs (A-REVs) and Atto DPPE 488-labeled LPs (AD-LPs, AD-HDL, AD-LDL, and AD-VLDL) were characterized by DLS, fluorimetry, and FCS. Fluorescence emission spectra of the labeled NPs were acquired to optimize the detector range for FCS and FCCS measurements (Fig. 2.5B-C). Notably, the labeling process didn't affect the emission spectra of the fluorophore. DLS analyses indicated no significant changes in the size distribution or average HD of NPs due to the labeling process (Fig. 2.5D).

FCS was employed to measure the diffusion coefficients of the free fluorophores (used to calibrate the instrument by defining the confocal volume) and to characterize labeled NPs preparations by determining the amount of free fluorophore. Fluorophores diffusion coefficients measured were

360 cm²/sec for Atto DPPE 488 (Fig. 2.5E, green dot) and 340 cm²/sec for Atto NHS 633 (Fig. 2E, red dot), corresponding to hydrodynamic diameters of 1.21 nm for Atto DPPE 488 (Fig. 2E, green triangle) and 1.29 nm for Atto NHS 633 (Fig. 2.5E, red triangle). FCS characterization of A-REVs indicated nearly 100% labeling efficiency (Fig. 2.5F, blue dots), meaning that all the Atto NHS 633 added to the REV preparation is bound to the EV surface. Regarding AD-LPs, FCS measurements showed labeling yields of 59% for AD-HDL (red dots), 73% for AD-LDL (green dots), and 99% for AD-VLDL (purple dots, Fig. 2.5F). Notably, due to the lipid nature of the DPPE probe, potential lipid exchange, or "kissing" effect, between NPs could impact labeling stability[33]. Additionally, we tried to label LPs following different strategies (i.e., NHS ester coupling, similarly to REVs) and adding washing steps (via ultracentrifugation, size exclusion chromatography, and dialysis) to remove the free fluorophore in the preparation (data not shown). However, all these strategies failed to improve the labeling yield of the preparation.

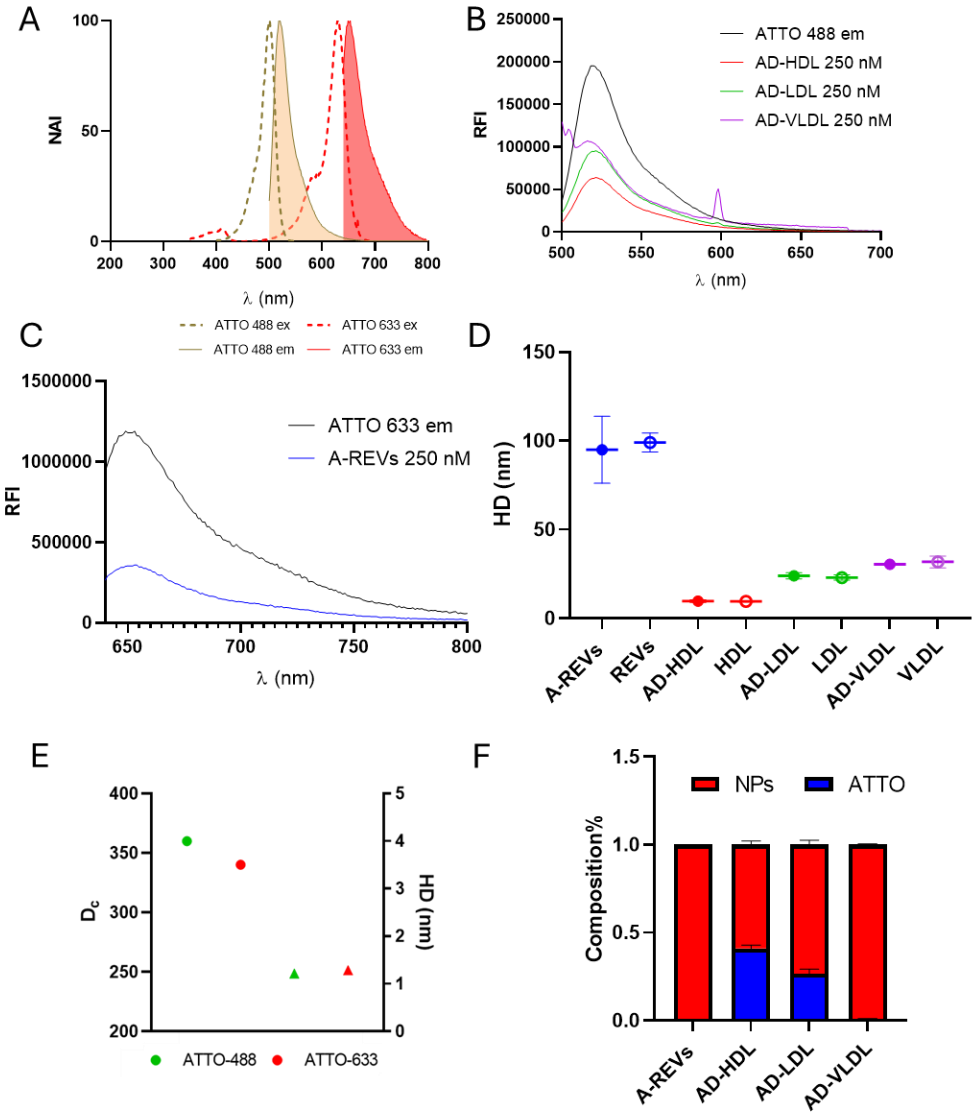

Figure 2.5: A) Emission and excitation spectra graph, based on spectrofluorometer measurements. The analysis indicated that the two fluorophores have distinct and non-overlapping spectra. B) Emission spectra of labeled LPs. C) Emission spectra of labeled REVs. D) HD of NPs before and after the labeling protocol measured by DLS. E) FCS measurements confirmed the diffusion coefficients of the two free fluorophores and their HDs. F) Labelling yields of NPs. The red portion represents labeled NPs, whereas the blue portion represents free fluorophores. The low labeling yield indicated significant contamination of free fluorophore and low labeling efficiency.

5.3.3 Interaction between EVs and LPs

FCCS is an advanced analytical technique used to study interactions between different molecular species in solutions (principle sketched in Fig. 3.5).

100 µL of each type of AD-LPs (corresponding to 1.04×10^{13} AD-HDL, 4.60×10^{12} AD-LDL, and 6.47×10^{11} AD-VLDL) were mixed singularly with 50 µL of A-REVs (corresponding to 3.83×10^{10} A-REVs) and incubated for 24 hours. We chose concentrations and ratios between A-REVs and AD-LPs to mimic physiological conditions at best. Indeed, it is estimated that physiological

concentrations of EVs, HDL, LDL, and VLDL are respectively 10^{11}, 10^{14}, 10^{13}, and 10^{12} prt/ml, despite an intrinsic high variability in these values due to circadian cycle and pathophysiological conditions[34,35]. First FCCS measurements were then performed (T1). Subsequently, 25 µL of depleted human plasma were added to the mixture to a final concentration of 3 µg/ml of proteins, followed by 24 hours of incubations and additional FCCS measurements (T2). These analyses aimed to demonstrate the interaction between LPs and REVs in two different environments (PBS and plasma, respectively T1 and T2, the experimental protocol is also described in Fig. 4.5A). Data analysis of correlograms and cross-correlograms (detailed in the Experimental Section) returned, for each sample, the fraction (ρ) of interacting NPs.

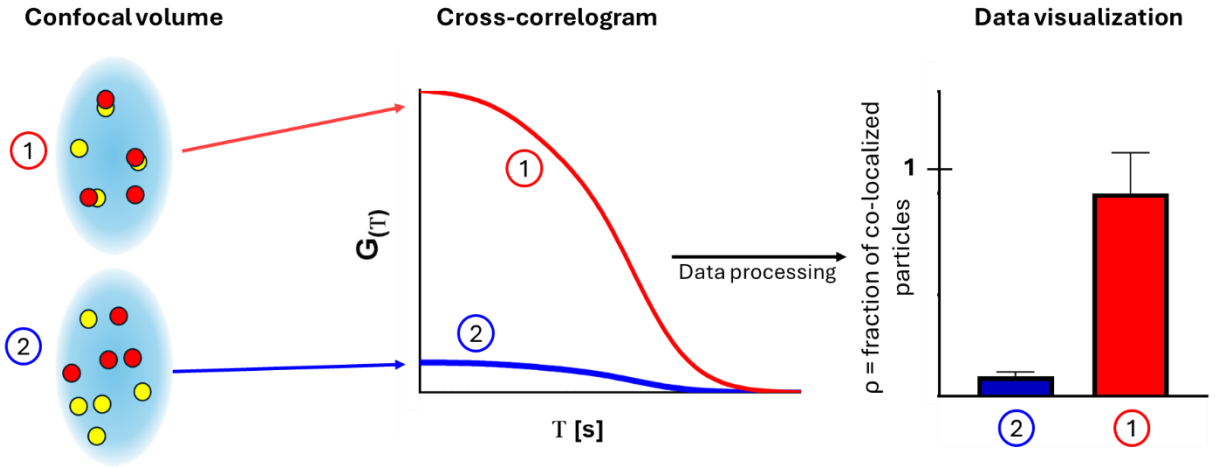

Figure 3.5: Schematic representation of FCCS principle. Fluorescently labeled particles (red and green) diffuse through a detection volume, and their fluorescence intensity is recorded over time. Simultaneous detection of red and green signals indicates particle-particle interaction. Cross-correlation analysis reveals the extent of interaction between the two species, with a higher bar representing strong correlation and interaction.

As shown in Fig. 4.5B, ρ of interacting LPs is small (between 0.01 and 0.02) for every LPs considered. This data could be explained by the stoichiometric excess of LPs present in each preparation compared to REVs. Furthermore, no significant differences were detected between T1 and T2, indicating that plasma addition to the preparation didn't impact the number of LPs involved in the interaction with REVs. On the other hand, we found variable ρ of interacting REVs (from 0.2 to 1, Fig. 4.5C) depending on the interacting LPs and, especially in the case of the AD-HDL, on the environment.

Interestingly, data show a great variation of ρ of interacting REVs in the case of AD-HDL between T1 and T2 (which passed from 0.45 to 1, black bars in Fig. 4.5C), despite no differences in ρ of interacting LPs at the same time points (black bars in Fig. 4.5B). This suggests a redistribution of AD-HDL nanoparticles after the addition of plasma. We speculate that this happens only in the case of AD-HDL due to their smaller size (around 10 nm) which is close to the one of some plasma

proteins and aggregates. This could facilitate the competition of plasma components for sites on the REV surface displacing weakly adsorbed AD-HDL that are consequently redistributed among REVs in the solution[36]. Finally, evaluating the data obtained in T2 which better mimics physiological conditions, we found different ρ of interacting REVs depending on the interacting LP. Specifically, AD-HDL showed the higher ρ of interacting REVs (black bar in Fig 4.5C), AD-LDL an intermediate one (light grey bar in Fig. 4.5C), while AD-VLDL the lowest (dark gray bar in Fig. 4.5C). From this data, we calculated the number of interacting LP per REVs for each type of LP (see Experimental Section) estimating that for AD-HDL, the interaction occurs for approximately 30 particles per REVs, 10 in the case of AD-LDL, and only 1 for AD-VLDL.

We found two different correlations to this data: i) a direct correlation with the number of LPs in the preparation (which is higher for AD-HDL, intermediate for AD-LDL, and lowest for AD-VLDL), and ii) an inverse correlation between LP size and ρ of interacting REVs, which could suggest a limitation in the interaction of bigger LPs, such as AD-LDL and AD-VLDL, possibly due to steric hindrance.

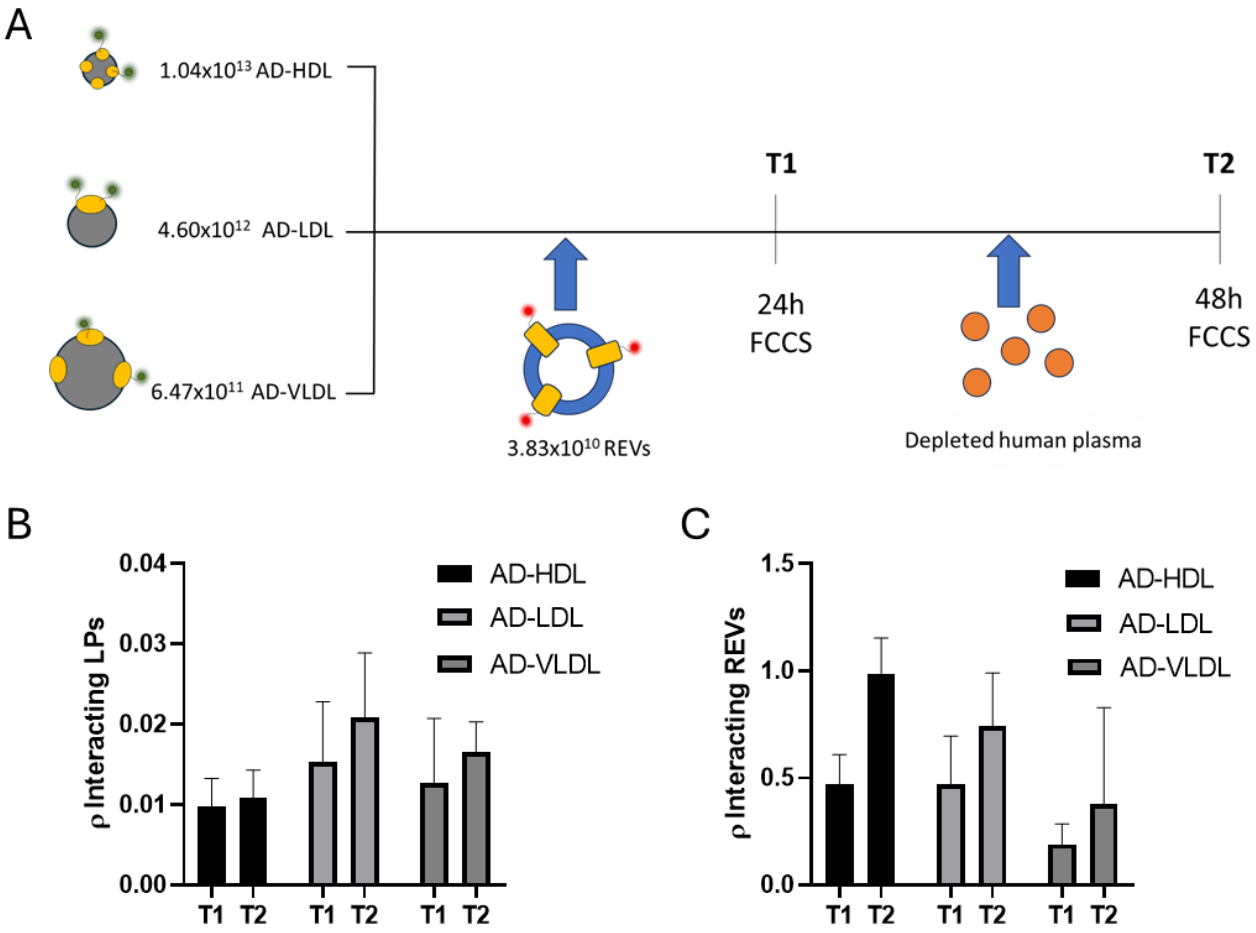

Figure 4.5: A) Sketched representation of the experimental protocol applied to study the interaction between EVs and LPs in physiological conditions. B) Representation of the fraction (ρ) of interacting LPs (AD-HDL in black, AD-LDL in light grey, and AD-VLDL in dark grey) at T1 (in PBS) and at T2 (in plasma). C) Representation of the fraction (ρ) of interacting REVs (AD-HDL in black, AD-LDL in light grey, and AD-VLDL in dark grey) at T1 (in PBS) and at T2 (in plasma). N = 3

These data indicate that in PBS and in physiological-like conditions REVs (and possibly every EV) interact with lipoproteins of different types in different ways, validating our model and supporting the literature[13–17]. To further explore and characterize these interactions we performed dose-response experiments to evaluate the apparent affinity constant for REVs-LPs interactions. Apparent affinity constants are values that qualitatively describe the dynamic of an interaction between two components[37,38]. Thus, comparing these values for each LP used in this work we can estimate physiologically which LP is more favored to interact with REVs. 100 µL of seven different LP concentrations were tested, each mixed with a constant amount of REVs and plasma, following the protocol described above. For AD-HDL, the prepared concentrations were 3.03×10^{12} prt/ml, 1.10×10^{13} prt/ml, 3.43×10^{13} prt/ml, 1.04×10^{14} prt/ml, 3.12×10^{14} prt/ml, 9.37×10^{14} prt/ml, and 2.81×10^{15} prt/ml. For AD-LDL, concentrations ranged from 1.30×10^{12} prt/ml to 1.24×10^{15}

prt/ml, while AD-VLDL concentrations ranged from 2.21×10^{11} prt/ml to 1.74×10^{14} prt/ml. FCCS results are expressed as ρ of interacting REVs in the function of the LP concentration.

Dose-response curves are represented in Fig. 5.5A (red for AD-HDL, green for AD-LDL, and purple for AD-VLDL). To fit our data, we applied the Hill model, which is used to describe cooperative binding or interaction phenomena[37,38]. It is based on the idea that the binding of a ligand to one site can influence the binding of additional ligands to nearby sites, leading to either positive or negative cooperation[39]. However, considering the complex dynamic interactions occurring in EVs-LPs association, it's important to note that the Hill model is a simplification, and may not perfectly represent this system, but it can still provide qualitative information (Kd, Bmax, and n) to compare the different types of interaction considered in this study[38].

The Hill model is described by the equation:

$$\rho = \frac{[L]^n}{K_d + [L]^n}$$

- ρ: is the fraction of occupied binding sites,
- [L]: is the concentration of the ligand,
- K_d: is the apparent dissociation constant,
- n: is the Hill coefficient, which indicates the degree of cooperativity. Specifically, if $n = 1$: No cooperativity, the binding follows the classical Langmuir behavior (independent binding). $n > 1$: Positive cooperativity, meaning that the binding of one ligand increases the affinity of other ligands for nearby sites. $n < 1$: Negative cooperativity, where the binding of one ligand decreases the affinity of other ligands for nearby sites.

Through fitting analysis, we extrapolated the key parameters Bmax (representing the maximum number of binding sites), n (the Hill coefficient), and Kd (the dissociation constant) to compare the interaction between REVs and different lipoproteins (LPs) qualitatively. As depicted in Fig. 5.5B, the interaction between HDL and REVs shows a higher Bmax compared to LDL and VLDL, which exhibit similar values. This finding supports the hypothesis of steric limitations in the interaction of LDL and VLDL with REVs. Although all LPs in this study likely have access to the same number of binding sites on the REV surface, the larger dimensions of LDL and VLDL may hinder access to some of these sites due to steric hindrance, thus reducing the effective number of occupiable binding sites. Interestingly, the analysis of the Hill coefficient, n, revealed distinct interaction mechanisms for each LP (Fig. 5.5C). The HDL-REV interaction has an $n > 1$, indicative of cooperative binding. This is consistent with the similar size of HDL to plasma proteins, which typically adsorb onto surfaces forming a biomolecular corona (BC) that promotes the aggregation

of additional proteins[40,41], as demonstrated in our previous work (Chapter 4)[42]. In contrast, the LDL-REV interaction displays an $n \approx 1$, suggesting a Langmuir-like binding, which reflects a reversible, non-cooperative, and saturable interaction[38]. Finally, the VLDL-REV interaction, characterized by $n < 1$, indicates negative cooperation. This is expected due to the larger size of VLDL, like that of REVs, which leads to steric and thermodynamic limitations in interaction, possibly due to analogous membrane curvatures[41,43]. A comparison of apparent Kd values (Fig. 5.5D) reveals that LDL exhibits the lowest Kd, and, in turn, the highest affinity for REVs, while HDL and VLDL display affinities approximately an order of magnitude lower. This observation is particularly intriguing, as it aligns with previous studies that identified LDL-REV interactions as the most significant under physiological conditions[14]. Notably, LDL-EV aggregation is one of the few biogenic nanoparticle interactions with established biological significance. Busatto et al. demonstrated that cancer-derived EVs form aggregates with LDL, facilitating their passage across biological barriers, such as the blood-brain barrier[16].

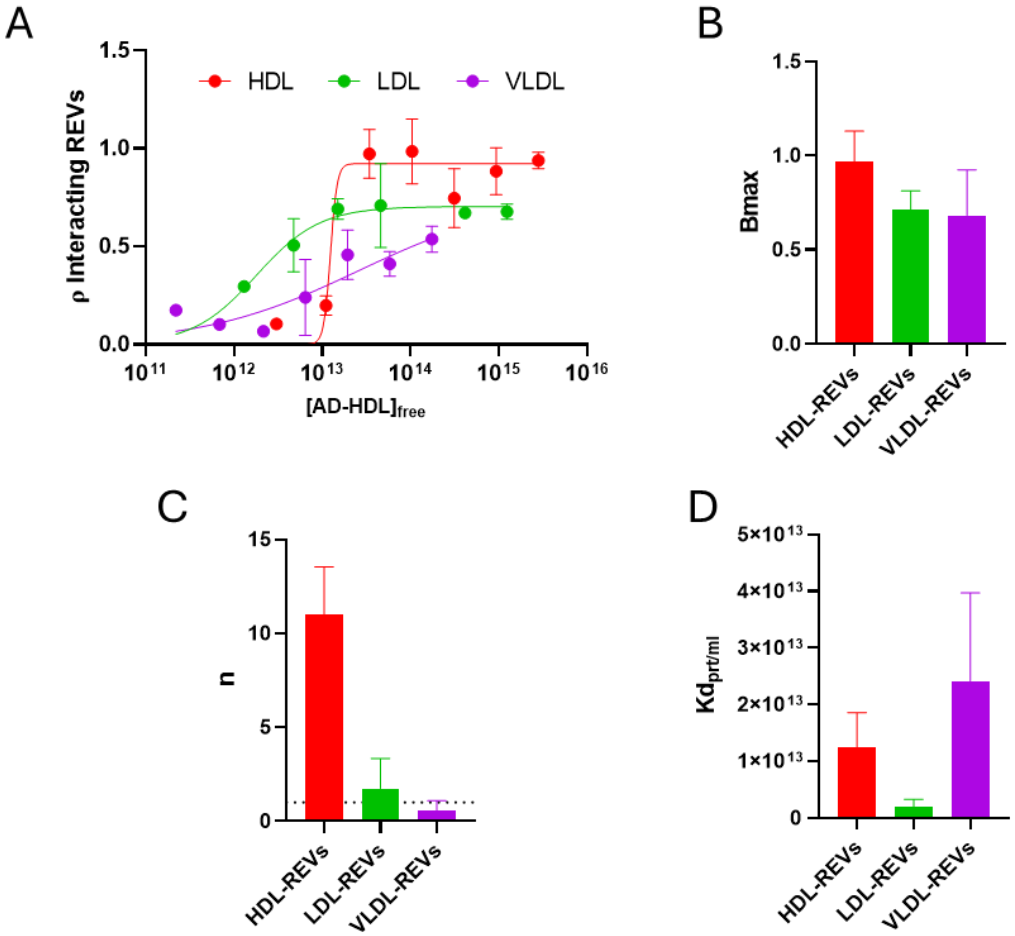

Figure 5.5: A) dose-response curve fitted with the Hill model of EVs-LPs interaction (red for AD-HDL, green for AD-LDL, and purple for AD-VLDL). B) Graphical representation of Bmax extrapolated from the fitting for each EV-LP interaction (red for AD-HDL, green for AD-LDL, and purple for AD-VLDL). C) Graphical representation of n extrapolated from the fitting for each EV-LP interaction (red for AD-HDL, green for AD-LDL, and purple for AD-VLDL), the dotted line represents n = 1. D) Graphical representation of Kd extrapolated from the fitting for each EV-LP interaction (red for AD-HDL, green for AD-LDL, and purple for AD-VLDL). N = 3

5.4 Conclusions

In this study, we explored the interactions between red blood cell-derived extracellular vesicles (REVs) and three distinct lipoprotein (LP) classes: HDL, LDL, and VLDL. Through fluorescence cross-correlation spectroscopy (FCCS), we characterized the nature of these interactions in both PBS and plasma environments. Summarizing, results indicate distinct interaction patterns for each lipoprotein with REVs. HDL-REV interactions show the highest Bmax, suggesting that HDL can access a greater number of binding sites compared to LDL and VLDL. This is likely due to HDL's smaller size, which reduces steric hindrance, and its cooperative binding behavior (n > 1). This could be related to HDL's similarity in size to plasma proteins, which typically form a biomolecular corona that promotes the aggregation of other proteins. In contrast, LDL-REV interactions, despite

a lower Bmax, exhibit the highest affinity (Kd) among the three lipoproteins, indicating a stronger binding. The binding mechanism follows a Langmuir-like model ($n \approx 1$), reflecting a non-cooperative, saturable interaction between LDL and REVs. VLDL-REV interactions, on the other hand, display both the lowest Bmax and affinity, with negative cooperativity ($n < 1$). This suggests that VLDL's larger size leads to steric limitations, reducing the number of available binding sites and possibly introducing thermodynamic constraints due to membrane curvature similarities between VLDL and REVs. Overall, these results provide new insights into the specific dynamics of LP-EV interactions. The distinct binding profiles observed may reflect fundamental biophysical constraints imposed by LP size and structure, offering valuable implications for the design of EV-based therapeutic strategies. Moreover, the confirmed interactions between LDL and REVs reinforce previously published findings regarding the biological significance of LDL-EV aggregates, which may play a role in disease processes such as cancer metastasis across biological barriers. However, the FCCS settings used in this study are not able to resolve complex, heterogeneous models, such as mixtures of all three lipoproteins with REVs in plasma, which would better mimic physiological conditions. As a result, we cannot precisely determine the physiological ratios of interaction, especially given the competition between different lipoproteins for REV surface binding. Therefore, new technologies and approaches are needed to overcome these limitations and provide a deeper understanding of EV-LP interactions *in vivo*.

5.5 References

(1) Buzás, E. I.; Tóth, E.; Sódar, B. W.; Szabó-Taylor, K. Molecular Interactions at the Surface of Extracellular Vesicles. *Seminars in Immunopathology*. Springer Verlag September 1, 2018, pp 453–464. https://doi.org/10.1007/s00281-018-0682-0.

(2) Tóth, E.; Turiák, L.; Visnovitz, T.; Cserép, C.; Mázló, A.; Sódar, B. W.; Försönits, A. I.; Petővári, G.; Sebestyén, A.; Komlósi, Z.; Drahos, L.; Kittel, Á.; Nagy, G.; Bácsi, A.; Dénes, Á.; Gho, Y. S.; Szabó-Taylor, K.; Buzás, E. I. Formation of a Protein Corona on the Surface of Extracellular Vesicles in Blood Plasma. *J Extracell Vesicles* **2021**, *10* (11). https://doi.org/10.1002/jev2.12140.

(3) Monopoli, M. P.; Åberg, C.; Salvati, A.; Dawson, K. A. Biomolecular Coronas Provide the Biological Identity of Nanosized Materials. *Nat Nanotechnol* **2012**, *7* (12), 779–786. https://doi.org/10.1038/nnano.2012.207.

(4) Hajipour, M. J.; Laurent, S.; Aghaie, A.; Rezaee, F.; Mahmoudi, M. Personalized Protein Coronas: A "Key" Factor at the Nanobiointerface. *Biomater Sci* **2014**, *2* (9), 1210–1221. https://doi.org/10.1039/c4bm00131a.

(5) Monopoli, M. P.; Walczyk, D.; Campbell, A.; Elia, G.; Lynch, I.; Baldelli Bombelli, F.; Dawson, K. A. Physical-Chemical Aspects of Protein Corona: Relevance to in Vitro and in Vivo Biological Impacts of Nanoparticles. *J Am Chem Soc* **2011**, *133* (8), 2525–2534. https://doi.org/10.1021/ja107583h.

(6) Pitt, J. M.; Kroemer, G.; Zitvogel, L. Extracellular Vesicles: Masters of Intercellular Communication and Potential Clinical Interventions. *Journal of Clinical Investigation*. American Society for Clinical Investigation April 1, 2016, pp 1139–1143. https://doi.org/10.1172/JCI87316.

(7) Paolicelli, R. C.; Bergamini, G.; Rajendran, L. Cell-to-Cell Communication by Extracellular Vesicles: Focus on Microglia. *Neuroscience*. Elsevier Ltd May 1, 2019, pp 148–157. https://doi.org/10.1016/j.neuroscience.2018.04.003.

(8) Radeghieri, A.; Bergese, P. The Biomolecular Corona of Extracellular Nanoparticles Holds New Promises for Advancing Clinical Molecular Diagnostics. *Expert Review of Molecular Diagnostics*. Taylor and Francis Ltd. 2023, pp 471–474. https://doi.org/10.1080/14737159.2023.2215927.

(9) Dietz, L.; Oberländer, J.; Mateos-Maroto, A.; Schunke, J.; Fichter, M.; Krämer-Albers, E. M.; Landfester, K.; Mailänder, V. Uptake of Extracellular Vesicles into Immune Cells Is Enhanced by the Protein Corona. *J Extracell Vesicles* **2023**, *12* (12). https://doi.org/10.1002/jev2.12399.

(10) Busatto, S.; Zendrini, A.; Radeghieri, A.; Paolini, L.; Romano, M.; Presta, M.; Bergese, P. The Nanostructured Secretome. *Biomaterials Science*. Royal Society of Chemistry January 1, 2020, pp 39–63. https://doi.org/10.1039/c9bm01007f.

(11) Nguyen, P. H. D.; Le, A. H.; Pek, J. S. Q.; Pham, T. T.; Jayasinghe, M. K.; Do, D. V.; Phung, C. D.; Le, M. T. N. Extracellular Vesicles and Lipoproteins – Smart Messengers of Blood Cells in the Circulation. *Journal of Extracellular Biology* **2022**, *1* (7). https://doi.org/10.1002/jex2.49.

(12) Karimi, N.; Cvjetkovic, A.; Jang, S. C.; Crescitelli, R.; Hosseinpour Feizi, M. A.; Nieuwland, R.; Lötvall, J.; Lässer, C. Detailed Analysis of the Plasma Extracellular Vesicle Proteome after Separation from Lipoproteins. *Cellular and Molecular Life Sciences* **2018**, *75* (15), 2873–2886. https://doi.org/10.1007/s00018-018-2773-4.

(13) Ridolfi, A.; Conti, L.; Brucale, M.; Frigerio, R.; Cardellini, J.; Musicò, A.; Romano, M.; Zendrini, A.; Polito, L.; Bergamaschi, G.; Gori, A.; Montis, C.; Panella, S.; Barile, L.; Berti, D.; Radeghieri, A.; Bergese, P.; Cretich, M.; Valle, F. Particle Profiling of EV-Lipoprotein Mixtures by AFM Nanomechanical Imaging. *J Extracell Vesicles* **2023**, *12* (10). https://doi.org/10.1002/jev2.12349.

(14) Lozano-Andrés, E.; Enciso-Martinez, A.; Gijsbers, A.; Ridolfi, A.; Van Niel, G.; Libregts, S. F. W. M.; Pinheiro, C.; van Herwijnen, M. J. C.; Hendrix, A.; Brucale, M.; Valle, F.; Peters, P. J.; Otto, C.; Arkesteijn, G. J. A.; Wauben, M. H. M. Physical Association of Low Density Lipoprotein Particles and Extracellular Vesicles Unveiled by Single Particle Analysis. *J Extracell Vesicles* **2023**, *12* (11). https://doi.org/10.1002/jev2.12376.

(15) Ghebosu, R. E.; Pendiuk Goncalves, J.; Wolfram, J. Extracellular Vesicle and Lipoprotein Interactions. *Nano Letters*. American Chemical Society January 10, 2024, pp 1–8. https://doi.org/10.1021/acs.nanolett.3c03579.

(16) Busatto, S.; Yang, Y.; Walker, S. A.; Davidovich, I.; Lin, W. H.; Lewis-Tuffin, L.; Anastasiadis, P. Z.; Sarkaria, J.; Talmon, Y.; Wurtz, G.; Wolfram, J. Brain Metastases-Derived Extracellular Vesicles Induce Binding and Aggregation of Low-Density Lipoprotein. *J Nanobiotechnology* **2020**, *18* (1). https://doi.org/10.1186/s12951-020-00722-2.

(17) Busatto, S.; Yang, Y.; Iannotta, D.; Davidovich, I.; Talmon, Y.; Wolfram, J. Considerations for Extracellular Vesicle and Lipoprotein Interactions in Cell Culture Assays. *Journal of Extracellular Vesicles*. John Wiley and Sons Inc April 1, 2022. https://doi.org/10.1002/jev2.12202.

(18) Wolf, M.; Poupardin, R. W.; Ebner-Peking, P.; Andrade, A. C.; Blöchl, C.; Obermayer, A.; Gomes, F. G.; Vari, B.; Maeding, N.; Eminger, E.; Binder, H. M.; Raninger, A. M.; Hochmann, S.; Brachtl, G.; Spittler, A.; Heuser, T.; Ofir, R.; Huber, C. G.; Aberman, Z.; Schallmoser, K.; Volk, H. D.; Strunk, D. A Functional Corona around Extracellular Vesicles Enhances Angiogenesis, Skin Regeneration and Immunomodulation. *J Extracell Vesicles* **2022**, *11* (4). https://doi.org/10.1002/jev2.12207.

(19) Liam-Or, R.; Faruqu, F. N.; Walters, A.; Han, S.; Xu, L.; Wang, J. T. W.; Oberlaender, J.; Sanchez-Fueyo, A.; Lombardi, G.; Dazzi, F.; Mailaender, V.; Al-Jamal, K. T. Cellular Uptake and in Vivo Distribution of Mesenchymal-Stem-Cell-Derived Extracellular Vesicles Are Protein Corona Dependent. *Nat Nanotechnol* **2024**, *19* (6), 846–855. https://doi.org/10.1038/s41565-023-01585-y.

(20) Martinez-Moro, M.; Di Silvio, D.; Moya, S. E. Fluorescence Correlation Spectroscopy as a Tool for the Study of the Intracellular Dynamics and Biological Fate of Protein Corona. *Biophys Chem* **2019**, *253*. https://doi.org/10.1016/j.bpc.2019.106218.

(21) Fu, X.; Song, Y.; Masud, A.; Nuti, K.; DeRouchey, J. E.; Richards, C. I. High-Throughput Fluorescence Correlation Spectroscopy Enables Analysis of Surface Components of Cell-Derived Vesicles. *Anal Bioanal Chem* **2020**, *412* (11), 2589–2597. https://doi.org/10.1007/s00216-020-02485-z.

(22) Müller, C. B.; Loman, A.; Pacheco, V.; Koberling, F.; Willbold, D.; Richtering, W.; Enderlein, J. Precise Measurement of Diffusion by Multi-Color Dual-Focus Fluorescence Correlation Spectroscopy. *EPL* **2008**, *83* (4). https://doi.org/10.1209/0295-5075/83/46001.

(23) Usman, W. M.; Pham, T. C.; Kwok, Y. Y.; Vu, L. T.; Ma, V.; Peng, B.; Chan, Y. S.; Wei, L.; Chin, S. M.; Azad, A.; He, A. B. L.; Leung, A. Y. H.; Yang, M.; Shyh-Chang, N.; Cho, W. C.; Shi, J.; Le, M. T. N. Efficient RNA Drug Delivery Using Red Blood Cell Extracellular Vesicles. *Nat Commun* **2018**, *9* (1). https://doi.org/10.1038/s41467-018-04791-8.

(24) Musicò, A.; Zenatelli, R.; Romano, M.; Zendrini, A.; Alacqua, S.; Tassoni, S.; Paolini, L.; Urbinati, C.; Rusnati, M.; Bergese, P.; Pomarico, G.; Radeghieri, A. Surface Functionalization of Extracellular Vesicle Nanoparticles with Antibodies: A First Study on the Protein Corona "Variable." *Nanoscale Adv* **2023**, *5* (18), 4703–4717. https://doi.org/10.1039/D3NA00280B.

(25) Fischer, K.; Schmidt, M. Pitfalls and Novel Applications of Particle Sizing by Dynamic Light Scattering. *Biomaterials* **2016**, *98*, 79–91. https://doi.org/10.1016/j.biomaterials.2016.05.003.

(26) Shang, L.; Nienhaus, G. U. In Situ Characterization of Protein Adsorption onto Nanoparticles by Fluorescence Correlation Spectroscopy. *Acc Chem Res* **2017**, *50* (2), 387–395. https://doi.org/10.1021/acs.accounts.6b00579.

(27) Krüger, D.; Ebenhan, J.; Werner, S.; Bacia, K. Measuring Protein Binding to Lipid Vesicles by Fluorescence Cross-Correlation Spectroscopy. *Biophys J* **2017**, *113* (6), 1311–1320. https://doi.org/10.1016/j.bpj.2017.06.023.

(28) Théry, C.; Witwer, K. W.; Aikawa, E.; Jose Alcaraz, M.; Anderson, J. D.; Andriantsitohaina, R.; Antoniou, A.; Bach, M.; Bachurski, D.; Baharvand, H.; Balaj, L.; Baldacchino, S.; Bauer, N. N.; Baxter, A. A.; Bebawy, M.; Beckham, C.; Bedina Zavec, A.; Benmoussa, A.; Berardi, A. C.; Bergese, P.; Bielska, E.; Blenkiron, C.; Bobis-Wozowicz, S.; Boilard, E.; Boireau, W.; Bongiovanni, A.; Borràs, F. E.; Bosch, S.; Boulanger, C. M.; Breakefield, X.; Breglio, A. M.; Á Brennan, M.; Brigstock, D. R.; Brisson, A.; Broekman, M. L.; Bromberg, J. F.; Bryl-Górecka, P.; Buch, S.; Buck, A. H.; Burger, D.; Busatto, S.; Buschmann, D.; Bussolati, B.; Buzás, E. I.; Bryan Byrd, J.; Camussi, G.; Carter, D. R.; Caruso, S.; Chamley, L. W.; Chang, Y.-T.; Chen, C.; Chen, S.; Cheng, L.; Chin, A. R.; Clayton, A.; Clerici, S. P.; Cocks, A.; Cocucci, E.; Coffey, R. J.; Cordeiro-da-Silva, A.; Couch, Y.; Coumans, F. A.; Coyle, B.; Crescitelli, R.; Ferreira Criado, M.; Das, S.; Datta Chaudhuri, A.; de Candia, P.; De Santana Junior, E. F.; De Wever, O.; del Portillo, H. A.; Demaret, T.; Deville, S.; Devitt, A.; Dhondt, B.; Di Vizio, D.; Dieterich, L. C.; Dolo, V.; Paula Dominguez Rubio, A.; Dominici, M.; Dourado, M. R.; Driedonks, T. A.; Duarte, F. V; Duncan, H. M.; Eichenberger, R. M.; Ekström, K.; Andaloussi, S. EL; Elie-

Caille, C.; Erdbrügger, U.; Falcón-Pérez, J. M.; Fatima, F.; Fish, J. E.; Flores-Bellver, M.; Försönits, A.; Frelet-Barrand, A.; Fricke, F.; Fuhrmann, G.; Gabrielsson, S.; Gámez-Valero, A.; Gardiner, C.; Gärtner, K.; Gaudin, R.; Song Gho, Y.; Giebel, B.; Gilbert, C.; Gimona, M.; Giusti, I.; Goberdhan, D. C.; Görgens, A.; Gorski, S. M.; Greening, D. W.; Christina Gross, J.; Gualerzi, A.; Gupta, G. N.; Gustafson, D.; Handberg, A.; Haraszti, R. A.; Harrison, P.; Hegyesi, H.; Hendrix, A.; Hill, A. F.; Hochberg, F. H.; Hoffmann, K. F.; Holder, B.; Holthofer, H.; Hosseinkhani, B.; Hu, G.; Huang, Y.; Huber, V.; Hunt, S.; Gamal-Eldin Ibrahim, A.; Ikezu, T.; Inal, J. M.; Isin, M.; Ivanova, A.; Jackson, H. K.; Jacobsen, S.; Jay, S. M.; Jayachandran, M.; Jenster, G.; Jiang, L.; Johnson, S. M.; Jones, J. C.; Jong, A.; Jovanovic-Talisman, T.; Jung, S. Journal of Extracellular Vesicles Minimal Information for Studies of Extracellular Vesicles 2018 (MISEV2018): A Position Statement of the International Society for Extracellular Vesicles and Update of the MISEV2014 Guidelines.

(29) Welsh, J. A.; Goberdhan, D. C. I.; O'Driscoll, L.; Buzas, E. I.; Blenkiron, C.; Bussolati, B.; Cai, H.; Di Vizio, D.; Driedonks, T. A. P.; Erdbrügger, U.; Falcon-Perez, J. M.; Fu, Q.; Hill, A. F.; Lenassi, M.; Lim, S. K.; Mahoney, M. G.; Mohanty, S.; Möller, A.; Nieuwland, R.; Ochiya, T.; Sahoo, S.; Torrecilhas, A. C.; Zheng, L.; Zijlstra, A.; Abuelreich, S.; Bagabas, R.; Bergese, P.; Bridges, E. M.; Brucale, M.; Burger, D.; Carney, R. P.; Cocucci, E.; Crescitelli, R.; Hanser, E.; Harris, A. L.; Haughey, N. J.; Hendrix, A.; Ivanov, A. R.; Jovanovic-Talisman, T.; Kruh-Garcia, N. A.; Ku'ulei-Lyn Faustino, V.; Kyburz, D.; Lässer, C.; Lennon, K. M.; Lötvall, J.; Maddox, A. L.; Martens-Uzunova, E. S.; Mizenko, R. R.; Newman, L. A.; Ridolfi, A.; Rohde, E.; Rojalin, T.; Rowland, A.; Saftics, A.; Sandau, U. S.; Saugstad, J. A.; Shekari, F.; Swift, S.; Ter-Ovanesyan, D.; Tosar, J. P.; Useckaite, Z.; Valle, F.; Varga, Z.; van der Pol, E.; van Herwijnen, M. J. C.; Wauben, M. H. M.; Wehman, A. M.; Williams, S.; Zendrini, A.; Zimmerman, A. J.; Théry, C.; Witwer, K. W. Minimal Information for Studies of Extracellular Vesicles (MISEV2023): From Basic to Advanced Approaches. *J Extracell Vesicles* **2024**, *13* (2). https://doi.org/10.1002/jev2.12404.

(30) Sverdlov, E. D. Amedeo Avogadro's Cry: What Is 1μg of Exosomes? *BioEssays* **2012**, *34* (10), 873–875. https://doi.org/10.1002/bies.201200045.

(31) Zendrini, A.; Guerra, G.; Sagini, K.; Vagner, T.; Di Vizio, D.; Bergese, P. On the Surface-to-Bulk Partition of Proteins in Extracellular Vesicles. *Colloids Surf B Biointerfaces* **2022**, *218*. https://doi.org/10.1016/j.colsurfb.2022.112728.

(32) Gordon, S. M.; Deng, J.; Lu, L. J.; Davidson, W. S. Proteomic Characterization of Human Plasma High Density Lipoprotein Fractionated by Gel Filtration Chromatography. *J Proteome Res* **2010**, *9* (10), 5239–5249. https://doi.org/10.1021/pr100520x.

(33) Takov, K.; Yellon, D. M.; Davidson, S. M. Confounding Factors in Vesicle Uptake Studies Using Fluorescent Lipophilic Membrane Dyes. *J Extracell Vesicles* **2017**, *6* (1). https://doi.org/10.1080/20013078.2017.1388731.

(34) Sun, Y.; Saito, K.; Saito, Y. Lipid Profile Characterization and Lipoprotein Comparison of Extracellular Vesicles from Human Plasma and Serum. *Metabolites* **2019**, *9* (11). https://doi.org/10.3390/metabo9110259.

(35) Wojczynski, M. K.; Glasser, S. P.; Oberman, A.; Kabagambe, E. K.; Hopkins, P. N.; Tsai, M. Y.; Straka, R. J.; Ordovas, J. M.; Arnett, D. K. High-Fat Meal Effect on LDL, HDL, and VLDL Particle Size and Number in the Genetics of Lipid-Lowering Drugs and Diet Network (GOLDN): An Interventional Study. *Lipids Health Dis* **2011**, *10*. https://doi.org/10.1186/1476-511X-10-181.

(36) Nandakumar, A.; Wei, W.; Siddiqui, G.; Tang, H.; Li, Y.; Kakinen, A.; Wan, X.; Koppel, K.; Lin, S.; Davis, T. P.; Leong, D. T.; Creek, D. J.; Ding, F.; Song, Y.; Ke, P. C. Dynamic Protein Corona of Gold Nanoparticles with an Evolving Morphology. *ACS Appl Mater Interfaces* **2021**, *13* (48), 58238–58251. https://doi.org/10.1021/acsami.1c19824.

(37) Swenson, H.; Stadie, N. P. Langmuir's Theory of Adsorption: A Centennial Review. *Langmuir* **2019**, *35* (16), 5409–5426. https://doi.org/10.1021/acs.langmuir.9b00154.

(38) Latreille, P. L.; Le Goas, M.; Salimi, S.; Robert, J.; De Crescenzo, G.; Boffito, D. C.; Martinez, V. A.; Hildgen, P.; Banquy, X. Scratching the Surface of the Protein Corona: Challenging Measurements and Controversies. *ACS Nano*. American Chemical Society February 22, 2022, pp 1689–1707. https://doi.org/10.1021/acsnano.1c05901.

(39) Röcker, C.; Pötzl, M.; Zhang, F.; Parak, W. J.; Nienhaus, G. U. A Quantitative Fluorescence Study of Protein Monolayer Formation on Colloidal Nanoparticles. *Nat Nanotechnol* **2009**, *4* (9), 577–580. https://doi.org/10.1038/nnano.2009.195.

(40) Li, Y.; Lee, J. S. Insights into Characterization Methods and Biomedical Applications of Nanoparticle-Protein Corona. *Materials*. MDPI AG July 1, 2020. https://doi.org/10.3390/ma13143093.

(41) Maffre, P.; Brandholt, S.; Nienhaus, K.; Shang, L.; Parak, W. J.; Nienhaus, G. U. Effects of Surface Functionalization on the Adsorption of Human Serum Albumin onto Nanoparticles - A Fluorescence Correlation Spectroscopy Study. *Beilstein Journal of Nanotechnology* **2014**, *5* (1), 2036–2047. https://doi.org/10.3762/bjnano.5.212.

(42) Musicò Ab !, A.; Zendrini Ab !, A.; Gimenez, S.; Cd, R.; Mangolini, V.; Paolini, L.; Romano, M.; Papait, A.; Silini, A. R.; Gianvincenzo, P. Di; Neva, A.; Cretich, M.; Parolini, O.; Almici, C.; Moya, S.; Radeghieri, A.; Bergese, P. Extracellular Vesicles Derived from

Mesenchymal Stromal Cells and Red Blood Cells Feature Distinct Biomolecular Corona Dynamics. https://doi.org/10.26434/chemrxiv-2024-65x2m-v2.

(43) Treuel, L.; Brandholt, S.; Maffre, P.; Wiegele, S.; Shang, L.; Nienhaus, G. U. Impact of Protein Modification on the Protein Corona on Nanoparticles and Nanoparticle-Cell Interactions. *ACS Nano* **2014**, *8* (1), 503–513. https://doi.org/10.1021/nn405019v.

Chapter 6: Extracellular vesicle-mediated delivery of Cisplatin and Cetuximab for multimodal therapy against triple-negative breast cancer

This work has been carried out thanks to the collaboration with ITB-CNR, University of Milan, Sapienza-University of Rome, IRCCS Maugeri, and University of Milan Bicocca, in the context of the PRIN project "Development of a biotechnological nanoparticle platform for the delivery of antitumor therapies using Patient Derived-organoid library of Breast cancer" (Italian Ministry of Education, University and Research, PRIN 2017, Grant No. 2017E3A2NR_004, Scientific coordinator: prof. D.Prosperi, University of Milano-Bicocca, Italy). Results presented in this work highlight the synergistic and multimodal anticancer mechanisms and effects of cisplatin-loaded and CTX surface-engineered EV (developed in Chapters 3 and 4).

6.1 Introduction

Triple-negative breast cancer (TNBC) is among the most aggressive subtypes of breast cancer, characterized by the absence of three key receptors: human epidermal growth factor receptor 2 (HER2), estrogen receptors (ER), and progesterone receptors (PR). This receptor profile makes TNBC resistant to many targeted therapies[1]. Recent research has demonstrated that TNBC is particularly sensitive to platinum-based drugs, such as carboplatin and cisplatin, due to defects in DNA repair pathways, specifically homologous recombination[2,3]. These drugs induce DNA damage by forming intra- and interstrand crosslinks, triggering apoptosis and cell death[2–4]. Among platinum-based therapies, cisplatin has been extensively studied for TNBC, both as a standalone treatment and in combination with other interventions, including surgery[5] and other chemotherapeutic agents like gemcitabine or paclitaxel[6]. Cisplatin is a small hydrophilic molecule that exerts its cytotoxic effects primarily in the nucleus. However, its efficacy in TNBC is often compromised by the activation of cellular resistance mechanisms, such as altered drug transport and detoxification processes, which can limit its nuclear accumulation and consequent cytotoxicity[7]. Recent findings have highlighted the potential of ferroptosis, a form of cell death driven by iron-dependent reactive oxygen species (ROS) accumulation and lipid peroxidation, to enhance TNBC's sensitivity to cisplatin[8,9]. Cisplatin interacts with reduced glutathione (GSH), disrupting glutathione peroxidase 4 (GPX4), an enzyme crucial for neutralizing lipid peroxides. This disruption shifts the cell's redox equilibrium, leading to oxidative stress and cell death via ferroptosis[1,5,6]. However, hypoxic conditions can inhibit ferroptosis through the stabilization of

hypoxia-inducible factor 1-alpha (HIF-1α), a transcription factor that TNBC cells often overexpress[7,10]. This overexpression is further amplified by epidermal growth factor receptor (EGFR) signaling, enabling TNBC cells to survive in hypoxic environments and resist cisplatin treatment.

Cetuximab (CTX, Erbitux®), an FDA-approved monoclonal antibody targeting EGFR[11–13], presents a promising strategy to overcome this resistance. By binding to EGFR's extracellular domain, CTX inhibits downstream signaling, potentially downregulating HIF-1α[13]. Combining cisplatin with CTX could therefore offer synergistic benefits, enhancing cisplatin's anti-tumor activity, overcoming resistance mechanisms[14], and promoting ferroptosis. However, current combination therapies administer cisplatin and CTX separately, which can result in overdosing and increased toxicity[15]. Nanotechnology offers a potential solution by co-delivering both agents within a single nanoplatform, improving selectivity and reducing off-target effects[16–18]. Biocompatible nano drug delivery systems (DDS) could further minimize systemic toxicity and avoid immune system activation.

In this context, extracellular vesicles (EVs) have emerged as promising nanocarriers due to their natural ability to transport biological molecules while being ‘’self’’ recognized by the body[19]. EVs are membrane-bound nanoparticles that encapsulate proteins, nucleic acids, and metabolites. Several EV types have been explored for cancer therapy, including the delivery of cisplatin via milk-derived EVs in resistant ovarian cancer models[20]. Among the various EV sources, red blood cell-derived EVs (RBC-EVs) are particularly advantageous because they lack oncogenic material, reducing the risk of tumorigenesis[21]. RBC-EVs can also be easily modified and, importantly, lack EGFR, preventing interference with CTX during surface engineering[22].

In this study, we developed a nanoplatform based on RBC-EVs loaded with cisplatin and surface-functionalized with CTX (^{CTX}RBC-EV$_{cispt}$). This platform displayed enhanced cisplatin uptake, increased cytotoxicity, and reduced chemoresistance by downregulating hypoxia-related genes, achieving superior results compared to the administration of free drugs. Moreover, the ^{CTX}RBC-EV$_{cispt}$ system mitigated ex vivo toxicity towards red blood cells, highlighting its potential as an innovative and effective therapeutic strategy for TNBC.

6.2 Experimental section

6.2.1 Production and separation of RBC-EVs

REV extraction and purification were conducted according to *Chapter 4.2.3.*

6.2.2 Biophysical and biochemical characterization of RBC-EVs

The purity of RBC-EVs for soluble contaminants and cellular residues was checked with the CONAN assay, following the protocol previously described[24,25]. Nanoparticle tracking analysis (NTA) was performed according to the manufacturer's instructions using a NanoSight NS300 system configured with a 532 nm laser. The samples were diluted 1:1000 in filtered PBS (0.22 μm) to a final volume of 1 mL to obtain the optimal particle per frame value (20–100 particles/frame). A syringe pump with constant flow injection was used (20 μL·min−1), and the temperature was set constant at 25 °C. Particles were detected at a camera level of 10 and three videos of 60 s were captured and analyzed with NTA software version 3.2. Atomic force microscopy (AFM) imaging was performed on a Nanosurf NaioAFM equipped with a Multi75-AI-G tip (Budget Sensors). For sample preparation, RBC-EVs were resuspended in 100 μL sterile H 2O (Milli-Q, Merck Millipore) and diluted 1:10 in H2O. 5 μL of the samples were then spotted onto freshly cleaved mica sheets (Grade V-1, thickness 0.15 mm, size 15 × 15 mm2) and dried at 50 °C for 10 minutes. Images were acquired in tapping mode, with a scan size ranging from 1.5 to 25 μm and a scan speed of 1 s per scanning line. Image processing was performed on Gwyddion ver. 2.61. Protein concentrations of RBC-EVs and RBC homogenate samples were determined with a Pierce™ BCA Protein Assay Kit (ThermoFisher, Rockford, USA), following the manufacturer's instructions. RBC-EV biochemical characterization was carried out with SDS-PAGE followed by Western Blot analysis. Samples were mixed with 6X Laemmli buffer and boiled for 5 min at 95°C. 30μg of proteins were separated by SDS-PAGE (10% polyacrylamide) and transferred onto a PVDF membrane. The blocking step was carried out with a 5% fat-free milk in PBS-0.05% Tween-20 (PBS-T) for 1h at 37°C. Membranes were incubated overnight at 4°C with the following primary antibodies diluted in 1% fat-free milk PBS-T: anti-BAND3 (1:1000, clone A-6, sc-133190, Santa Cruz Biotechnology, USA), anti-Flotillin (1:500, clone C-2, sc-74566, Santa Cruz Biotechnology, USA) and anti-Hemoglobin subunit β (HBB, 1:500, H00003043-M02A, Abnova, Taiwan). The membranes were washed thrice for 10 min with PBS-T and incubated for 1 h with rabbit anti-mouse HRP conjugated secondary antibody diluted 1:3000 in 1% fat-free milk PBS-T (Bethyl, TX, USA). Images were acquired with Chemibox Syngene.

6.2.3 Membrane engineering of RBC-EVs with Cetuximab

REVs were membrane-engineered according to *Chapter 4.2.11.*

6.2.4 Cisplatin encapsulation and quantification

200 μL of RBC-EVs or ^{CTX}RBC-EVs (2 x 1012 EVs/mL) were incubated with 200 μL of 1.4 mg/L cisplatin (Sandoz AG, Novartis, Switzerland) for 4h or 24h at 37°C in agitation. Cisplatin-loaded

RBC-EVs and ^{CTX}RBC-EVs (hereafter referred to as RBC-EV$_{cispt}$ and ^{CTX}RBC-EV$_{cispt}$, respectively) were rinsed to 1mL with PBS 1X without CaCl2 and MgCl2 (21-040-CV, Corning, USA) and ultracentrifuged at 100,000 xg for 2h (Optima MAX-XP centrifuge equipped with a TLA-55 rotor, Beckman Coulter, USA). The amount of platinum in RBC-EV$_{cispt}$ was measured by inductively coupled plasma mass spectrometry (ICP-MS) Elan DRC II (Perkin Elmer) employing the external calibration quantitative analysis method. The instrument was calibrated with a calibration curve of different platinum concentrations of 1-5-10 ppb, starting from the smart solutions O2Si Platinum standard solution at 1000 ppm in 5% HCl. Samples were diluted 1:1000 in distilled water. The intra-series coefficient of variation ranged between 4% and 8%, while the inter-series coefficient of variation varied between 2% and 6%. The detection limit was calculated with a 3x standard deviation of the blank and was established as 0.05 ppb. The measurement range spanned from 0.1 ppb to 500 ppb. Cisplatin concentration was calculated as (Platinum concentration, g/L x cisplatin molecular weight, g/mol) / Platinum molecular weight, g/mol). For the optimization of the protocol for cisplatin encapsulation, results from six different preparations were used and here expressed as mean ± SEM. For the comparison of cisplatin encapsulation between ^{CTX}RBC-EV$_{cispt}$ and RBC-EV$_{cispt}$, results from four different preparations were used and expressed as mean ± SEM.

6.2.5 Cell line and culture conditions

Human Triple-Negative Breast Cancer (TNBC) MDA-MB-231 cells (HTB-26, ATCC, USA) and the Her2-enriched Human Breast Cancer BT-474 cell lines were cultured in Dulbecco's Modified Eagle Medium with 4.5 g/L glucose, L-glutamine and sodium pyruvate (DMEM, 10-013-CV, Corning, USA) supplemented with 10% (v/v) fetal bovine serum (FBS, EU-000-500, Immunological Science, United Kingdom), 1% (v/v) penicillin/streptomycin (30-002-CI, Corning, USA) and hereafter referred to as complete media. Cells were maintained in a humidified 5% CO2 incubator at 37°C and routinely tested for mycoplasma contamination using the MycoBlue Mycoplasma Detection kit (D101, Vazyme, China).

6.2.6 Patient-derived organoids establishment

Two patients (patient #1 and patient #2) bearing TNBC and enrolled at the Breast Unit of ICS Maugeri IRCCS (Pavia, Italy) in the protocol of “Bruno Boerci Oncological Biobank” (ICS Maugeri IRCCS’s ethical committee approvation of 27 July 2009) between April 2019 and July 2020, were a 45 and a 60-years-old womans, respectively. Patient#1 [SM1] displayed an invasive ductal carcinoman of over 6 cm in right mammary gland and reported familiarity for breast and ovarian neoplasia, as confirmed by the presence of mutation on BRCA1 gene. Patient#1 has been

subjected to neoadjuvant chemotherapy (NAC) with 4 cycles of Epirubicin and Cyclophosphamide, and 12 cycles of paclitaxel and carboplatin followed by radical mastectomy. During surgery, a biopsy specimen was collected, analysed and used to establish PDO#1 culture. Pathological evaluations performed on this specimen confirmed the classification as invasive ductal carcinoma, with a Triple negative (TNBC) molecular subtype (Estrogen 0%, Progesterone 0%, Ki67 60%, c-erbB2 1+). Patient#2 [SM2] displayed a lesion of 21 mm classified as invasive ductal carcinoma, TNBC molecular subtype (Estrogen 0%, Progesterone 0%, Ki67 70%, c-erbB2 0) in right mammary gland and reported familiarity for breast and ovarian neoplasia, despite only the presence of a BRCA1 gene variant with unknown significance has been detected. During clip positioning, another biopsy specimen was collected, analysed and used to establish PDO#2 culture. The bioptic samples from patient #1 and #2 have been collected in Ad-DF +++ medium (Hyclone DMEM-F/12 1:1 supplemented with 10 mM HEPES, 1% Penicillin/Streptomicin and 1% L-glutamine) and stored at 4°C until processing. Then, were cut into 1-3 mm3 and two random pieces were fixed in formalin and embedded in paraffin to perform Hematoxylin and Eosin staining (H&E) and Immunohistochemistry (IHC) labelling by using routine procedures. Primary PDO#1 and PDO#2 cultures were obtained following the procedure described in a consolidated protocol. Briefly, the collected tissue was removed of the adipose tissue and mechanically and enzymatically digested in 10 mL Ad-DF +++ medium supplemented with 500 µL of Collagenase 20 mg/mL and 10 µL of Y27632 10 mM for 1-2 hours at 37°C. The sample was filtered to remove the undigested tissue, collected in a 15 mL tube and centrifuged. The pellet was washed twice and then resuspended in the appropriate amount of BME and seeded in a pre-warmed multi-well plate. Once BME-PDO drops were solidified, the appropriate amount of Culture medium (CM; DMEM/F12 1×, L-glutamine 1%, Penicillin/Streptomicin 1%, Hepes 10mM, Noggin conditioned medium 25×, B27 supplement 1×, N-acetyl-cysteine 1.25 mM, Nicotinamide 0.2 mM, A 83-01 500 nM, Y-27632 5 µM, R-spondin1 conditioned medium 10%, Primocin 50 µg/mL, Human EGF 5 ng/mL, FGF-10 Human recombinant 20 ng/mL, KGF/FGF-7 Human recombinant 5 ng/mL, Heregulin-beta-1 Human recombinant 37.5 ng/mL, SB 202190 500 nM) was added depending on the multi-well size, and changed every 2-3 days. Every 7-10 days when confluence was achieved, PDO#1 and PDO#2 cultures have been collected and passed. Each organoid culture has been frozen in Cell Culture Freezing medium (Gibco, 12648-010) and has been transferred to liquid nitrogen for long-term storage.

6.2.7 Patient-derived organoids characterization

BME-organoid drops were removed with a sterile cell lifter from the plate and transferred into a mould containing a layer of optimal cutting temperature compound (OCT). Once the drops were

included in OCT, the mould was kept at -80°C until processing. The OCT-embedded PDO were sectioned to obtain histological slices of about 3 µm thicknesses. After the fixation, the histological slides were stained with H&E, labelled with VENTANA, BenchMark ULTRA following automatized IHC protocols for Estrogen receptor, Progesterone receptor, c-ErbB2 (i.e. HER2) and Ki67. For the comparison between organoids and the tumour of origin, two random pieces of the surgical tissues were fixed in formalin and embedded in paraffin to perform H&E and IHC labelling by using routine procedures. For morphological Transmission Electron Microscopy (TEM) and Scanning Electron Microscopy (SEM) analysis, PDO#1 and PDO#2 has been processed and analysed as previously described. For immunofluorescence analysis, 3×106 organoids have been isolated from BME after a treatment with Dispase (1 µg/mL at 37°C for 1-2 hours). Then, PDOs were collected, washed in Phosphate buffer (PBS) thrice and fixed with Paraformaldehyde (PFA) 4% for 15 minutes at room temperature (RT). After the fixation, PDOs were washed in PBS thrice and then were permeabilized using Triton X-100 0.1% for 10 minutes at RT. After three washing, PDO pellets were resuspended in 500 µL of blocking solution containing 2% goat serum 2% Bovine Serum Albumin (BSA) in PBS 1X for 1 hour at RT. PDOs were incubated with the primary antibodies in blocking solution for 2 hours at RT. We have used the following primary rabbit antibodies directed to Ki67 (Abcam ab243878, 1:500), EGFR (Genetex GTX35199, 1:200), Vimentin (Genetex GTX100619, 1:500) and HER-2 (Cell Signalling Technologies #2165, 1:200) molecules. PDOs were washed thrice in PBS and incubated with the secondary antibody anti-Rabbit Alexa Fluor 546 (1:300), Wheat Germ Agglutinin FITC (1:300), DAPI (1:10000) in blocking solution overnight at 4°C. After the staining, PDOs were washed three times in PBS 1× and seeded on specimen slide in mounting medium ProLongTM Gold (Invitrogen, P36935) for the acquisition with the Leica confocal microscope SP8 equipped with 405, 488 and 513 nm lasers. Acquisition has been performed at 1024×1024 dpi resolution. For CD24, CD44, CD49f and EPCAM staining, 3×106 organoids have been isolated from BME by incubating them with Dispase 1 µg/mL. Once collected, PDO have been reduced into single cells through the shearing procedure using TrypLeTM Select (1×; Gibco, 12563-029). After three washes with Hank's Balanced Salt Solution (HBSS from HyClone), SH30268.02), the cells were fixed with PFA 4% for 5-10 minutes in ice. Fixed cells have been washed thrice with HBSS supplemented with FBS 2% and aliquoted into four tubes containing about 7.5 × 105 cells each. The first tube has been labelled with the Lineage PE cocktail of antibodies (PE mouse anti-human CD2, Cod. 555327, 1:100; PE mouse anti-human CD3, Cod. 555333, 1:00; PE mouse anti-human CD10, Cod. 555375, 1:100; PE mouse anti-human CD16, Cod.555407, 1:100; PE mouse anti-human CD18, Cod. 555924, 1:100; PE mouse anti-human CD31, Cod. 555446, 1:100; PE mouse anti-human

CD64, Cod. 558592, 1:100; PE mouse anti-human CD140b, Cod. 558821, 1:100; BD Biosciences) for 15 min at RT to set the gate of lineage positive cells, which should be excluded from the analysis. The second tube contains only unstained cells, to acquire negative signals. A third tube has been labelled 15 min at RT with lineage cocktail, FITC mouse anti-human CD24 (Cod. 555427, 1:50, BD Biosciences) and APC mouse anti-human CD44 (Cod. 559942, 1:50, BD Biosciences), to identify CD24/CD44 cell population, while the fourth tube has been labelled with lineage cocktail, supplemented with FITC rat anti-human CD49f (Cod. 555735, 1:50, BD Biosciences) and APC mouse anti-human EPCAM (Cod. 347200, 1:100, BD Biosciences), to identify CD49f/EPCAM populations. After the staining, labeled cells were washed thrice with HBSS supplemented with FBS 2% and analyzed using CytoFLEX flow cytometer (Beckman Coulter). The acquisition was performed on 20,000 events, within the selected region of singlet viable cells. For EGFR evaluation, 1.5×106 organoids were isolated from BME, reduced into single cells, and fixed with 4% paraformaldehyde (PFA, 76240, Thermo Fisher Scientific, USA) for 5 minutes at 4°C. Cells were washed thrice with HBSS supplemented with FBS 2% and were transferred into two tubes containing about 7.5×105 cells for each. A tube was labeled with the primary chimeric monoclonal antibody Cetuximab (CTX, 1:200) for 15 min at RT. Labeled cells were washed thrice with HBSS supplemented with FBS 2%. Both tubes were labelled with the AlexaFluor488 (AF488) goat anti-Human secondary antibody (ThermoFisher, 1:300). The tube containing cells labelled with only the secondary antibody was used to set the region of positivity. After the staining, labeled cells were washed thrice with HBSS supplemented with FBS 2% and analyzed as described above.

6.2.8 Labelling of RBC-EV preparations

RBC-EV preparations were labelled with MemGlow™ 488 (MG01-10, Cytoskeleton Inc., USA) as previously described[26]. Briefly, RBC-EV samples were incubated with 100 nM MemGlow™ 488 for 30 minutes at room temperature (RT). Excess of free probe was removed by ultracentrifugation at 100,000 xg for 2 hours at 4°C (Optima MAX-XP equipped with a TLA-55 rotor, Beckman Coulter, USA).

6.2.9 Assessment of EGFR expression on MDA-MB-231 cells

2×106 MDA-MB-231 cells and 2×106 of BT-474 cells (used as control for low EGFR expression) were harvested and fixed with 4% paraformaldehyde (PFA, 76240, Thermo Fisher Scientific, USA) for 5 minutes at 4°C. Cells were washed in PBS for three times and the pellet was resuspended in PBS, 2% Bovine Serum Albumin (BSA, A2153, Sigma-Aldrich, USA), 2% goat serum (G9023, Sigma-Alrdich, USA). About 5×105 of fixed cells were transferred in tubes and

immunodecorated with the anti-EGFR antibody (Cetuximab, CTX, 1 µg/tube;) in Phosphate buffer (PBS), 2% Bovine Serum Albumin (BSA; Sigma) and 2% goat serum (Euroclone) for 30 min at RT. Then, cells were washed thrice with PBS and immunodecorated with Alexa Fluor 488 goat anti-human secondary antibody (1 µL/tube; Thermo Fischer Scientific) in PBS, 2% BSA and 2% goat serum for 30 min at RT. After three washes with PBS cells (n=3) were analyzed by CytoFLEX flow cytometer (Beckman Coulter). 20,000 events were acquired for each analysis, after gating on viable cells and on singlets. A sample of cells immunodecorated with the secondary antibody only was used to set the region of positivity.

6.2.10 Cellular RBC-EV uptake studies in 2D cell culture system by confocal imaging

For imaging analysis, MDA-MB-231 cells were seeded onto 12 mm-sized coverslips pre-coated with 50 µg/mL collagen (TB03, Clinisciences, France) as 300000 cells/coverslip (26549 cells/cm2) placed in 12-well tissue culture plates (ET3012, Euroclone, Italy). After 24h, cells were treated MemGlow488-labelled-RBC-EVs, ^{CTX}RBC-EVs, RBC-EV$_{cispt}$, and ^{CTX}RBC-EV$_{cispt}$ for 4h and 24h in 1 mL of complete media. For the investigation of the comparison of RBC-EVs and ^{CTX}RBC-EVs uptake, the following RBC-EV and CTX final concentrations were used: 6.2x1010 RBC-EVs (corresponding to 1.8x1010 EVs/cm2) and 35 nM CTX. For the comparison of RBC-EV$_{cispt}$ and ^{CTX}RBC-EV$_{cispt}$ uptake, the followings: 7.3x1010 RBC-EVs (corresponding to 2.7x1010 EVs/cm2), 5µM cisplatin and 22 nM CTX. Cells were washed twice with PBS without CaCl2 and MgCl2 (21-040-CV, Corning, USA) and fixed with a 3% paraformaldehyde (PFA, 76240, Thermo Fisher Scientific, USA) solution for 15 min at RT. PFA was quenched with 50 mM NH4Cl for 10 minutes at RT. The cells were washed twice with PBS 1X and permeabilized with 0.3% saponin (47036, Thermo Fisher Scientific, USA) in PBS 1X (PBS-S) for 10 minutes at RT. Intracellular hemoglobin was stained with anti-HBB antibody diluted 1:50 (H00003043-M02A, Abnova, Taiwan) in PBS-S for 1 hour at RT. The coverslips were washed twice with PBS-S and incubated with the AlexaFluor 647-secondary antibody Rabbit anti-Mouse diluted 1:400 (IS20285-1, Immunological Sciences, United Kingdom) and DAPI diluted 1:600 in PBS-S (D3571, Invitrogen, USA) for 30 minutes at 37°C. Coverslips were washed twice with PBS 1X and once with double-distilled water (ddH2O), and finally mounted with ProLong™ Gold Antifade Mountant (P36934, Invitrogen, USA). 1024 × 1024 pixel images were acquired with a Zeiss LSM 900 confocal microscope with a Plan-Apochromat 63×/1.4 Oil DIC or EC Plan-Neofluar 40x/1.3 Oil DIC objectives, with a 0.2% 405 nm laser for DAPI, 0.2% 488 nm laser for MemGlow™ 488 and 0.4% 633 nm laser for AlexaFluor 647-secondary antibody.

6.2.11 Cell binding assay

5×105 MDA-MB-231 cells were incubated 2 h at 4°C in Phosphate buffer (PBS), 2% Bovine Serum Albumin (BSA; Sigma) and 2% goat serum (Euroclone) supplemented with 109 or 1010 RBC-EV/mL, 109 or 1010 CTXRBC-EV/mL or CTX free (2.43nM or 24.3 nM) in 5 mL tubes. RBC-EVs were fluorescent-labelleb with Memglow88, while CTX free or conjugated to RBC-EVs were labelled with Cy7.5, as previously described. Then, cells were washed thrice with PBS and cells were analyzed by CytoFLEX flow cytometer (Beckman Coulter). 20,000 events were acquired for each analysis, after gating on viable cells and on singlets. Samples of untreated cells were used to set the regions of positivity.

6.2.12 Competition assay

5×105 MDA-MB-231 cells/sample were incubated 1 h at 4°C with 2.8 uM of free unlebelled CTX as competitor (1 mL) in PBS supplemented with 0.3% BSA. Then, cells were centrifuged to remove unbound CTX and were incubated with Cy7.5-labelled CTX or Cy7.5-labelled ^{CTX}RBC-EV for 1h at 4°C. At the end of incubation, cells were washed thrice, resuspended in PBS (500 µL) and analyzed by CytoFLEX flow cytometer (Beckman Coulter). 20,000 events were acquired for each analysis, after gating on viable cells and on singlets. A sample of untreated cells was used to set the appropriate gates.

6.2.13 Cellular cisplatin uptake studies in 2D and 3D cell culture systems

For cisplatin uptake analysis in 2D culture conditions, MDA-MB-231 cells were seeded into collagen-precoated 35 mm tissue culture dishes (ET2035, Euroclone, Italy) as 22500 cells/cm2. After 24h, cells were washed once with PBS 1X without CaCl2 and MgCl2 and treated for 30 min and 24h with RBC-EV$_{cispt}$, ^{CTX}RBC-EV$_{cispt}$, and cisplatin in 2 mL of complete media. Treatments were carried out using the following final concentrations: 5.6 x 1010 RBC-EVs/mL (corresponding to 1.4x1010 EVs/cm2), 5µM cisplatin and 11.5 nM CTX. Cells were washed once with PBS 1X without CaCl2 and MgCl2 and harvested using 0.25% trypsin-EDTA solution (25-053-CI, Corning, USA). Cells were counted with a Burker chamber and centrifuged twice at 800 xg for 10 minutes at 4°C (5417C, Eppendorf, Germany). The obtained pellets were digested with 200 µL of HNO3 and 200 µL of ddH2O and incubated at 70°C for 1h. The digested pellets were diluted 1:50 and measured with ICP-MS as previously described. Data from three independent experiments are expressed as mean ± SEM.

6.2.14 Subcellular fractionation

MDA-MB-231 cells were seeded into collagen-precoated 35 mm tissue culture dishes as 22500 cells/cm2. After 24h, cells were washed once with PBS 1X without CaCl2 and MgCl2 and treated

in triplicate for 24h with RBC-EV_{cispt}, cisplatin and ^{CTX}RBC-EV_{cispt}. Treatments were carried out using the following final concentrations (final volume of 2 mL): 7.3 x 1010 EVs/mL (corresponding to 1.8x1010 EVs/cm2), 5µM cisplatin and 19.5 nM CTX. Cellular fractioning was carried out following the procedure described in Alvisi, G., et al. Briefly, cells were washed twice with cold PBS 1X without CaCl2 and MgCl2, scraped and spinned for 10 seconds at 4°C. Pellets were resuspended in 100 µL of PBS 1X containing 0.1% NP-40 (A1694, PanReac Applichem, USA). 20µL of the whole homogenate was used for Western Blot analysis. Samples were further centrifuged for 10 seconds and 80 µL of the supernatant, corresponding to the cytoplasm fraction, was transferred into a new tube: 50µL were used for ICP-MS measurements while 30 µL for Western Blot analysis. Pellets were washed once with PBS 1X containing 0.1% NP-40 and spinned down for 10 seconds. Pellets, corresponding to the nuclear fraction, were resuspended in 80 µL of PBS 1X containing 0.1% NP-40: 50µL were used for ICP-MS measurements while 30 µL for Western Blot analysis. For ICP-MS, the platinum content was measured by diluting the sample 1:50 and digested with 200 µL of HNO3 and 200 µL of ddH2O. Samples were incubated at 70°C for 1h and diluted 1:50 with ddH2O. Data are expressed as mean ± SD. For Western Blot analysis, fractions were heated in 6X Laemmli buffer and separated by SDS–PAGE on acrylamide/bisacrylamide gels and then transferred onto a PVDF membrane as described above. The following secondary antibodies were used: α-LAMP-1 (1:500, Clone H4A3, sc200-11, Santa Cruz Biotechnology Inc., USA) for the cytoplasmatic fraction, α-lamin A/C (1:1000, mab636, Thermo Fisher Scientific, USA) for the nuclear fraction and anti-HBB (1:500, H00003043-M02A, Abnova, Taiwan) to confirm hemoglobin uptake.

6.2.15 3-(4,5-dimethylthiazol-2-yl)-2,5-diphenyl-2H-tetrazolium bromide (MTT) assay

MDA-MB-231 cells were seeded in 96-well plates in complete media as 15000 cells/cm2. After 24h, cells were treated in quadruplicate for 4h and 24h with RBC-EV preparations, cisplatin, and CTX. Treatments were carried out using the following average concentrations in 0.1 mL: 6.2 x 1010 EVs/mL (corresponding to 1.94 x 1010 EVs/cm2), 5µM cisplatin, and 15 nM CTX. After the treatments, 0.01mL of the 5 mg/mL MTT solution (M2128-1G, Sigma-Aldrich, USA) was added and the cells were further incubated for 4h. The formazan crystals were dissolved with 0.1 mL of DMSO (276855, Sigma-Aldrich, USA) and the absorbance was measured with Ensight MultiMode Reader (Perkin Elmer) at 595 nm. The absorbance values of the blank solution (DMSO) were removed from each sample. Cell viability percentage was calculated as follows: (Abs595 treated cells/ Abs595 untreated cells) x 100. Data from three independent experiments are expressed as mean ± SEM. The dose- and time-dependent cytotoxicity assessment of all the

building blocks (namely, cisplatin and cetuximab as free drugs and RBC-EVs) were performed at the reported concentrations and time as mentioned above.

6.2.16 RNA-seq library preparation and bioinformatic data analysis

MDA-MB-231 cells were seeded into 35 mm tissue culture dishes as 22500 cells/cm2. After 24h, cells were treated for 24h with 4.6 x 1010 RBC-EVs/mL, 4.6 x 1010 RBC-EV_{cispt}/mL (5µM cisplatin), 4.6 x 1010 ^{CTX}RBC-EV_{cispt}/mL (5µM cisplatin e 7.7 nM CTX), 4.6 x 1010 ^{CTX}RBC-EVs/mL (7.7 nM Cetuximab), 7.7 nM Cetuximab, 5 µM Cisplatin, and a mix of 7.7 nM cetuximab + 5 µM Cisplatin in 2mL for each treatment. Each treatments were carried out in triplicate. Then, cells were detached using 0.25% trypsin-EDTA solution, washed in PBS 1X and centrifuged at 1000 xg for 5min. Pellets were snap-frozen in dry ice and stored at -80°C until use. For each treatment condition, total RNA was extracted by using RNeasy Mini Kit (Qiagen, Hilden, Germany), according to the manufacturer's protocol, and treated with RNase-free DNAse I (ThermoFisher Scientific, Waltham, MA, USA). RNA samples were checked for quality on Agilent 2200 TapeStation System (Agilent Technologies, Santa Clara, CA, USA) and quantified by Qubit 4 Fluorometer using the Qubit RNA HS Assay Kit (ThermoFisher, Invitrogen). Starting from 400 ng of each isolated RNA, RNA-seq libraries were prepared using the Illumina TruSeq Stranded mRNA Library Prep Kit (Illumina, San Diego, CA, USA), according to manufacturer's instructions. Each library was checked on Agilent 2200 TapeStation System (Agilent Technologies) and quantified by Qubit 4 Fluorometer using the Qubit DNA HS Assay Kit (ThermoFisher). Sequencing was carried out in 2×150-cycle runs on Illumina HiSeq4000 platform. Three independent biological replicates were prepared and sequenced for each condition. After fastq quality control by using FastQC tool (v.0.11.8), raw reads were trimmed to 100 bases and mapped to the human reference genome using STAR aligner (v.2.7.10a)[27]. Gene counts were calculated by HTSeq package (v.0.11.1)[28], using the hg38 Encode-Gencode GTF file (v39) as gene annotation file. Differential gene expression analysis was carried out using DESeq2 Bioconductor/R package (v.1.30.1)[29]. RUVSeq R package (v.1.24.0) was used for batch effect removal[30]. Low-expressed genes (sum of read counts across all samples < 10), as well as outlier samples, were filtered out before testing genes for statistical significance. A |log2FC| > 1 and adjusted p-value (padj, Benjamini-Hochberg (BH) correction) < 0.1 were used as a cut-off to define statistically significant differentially expressed genes (DEGs). ClusterProfiler R package (v.4.6.2) was used to perform functional enrichment over-representation analysis (ORA) on Gene Ontology Biological Process (GO-BP) categories and biological pathway collections (KEGG, Reactome, WikiPathways, MSigDB hallmark gene sets)[31]. A false discovery rate (FDR, BH correction) < 0.05 was applied to all the annotation terms to define statistically significant

enrichments. Raw sequence data are available in NCBI Short Reads Archive (SRA) under Accession Number PRJNA1067532.

6.2.17 3D cytotoxicity assay

To establish a cells viability assay, the organoids have been sheared 2-3 days before the seeding to obtain smaller and uniform in size PDOs. The organoids were isolated from BME by Dispase treatment, collected in 15 mL tube and they were washed twice with Ad-DF +++. The PDOs were counted, diluted in CM containing 10% BME and seeded 10.000 cells/well in a 96-wells spheroid microplate (Corning, 4520) at the concentration of 200 cells/µL. After 24 hours, 4 different concentrations of Cetuximab (Erbitux® 5mg/mL, Merck) and of Cisplatin (1 mg/mL, Sandoz) (both ranging from 0.5 nM to 200 nM) were added in 10 replicates. Untreated cells were used as negative control. After 3 days of expansion at 37°C and 5% CO2, the Cell Titer Glo 3D Kit (Promega, G9682) was used, according manufacturer's instructions, to measure the ATP content as an indicator of cell viability. Emitted luminescence was read in microplate reader (PerkinElmer, Victor Nivo Multimode) and data were analysed using GraphPad Prism 8.

6.2.18 Ex vivo cisplatin toxicity assessment on red blood cell morphology

RBC concentrates were extracted from a healthy donor (0+) and stored at 4°C. $6.23x10^9$ RBCs were incubated with cisplatin (5µM and 25µM), $5.5x10^{10}$ ^{CTX}RBC-EV_{cispt}/mL (5µM cisplatin, 20 nM CTX) for 3 hours in 1mL final volume. After incubation, the blood smear was performed, and RBCs were fixed on the glass slides in 100% ethanol for 5 minutes. PBS was used as vehicle. RBC morphologies after treatments were examined at 20x magnification with a Axio Vert microscope. Cell counting was performed with Fiji software and the relative percentage of RBC morphologic alterations were calculated as follow: (Number of RBCs with a specificic morphology/Total counted RBCs) x 100. Data are expressed as mean ± SD[32].

6.2.19 Statistical analysis

For cisplatin loading optimization, statistical analysis was performed using GraphPad Prism software with an unpaired t-test, with a two-sided p-value calculations (95% confidence interval, statistical significance when $p < 0.05$). For MDA-MB-231 cytotoxicity screening and cisplatin uptake, statistical analysis was performed using the ordinary one-way ANOVA with Tukey's multiple comparison tests, with a single pooled variance. For the dose- and time-dependent cytotoxicity assessment of all the building blocks, statistical analysis was performed using the ordinary two-way ANOVA with Tukey's multiple comparison test. For EGFR expression statistical significance was determined by two-tailed unpaired Student's t-test with Welch's correction. For

binding and competition assay significance was determined by ordinary one-way ANOVA corrected with Sidak's multiple comparison tests. Drug screening results have been analyzed by ordinary one-way ANOVA performing Dunnett's multiple comparison test, analyzing both the effect of drug and organoid type. Statistics was evaluated using GraphPad Prism 8.0a version (GraphPad Software Inc., La Jolla, USA). Data are reported as mean ± Standard Error Mean (SEM). The level of statistical significance was set at $p = 0.05$.

6.3 Results and Discussion

6.3.1 Cisplatin encapsulation in RBC-EVs via co-incubation method

Red Blood Cell-derived EVs (RBC-EVs) were produced upon induction with calcium and calcium ionophore and characterized according to their biochemical and biophysical properties, following MISEV2018 and MISEV2023 guidelines[33,34]. RBC-EVs were enriched in typical RBC-markers, such as Band 3 anion transport protein, hemoglobin (subunit β, HBb), and the EV-marker flotillin-1 (Fig. 1.6A). COlorimetric NANoplasmonic (CONAN) assay revealed that RBC-EV preparations contained a negligible amount of soluble non-EV associated proteins (SAPs), and therefore considered as pure from free contaminants (AI ≤ 20%, Fig. 1.6B). From ≈300 mL, we obtained RBC-EV preparations with an average protein concentration of 703 μg/mL ± 123 μg/mL, while Nanoparticle Tracking Analysis (NTA) confirmed the presence of 2.4×10^{12} EVs/mL ± 5.0×10^{10} EVs/mL, with a mean diameter of 193 nm ± 7.3 nm (Fig. 1.6C).

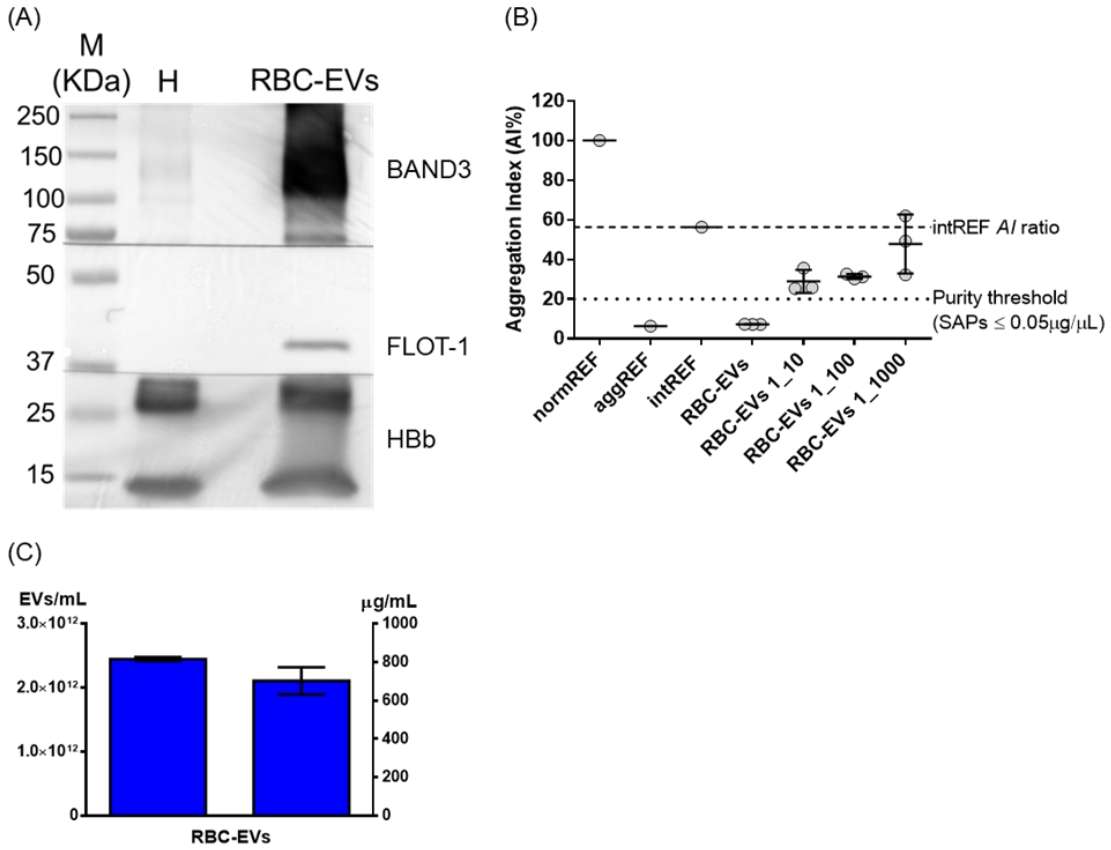

Figure 1.6: Biophysical and biochemical characterization of RBC-EVs. A) Western blot analysis demonstrating the expression of proteins related to RBA-EVs; H = RBC homogenate (30µg), B) CONAN assay on RBC-EV formulation at different dilutions; C) Q quantitative analysis of protein and nanoparticle concentration, represented in bar graphs.

Subsequentially, we optimized cisplatin loading into RBC-EVs by a co-incubation reaction at 37°C for both 4h and 24h in agitation, adapting protocols previously described for other hydrophilic drugs[20,35–37]. Cisplatin loading yield per EVs was calculated by Inductively Coupled-Plasma Mass Spectrometry (ICP-MS, Fig. 2.6A). We obtained a statistically significant 3-fold increase in cisplatin loaded amount after 24h co-incubation compared to the 4h co-incubation (4.4 x 10-14 µmol cis/EV for 4h vs. 1.4 x 10-13 µmol cis/EVs for 24h co-incubation, Fig. 2.6B). Considering this, we decided to continue using the 24-hour incubation period. We compared RBC-EVs and RBC-EV$_{cispt}$ morphology and size distributions by Atomic Force Microscopy (AFM) imaging and NTA, respectively. AFM imaging revealed the presence of round-shaped nanoparticles in both RBC-EV samples and the absence of broken vesicles or lipid-debris in RBC-EV$_{cispt}$ preparation (Fig. 2.6C). Both RBC-EVs and RBC-EV$_{cispt}$ showed similar size distribution profiles (Fig. 2.6D), although it was possible to observe bigger NPs in RBC-EV$_{cispt}$ formulation and the mean diameter shifted from 193 nm ± 7.3 nm for RBC-EVs to 218 nm ± 9 nm for RBC-EV$_{cispt}$. The shift of the size distribution profiles and consequently of the mean diameter for RBC-EV$_{cispt}$ could be due to

the process of cisplatin loading which might cause restructuring of the lipid bilayer, leading to vesicle shape changes and, consequently, larger apparent size[37].

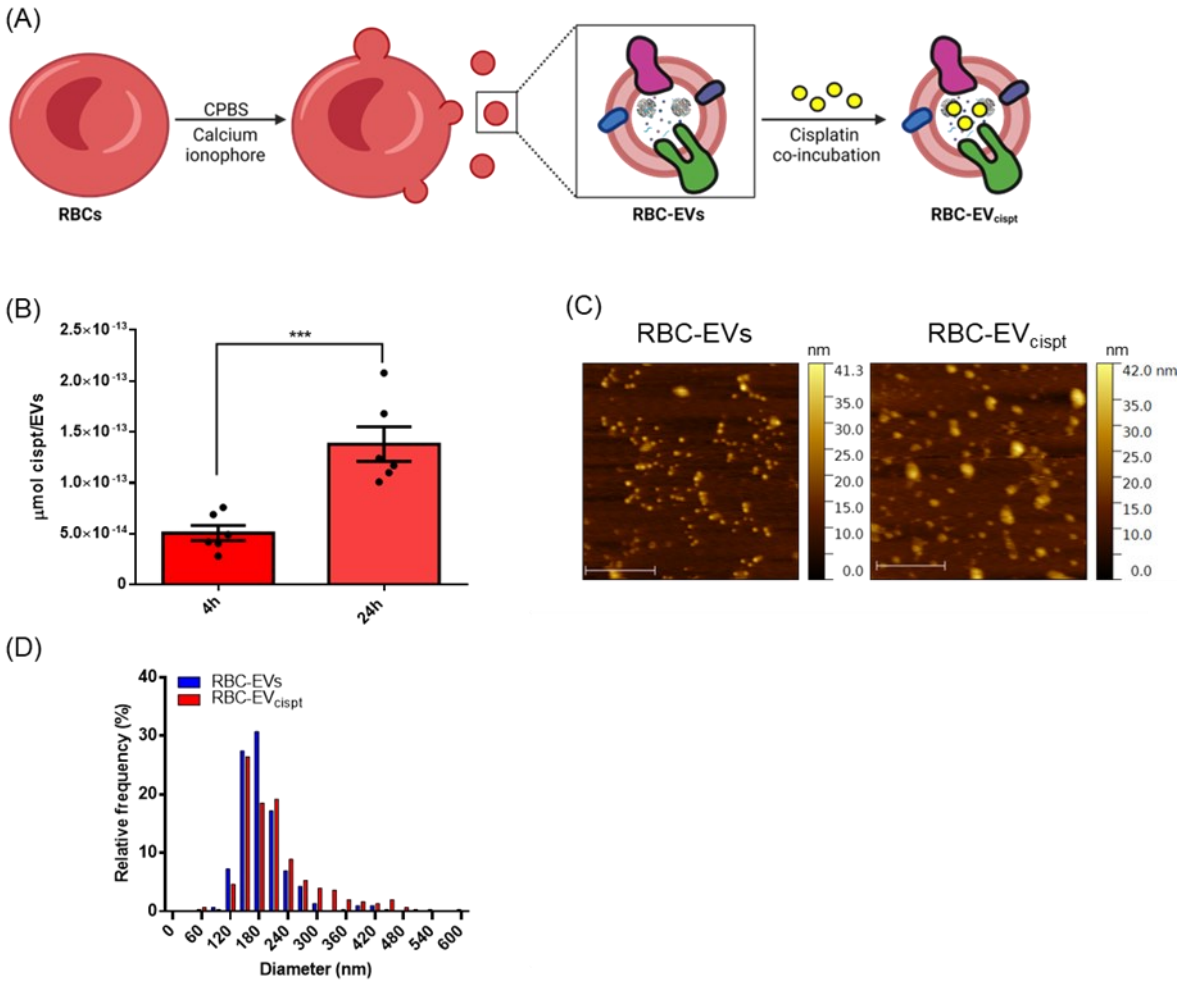

*Figure 2.6: Characterization of cisplatin-loaded RBC-EVs. (A) Scheme on the production of RBC-EV$_{cispt}$ via co-incubation method carried out at 37°C for 4 and 24 hours. (B) Comparison between the 4h- and 24-hour incubation in RBC-EV$_{cispt}$ in terms of cisplatin encapsulation yield. Unpaired t-test: $p < 0.05$, ***$p = 0.0008$. (C) Representative AFM images of RBC-EVs and RBC-EV$_{cispt}$ after 24 hours co-incubation with cisplatin. Scale bar 1µm. (D) Size distributions of RBC-EVs and RBC-EV$_{cispt}$ after 24 hours co-incubation with cisplatin obtained with NTA measurements. (E) Release pattern of Cisplatin from cisplatin and RBC-EV$_{cispt}$. N = 3*

6.3.2 Membrane engineering of RBC-EVs with cetuximab

In parallel with cisplatin encapsulation, we set up RBC-EV functionalization with the monoclonal antibody CTX, as sketched in Figure 3.6A. CTX was added onto RBC-EV membrane (^{CTX}RBC-EVs) using a click chemistry approach as we have previously described (Chapter 3 and [22]). CTX was functionalized with the fluorophore Cy7.5 and with a DBCO group by coupling between primary amines and activated esters. The functionalization process led to a yield of approximately 220 ± 70 CTX molecules *per* EV (Fig. 3.6B). This was determined by measuring the fluorescence of the Cyanine7.5 fluorophore, which was attached to the cetuximab on RBC-derived EVs after

SDS-PAGE analysis, and by using NTA to determine the number of EV particles. To test ^{CTX}RBC-EV EGFR-targeting ability, we first confirmed the overexpression of EGFR in MDA-MB-231 TNBC cell line model by flow cytometry (Figure 3.6C), which resulted in being significantly different ($p= 0.0009$) compared with a negative control (NC) constituted of BT-474 cells. Both pristine RBC-EVs and ^{CTX}RBC-EVs were previously labeled with Memglow488, a fluorogenic, non-toxic membrane probe that fluoresces exclusively upon integration into biological membranes[38]. Cells were incubated for 2 h at 4°C with two different amounts of RBC-EVs (i.e. 1×10^9 EVs/mL and 1×10^{10} EVs/mL). RBC-EV at both tested concentrations were able to recognize whole MDA-MB-231 cells as evidenced by the ≈100% of recognition displayed in Fig. 3.6D. However, when we considered the values of mean fluorescence intensity (MFI), a specific and dose-dependent contribution of CTX functionalization was evidenced (Fig. 3.6E). To date, it seemed clear that a quote of unspecific binding occurred since RBC-EVs could bind and recognize MDA-MB-231 cells even in absence of CTX functionalization. Considering that, we have tried to define if the CTX on ^{CTX}RBC-EVs was fully engaged in EGFR recognition performing a binding assay tracking the Cy7.5 added to the CTX as previously described. As a control, free CTX was used in the same amount. Flow cytometry results evidenced that CTX on ^{CTX}RBC-EVs was able to mark only a limited percentage of cells, despite in a dose-dependent manner (Fig. 3.6F). Moreover, at the highest concentration, the CTX on ^{CTX}RBC-EVs was more efficient in MDA-MB-231 binding than free CTX (Fig. 3.6G). To define the specificity of this CTX-mediated binding, we performed a competition assay using free unlabeled CTX as competitor. Flow cytometry results summarized in Fig. 3.6I evidenced that in the fraction of ^{CTX}RBC-EVs bound to MDA-MB-231 cells, there was almost a complete binding depletion in the presence of 100-fold molar excess of CTX, suggesting that the interaction between ^{CTX}RBC-EVs and the cells was specifically mediated by EGFR (Fig. 3.6H). To assess RBC-EV uptake by MDA-MB-231 cells, both pristine RBC-EVs and ^{CTX}RBC-EVs were labeled with Memglow488. Given Memglow488 rapid diffusion into biological membranes, we also assessed RBC-EV uptake by analyzing the intracellular fluorescence signal resulting from the hemoglobin delivered by RBC-EVs. MDA-MB-231 cells were treated with Memglow488@RBC-EVs and Memglow488@^{CTX}RBC-EVs for 4 h and 24 hours. In both cases, a distinct intracellular fluorescence distribution was noticed concerning both Memglow488 and hemoglobin, with the former diffused throughout the cytoplasm, while the latter was visible as distinct dots (Fig. 3.6I).

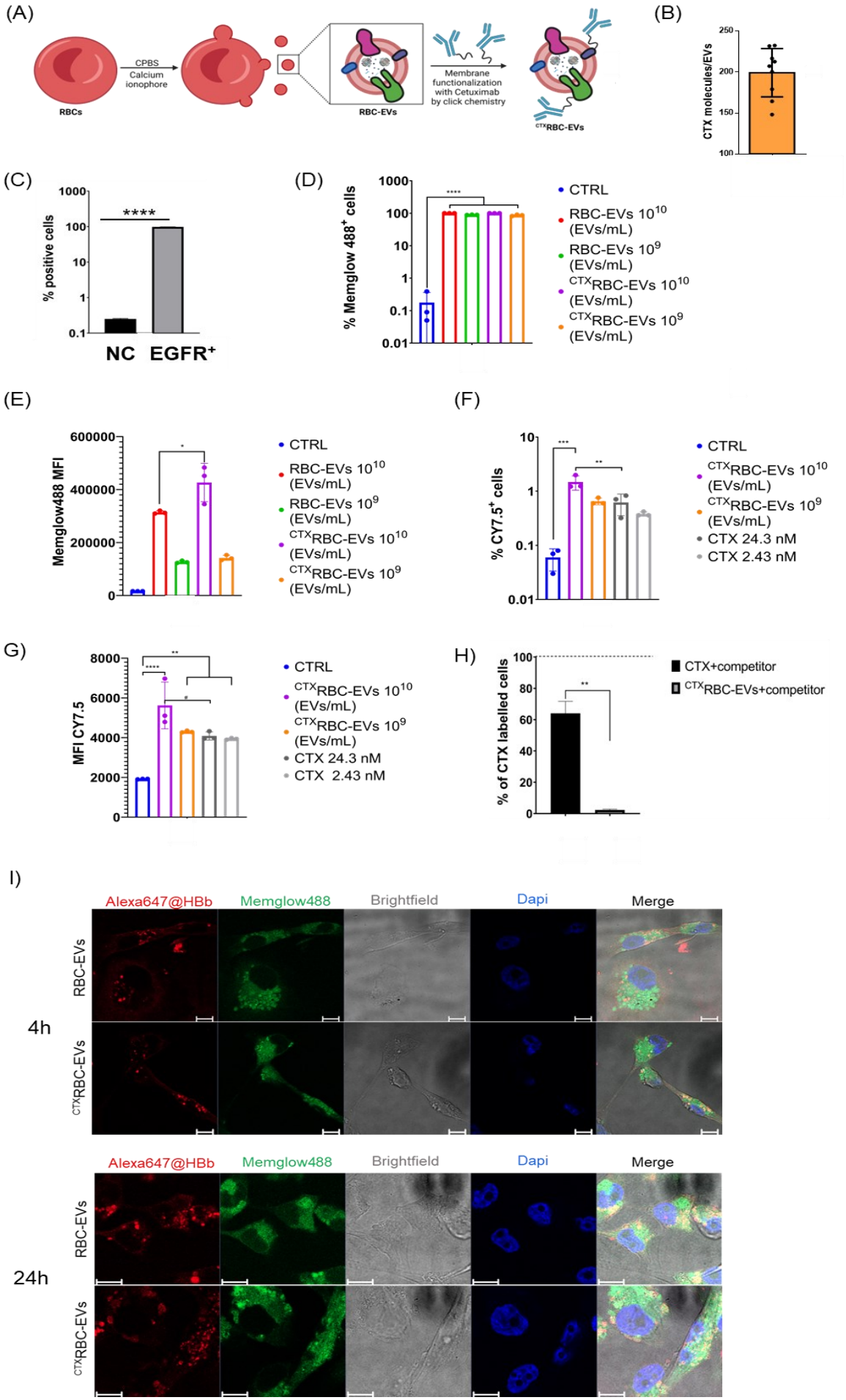
(A)
RBCs
CPBS
Calcium ionophore
RBC-EVs
Membrane functionalization with Cetuximab by click chemistry
CTXRBC-EVs
(B)
CTX molecules/EVs
250
200
150
100
(C)
% positive cells
1000
100
10
1
0.1
****
NC
EGFR+
(D)
% Memglow 488+ cells
1000
100
10
1
0.1
0.01
****
CTRL
RBC-EVs 10^10 (EVs/mL)
RBC-EVs 10^9 (EVs/mL)
CTXRBC-EVs 10^10 (EVs/mL)
CTXRBC-EVs 10^9 (EVs/mL)
(E)
Memglow488 MFI
600000
400000
200000
0
*
CTRL
RBC-EVs 10^10 (EVs/mL)
RBC-EVs 10^9 (EVs/mL)
CTXRBC-EVs 10^10 (EVs/mL)
CTXRBC-EVs 10^9 (EVs/mL)
(F)
% CY7.5+ cells
10
1
0.1
0.01
***
**
CTRL
CTXRBC-EVs 10^10 (EVs/mL)
CTXRBC-EVs 10^9 (EVs/mL)
CTX 24.3 nM
CTX 2.43 nM
G)
MFI CY7.5
8000
6000
4000
2000
0
**
****
*
CTRL
CTXRBC-EVs 10^10 (EVs/mL)
CTXRBC-EVs 10^9 (EVs/mL)
CTX 24.3 nM
CTX 2.43 nM
H)
% of CTX labelled cells
100
80
60
40
20
0
**
CTX+competitor
CTXRBC-EVs+competitor
I)
Alexa647@HBb
Memglow488
Brightfield
Dapi
Merge
4h
RBC-EVs
CTXRBC-EVs
24h
RBC-EVs
CTXRBC-EVs

Figure 3.6: Characterization and in vitro uptake experiments of ^{CTX}RBC-EVs on MDA-MB-231 TNBC cells. (A) Sketched scheme of the workflow followed for the production of ^{CTX}RBC-EVs via biorthogonal click-chemistry. (B) CTX amount determination on the surface of RBC-EVs after click chemistry reaction. (C) Analysis of mean EGFR expression on MDA-MB-231 cell line. BT474 cells were used as negative control (NC). (D and E) Binding assay performed on MDA-MB-231 cell line with RBC-EV and ^{CTX}RBC-EV labelled with Memglow AF488. Results are expressed as percentage of Memglow AF488 positive cells (E) and MFI (F). (F and G) Binding assay performed on MDA-MB-231 cell line with Cy7.5 CTX free or immobilized on ^{CTX}RBC-EV. Results are expressed as percentage of Cy7.5 positive cells (G) and MFI (H). (H) Competition assay performed with Cy7.5 CTX and ^{CTX}RBC-EV using a 100-fold molar excess of CTX as competitor. (I) Representative confocal microscopy images of MDA-MB-231 cells treated for 4 and 24 hours with Memglow488@RBC-EV and Memglow488@^{CTX}RBC-EV. HBb, Hemoglobin, β subunit, scale bar 10μm. N = 3

6.3.3 Cisplatin encapsulation in ^{CTX}RBC-EV$_{cispt}$ and cytotoxicity evaluation

Once the cisplatin encapsulation and CTX functionalization procedures were optimized, we undertook the preparation and evaluation of cisplatin-loaded ^{CTX}RBC-EVs to produce the ^{CTX}RBC-EV$_{cispt}$ nano platform (Fig. 4.6A). We first compared cisplatin encapsulation efficiency between ^{CTX}RBC-EVs and RBC-EVs. As shown in Fig. 4.6B, the encapsulation rate was similar between the two RBC-EV samples (n.s., no significant differences), concluding that CTX functionalization did not hamper cisplatin encapsulation. Then, we compared the size distribution of ^{CTX}RBC-EV$_{cispt}$ and ^{CTX}RBC-EVs by NTA and we observed the presence of big NPs as in the case of RBC-EV$_{cispt}$ with an average diameter for ^{CTX}RBC-EV$_{cispt}$ of 230 nm ± 12.2 nm (Fig. 4.6C). For all the experiments, we selected final doses of 5 μM for cisplatin and 10-40 nM for CTX. These doses were chosen based on cytotoxicity and metabolic activity assessments of cisplatin and CTX (data not shown), showing that they could lead to a cellular response without significantly impacting cell viability. We next compared the amount of cisplatin delivered into cells by RBC-EV$_{cispt}$ and ^{CTX}RBC-EV$_{cispt}$ or in its free form by ICP-Mass spectrometry. We incubated MDA-MB-231 cells with the three preparations at a sublethal dose of cisplatin (5 μM) for 30 minutes and 24 h. After 30 minutes, cisplatin was already detected in cells, especially when it was delivered *via* RBC-EVs (Fig. 4.6D), with a statistically significant difference between RBC-EV$_{cispt}$ and ^{CTX}RBC-EV$_{cispt}$ and a 3-fold increase when cisplatin was delivered through ^{CTX}RBC-EV$_{cispt}$ compared to when it was delivered by RBC-EV$_{cispt}$. This suggests that ^{CTX}RBC-EV$_{cispt}$ may utilize a more efficient or targeted uptake mechanism, likely facilitated by the interaction of cetuximab with its target on the cell surface. After 24h, the amount of intracellular cisplatin was still detectable and higher when it was delivered by RBC-EV$_{cispt}$ or ^{CTX}RBC-EV$_{cispt}$ than the free drug. However, we did not observe significant differences between RBC-EV$_{cispt}$ and ^{CTX}RBC-EV$_{cispt}$ at this time point (Fig. 4.6E), suggesting that the initial advantage of ^{CTX}RBC-EV$_{cispt}$ in rapid uptake does not necessarily translate into long-term differences in intracellular cisplatin concentration.

These findings highlight that while both RBC-EV$_{cispt}$ and ^{CTX}RBC-EV$_{cispt}$ improve the cellular delivery of cisplatin compared to the free drug, ^{CTX}RBC-EV$_{cispt}$ shows a more efficient uptake initially, possibly due to targeted endocytosis.

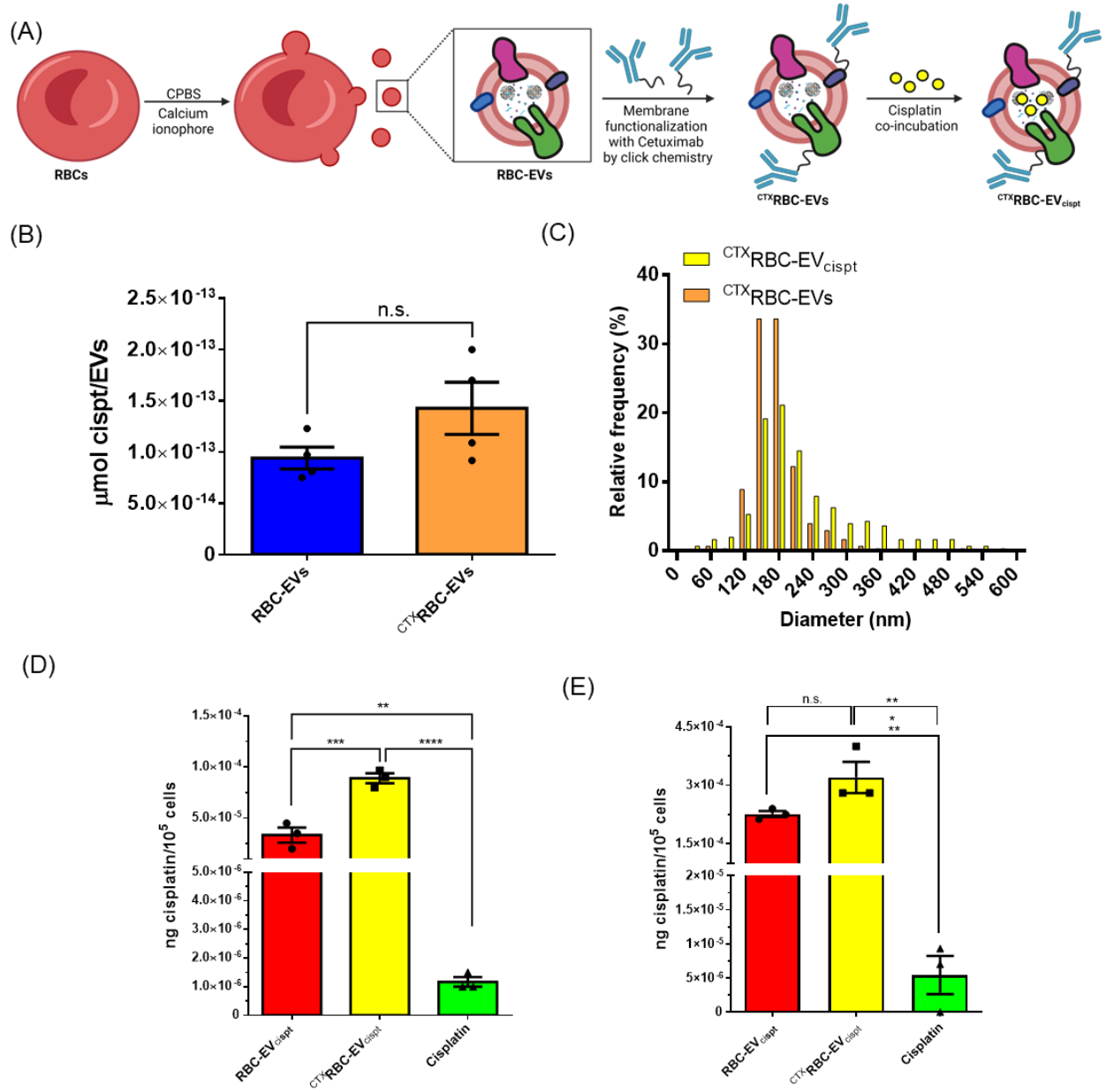

*Figure 4: Characterization and in vitro uptake analysis of CTXRBC-EVcispt in MDA-MB-231 TNBC cells. (A) Schematics of functionalization and engineering process towards the production of CTXRBC-EVcispt. (B) Comparison of cisplatin encapsulation yield between CTXRBC-EVs and RBC-EVs after 24 h incubation. Unpaired t-test: p < 0.05, n.s. = not significant. (C) Size distribution of CTXRBC-EVcispt and RBC-EVcispt obtained by NTA measurements. (D) Quantification of intracellular cisplatin delivery after 30 min treatments with RBC-EVcispt, CTXRBC-EVcispt and free cisplatin (cisplatin final concentration = 5µM; Cetuximab final concentration = 20 nM). Ordinary one-way anova: P < 0.05, *****p value < 0.0001. (E) Quantification of intracellular cisplatin delivery after 24 h treatments with RBC-EVcispt, CTXRBC-EVcispt and free cisplatin (cisplatin final concentration = 5µM; Cetuximab final concentration = 20 nM). Ordinary one-way anova: P <0.05, *****p < 0.0001. N = 3*

Since cisplatin can exert toxicity at both nuclear and cytoplasmic levels, we checked its subcellular distribution between the cytoplasm and the nuclei. MDA-MB-231 were treated for 24 hours either with free cisplatin or RBC-EV$_{cispt}$ and ^{CTX}RBC-EV$_{cispt}$ and their nuclear fraction was separated from the cytoplasm as explained in the Experimental Section[39]. Western blot analysis confirmed the subcellular fractioning, highlighting the presence of the Lysosomal Associated Membrane Protein 1 (LAMP1) exclusively in the whole cellular homogenate and in the cytoplasmic fraction, while lamin A/C (a protein expressed in the nuclear lamina) was detected as expected in the whole homogenate and in the nuclear fraction. Hemoglobin, (HBb) was found mostly in the cytoplasm (confirming the imaging data) although a low signal was also found in the nuclear fraction. This suggests that some RBC-EV-derived components might translocate into the nucleus, although the mechanism and significance of this minor nuclear presence remain unclear. (Fig. 5.6A). Interestingly, we noticed that cells treated with ^{CTX}RBC-EV$_{cispt}$ showed a low expression of lamin A/C. The reduction in lamin A/C could indicate changes in nuclear structure or integrity, potentially influencing nuclear functions such as DNA repair and cell cycle regulation[40]. This could be a direct result of the targeted delivery mechanism of ^{CTX}RBC-EV$_{cispt}$, which may facilitate a more pronounced impact also on nuclear pathways compared to free cisplatin or RBC-EV$_{cispt}$. We also checked the intracellular localization of CTX by analyzing the fluorescence signal of the Cy7.5 bound to CTX. We observed that although the majority of CTX was in the cytoplasm, a small amount was also detected in the nuclear fraction (Fig. 5.6B)[41]. We then quantified the nuclear/cytoplasmic distribution of cisplatin by ICP-MS and normalized the amount of cisplatin in each fraction on the total amount of cisplatin detected in that sample (cytosolic cisplatin + nuclear cisplatin) (Fig. 5.6C). In cells treated with the free drug, 100 % of the total cisplatin was localized in the cytoplasm with no cisplatin detected in the nuclei. In cells treated with RBC-EV$_{cispt}$ or ^{CTX}RBC-EV$_{cispt}$, still most of the cisplatin was found in the cytoplasm (≈75% and ≈70%, respectively) although a nuclear localization is also present indicating that the different way of cisplatin administration changes the subcellular localization of the cargo. The predominance of cytoplasmic localization in all treatment conditions indicates that, even when some cisplatin reaches the nucleus *via* RBC-EV delivery, a significant portion remains cytoplasmic. This suggests that cisplatin's primary mode of action could still be largely cytoplasmic, particularly at the sub-lethal concentration of 5 μM.

Then, we assessed the potential cytotoxicity of the ^{CTX}RBC-EV$_{cispt}$ formulation due to its combinatorial way of action. Therefore, we treated the cells for 4h and 24h with ^{CTX}RBC-EV$_{cispt}$, RBC-EV$_{cispt,}$ and all the relative controls using the doses previously determined. After 4h, both

RBC-EV$_{cispt}$ and ^{CTX}RBC-EV$_{cispt}$ demonstrated a slight effect on cellular viability as compared to the free cisplatin or cetuximab, without significant differences (Fig. 5.6D). After 24h, both RBC-EV$_{cispt}$ and ^{CTX}RBC-EV$_{cispt}$ significantly decreased cell viability compared to the untreated cells and the cells treated with pristine RBC-EVs. However, treatments carried out with ^{CTX}RBC-EV$_{cispt}$ had the most critical impact resulting in a reduction of approximately 50% of cellular viability, differently from when cells were treated with RBC-EV$_{cispt}$ (Fig. 5.6E).

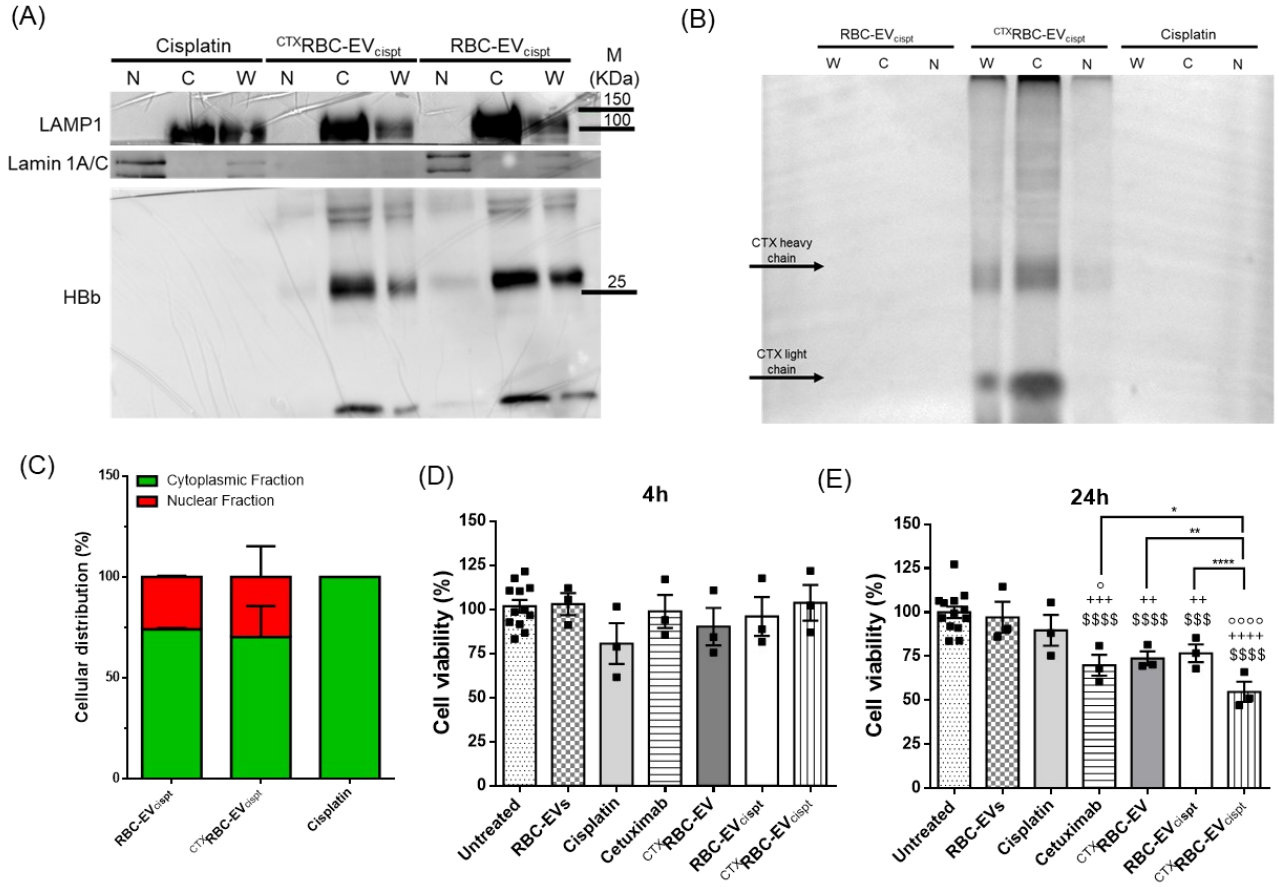

*Figure 5.6: (A) Western blot analysis of MDA-MB-231 cytoplasmic and nuclear fractions after 24h treatments with RBC-EVcispt, CTXRBC-EVcispt and free cisplatin. N = Nuclei, C = Cytoplasm, W = Whole cell lysate. (B) SDS-PAGE and fluorescence detection of Cy7.5-CTX in cytoplasmic and nuclear fractions obtained as in (A). (C) % of Cisplatin subcellular distribution in cytoplasmic and nuclear fractions obtained by dividing the amount of cisplatin in each fraction (ng) to the sum of cisplatin content in nuclear + cytoplasmic fractions, ng). (D) Cell viability analysis after 4 hours treatments, data normalized on untreated cells. (E) Cell viability analysis after 24 h treatments. Ordinary one-way ANOVA: $ = significance vs. untreated, + = significance vs. RBC-EVs, ° = significance vs. cisplatin, *p < 0.05, **p < 0.01, ****p < 0.0001. N = 3*

6.3.4 Assessment of ^{CTX}RBC-EV$_{cispt}$ action as pro-ferroptosis nanoplatform

To investigate the molecular mechanisms underlying the observed cytotoxic and cellular effects of the different formulations, we performed the RNA-seq transcriptome profiling of MDA-MB-231 cells subjected to different treatments (namely, RBC-EVs, RBC-EV$_{cispt}$, ^{CTX}RBC-EVs, ^{CTX}RBC-

EV_{cispt}, free cisplatin, free CTX, and a mix of free CTX + free cisplatin) after 24 hours as well as untreated cells (wild type) as control. From the sequencing, we obtained at least 21 M read pairs/sample, with a mean of 94% uniquely mapped reads on genome and 84% reads uniquely assigned to genes. Concerning the single-agent treatments, differential expression analysis did not find any differentially expressed genes (DEGs, adjusted p-value < 0.1 and |log2FC| >1) in cells treated with RBC-EVs as compared to untreated cells, and only one DEG in CTX vs. untreated cells, confirming the non-toxicity of these two agents at such doses and times. On the other hand, free cisplatin-treated cells showed 11 DEGs as compared to untreated cells (Table 1.6_DEG counts). Then, we focused on the formulations of our interest, i.e. the combined treatments, and we identified 22 DEGs for CTX + Cisplatin, 22 DEGs for RBC-EV_{cispt} and 19 DEGs for ^{CTX}RBC-EV_{cispt} as compared to untreated cells (Table 1.6_DEG counts). Interestingly, three DEGs were deregulated by both cisplatin and the mix of CTX and cisplatin treatments (PARD6G as up- and SHANK2 and RPLP0P9 as down-regulated DEGs), and two DEGs were in common between RBC-EV_{cispt} and ^{CTX}RBC-EV_{cispt} treatments (CYP1B1 as up- and STC1 as down-regulated DEGs).

	Total DEGs	UP	DOWN	Up-regulated genes	Down-regulated genes
Cisplatin vs. untreated	11	7	4	RAB24, TMEM160, MESP1, RAB5IF, PARD6G[#], C4orf48, SNHG9	ABLIM2, MTND1P23, SHANK2[#], RPLP09[#]
Cisplatin + Cetuximab vs. untreated	22	10	12	TMEM256, MRPL12, ZNRF2, SMIM26, IER3IP1, XKR9, CMTM8, PARD6G[#], ICAM2	EEF1B2P3, SHANK2[#], RPS2P46, RPL13P12 RPL7P9, RPLP09[#], RPS15P4, RPL3P4, RPL15P3, RPSAP19, RPL21P16
RBC-EV_{cispt} vs. untreated	22	20	2	SEM1, RPS27, CYP1B1[§], PPIG, TOMM7, PRPF38B, RPS25, RPS29, UQCRH, SRSF5, RBM25, RPL21, LARP7, CDC5L, SEC62, C11orf58, FUBP1, TRA2A, PRELID3B, KIF20B	ALKBH5, STC1[§]
^{CTX}RBC-EV_{cispt} vs. untreated	19	4	15	CYP1B1[§], ANKRD36C, PHF11, SLC7A11	PCDH1, RAB20, TMEM45A, SLCO4A1, CA9, SPAG4, STC1[§], PPFIA4, DDIT4, IL11, SLCO4A1-AS1, DNAH11, PFKFB4, NDRG1, MIR210HG

Table 1.6: DEG counts (adjusted p-value < 0.1 and |log2FC| > 1). For each comparison, DEGs are listed according to decreasing fold-change values. RBC-EVs, red blood cell extracellular vesicles; wt, untreated cells; CTX, Cetuximab; cispt, Cisplatin; [#], common genes between Cisplatin and the mix of cetuximab and cisplatin treatments; [§], common genes between RBC-EV_{cispt} and ^{CTX}RBC-EV_{cispt} treatments.

To explore the functional processes altered by the different formulations and related to the cytotoxic effects in MDA-MB-231 treated cells, we performed the functional enrichment analysis of DEGs on Gene Ontology Biological Process (GO-BP) terms and several pathway collections (Table 1.6_Selection Functional enrichments). After treatments with free cisplatin, we found that genes like Mesoderm Posterior BHLH Transcription Factor 1 (MESP1) and Partitioning Defective 6 Homolog Gamma (PARD6G) were significantly upregulated. MESP1 is a transcription factor with a crucial role in Epithelial–mesenchymal transition (EMT), and cell migration. EMT has been observed to be linked to the activation of HIF-1α signaling, which can enhance cell motility, support cellular nutrient metabolism, and stimulate angiogenesis to boost energy supply, enabling cancer cells to survive in challenging conditions. On the other side, PARD6G is a key component

of the Par6/aPKC complex, which regulates cell polarity, tight junction formation, and asymmetric cell division and it is correlated to cancer development; as for MESP1, its up-regulation could have several implications in the context of TNBC and response to cisplatin, as the activation of compensatory mechanism where the cells are attempting to restore polarity and adhesion post-EMT, increasing motility or invasiveness. All these functions are already known mechanisms associated with an increased cisplatin resistance already observed in cancer[42].

We also observed the downregulation of SH3 And Multiple Ankyrin Repeat Domains 2 (SHANK2), component of the Hippo signaling. The Hippo pathway plays a crucial role in regulating cell proliferation, apoptosis, and ferroptosis through its effectors YAP and TAZ. When SHANK2 is downregulated, it alters this pathway, potentially diminishing the effectiveness of ferroptosis-based therapies. Furthermore, in TNBC, Hippo pathway showed also to induce cisplatin resistance *via* EMT activation. Thus, FDA-approved drugs that indirectly block Hippo/YAP signaling are showing promise in the clinic for reducing cancer chemoresistance.

PARD6G up-regulation was also found after treatments with the mix of free cisplatin and free cetuximab, as well as the downregulation of SHANK2, in addition to the modulation of other interesting genes. For example, among the genes upregulated, TMEM256, a transmembrane protein, showed a significant fold-change, suggesting an increased role in cellular interactions or signaling under this treatment[43]. Additionally, mitochondrial ribosomal protein L12 (MRPL12) was also upregulated, highlighting alterations in mitochondrial functions and possibly energy metabolism, which are critical in maintaining cell survival under stress conditions like chemotherapy. Conversely, several pseudogenes involved in protein synthesis pathways were downregulated, such as RPL13P12 and RPS2P46, indicating potential dysregulation in translational machinery, which might affect the cells' ability to produce proteins needed for survival or repair[44]. Finally, no term related to drug cytotoxic effects was found enriched when cisplatin was administered as free drug (free cisplatin and mix of CTX and cisplatin), thus supporting our observations on cell viability after free drug treatments above described.

Differently, when MDA-MB-231 cells were treated with RBC-EV_{cispt} and, even more, in with ^{CTX}RBC-EV_{cispt}, we observed many enriched terms concerning drug cytotoxic effects (TableX_Selection Functional enrichments and full list of enrichments in SupplFileX_Functional enrichment analysis). Indeed, cells treated with RBC-EV_{cispt} over-expressed a group of functions all related to RNA splicing, RNA processing, spliceosome and RNA metabolism (with up-regulation of PPIG, PRPF38B, SRSF5, RBM25, LARP7, CDC5L, TRA2A, RPS27, RPS25, RPS29, SEM1, RPL21), which have been functionally linked to the cell death induced by cisplatin[45]. We found the up-regulation of SEM1 and RPS27 (Ribosomal Protein S27), both

involved in protein degradation and ribosome function, suggesting heightened protein synthesis and cellular stress response, which is crucial when cancer cells are exposed to cisplatin. Additionally, CYP1B1, a member of the cytochrome P450 family, was significantly upregulated. This enzyme is involved in xenobiotic metabolism and has been previously associated with chemotherapy resistance in cancer cells, indicating a possible mechanism for cisplatin resistance[46]. Interestingly, CYP1B1 is involved in the metabolism of polyunsaturated fatty acids, leading to the production of reactive oxygen species (ROS) that can promote lipid peroxidation and ferroptosis[47]. Other notable upregulated genes include TOMM7, involved in mitochondrial function and protein import into the mitochondria: this suggests alterations in mitochondrial activity and RNA processing, critical in cellular stress responses during chemotherapy[48]. Interestingly, ALKBH5, a known RNA demethylase, was significantly downregulated. This gene is involved in RNA stability and methylation, processes critical for gene expression regulation. Downregulation of ALKBH5 might affect cancer cell proliferation and survival, potentially increasing their sensitivity to ferroptosis and contributing to the effectiveness of cisplatin-loaded RBC-EVs[49].

Finally, after treatments with ^{CTX}RBC-EV$_{cispt}$ we found the modulation of several genes related to ferroptosis. First, we found again the up-regulation of CYP1B1 and the downregulation of NDRG1 - that is implicated in cellular stress responses, including iron homeostasis and oxidative stress management. Its downregulation may enhance susceptibility to ferroptosis. DDIT4 is involved in autophagy and stress responses[50]. Its downregulation can reduce autophagic flux and increase sensitivity to ferroptosis. Up-regulation of SLC7A11, which is essential for the uptake of cystine, a precursor for the antioxidant glutathione (GSH). When SLC7A11 is upregulated, there is an increase in cystine uptake, leading to elevated GSH levels, which helps in maintaining cellular redox homeostasis[51]. Conversely, if cisplatin depletes GSH, it can create a feedback loop where the expression of SLC7A11 might be further increased to restore GSH levels. Interestingly, we also found a slight downregulation of EGFR, that could lead to sensitizing the cells to chemotherapy and potentially contributing to HIF1A regulation and ferroptosis activation. In fact, the downregulation of the Signal Transducer and Activator of Transcription 3 (STAT3) is crucial in EGFR-HIF1a crosslink. STAT3 is a survival and oncogenic factor frequently activated downstream of EGFR[52]. Its downregulation suggests a disruption in pro-survival signaling cascades. STAT3 is known to promote cell proliferation, inhibit apoptosis, and regulate HIF1A under hypoxic conditions: its downregulation might interfere with HIF1A stabilization, lowering the expression of genes associated with cell survival and resistance to oxidative stress, thereby sensitizing cells to ferroptosis. In this context, we also found the downregulation of CRISPR-associated protein 9 (CAS9), Stanniocalcin 1(STC1), DNA Damage Inducible Transcript 4

(DDIT4), N-myc Downstream Regulated Gene 1 (NDRG1), Peptidylprolyl Isomerase A4 (PPIA4) and Transmembrane Protein 45A (TMEM45A), genes that are regulated by HIF1a (KEGG database). The observed downregulation of EGFR, STAT3, CAS9, STC1, DDIT4, NDRG1, PPIA4, and TMEM45A in TNBC cells treated with ^{CTX}RBC-EV$_{cispt}$ likely reflects the disruption of key survival and stress response pathways. This could impair HIF1A-mediated hypoxic adaptation, sensitizing the cells to oxidative stress and promoting ferroptosis.

6.3.5 ^{CTX}RBC-EV$_{cispt}$ nanoplatform limited cisplatin ex vivo toxicity by limiting the production of ghost red blood cells

In addition to resistance, off-target toxicity represents one of the major drawbacks of cancer therapies. Cisplatin-based treatments suffer from numerous systemic toxicity effects, among which hematotoxicity and anemia are considered ones of the most diffused[53,54]. For cisplatin, anemia can occur because of the ability of cisplatin to interact with the red blood cell-plasma membrane[55] causing (i) a reduction in the number of erythrocytes and (ii) morphological changes towards stomatocytic shape[32]. We performed an *ex vivo* toxicity assay, by incubating red blood cells with ^{CTX}RBC-EV$_{cispt}$ (5 μM cisplatin) and soluble cisplatin at both sub-lethal (5 μM) and lethal doses (25 μM) for 3 hours at 37°C. In all samples, we observed the presence of erythrocytes with altered morphology (yellow arrows in Fig. 6.6A, i.e., stomatocytes, acanthocytes) although with different percentages (17.1 ± 2.2 % for untreated, 23.2 ± 2.5% for the vehicle, 43.1 ± 4.3% for cisplatin 5 μM, 34.3 ± 12.7% for cisplatin 25 μM and 32.5 ± 0.1% for ^{CTX}RBC-EV$_{cispt}$). Ghost RBCs were obtained only after treatments with the free drug, with the highest percentages when erythrocytes were incubated with 25 μM cisplatin. Altogether, these results demonstrated the low hematotoxicity effects of ^{CTX}RBC-EV$_{cispt.}$

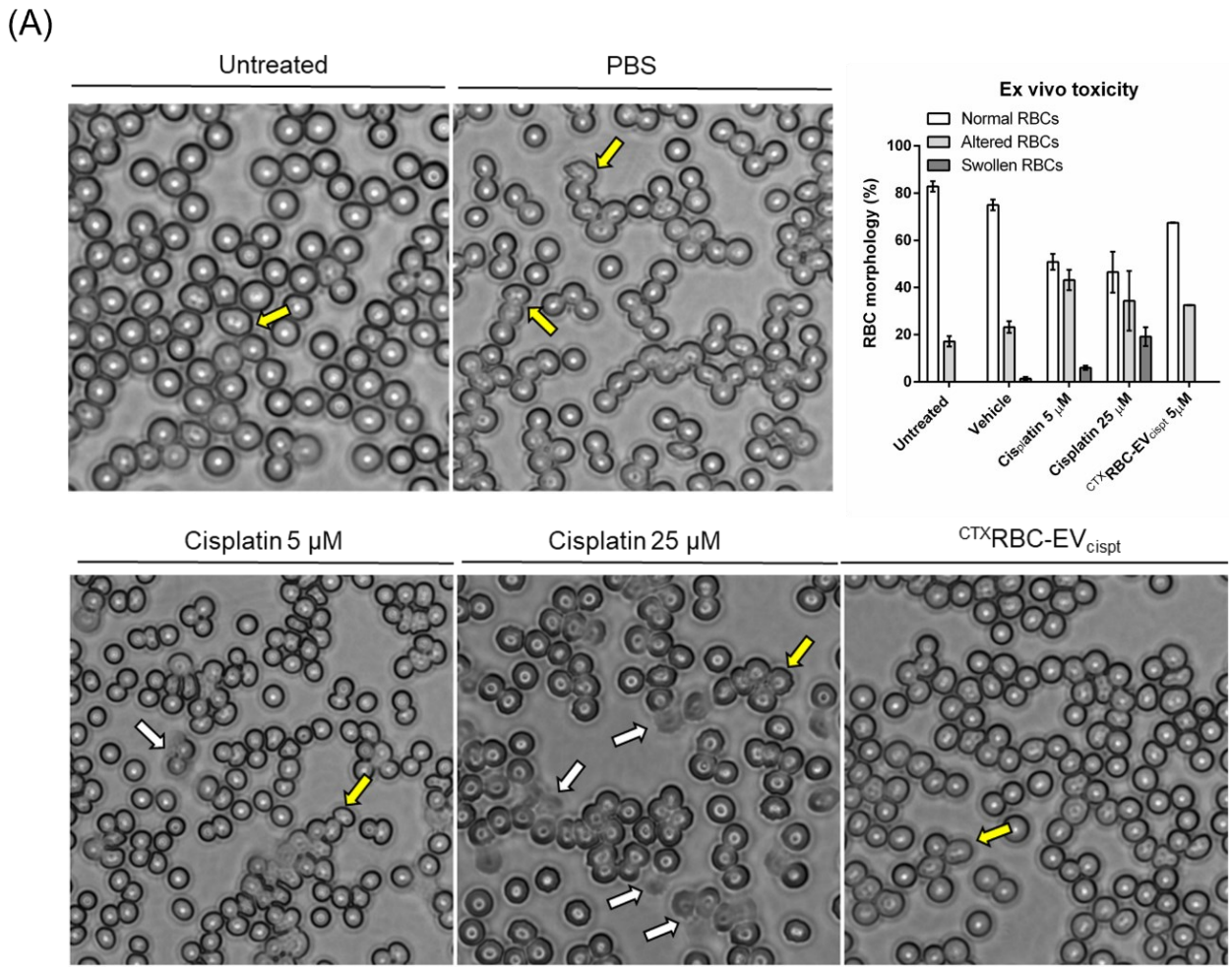

Figure 6.6: A) Ex vivo morphological analysis of red blood cells after 3 hours of treatments with cisplatin and CTXRBC-EVcispt. Yellow arrow = altered RBCs, white arrow = ghost RBCs. N = 3

6.3.6 Action of ^{CTX}RBC-EV$_{cispt}$ in ex vivo 3D TNBC patient-derived organoids

To demonstrate the activity of engineered RBC-EVs as tumor-targeted delivery vehicles of Cisplatin, we decided to assess their performances on two PDOs models of TNBC, PDO#1 and PDO#2, which were fully characterized (Fig. 7.6). PDO#1 and PDO#2 were both derived from invasive ductal carcinoma, with a TNBC molecular subtype. The histological staining and immunohistochemistry performed on PDO#1 and PDO#2 showed that both organoids mirror the molecular features of the original tumors (Fig. 7.6A). Neither the tumor tissues nor the PDOs exhibit expression of estrogen (ER) or progesterone (PR) receptors, indicating the absence of these hormone receptors. Transmission electron microscopy (TEM) images reveal characteristic tumor-associated morphological features in both PDOs (Fig. 7.6B).

Confocal microscopy (Fig. 7.6C) confirmed the expression of various markers in both PDOs, including the folate receptor (FolR), vimentin (Vim), transferrin receptor 1 (Tfr1), and pancytokeratin (PanCytok). Finally, flow cytometry analysis evaluates the surface markers CD24, CD44, EpCAM, and CD49f, which are linked to stem cell-like properties and tumor-initiating

potential. Both PDOs exhibit distinct profiles for these markers, reflecting the diversity in their cellular phenotypes and potential differences in tumorigenicity (Fig. 7.6D).

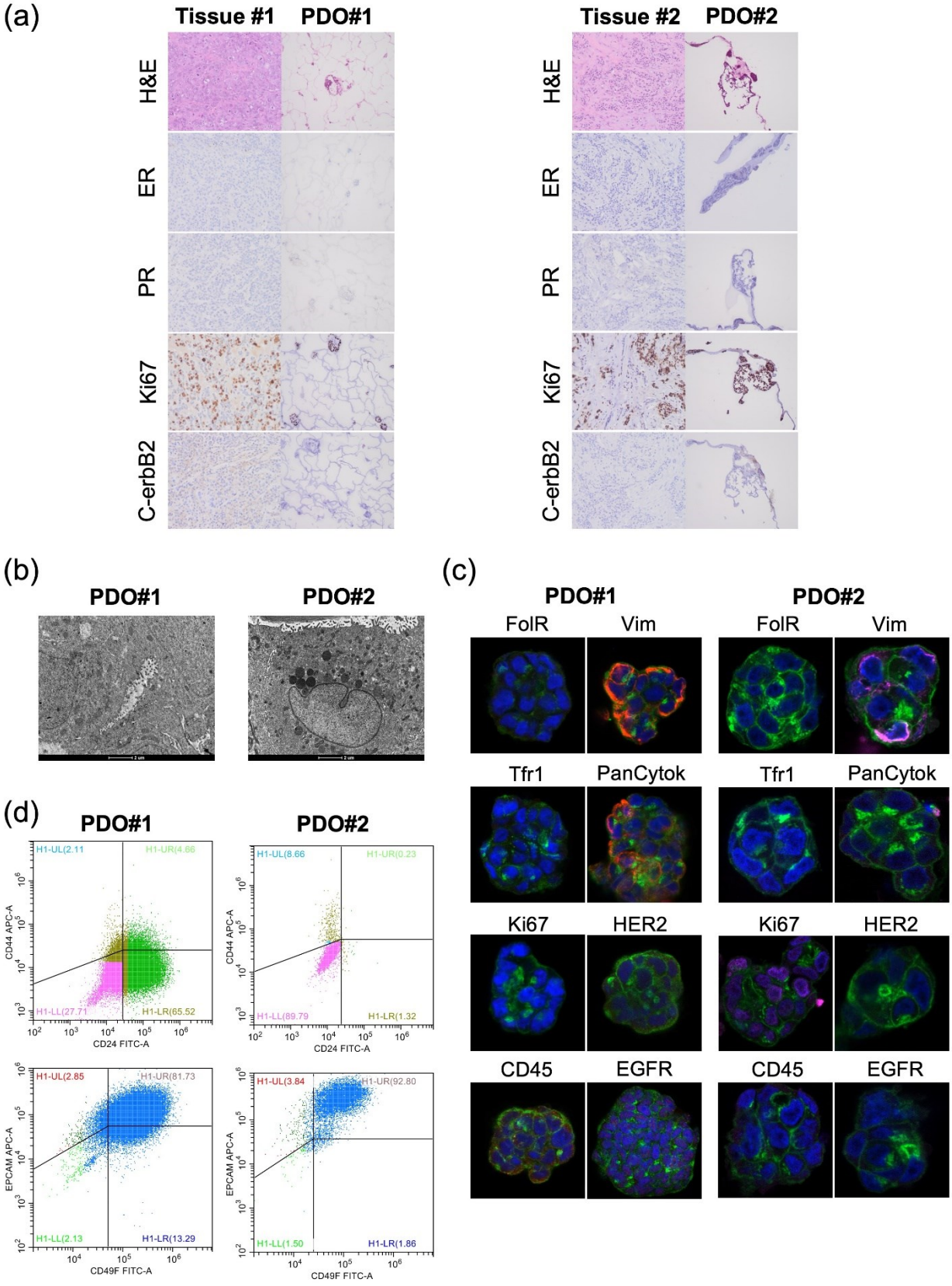

Figure 7.6: Histological and molecular characterization of tumor tissues (Tissue #1 and Tissue #2) matched with PDOs (PDO#1 and PDO#2), (A) by H&E staining and IHC for estrogen (ER), progesterone (PR) receptors, Ki67 proliferation index and c-ErbB2 receptor. (B) TEM images of PDO#1 and PDO#2, showing tumor-associated morphological features: intracellular lumens rich in microvilli (PDO#1) and mitochondria rich in ridges (PDO#2); scale bar 2 µm. (C) Confocal

microscopy analyses assessing the expression of Folate receptor (FolR), Vimentin (Vim), Transferrin receptor 1 (Tfr1), Pancytokeratin (PanCytok), Ki67, HER2, CD45, EGF receptor (EGFR) on both PDO#1 and PDO#2. Nuclei (blue, DAPI), membrane (green, WGA FITC), and markers (pink, anti-Rb AF546) are labelled. (D) PDO#1 and PDO#2 evaluation by flow cytometry for the cell surface markers CD24/CD44 and EpCAM/CD49f.

We conducted a cell viability assay to compare the efficacy of free Cisplatin with the cisplatin-based nanoformulations, RBC-EV$_{cispt}$ and ^{CTX}RBC-EV$_{cispt}$, at two different concentrations (5 µM and 25 µM, Fig. 8.6). After 72 hours of treatment, ATP content was measured to assess cell viability. PDO#1 showed a significantly higher sensitivity to both doses of free Cisplatin ($p<0.0001$), while the nanoformulated Cisplatin appeared largely ineffective, except for a slight but statistically significant reduction in cell viability observed at the 25 µM dose of RBC-EV$_{cispt}$. Notably, the addition of CTX to the nanoformulation (^{CTX}RBC-EV$_{cispt}$) did not enhance efficacy in PDO#1, which aligns with the low EGFR expression in this model. In contrast, PDO#2 responded only to the higher concentration (25 µM) of Cisplatin, RBC-EV$_{cispt}$, and ^{CTX}RBC-EV$_{cispt}$. In this case, the functionalization with CTX led to improved treatment efficacy, likely due to enhanced intracellular penetration and uptake of the drug. These results suggest that multimodal engineering of RBC-EVs with both Cisplatin and CTX facilitates better drug delivery in PDO#2, ultimately reducing cell viability. Thus, the functionalization of RBC-EVs with CTX may be particularly beneficial in models with low responsiveness to standard Cisplatin treatment.

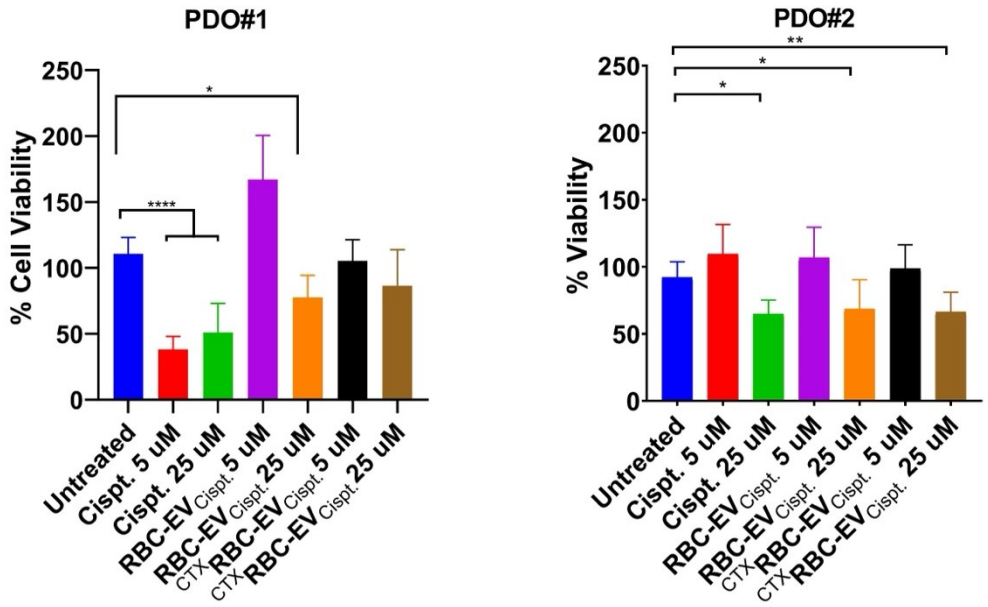

*Figure 8.6: Cell Viability assay to assess sensitivity of PDO#1 and PDO#2 to Cisplatin (Cispt.), RBC-EV$_{Cispt}$ and ^{CTX}RBC-EV$_{Cispt}$ at two different concentrations (5 and 25 µM). Ten replicates for each condition were tested, at least two biological replicates were performed. Untreated organoids were used as negative control. The data are reported as the means ± SDs; *p<0.05, **p<0.001, ****p<0.0001.*

6.4 Conclusions

The development of the ^{CTX}RBC-EV$_{cispt}$ nanoplatform represents a promising advancement in targeted therapy for triple-negative breast cancer (TNBC). By combining the cytotoxic effects of cisplatin and the EGFR-targeting properties of CTX within a RBC-EV delivery system, this approach enhances drug delivery efficiency, mitigates chemoresistance, and improves treatment outcomes. Our work demonstrates that ^{CTX}RBC-EV$_{cispt}$ improves cisplatin uptake, facilitates its intracellular distribution, and exhibits a more potent cytotoxic effect compared to free drug administration or RBC-EVs loaded with cisplatin alone. Moreover, the ability of ^{CTX}RBC-EV$_{cispt}$ to engage specific molecular pathways, such as ferroptosis, highlights its potential to overcome TNBC's inherent resistance mechanisms, particularly those related to hypoxia and EGFR signaling.

Furthermore, our transcriptomic analysis identified key genetic changes associated with ferroptosis activation and drug resistance modulation, supporting the therapeutic potential of ^{CTX}RBC-EV$_{cispt}$ in sensitizing TNBC cells to cisplatin. These findings pave the way for further investigation of this multimodal therapeutic strategy, with the goal of enhancing clinical outcomes for patients suffering from TNBC and potentially other malignancies resistant to conventional treatments.

Future studies will be necessary to explore the *in vivo* efficacy and safety of this nanoplatform, as well as its potential for application in other cancer types. Additionally, expanding our understanding of the molecular mechanisms driving the enhanced sensitivity to ferroptosis could inform the design of even more effective combination therapies, offering new hope in the fight against aggressive and treatment-resistant cancers.

6.5 References

(1) Zagami, P.; Carey, L. A. Triple Negative Breast Cancer: Pitfalls and Progress. *NPJ Breast Cancer* 2022, *8* (1). https://doi.org/10.1038/s41523-022-00468-0.

(2) Maqbool, M.; Bekele, F.; Fekadu, G. Treatment Strategies Against Triple-Negative Breast Cancer: An Updated Review. *Breast Cancer (Dove Med Press)* 2022, *14*, 15–24. https://doi.org/10.2147/BCTT.S348060.

(3) Dasari, S.; Tchounwou, P. B. Cisplatin in Cancer Therapy: Molecular Mechanisms of Action. *Eur J Pharmacol* 2014, *740*, 364–378. https://doi.org/10.1016/j.ejphar.2014.07.025.

(4) Siddik, Z. H. Cisplatin: Mode of Cytotoxic Action and Molecular Basis of Resistance. *Oncogene* 2003, *22* (47), 7265–7279. https://doi.org/10.1038/sj.onc.1206933.

(5) Mason, S. R.; Willson, M. L.; Egger, S. J.; Beith, J.; Dear, R. F.; Goodwin, A. Platinum-Based Chemotherapy for Early Triple-Negative Breast Cancer. *Cochrane Database Syst Rev* 2023, *9* (9), CD014805. https://doi.org/10.1002/14651858.CD014805.pub2.

(6) Wang, B.; Sun, T.; Zhao, Y.; Wang, S.; Zhang, J.; Wang, Z.; Teng, Y.-E.; Cai, L.; Yan, M.; Wang, X.; Jiang, Z.; Pan, Y.; Luo, J.; Shao, Z.; Wu, J.; Guo, X.; Hu, X. A Randomized Phase 3 Trial of Gemcitabine or Nab-Paclitaxel Combined with CisPlatin as First-Line Treatment in Patients with Metastatic Triple-Negative Breast Cancer. *Nat Commun* 2022, *13* (1), 4025. https://doi.org/10.1038/s41467-022-31704-7.

(7) Hill, D. P.; Harper, A.; Malcolm, J.; McAndrews, M. S.; Mockus, S. M.; Patterson, S. E.; Reynolds, T.; Baker, E. J.; Bult, C. J.; Chesler, E. J.; Blake, J. A. Cisplatin-Resistant Triple-Negative Breast Cancer Subtypes: Multiple Mechanisms of Resistance. *BMC Cancer* 2019, *19* (1), 1039. https://doi.org/10.1186/s12885-019-6278-9.

(8) Guo, J.; Xu, B.; Han, Q.; Zhou, H.; Xia, Y.; Gong, C.; Dai, X.; Li, Z.; Wu, G. Ferroptosis: A Novel Anti-Tumor Action for Cisplatin. *Cancer Res Treat* 2018, *50* (2), 445–460. https://doi.org/10.4143/crt.2016.572.

(9) Xu, N.; Li, B.; Liu, Y.; Yang, C.; Tang, S.; Cho, W. C.; Huang, Z. Ferroptosis and Triple-Negative Breast Cancer: Potential Therapeutic Targets. *Front Oncol* 2022, *12*. https://doi.org/10.3389/fonc.2022.1017041.

(10) Fan, Y.; Ma, L.; Fang, X.; Du, S.; Mauck, J.; Loor, J. J.; Sun, X.; Jia, H.; Xu, C.; Xu, Q. Role of Hypoxia-Inducible-Factor-1α (HIF-1α) in Ferroptosis of Adipose Tissue during Ketosis. *J Dairy Sci* 2024. https://doi.org/10.3168/jds.2024-24822.

(11) Roy, S.; Rizvi, Z. A.; Clarke, A. J.; Macdonald, F.; Pandey, A.; Zaiss, D. M. W.; Simon, A. K.; Awasthi, A. EGFR-HIF1α Signaling Positively Regulates the Differentiation of IL-9 Producing T Helper Cells. *Nat Commun* 2021, *12* (1). https://doi.org/10.1038/s41467-021-23042-x.

(12) Chaudhary, R.; Slebos, R. J. C.; Noel, L. C.; Song, F.; Poole, M. I.; Hoening, D. S.; Hernandez-Prera, J. C.; Conejo-Garcia, J. R.; Guevara-Patino, J. A.; Wang, X.; Xie, M.; Tan, A. C.; Chung, C. H. EGFR Inhibition by Cetuximab Modulates Hypoxia and IFN Response Genes in Head and Neck Squamous Cell Carcinoma. *Cancer Research Communications* 2023, *3* (5), 896–907. https://doi.org/10.1158/2767-9764.CRC-22-0443.

(13) Lu, H.; Liang, K.; Lu, Y.; Fan, Z. The Anti-EGFR Antibody Cetuximab Sensitizes Human Head and Neck Squamous Cell Carcinoma Cells to Radiation in Part through Inhibiting Radiation-Induced Upregulation of HIF-1α. *Cancer Lett* 2012, *322* (1), 78–85. https://doi.org/10.1016/j.canlet.2012.02.012.

(14) Baselga, J.; Gómez, P.; Greil, R.; Braga, S.; Climent, M. A.; Wardley, A. M.; Kaufman, B.; Stemmer, S. M.; Pêgo, A.; Chan, A.; Goeminne, J.-C.; Graas, M.-P.; Kennedy, M. J.; Ciruelos Gil, E. M.; Schneeweiss, A.; Zubel, A.; Groos, J.; Melezínková, H.; Awada, A. Randomized Phase II Study of the Anti-Epidermal Growth Factor Receptor Monoclonal Antibody Cetuximab with Cisplatin versus Cisplatin Alone in Patients with Metastatic Triple-Negative Breast Cancer. *J Clin Oncol* 2013, *31* (20), 2586–2592. https://doi.org/10.1200/JCO.2012.46.2408.

(15) Barabas, K.; Milner, R.; Lurie, D.; Adin, C. Cisplatin: A Review of Toxicities and Therapeutic Applications. *Veterinary and Comparative Oncology*. 2008, pp 1–18. https://doi.org/10.1111/j.1476-5829.2007.00142.x.

(16) Avvakumova, S.; Pandolfi, L.; Soprano, E.; Moretto, L.; Bellini, M.; Galbiati, E.; Rizzuto, M. A.; Colombo, M.; Allevi, R.; Corsi, F.; Sánchez Iglesias, A.; Prosperi, D. Does Conjugation Strategy Matter? Cetuximab-Conjugated Gold Nanocages for Targeting Triple-Negative Breast Cancer Cells. *Nanoscale Adv* 2019, *1* (9), 3626–3638. https://doi.org/10.1039/c9na00241c.

(17) Colombo, M.; Rizzuto, M. A.; Pacini, C.; Pandolfi, L.; Bonizzi, A.; Truffi, M.; Monieri, M.; Catrambone, F.; Giustra, M.; Garbujo, S.; Fiandra, L.; Corsi, F.; Prosperi, D.; Mazzucchelli, S. Half-Chain Cetuximab Nanoconjugates Allow Multitarget Therapy of Triple Negative Breast Cancer. *Bioconjug Chem* 2018, *29* (11), 3817–3832. https://doi.org/10.1021/acs.bioconjchem.8b00667.

(18) Fan, W.; Yung, B.; Huang, P.; Chen, X. Nanotechnology for Multimodal Synergistic Cancer Therapy. *Chem Rev* 2017, *117* (22), 13566–13638. https://doi.org/10.1021/acs.chemrev.7b00258.

(19) Wang, L.; Yu, X.; Zhou, J.; Su, C. Extracellular Vesicles for Drug Delivery in Cancer Treatment. *Biol Proced Online* 2023, *25* (1), 28. https://doi.org/10.1186/s12575-023-00220-3.

(20) Go, G.; Park, H. J.; Lee, J. H.; Yun, C. W.; Lee, S. H. Inhibitory Effect of Oxaliplatin-Loaded Engineered Milk Extracellular Vesicles on Tumor Progression. *Anticancer Res* 2022, *42* (2), 857–866. https://doi.org/10.21873/anticanres.15543.

(21) Chen, M.; Leng, Y.; He, C.; Li, X.; Zhao, L.; Qu, Y.; Wu, Y. Red Blood Cells: A Potential Delivery System. *J Nanobiotechnology* 2023, *21* (1), 288. https://doi.org/10.1186/s12951-023-02060-5.

(22) Musicò, A.; Zenatelli, R.; Romano, M.; Zendrini, A.; Alacqua, S.; Tassoni, S.; Paolini, L.; Urbinati, C.; Rusnati, M.; Bergese, P.; Pomarico, G.; Radeghieri, A. Surface Functionalization of Extracellular Vesicle Nanoparticles with Antibodies: A First Study on the Protein Corona "Variable". *Nanoscale Adv* 2023, *5* (18), 4703–4717. https://doi.org/10.1039/d3na00280b.

(23) Usman, W. M.; Pham, T. C.; Kwok, Y. Y.; Vu, L. T.; Ma, V.; Peng, B.; Chan, Y. S.; Wei, L.; Chin, S. M.; Azad, A.; He, A. B. L.; Leung, A. Y. H.; Yang, M.; Shyh-Chang, N.; Cho, W. C.; Shi,

J.; Le, M. T. N. Efficient RNA Drug Delivery Using Red Blood Cell Extracellular Vesicles. *Nat Commun* 2018, *9* (1). https://doi.org/10.1038/s41467-018-04791-8.

(24) Maiolo, D.; Paolini, L.; Di Noto, G.; Zendrini, A.; Berti, D.; Bergese, P.; Ricotta, D. Colorimetric Nanoplasmonic Assay to Determine Purity and Titrate Extracellular Vesicles. *Anal Chem* 2015, *87* (8), 4168–4176. https://doi.org/10.1021/ac504861d.

(25) Zendrini, A.; Paolini, L.; Busatto, S.; Radeghieri, A.; Romano, M.; Wauben, M. H. M.; van Herwijnen, M. J. C.; Nejsum, P.; Borup, A.; Ridolfi, A.; Montis, C.; Bergese, P. Augmented COlorimetric NANoplasmonic (CONAN) Method for Grading Purity and Determine Concentration of EV Microliter Volume Solutions. *Front Bioeng Biotechnol* 2020, *7*. https://doi.org/10.3389/fbioe.2019.00452.

(26) Musicò, A.; Zenatelli, R.; Romano, M.; Zendrini, A.; Alacqua, S.; Tassoni, S.; Paolini, L.; Urbinati, C.; Rusnati, M.; Bergese, P.; Pomarico, G.; Radeghieri, A. Surface Functionalization of Extracellular Vesicle Nanoparticles with Antibodies: A First Study on the Protein Corona "Variable." *Nanoscale Adv* 2023, *5* (18), 4703–4717. https://doi.org/10.1039/D3NA00280B.

(27) Dobin, A.; Davis, C. A.; Schlesinger, F.; Drenkow, J.; Zaleski, C.; Jha, S.; Batut, P.; Chaisson, M.; Gingeras, T. R. STAR: Ultrafast Universal RNA-Seq Aligner. *Bioinformatics* 2013, *29* (1), 15–21. https://doi.org/10.1093/bioinformatics/bts635.

(28) Anders, S.; Pyl, P. T.; Huber, W. HTSeq-A Python Framework to Work with High-Throughput Sequencing Data. *Bioinformatics* 2015, *31* (2), 166–169. https://doi.org/10.1093/bioinformatics/btu638.

(29) Love, M. I.; Huber, W.; Anders, S. Moderated Estimation of Fold Change and Dispersion for RNA-Seq Data with DESeq2. *Genome Biol* 2014, *15* (12). https://doi.org/10.1186/s13059-014-0550-8.

(30) Risso, D.; Ngai, J.; Speed, T. P.; Dudoit, S. Normalization of RNA-Seq Data Using Factor Analysis of Control Genes or Samples. *Nat Biotechnol* 2014, *32* (9), 896–902. https://doi.org/10.1038/nbt.2931.

(31) Yu, G. Using Meshes for MeSH Term Enrichment and Semantic Analyses. *Bioinformatics* 2018, *34* (21), 3766–3767. https://doi.org/10.1093/bioinformatics/bty410.

(32) Kutwin, M.; Sawosz, E.; Jaworski, S.; Kurantowicz, N.; Strojny, B.; Chwalibog, A. Structural Damage of Chicken Red Blood Cells Exposed to Platinum Nanoparticles and Cisplatin. *Nanoscale Res Lett* 2014, *9* (1), 257. https://doi.org/10.1186/1556-276X-9-257.

(33) Théry, C.; Witwer, K. W.; Aikawa, E.; Jose Alcaraz, M.; Anderson, J. D.; Andriantsitohaina, R.; Antoniou, A.; Bach, M.; Bachurski, D.; Baharvand, H.; Balaj, L.; Baldacchino, S.; Bauer, N. N.; Baxter, A. A.; Bebawy, M.; Beckham, C.; Bedina Zavec, A.; Benmoussa, A.; Berardi, A. C.;

Bergese, P.; Bielska, E.; Blenkiron, C.; Bobis-Wozowicz, S.; Boilard, E.; Boireau, W.; Bongiovanni, A.; Borràs, F. E.; Bosch, S.; Boulanger, C. M.; Breakefield, X.; Breglio, A. M.; Á Brennan, M.; Brigstock, D. R.; Brisson, A.; Broekman, M. L.; Bromberg, J. F.; Bryl-Górecka, P.; Buch, S.; Buck, A. H.; Burger, D.; Busatto, S.; Buschmann, D.; Bussolati, B.; Buzás, E. I.; Bryan Byrd, J.; Camussi, G.; Carter, D. R.; Caruso, S.; Chamley, L. W.; Chang, Y.-T.; Chen, C.; Chen, S.; Cheng, L.; Chin, A. R.; Clayton, A.; Clerici, S. P.; Cocks, A.; Cocucci, E.; Coffey, R. J.; Cordeiro-da-Silva, A.; Couch, Y.; Coumans, F. A.; Coyle, B.; Crescitelli, R.; Ferreira Criado, M.; Das, S.; Datta Chaudhuri, A.; de Candia, P.; De Santana Junior, E. F.; De Wever, O.; del Portillo, H. A.; Demaret, T.; Deville, S.; Devitt, A.; Dhondt, B.; Di Vizio, D.; Dieterich, L. C.; Dolo, V.; Paula Dominguez Rubio, A.; Dominici, M.; Dourado, M. R.; Driedonks, T. A.; Duarte, F. V; Duncan, H. M.; Eichenberger, R. M.; Ekström, K.; Andaloussi, S. EL; Elie-Caille, C.; Erdbrügger, U.; Falcón-Pérez, J. M.; Fatima, F.; Fish, J. E.; Flores-Bellver, M.; Försönits, A.; Frelet-Barrand, A.; Fricke, F.; Fuhrmann, G.; Gabrielsson, S.; Gámez-Valero, A.; Gardiner, C.; Gärtner, K.; Gaudin, R.; Song Gho, Y.; Giebel, B.; Gilbert, C.; Gimona, M.; Giusti, I.; Goberdhan, D. C.; Görgens, A.; Gorski, S. M.; Greening, D. W.; Christina Gross, J.; Gualerzi, A.; Gupta, G. N.; Gustafson, D.; Handberg, A.; Haraszti, R. A.; Harrison, P.; Hegyesi, H.; Hendrix, A.; Hill, A. F.; Hochberg, F. H.; Hoffmann, K. F.; Holder, B.; Holthofer, H.; Hosseinkhani, B.; Hu, G.; Huang, Y.; Huber, V.; Hunt, S.; Gamal-Eldin Ibrahim, A.; Ikezu, T.; Inal, J. M.; Isin, M.; Ivanova, A.; Jackson, H. K.; Jacobsen, S.; Jay, S. M.; Jayachandran, M.; Jenster, G.; Jiang, L.; Johnson, S. M.; Jones, J. C.; Jong, A.; Jovanovic-Talisman, T.; Jung, S. Journal of Extracellular Vesicles Minimal Information for Studies of Extracellular Vesicles 2018 (MISEV2018): A Position Statement of the International Society for Extracellular Vesicles and Update of the MISEV2014 Guidelines.

(34) Welsh, J. A.; Goberdhan, D. C. I.; O'Driscoll, L.; Buzas, E. I.; Blenkiron, C.; Bussolati, B.; Cai, H.; Di Vizio, D.; Driedonks, T. A. P.; Erdbrügger, U.; Falcon-Perez, J. M.; Fu, Q.; Hill, A. F.; Lenassi, M.; Lim, S. K.; Mahoney, M. G.; Mohanty, S.; Möller, A.; Nieuwland, R.; Ochiya, T.; Sahoo, S.; Torrecilhas, A. C.; Zheng, L.; Zijlstra, A.; Abuelreich, S.; Bagabas, R.; Bergese, P.; Bridges, E. M.; Brucale, M.; Burger, D.; Carney, R. P.; Cocucci, E.; Crescitelli, R.; Hanser, E.; Harris, A. L.; Haughey, N. J.; Hendrix, A.; Ivanov, A. R.; Jovanovic-Talisman, T.; Kruh-Garcia, N. A.; Ku'ulei-Lyn Faustino, V.; Kyburz, D.; Lässer, C.; Lennon, K. M.; Lötvall, J.; Maddox, A. L.; Martens-Uzunova, E. S.; Mizenko, R. R.; Newman, L. A.; Ridolfi, A.; Rohde, E.; Rojalin, T.; Rowland, A.; Saftics, A.; Sandau, U. S.; Saugstad, J. A.; Shekari, F.; Swift, S.; Ter-Ovanesyan, D.; Tosar, J. P.; Useckaite, Z.; Valle, F.; Varga, Z.; van der Pol, E.; van Herwijnen, M. J. C.; Wauben, M. H. M.; Wehman, A. M.; Williams, S.; Zendrini, A.; Zimmerman, A. J.; Théry, C.; Witwer, K.

W. Minimal Information for Studies of Extracellular Vesicles (MISEV2023): From Basic to Advanced Approaches. *J Extracell Vesicles* 2024, *13* (2). https://doi.org/10.1002/jev2.12404.

(35) Hettich, B. F.; Bader, J. J.; Leroux, J.-C. Encapsulation of Hydrophilic Compounds in Small Extracellular Vesicles: Loading Capacity and Impact on Vesicle Functions. *Adv Healthc Mater* 2022, *11* (5), 2100047. https://doi.org/https://doi.org/10.1002/adhm.202100047.

(36) Ringhieri, P.; Pannunzio, A.; Boccarelli, A.; Morelli, G.; Coluccia, M.; Tesauro, D. Effect of Cisplatin Containing Liposomes Formulated by Unsaturated Chain-Containing Lipids on Gynecological Tumor Cells. *J Liposome Res* 2016, *26* (4), 307–312. https://doi.org/10.3109/08982104.2015.1127257.

(37) Schulz, E.; Karagianni, A.; Koch, M.; Fuhrmann, G. Hot EVs - How Temperature Affects Extracellular Vesicles. *Eur J Pharm Biopharm* 2020, *146*, 55–63. https://doi.org/10.1016/j.ejpb.2019.11.010.

(38) Loconte, L.; Arguedas, D.; El, R.; Zhou, A.; Chipont, A.; Guyonnet, L.; Guerin, C.; Piovesana, E.; Vázquez-Ibar, J. L.; Joliot, A.; Théry, C.; Martín-Jaular, L. Detection of the Interactions of Tumour Derived Extracellular Vesicles with Immune Cells Is Dependent on EV-Labelling Methods. *J Extracell Vesicles* 2023, *12* (12), e12384. https://doi.org/10.1002/jev2.12384.

(39) Alvisi, G.; Paolini, L.; Contarini, A.; Zambarda, C.; Di Antonio, V.; Colosini, A.; Mercandelli, N.; Timmoneri, M.; Palù, G.; Caimi, L.; Ricotta, D.; Radeghieri, A. Intersectin Goes Nuclear: Secret Life of an Endocytic Protein. *Biochemical Journal* 2018, *475* (8), 1455–1472. https://doi.org/10.1042/BCJ20170897.

(40) Gurdal, H.; Tuglu, M. M.; Bostanabad, S. Y.; Dalkiliç, B. Partial Agonistic Effect of Cetuximab on Epidermal Growth Factor Receptor and Src Kinase Activation in Triple-Negative Breast Cancer Cell Lines. *Int J Oncol* 2019, *54* (4), 1345–1356. https://doi.org/10.3892/ijo.2019.4697.

(41) Patel, D.; Lahiji, A.; Patel, S.; Franklin, M.; Jimenez, X.; Hicklin, D. J.; Kang, X. Monoclonal Antibody Cetuximab Binds to and Down-Regulates Constitutively Activated Epidermal Growth Factor Receptor VIII on the Cell Surface. *Anticancer Res* 2007, *27* (5A), 3355–3366.

(42) Kryczka, J.; Kryczka, J.; Czarnecka-Chrebelska, K. H.; Brzeziańska-Lasota, E. Molecular Mechanisms of Chemoresistance Induced by Cisplatin in NSCLC Cancer Therapy. *Int J Mol Sci* 2021, *22* (16). https://doi.org/10.3390/ijms22168885.

(43) Bi, J.; Wu, Z.; Zhang, X.; Zeng, T.; Dai, W.; Qiu, N.; Xu, M.; Qiao, Y.; Ke, L.; Zhao, J.; Cao, X.; Lin, Q.; Chen, X. L.; Xie, L.; Ouyang, Z.; Guo, J.; Zheng, L.; Ma, C.; Guo, S.; Chen, K.;

Mo, W.; Fu, G.; Zhao, T. J.; Wang, H. R. TMEM25 Inhibits Monomeric EGFR-Mediated STAT3 Activation in Basal State to Suppress Triple-Negative Breast Cancer Progression. *Nat Commun* 2023, *14* (1). https://doi.org/10.1038/s41467-023-38115-2.

(44) Huang, G.; Li, H.; Zhang, H. Abnormal Expression of Mitochondrial Ribosomal Proteins and Their Encoding Genes with Cell Apoptosis and Diseases. *International Journal of Molecular Sciences*. MDPI AG November 2, 2020, pp 1–19. https://doi.org/10.3390/ijms21228879.

(45) Gabriel, M.; Delforge, Y.; Deward, A.; Habraken, Y.; Hennuy, B.; Piette, J.; Klinck, R.; Chabot, B.; Colige, A.; Lambert, C. Role of the Splicing Factor SRSF4 in Cisplatin-Induced Modifications of Pre-MRNA Splicing and Apoptosis. *BMC Cancer* 2015, *15* (1). https://doi.org/10.1186/s12885-015-1259-0.

(46) Kwon, Y. J.; Baek, H. S.; Ye, D. J.; Shin, S.; Kim, D.; Chun, Y. J. CYP1B1 Enhances Cell Proliferation and Metastasis through Induction of EMT and Activation of Wnt/β-Catenin Signaling via Sp1 Upregulation. *PLoS One* 2016, *11* (3). https://doi.org/10.1371/journal.pone.0151598.

(47) Chen, C.; Yang, Y.; Guo, Y.; He, J.; Chen, Z.; Qiu, S.; Zhang, Y.; Ding, H.; Pan, J.; Pan, Y. CYP1B1 Inhibits Ferroptosis and Induces Anti-PD-1 Resistance by Degrading ACSL4 in Colorectal Cancer. *Cell Death Dis* 2023, *14* (4). https://doi.org/10.1038/s41419-023-05803-2.

(48) Cheng, H.; Sharen, G.; Wang, Z.; Zhou, J. Lncrna Uca1 Enhances Cisplatin Resistance by Regulating Cyp1b1-Mediated Apoptosis via Mir-513a-3p in Human Gastric Cancer. *Cancer Manag Res* 2021, *13*, 367–377. https://doi.org/10.2147/CMAR.S277399.

(49) Lv, D.; Zhong, C.; Dixit, D.; Yang, K.; Wu, Q.; Godugu, B.; Prager, B. C.; Zhao, G.; Wang, X.; Xie, Q.; Bao, S.; He, C.; Heiland, D. H.; Rosenfeld, M. G.; Rich, J. N. EGFR Promotes ALKBH5 Nuclear Retention to Attenuate N6-Methyladenosine and Protect against Ferroptosis in Glioblastoma. *Mol Cell* 2023, *83* (23), 4334-4351.e7. https://doi.org/10.1016/j.molcel.2023.10.025.

(50) Tang, B.; Wang, Y.; Zhu, J.; Song, J.; Fang, S.; Weng, Q.; Yang, Y.; Tu, J.; Zhao, Z.; Chen, M.; Xu, M.; Chen, W.; Ji, J. TACE Responser NDRG1 Acts as a Guardian against Ferroptosis to Drive Tumorgenesis and Metastasis in HCC. *Biol Proced Online* 2023, *25* (1). https://doi.org/10.1186/s12575-023-00199-x.

(51) Bae, T.; Hallis, S. P.; Kwak, M. K. Hypoxia, Oxidative Stress, and the Interplay of HIFs and NRF2 Signaling in Cancer. *Experimental and Molecular Medicine*. Springer Nature March 1, 2024, pp 501–514. https://doi.org/10.1038/s12276-024-01180-8.

(52) Zhang, C.; Xu, H.; Zhou, Z.; Tian, Y.; Cao, X.; Cheng, G.; Liu, Q. Blocking of the EGFR-STAT3 Signaling Pathway through Afatinib Treatment Inhibited the Intrahepatic

Cholangiocarcinoma. *Exp Ther Med* 2018, *15* (6), 4995–5000. https://doi.org/10.3892/etm.2018.6038.

(53) Wood, P. A.; Hrushesky, W. J. Cisplatin-Associated Anemia: An Erythropoietin Deficiency Syndrome. *J Clin Invest* 1995, *95* (4), 1650–1659. https://doi.org/10.1172/JCI117840.

(54) Martinho, N.; Santos, T. C. B.; Florindo, H. F.; Silva, L. C. Cisplatin-Membrane Interactions and Their Influence on Platinum Complexes Activity and Toxicity . *Frontiers in Physiology* . 2019. https://www.frontiersin.org/articles/10.3389/fphys.2018.01898.

(55) Qi, L.; Luo, Q.; Zhang, Y.; Jia, F.; Zhao, Y.; Wang, F. Advances in Toxicological Research of the Anticancer Drug Cisplatin. *Chem Res Toxicol* 2019, *32* (8), 1469–1486. https://doi.org/10.1021/acs.chemrestox.9b00204.

Chapter 7 - General Conclusions and Future Perspectives

This thesis highlights significant advancements in understanding and utilizing extracellular vesicles (EVs) as therapeutic and diagnostic tools in nanomedicine.

EVs are biogenic nanoparticles of great interest in nanomedicine, due to their potential application in disease treatment and diagnosis, particularly in personalized medicine. However, their exploitation in these fields is hampered by a lack of knowledge about their physicochemical properties, and, in turn, interaction at their surface with other components of the nanostructured secretome, which play pivotal roles in defining EV biological identity and function.

Results reported in this thesis advance the current knowledge of EV interfacial phenomena by the application of innovative approaches and provide a novel candidate EV-based drug delivery system for multimodal treatment of Triple Negative Brest Cancer (TNBC). In particular:

1- The work presented in Chapter 3 explores the role of the biomolecular corona (BC) in the surface functionalization of EVs with targeting antibodies. It highlights the importance of rigorously controlling all functionalization steps, from antibody preparation to in vitro evaluation, which is often overlooked in the literature. We developed a modified antibody by adding a fluorophore and a clickable unit (DBCO), using it to functionalize red blood cell-derived EVs (REVs) via chemisorption (covalent binding) and physisorption (formation of a corona). Both methods preserved REV morphology, but only the clicked EVs maintained stability in physiological conditions. Physisorbed EVs, indeed, lost functionality due to the exchange of the antibody with serum proteins, making covalent attachment essential for maintaining specific EV recognition and ensuring effective therapeutic delivery. These findings emphasize the need to consider BC formation when designing surface-functionalized EVs for drug delivery.

2- In Chapter 4, we developed a fluorescence correlation spectroscopy (FCS)-based method BC formation on two different EV populations under physiological conditions. Using an *in situ* approach, free from separation biases, we spiked EVs with plasma proteins and tracked the hydrodynamic diameter fluctuations to evaluate BC dynamics. Our results revealed that BC formation differs between populations. Further analysis suggested that BC does not form through a simple layer-by-layer process but instead creates discrete protein aggregates. These insights highlight that BC formation is influenced by the EV's origin and surface properties, adding complexity to circulating EVs. From a practical

standpoint, these findings stress that BC dynamics should be carefully considered when using EVs for therapeutic or diagnostic purposes.

3- In Chapter 5, we examined the interactions between EVs and three classes of lipoproteins: HDL, LDL, and VLDL, using fluorescence cross-correlation spectroscopy (FCCS) in both PBS and plasma environments. Our results show that each lipoprotein interacts uniquely with EVs. HDL demonstrated the highest binding capacity, LDL, while showing a lower Bmax, exhibited the strongest binding affinity, with a non-cooperative, saturable interaction following a Langmuir-like model. In contrast, VLDL displayed the lowest Bmax and affinity, with negative cooperativity. These findings provide new insights into the biophysical dynamics of lipoprotein-EV interactions, emphasizing how lipoprotein size and structure influence binding patterns. This has important implications for designing EV-based therapeutic strategies, particularly considering the confirmed role of LDL-EV aggregates in biological processes like cancer metastasis.

4- Chapter 6 reports the development of a surface-engineered and cisplatin-loaded EV-based nanoplatform, which offers a promising advancement in targeted therapy for TNBC. By combining the cytotoxic effects of cisplatin with the EGFR-targeting capability of cetuximab (CTX) within an EV system, this approach significantly enhances drug delivery, reduces chemoresistance, and improves therapeutic outcomes. Our study shows that this nanoplatform boosts cisplatin uptake, facilitates its intracellular distribution, and demonstrates stronger cytotoxic effects compared to free cisplatin. Additionally, it engages specific molecular pathways, such as ferroptosis, offering a strategy to overcome TNBC's resistance. These results lay the groundwork for future research into this EV-based multimodal approach to enhance clinical outcomes for TNBC and other difficult-to-treat cancers.

In conclusion, this thesis provides a foundation for the future development of EV-based technologies in precision medicine. Continued research into optimizing EV functionalization, understanding interfacial phenomena like BC dynamics, and investigating specific EV interactions will be crucial for advancing these promising therapeutic and diagnostic platforms toward clinical application.

Chapter 8 – Appendix

This last chapter of the thesis is dedicated to the side projects I followed during my PhD. These activities regard topics that are not entirely pertinent to the aim of my PhD project and, for this reason, are reported here in the form of the first page of the related publication.

Acknowledgments

I sincerely thank all the people who helped and supported me during these three years. The work I presented here was possible thanks to:

- Prof. Annalisa Radeghieri, Section of Biotechnology, Department of Molecular and Translational Medicine, University of Brescia, mentor, supervisor, and tutor.
- Prof. Paolo Bergese, Section of Biotechnology, Department of Molecular and Translational Medicine, University of Brescia, mentor, supervisor, and tutor.
- Dr. Sergio Moya, supervisor and tutor during my visiting period at the CICbiomaGUNE, San Sebastian, Spain.
- Prof. Giuseppe Pomarico, Dr. Lucia Paolini, Dr. Andrea Zendrini, Dr. Miriam Romano, Dr. Rossella Zenatelli, Dr. Silvia Alacqua, Valentina Mangolini, Dr. Serena Ducoli, Selene Tassoni, Sabrina Scolari, Roberto Frigerio, and all the colleagues who worked with me during these three years.
- Dr. Marina Cretich, SCITEC-CNR, Milan, mentor, supervisor, and tutor.
- Dr. Alessandro Gori, Dr. Greta Bergamaschi, and Dr. Paola Gagni, SCITEC-CNR, Milan.
- All the colleagues and collaborators of the PRIN project "Development of a biotechnological nanoparticle platform for the delivery of antitumor therapies using Patient Derived-organoid library of Breast cancer" (Italian Ministry of Education, University and Research, PRIN 2017, Grant No. 2017E3A2NR_004, Scientific coordinator: prof. D.Prosperi, University of Milano-Bicocca, Italy): Prof. Serena Mazzucchelli, Prof. Fabio Corsi, Dr. Marco Severgnini, Dr. Ingrid Cifola, Lorena Signati, Prof. Luisa Fiandra, Dr. Linda Barbieri
- Prof. Marco Presta and Stefania Mitola, Coordinators of the Ph.D. Course in Precision Medicine, Department of Molecular and Translational Medicine, University of Brescia.